

**SYNTHESIS AND CHARACTERIZATION OF Au  
NANOCRYSTALS IN VARIOUS DIELECTRIC OXIDES  
FOR NONVOLATILE MEMORY APPLICATION**

**Ph.D. Thesis**

**ARUN VINOD**

**(ID No: 2013RPH9530)**



**DEPARTMENT OF PHYSICS**

**MALAVIYA NATIONAL INSTITUTE OF TECHNOLOGY JAIPUR**

**July 2019**

***Synthesis and Characterization of Au Nanocrystals in  
Various Dielectric Oxides for Nonvolatile Memory  
Application***

*Submitted in*

*fulfillment of the requirements for the degree of*

***Doctor of Philosophy***

**by**

**ARUN VINOD**

**(ID No: 2013RPH9530)**

Under the Supervision of

**Dr. Srinivasa Rao Nelamarri**



**DEPARTMENT OF PHYSICS**

**MALAVIYA NATIONAL INSTITUTE OF TECHNOLOGY JAIPUR**

**July 2019**



**©Malaviya National Institute of Technology Jaipur, India**

**2019**

***All Rights Reserved.***





*Dedicated to My Family*



## DECLARATION

I, **Arun Vinod**, declare that this thesis titled, “**Synthesis and characterization of Au nanocrystals in various dielectric oxides for nonvolatile memory application**” and the work presented in it, are my own. I confirm that:

- This work was done wholly or mainly while in candidature for a research degree at this university.
- Where any part of this thesis has previously been submitted for a degree or any other qualification at this university or any other institution, this has been clearly stated.
- Where I have consulted the published work of others, this is always clearly attributed.
- Where I have quoted from the work of others, the source is always given. With the exception of such quotations, this thesis is entirely my own work.
- I have acknowledged all main sources of help.
- Where the thesis is based on work done by myself, jointly with others, I have made clear exactly what was done by others and what I have contributed myself.

Date:

Arun Vinod

ID: 2013RPH9530

This page is intentionally left blank

## CERTIFICATE

This is to certify that the thesis entitled “*Synthesis and characterization of Au nanocrystals in various dielectric oxides for nonvolatile memory application*” being submitted by Mr. Arun Vinod (ID No: 2013RPH9530) is a bonafide research work carried out under my supervision and guidance in fulfillment of the requirement for the award of the degree of **Doctor of Philosophy** in the Department of Physics, Malaviya National Institute of Technology Jaipur, India. The matter embodied in this thesis is original and has not been submitted to any other University or Institute for the award of any other degree.

Place: Jaipur

Date:

Dr. Srinivasa Rao Nelamarri  
Assistant Professor  
Department of Physics  
MNIT Jaipur



## ACKNOWLEDGEMENTS

First, I would like to thank the Lord Almighty by whose grace I could achieve this destination. With the deepest sense of gratitude, I would like to thank Dr. Srinivasa Rao Nelamarri, Supervisor and Mentor, for his inspiring guidance. His support and spiritual dedication towards the work, extending well beyond the office hours, inspired me to all the stage of my research work.

I am highly thankful to Prof. K. Sachdev, Prof. S. K. Sharma, Dr. Kamendra Awasthi, Dr. Rahul Singhal, Dr. C. Periasamy for their valuable suggestions and guidance. I am highly grateful to Prof. K. C. Swami and Dr. Amar Patnaik who helped me to correlate course work with research and to all faculty members of Department of Physics, MNIT Jaipur for their continuous support and encouragement. I am also thankful to departmental staff members Mr. Firoz Khan, Mr. Ramkishore, Mr. Sunil Batra, Mr. Khem Singh and Mr. Ritesh Kumar Dadhich for their support to make the departmental activities easy and cheerful.

I am very thankful to my co-authors for valuable time, help and fruitful discussion. I am also thankful to Dr. Blessen Thomas, Dr. Lintu Rajan, Mr. Veeresh Kumar, Mr. Mahendra Singh Rathore, Mr. Shushant Kumar Singh, Mr. Himanshu Sharma, Mr. Radhe Shyam, Mr. Deepak Negi, Ms. Meghna Rathore, Ms. Renu Dhayal, Mr. Abey Thomas, Ms. Ivy Abraham, Mr. Ajin Joy, Ms. Rachana Gupta, Ms. Mamta Yadav and Mr. Vijaykumar Gali, my friends and lab mates.

I pay my sincere thanks to Mr. Selva Kumar, Mr. Anoop Srivastava, Mr. Umesh Nayak from Hind High Vacuum, for helping me to understand the complexities of vacuum systems and to solve issues related to Electron beam evaporation unit. I express my heartiest thanks to Mr. Ramesh Chandra Prajapati, Mr. Sachin Survey, Mr. Hitesh Sharma, Mr. Shubham Gautam, Mr. Mohtashim Reza, Mr. Chetanya Prakash, Mr. Amit Kumar Sharma, Mr. Bhupesh Kumar Sharma and Dr. Srinivas Yadav Material Research Center MNIT Jaipur, Mr. Jit Dutta, Materials Science Engineering, National Cheng Kung University, Taiwan, Mr. Varadharaja Perumal and Ms. Ashwini Kumari A. S., MNCF, Indian Institute of Science, Bengaluru, Mr. Sunil Ojha & Mr. G. R. Umapathy, Scientists, IUAC New Delhi, Prof. K. Sreenivas, Director, USIC, Univ. of Delhi, who always helped me to solve the problems facing with the characterization facilities.



I express my thanks to all research scholars within the department and outside, friends and well-wishers for their unconditional support and making the journey memorable.

In Bible it is written, ‘Remember your leaders, those who spoke to you the word of God. Consider the outcome of their way of life and imitate their faith’ (Hebrews 13:7); Far from home and dear ones always make you prone to spiritual and emotional weakness. Even though I was far away from home, I was fortunate to have a home in Jaipur through the fellowship, guidance and help from Jaipur Mar Thoma Church and various Christian Fellowship groups. I remember with gratitude my elders, brothers, sisters and children through whom I was able to see the works of my Lord and Savior Jesus Christ.

From deep of my heart, I remember my grand father Late Mr. Thomas C. Varughese, (former high school teacher, a Naval officer who faced World War II and a freedom fighter during Indian Independence) who was one of my inspirations to join Ph.D. in MNIT Jaipur. I deeply thank Anu Liju (Sister), Liju K Mathew (Brother-in-law), Rohan (nephew) and Ruth (niece) and Mr. A.V. Abraham (Father-in-law), Mrs. Beena Abraham (Mother-in-law) and Mr. Emil Abraham (Brother-in-law) for their patience and emotional support

I am thankful to my parents Mr. Vinod George and Shyni Vinod, and my wife Christine Sara Abraham, who was with me in every face of my life holding me together to their life, inspiring, and supporting me. Without my Family, I would not have made it this far in one piece. They have always encouraged me to believe myself, pursue my goals and for always being my strength to face every difficulty and challenge in my life.

Date:

Arun Vinod

## ABSTRACT

The aim of the work presented in this thesis is to investigate the effects of annealing temperature on synthesis and characterization of Au nanocrystals in various dielectric oxides for nonvolatile memory application.

In the present study, various dielectric oxide layers such as  $\text{SiO}_2$ ,  $\text{HfO}_2$  and  $\text{Al}_2\text{O}_3$  acting as tunneling and blocking layers were deposited using RF magnetron sputtering and Au charge trapping layer was deposited using e-beam evaporation technique. Subsequently, trilayer structures such as  $\text{HfO}_2/\text{Au}/\text{HfO}_2$ ,  $\text{SiO}_2/\text{Au}/\text{SiO}_2$  and  $\text{Al}_2\text{O}_3/\text{Au}/\text{Al}_2\text{O}_3$  were annealed in  $\text{N}_2$  atmosphere at various temperatures.

The structure, composition and electrical properties of trilayer structures are drastically affected by annealing temperature. Various characterization techniques such as transmission electron microscope, Rutherford backscattering spectroscopy, X-ray diffraction, X-ray photoelectron spectroscopy, current-voltage (I-V) and capacitance-voltage (C-V) measurements were employed to study the structure, composition and electrical properties. Transmission electron microscopic images reveal the formation of Au nanocrystals. Rutherford backscattering spectroscopy was used to estimate the thickness of the trilayer structure. X-ray photoelectron spectroscopy results confirm the presence of Au nanocrystals. Electrical measurements show an improvement in leakage characteristics with annealing. The memory window indicates the role of Au nanocrystals in charge storage characteristics of these trilayer structures. The advantages and limitations of annealing temperature on charge storage characteristics of Au nanocrystals integrated with various blocking and tunneling layers have been investigated in detail.



# Contents

<b>ACKNOWLEDGEMENTS</b>	<b>i</b>
<b>ABSTRACT</b>	<b>iii</b>
<b>Contents</b>	<b>iv</b>
<b>List of Tables</b>	<b>vii</b>
<b>List of Figures</b>	<b>viii</b>
<b>List of Abbreviations</b>	<b>xi</b>
<b>Chapter-1 Introduction</b>	<b>1-12</b>
1.1. Introduction to nanoscience and nanotechnology	2
1.2. Approaches: Bottom-up and Top-down	2
1.3. Classification of nanostructured materials	4
1.4. Synthesis of nanostructured materials	4
1.5. Significance of thin films	5
1.6. Memory devices	6
1.6.1. Volatile memory	6
1.6.2. Nonvolatile memory	7
1.7. Scaling and replacement of SiO <sub>2</sub>	7
1.8. Requirement and choice of dielectric oxide materials	7
1.9. Nanocrystal memories	9
1.10. Au nanocrystal memory	10
1.11. Motivation of thesis	10
1.12. Organization of thesis	10
<b>Chapter-2 Literature Review</b>	<b>13-22</b>
2.1. Introduction	14
2.1.1. Semiconductor nanocrystal based memories	14
2.1.2. Au nanocrystal based memories	17
2.2. Research gap	21
2.3. Objective of thesis	21

<b>Chapter-3 Materials and Methods</b>	<b>23-42</b>
3.1. Introduction	24
3.2. Materials	24
3.2.1 Silicon dioxide	24
3.2.2 Aluminium oxide	24
3.2.3 Hafnium oxide	25
3.2.4 Gold	25
3.3. Deposition methods	25
3.3.1 RF magnetron sputtering	25
3.3.2 Electron beam evaporation	28
3.4 Thermal annealing	30
3.5. Characterization techniques	31
3.5.1 Raman spectroscopy	31
3.5.2 Transmission electron microscopy	32
3.5.3 Atomic force microscopy	34
3.5.4 X-ray photoelectron spectrometry	36
3.5.5 X-ray diffraction	37
3.5.6 Rutherford backscattering spectrometry	39
3.5.7 Electrical characterization	41
<b>Chapter-4 Synthesis and characterization of Au nanocrystals in HfO<sub>2</sub> tunneling and blocking layers</b>	<b>43 - 64</b>
<b>4.1. Growth and optimization of HfO<sub>2</sub> thin films</b>	<b>44 - 53</b>
4.1.1. Introduction	44
4.1.2. Experimental details	45
4.1.3. Results and discussion	46
<b>4.2. Charge storage characteristic of Au nanocrystals in HfO<sub>2</sub> tunneling and blocking layers</b>	<b>53-64</b>
4.2.1. Introduction	53
4.2.2. Experimental details	54

4.2.3. Results and discussion	55
4.2.4. Summary	64
<b>Chapter-5 Electrical and compositional properties of SiO<sub>2</sub>/Au/SiO<sub>2</sub> trilayer structure</b>	<b>65-78</b>
5.1. Introduction	66
5.2. Experimental details	67
5.3. Results and discussion	68
5.4. Summary	77
<b>Chapter-6 Fabrication and characterization of Al<sub>2</sub>O<sub>3</sub>/Au/Al<sub>2</sub>O<sub>3</sub> for nonvolatile memory application</b>	<b>79-88</b>
6.1. Introduction	80
6.2. Experimental details	80
6.3. Results and discussion	81
6.4. Summary	88
<b>Chapter 7 Conclusions and future work plan</b>	<b>89-92</b>
7.1. Conclusions of thesis work	91
7.2. Scope of future work	91
<b>References</b>	<b>93-102</b>
<b>Appendix</b>	
A-List of publications	103-104
B-Research articles	105

## **Bio-data**



## List of Tables

		<b>Page No.</b>
Table 1.	The roughness, kurtosis and skewness values of pristine and annealed HfO <sub>2</sub> thin films	48





## List of Figures

<b>Figure No.</b>	<b>Figure title</b>	<b>Page No.</b>
1.1	Schematic illustrations of bottom-up and top down approaches	3
1.2	Classification of nanostructured materials	4
1.3	Different methods used to synthesize nanostructured materials	5
1.4	Types of memory	6
3.1	Schematic mechanism of sputtering	26
3.2	Schematic diagram of RF magnetron sputtering	27
3.3	Schematic diagram of electron beam evaporation system	29
3.4	Typical vacuum furnace system	30
3.5	Schematic diagram of Raman spectrometer	32
3.6	Schematic illustration of TEM	33
3.7	Schematic diagram of basic AFM setup	35
3.8	Schematic diagram of XPS	37
3.9	Schematic diagram of X-ray diffractometer	39
3.10	Schematic illustration of RBS experimental setup	41
4.1	Raman spectra of HfO <sub>2</sub> thin films i) as-deposited and ii) annealed at a) 200°C b) 400°C c) 600°C.	47
4.2	X-ray diffraction pattern of as-deposited and annealed HfO <sub>2</sub> thin films	48
4.3	Surface morphology of as-deposited and annealed HfO <sub>2</sub> thin films	49
4.4	Survey XPS spectra of as-deposited and annealed HfO <sub>2</sub> thin films	50
4.5	Core elemental XPS spectra of Hf 4f regions of as-deposited and annealed HfO <sub>2</sub> thin films	51
4.6	I-V characteristics of as-deposited and annealed HfO <sub>2</sub> thin films	52
4.7	Schematic illustration of NVM structure	55
4.8	XRD pattern of NVM structure before and after annealing	56
4.9	a) TEM images of Au in HfO <sub>2</sub> and SAED pattern of b) HfO <sub>2</sub> & c) Au d) typical HR image of Au nanocrystals (e-f) EDX mapping images and h) STEM image of Au	57

4.10	Surface morphologies of HfO <sub>2</sub> blocking layer a) as-deposited b) annealed at 650°C c) annealed at 750°C and d) annealed at 850°C	58
4.11	Core elemental XPS spectra of Hf blocking layer of NVM structure a) as-deposited b) annealed at 750°C and c) annealed at 850°C	59
4.12	Core elemental XPS spectra of Au charge trapping layer of NVM structure a) as-deposited and annealed at b) 750°C and c) 850°C	60
4.13	Core elemental XPS spectra of HfO <sub>2</sub> tunneling layer of NVM structure a) as-deposited and annealed at b) 750°C and c) 850°C	61
4.14	Rutherford backscattering spectra of NVM structure annealed at 850°C	62
4.15	Leakage current versus applied voltage for as-deposited and annealed NVM structure	63
4.16	The capacitance-voltage curve of a) trilayer capacitor with Au nanocrystals and b) reference sample (HfO <sub>2</sub> only) without Au nanocrystals annealed at 850°C	64
5.1	Schematic illustration of SiO <sub>2</sub> /Au/SiO <sub>2</sub> NVM structure	68
5.2	a) TEM images of Au in SiO <sub>2</sub> b) Au SAED pattern c) HRTEM image of Au nanocrystal in SiO <sub>2</sub> annealed at 850°C	69
5.3	STEM – EDX mapping image of Au, Si and O	70
5.4	Surface morphology of blocking layer before and after annealing	71
5.5	Rutherford backscattering spectrum of SiO <sub>2</sub> /Au/SiO <sub>2</sub> structure annealed at 850°C	72
5.6	XRD pattern of trilayer structure	72
5.7	Leakage current - voltage characteristics of trilayer structure before and after annealing	73
5.8	C-V hysteresis of NVM structure with Au nanocrystals in SiO <sub>2</sub> tunneling and blocking layers	74
5.9	XPS spectra of as-deposited blocking, trapping and tunneling layer	75
5.10	XPS spectra of blocking, trapping and tunneling layer annealed at 750°C	76
5.11	XPS spectra of blocking, trapping and tunneling layer annealed at 850°C	76
6.1	Schematic illustration of Au nanocrystals sandwiched between Al <sub>2</sub> O <sub>3</sub> tunneling and blocking layers	81

6.2	a) TEM images of Au in Al <sub>2</sub> O <sub>3</sub> b) SAED pattern of Au and c) HR image of Au nanocrystals	81
6.3	Rutherford backscattering spectrum of Al <sub>2</sub> O <sub>3</sub> /Au/Al <sub>2</sub> O <sub>3</sub> annealed at 850°C	82
6.4	XRD pattern of as-deposited and annealed NVM structure	83
6.5	Leakage current–voltage characteristics of Al <sub>2</sub> O <sub>3</sub> /Au/Al <sub>2</sub> O <sub>3</sub> structure before and after annealing	84
6.6	C-V hysteresis of NVM structure with Au nanocrystals annealed at 850°C	85
6.7	XPS spectra of blocking, trapping and tunneling layers of as-deposited Al <sub>2</sub> O <sub>3</sub> /Au/Al <sub>2</sub> O <sub>3</sub> trilayer structure	86
6.8	XPS spectra of blocking, trapping and tunneling layers of Al <sub>2</sub> O <sub>3</sub> /Au/Al <sub>2</sub> O <sub>3</sub> trilayer structure annealed at 750°C	86
6.9	XPS spectra of blocking, trapping and tunneling layers of Al <sub>2</sub> O <sub>3</sub> /Au/Al <sub>2</sub> O <sub>3</sub> trilayer structure annealed at 850°C	87



## List of abbreviations

<b>Ge</b>	Germanium
<b>Si</b>	Silicon
<b>HfO<sub>2</sub></b>	Hafnium oxide or Hafnia
<b>SiO<sub>2</sub></b>	Silicon dioxide or Silica
<b>Al<sub>2</sub>O<sub>3</sub></b>	Aluminum oxide or Alumina
<b>Au</b>	Gold
<b>NVM</b>	Nonvolatile memory
<b>RAM</b>	Random Access Memory
<b>SRAM</b>	Static Random Access Memory
<b>DRAM</b>	Dynamic Random Access Memory
<b>EPROM</b>	Erasable Programmable Read Only Memory
<b>EEPROM</b>	Electrically Erasable Programmable Read Only Memory
<b>NCs</b>	Nanocrystals
<b>CVD</b>	Chemical Vapor Deposition
<b>PLD</b>	Pulsed Laser Deposition
<b>ALD</b>	Atomic Layer Deposition
<b>RBS</b>	Rutherford backscattering spectrometry
<b>XRD</b>	X-ray diffraction
<b>XPS</b>	X-ray Photoelectron Spectroscopy
<b>EDX</b>	Energy Dispersive X-ray Analysis
<b>TEM</b>	Transmission Electron Microscopy
<b>AFM</b>	Atomic force microscopy
<b>C-V</b>	Capacitance-Voltage
<b>I-V</b>	Current-Voltage
<b>a. u.</b>	arbitrary units / arb. units

# **Chapter 1**

## **Introduction**

## **1.1 Introduction to nanoscience and nanotechnology**

Nanoscience and nanotechnology are considered as one of the most promising interdisciplinary research fields [1]. Nanoscience mainly deals with the study that is related to the phenomena and manipulation of materials and their properties at atomic, molecular and macromolecular scale. Whereas, nanotechnology deals with the practical application, design, production and characterization of materials with nanoscale dimensions [2]. The properties at nanoscale drastically change as compared to bulk counterparts. The two main reasons for such a change are large surface to volume ratio and quantum size effects. Large surface area of nanomaterials leads to more chemical reactions and quantum effects dominate in materials at nanoscale than bulk resulting in the modification of properties of the materials. Currently, nanoscience and nanotechnology find application in various research areas such as information and communication technology, health, metrology, applied sciences and engineering [1,2].

Although the study and application of nanomaterials could be traced back to ancient civilizations, the present-day importance of nanoscience and nanotechnology is due to its ability to synthesize, characterize and manipulate these nanomaterials for various applications.

## **1.2 Approaches: Bottom-up and Top-down**

Two methods of approach for the synthesis of nanomaterials are bottom-up and top-down [3] and are schematically illustrated in figure 1.1 [4]. In bottom up approach, the synthesis occurs by adding up smaller building blocks to form nanomaterials. The material build-up initiates from atom by atom, molecule by molecule and cluster by cluster to form nanostructures. The deposition of thin films is an example for bottom-up approach. In thin films deposition, the formation of thin films occurs due to nucleation and growth process. Thus, different synthesis processes often result in variation of properties for the same material. The nanomaterials synthesized using bottom-up approach are in a state closer to the thermodynamic equilibrium due to the reduction of Gibbs free energy. Thus, films with less defects, better homogeneity and chemical composition could be obtained.



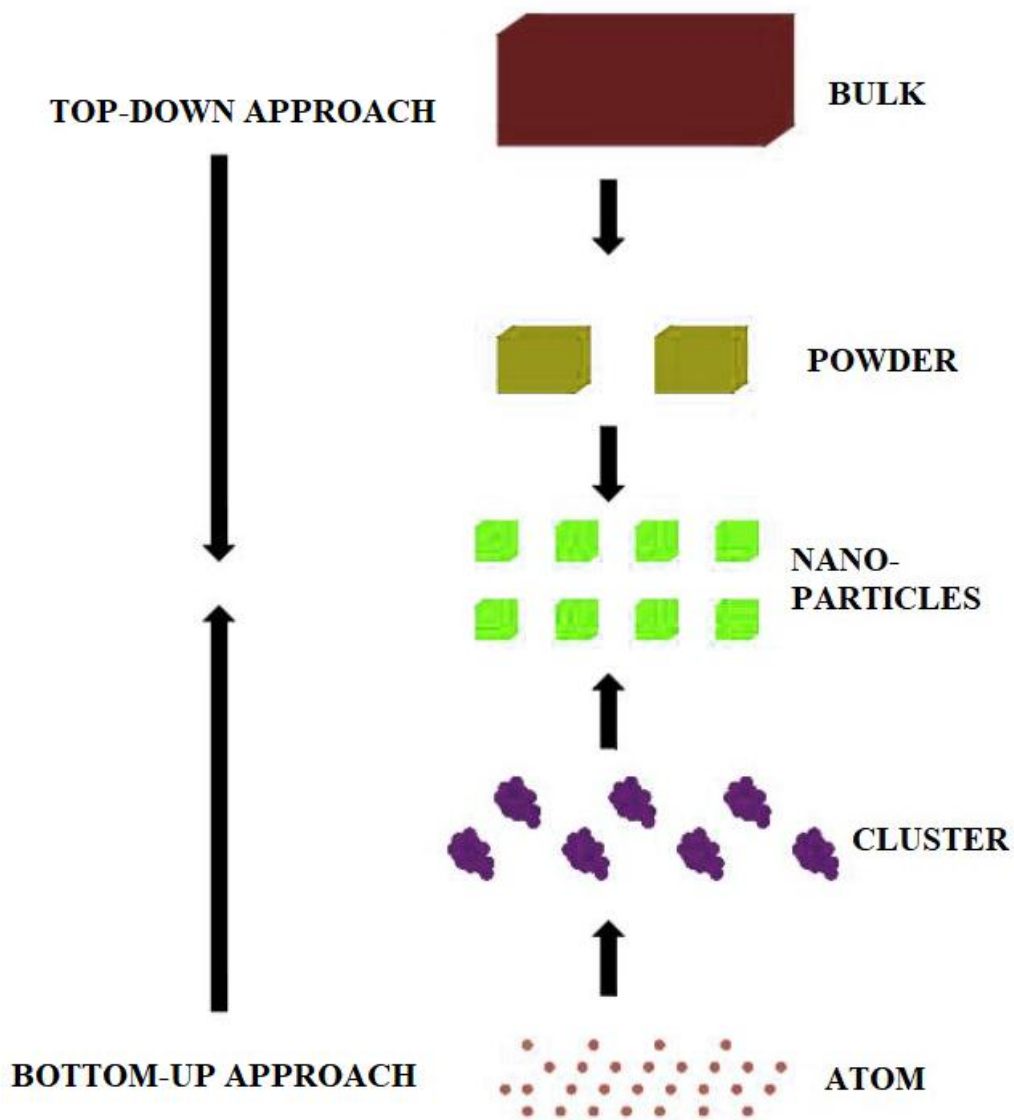


Figure 1.1 Schematic illustrations of bottom-up and top-down approaches

On the other hand, top-down approach involves the decrease in size of a large material to smaller materials until desired nanomaterial is formed. One of the best examples is the synthesis of nanoparticles using mechanical ball milling. In mechanical ball milling, the powder material is ball milled to create nanoparticles. The top-down approach mostly results in surface defects, contamination and internal stress formation. Regardless the imperfections, top-down approach plays a crucial role in nanomaterial synthesis and fabrication.

### 1.3 Classification of nanostructured materials

Generally, many methods prevail over the classification of nanostructured materials such as dimensionality, aspect ratio, composition and agglomeration [5]. The first classification idea of nanostructure materials with respect to dimensionality was given by Gleiter [6,7]. The method could not classify various nanostructured materials like fullerene, flowers and nanotubes. Better classification of nanostructured materials (figure 1.2) as 0D, 1D, 2D and 3D was proposed by Pokropivny and Skorokhod [8]. 0D nanostructured materials are particles with all dimensions within nanometer scale like quantum dots and clusters. 1D nanostructured materials have length of the order of few nanometres to few microns like nanofibers, nanorod, nanowires, and nanotubes. 2D nanostructures have one dimension in nanoscale and other two dimensions outside of the nanometric range. Examples for 2D nanostructures include thin films, coatings, nanosheets, nanoplates, etc. Nanomaterials in 3D class have all dimensions more than nanoscale like powder, nanoball, nanoflowers, etc [6].

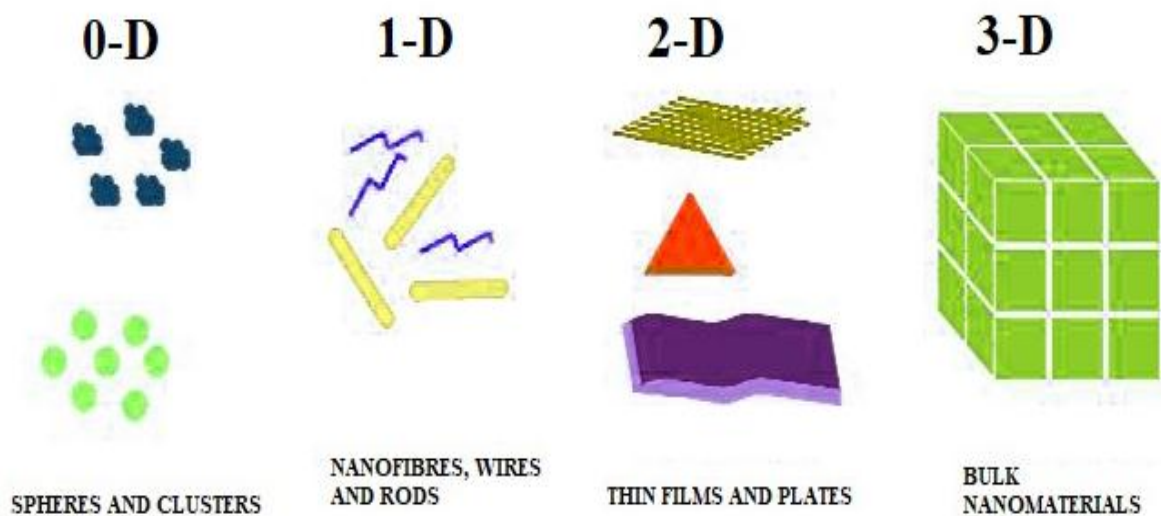


Figure 1.2 Classification of nanostructured materials

### 1.4 Synthesis of nanostructured materials

The unique properties exhibited by various nanostructured materials than their bulk counterparts have attracted great technological and scientific interest. Considerable changes in properties of same materials occur with a change in deposition methods. For

the synthesis and fabrication of nanostructured materials, various physical and chemical methods (shown in figure 1.3) are used. Elaborate description on sputtering and electron beam evaporation method is given in Chapter 3.

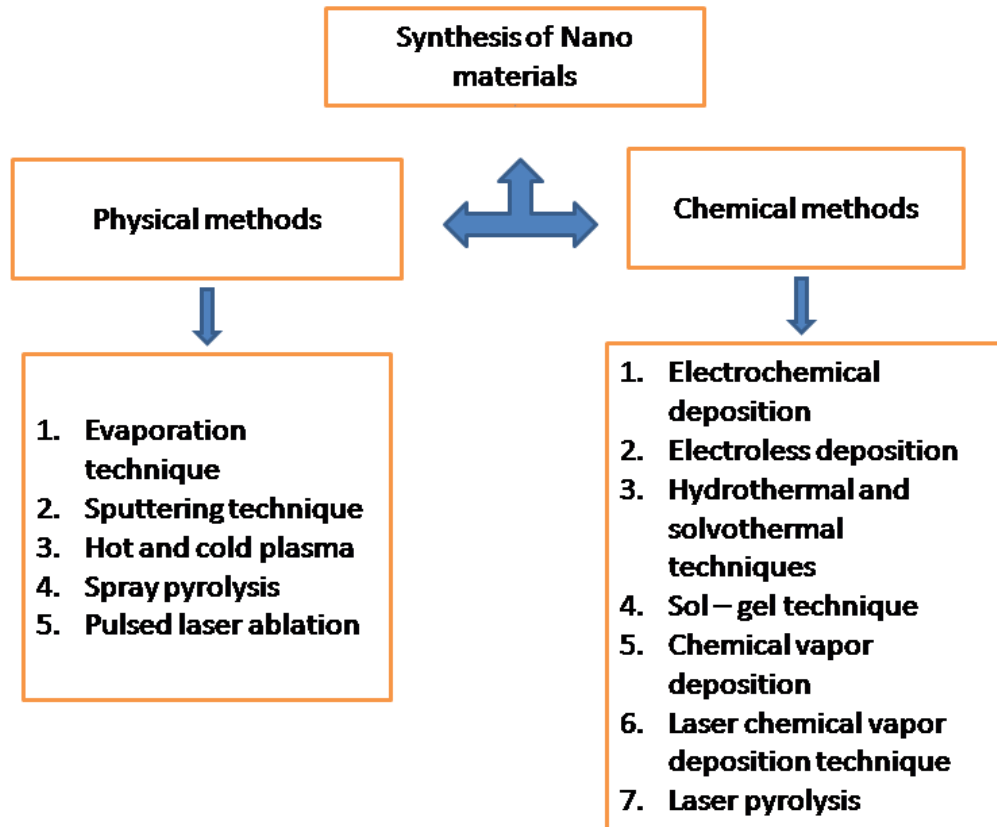


Figure 1.3 Different methods used to synthesize nanostructured materials

## 1.5 Significance of thin films

Films with a thickness from few to hundred nanometres come under the category of thin films and fall in the 2D nanomaterials. The progress of modern technology has been explicitly dependent on thin films. Thin films have been used for various applications such as storage, photonics, optoelectronics, electronics and sensing [9–11]. Memory device application of thin films has attracted much attention in recent years.

## 1.6 Memory devices

Memory is the continued possession of data which can be encoded, stored and retrieved whenever required. The different types of memory are listed in figure 1.4. Basically, memory is of two types – primary/volatile memory and secondary/nonvolatile memory [12]. Random access memory (RAM) comes under volatile memory and read only memory (ROM) is a nonvolatile memory.

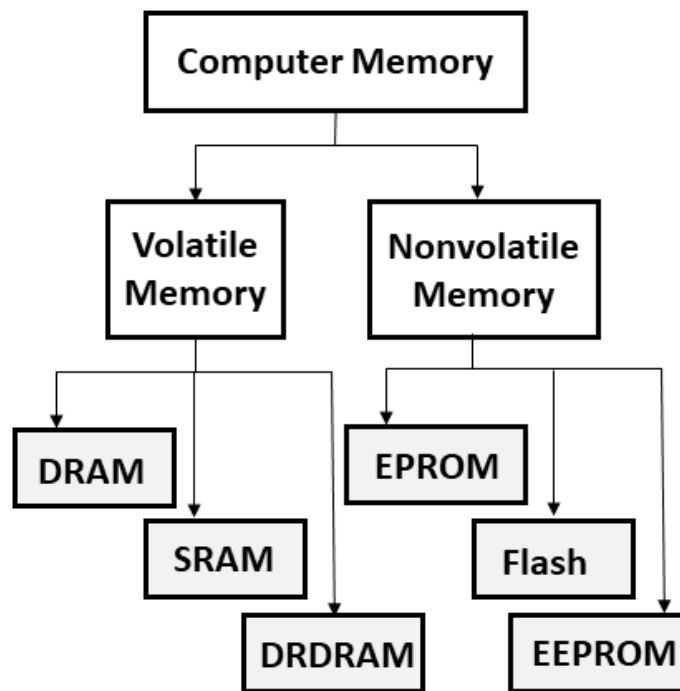


Figure 1.4 Types of memory

### 1.6.1 Volatile memory

Volatile memory or primary memory is a semiconductor technology that requires power source to function and maintain the stored information. The main advantage of volatile memory is that it protects the sensitive data and functions fast. But the drawback of such memory is that the data gets quickly and permanently deleted when the power failure is happened in the system. Major examples for volatile memory are RAM, SRAM and DRAM.

## 1.6.2 Nonvolatile memory

Nonvolatile memory or secondary memory is a permanent memory which retains data even when power is unavailable. It is mainly used as an external storage like floppy disk, flash devices, magnetic cache device and magnetic disks. ROM, EPROM, PROM, EEPROM and flash are examples of nonvolatile memory devices. Role of Au nanocrystals (NCs) in various oxide layers for nonvolatile memory application is explained in the present thesis work.

## 1.7 Scaling and replacement of SiO<sub>2</sub>

To meet the technology scaling in solid state memory devices, miniaturization of SiO<sub>2</sub> dielectric layer created tunneling problem and aging, which marked one of the biggest challenges in the semiconductor technology.

Two basic needs for new gate insulator materials are to prevent electron tunneling but permeable to electric field [13]. Different solutions were sorted out to tackle the current crisis of further shrinkage of the gate dielectric. The alternative for such a material was attained with high k dielectric. Some of these dielectric oxides were used as the insulation layer but found to have trapped charges at the interface between the dielectric and the gate electrode. High k oxides of Hafnium and Zirconium showed more stable electrical characteristics as compared to their counterparts deposited via sputtering and chemical vapor deposition.

## 1.8 Requirement and choice of dielectric oxide materials

Si is mainly used in semiconductor industry due to SiO<sub>2</sub> (used as gate oxide layer). SiO<sub>2</sub> is a good insulator, has less electronic defects and it can be easily grown on Si. But, with the scaling down of SiO<sub>2</sub> layer for faster and reliable electronic devices resulted in electron tunneling. Thus, the incorporation of high k dielectrics was proposed. Effective introduction of these materials in device technology faced problems such as occurrence of high defect density, continuity in scaling down of effective oxide thickness, loss of carrier

mobility, gate voltage threshold shifts and need for better gate electrode [14]. Thus, for device application it is required to optimize the oxides to achieve high performance.

To replace SiO<sub>2</sub> as gate dielectric material, there must be six fold requirements related to the new oxide material [15,16].

1. **Dielectric constant:** The dielectric constant and energy band gap play a vital role with band offset conditions and band alignments. The dielectric constant tends to be inversely proportional to band gap. The dielectric constant must be over 10, most preferably between 20-25, which makes HfO<sub>2</sub> more preferred than other high k oxides.
2. **Thermodynamic stability:** Oxides must be stable with Si without forming any additional oxide layer or any silicides.
3. **Kinetic stability:** The oxides must withstand a processing temperature around 1000°C without forming any leakage centres. Crystalline oxides cause higher leakage through grain boundary and can form silicates as compared to amorphous materials. Al<sub>2</sub>O<sub>3</sub> is reasonably preferred in this category.
4. **Insulator:** The selected oxide must be an excellent insulator. As compared to the SiO<sub>2</sub> (with band gap 9 eV) the new oxide material must have band gap more than 5 eV with consideration of band offsets conditions. This limits most of dielectric oxide material except Al<sub>2</sub>O<sub>3</sub>, HfO<sub>2</sub>, ZrO<sub>2</sub> and various lanthanum derivative dielectric oxides.
5. **Interface:** The interface of oxide-Si plays a crucial role for device performance. Usually, roughness, grain boundaries and defects occurring at the interface reduce the quality. The use of epitaxially grown crystalline films or the use of amorphous films helps to attain the desired interface quality.
6. **Defects:** Mostly in dielectric layers the defects are mainly created by the excess or deficiency of oxygen or due to the presence of impurities. Charges can be trapped in these defects resulting low performance, scattering and causing reliability issues for the device.

The use of SiO<sub>2</sub> as tunneling and blocking oxide layers in nonvolatile memory needed replacement for better memory performance due to leakage issues related to scaling down. Among various dielectric oxides, Al<sub>2</sub>O<sub>3</sub> and HfO<sub>2</sub> are widely studied as an alternative for SiO<sub>2</sub> tunneling and blocking layers. Various properties such as high band gap and dielectric constant make Al<sub>2</sub>O<sub>3</sub> and HfO<sub>2</sub> as promising materials to block unwanted charge leakages [16–18]. Thus, Au based Al<sub>2</sub>O<sub>3</sub> and HfO<sub>2</sub> trilayer structures have the potential to achieve better memory performance than conventional Au embedded SiO<sub>2</sub> structures.

## 1.9 Nanocrystal memories

After the introduction of solid-state memories in late 1960s, floating gate design generated immense interest among various nonvolatile memory structures. The information or data is stored as charge in a layer that is electrically insulated from channel and conventional gate electrode. The injecting or removing charges in this layer is referred to as writing or erasing. Restriction in further scaling down and improvement of charge storage are the prominent limitations of conventional floating gate devices. Urge for devices that are smaller, reliable and with increased storage capacity led to the scaling of gate dielectric layer between the channel and floating layer to 9-11 nm [19,20]. This layer is referred as tunneling layer. The thickness of dielectric layer that separated the control gate and floating gate (control layer) is usually 15-20 nm.

Floating layers in conventional nonvolatile memory devices are mainly continuous and even a small discharge path in tunneling oxide may affect the nonvolatility of the memory. Better method to solve this problem is to introduce distributed charge storage centres rather than conventional floating layer. This concept was successfully implemented by Tiwari et. al. [21], by introducing a new memory structure with Si NCs as charge storing element. In the NC based memories, the charge is stored in crystalline NCs that are mutually isolated and discrete rather than in a continuous layer.

## 1.10 Au nanocrystal memory

Ge NCs have attracted great significance than Si NCs in nonvolatile memory due to its smaller band gap and high dielectric constant. Further, improvement in device performance was achieved using metal NCs as storage nodes. Metal NCs are better than semiconductor counterparts due to their ability to enhance the electric field, high density of states, better control over nanocrystal size and provide better work-function engineering [22]. Among various metals, Au is one of the promising materials due to its high work function, low process temperature, chemical stability, ease of synthesis, restricts from oxidation and reactions with dielectric layers [23,24].

## 1.11 Motivation of the thesis

Since many decades, SiO<sub>2</sub> is used in semiconductor industry due to its excellent interface with Si, amorphous nature, less electronic defects and stability. Scaling down of gate oxide (SiO<sub>2</sub>) in solid state memory resulted in leakages. One of the possible solutions is to replace thin SiO<sub>2</sub> layer with physically thicker oxide that could provide better capacitance. The use of high dielectric oxide materials (such as Al<sub>2</sub>O<sub>3</sub> and HfO<sub>2</sub>) can provide physical thicker oxide layer as compared to SiO<sub>2</sub> due to its excellent electrical properties, dielectric constant, prevention of diffusion of metal in tunneling and blocking layers and band gap values. Furthermore, the memory characteristics can be increased by integrating Au NCs with these oxides.

## 1.12 Organization of thesis

**Chapter 1:** This chapter gives an outline of the thesis work and mainly explains about nanotechnology and the importance of metal NCs for nonvolatile memory applications. The general introduction, motivation of the work and organization of thesis are also mentioned.

**Chapter 2:** This chapter describes literature related to semiconductor and metal NCs based nonvolatile memories and ends with the research gap and objectives of the present thesis work.



**Chapter 3:** This chapter explains about materials and methods that are used in this thesis work. The methods are presented by a general introduction and instrumentation. Basic properties of various materials ( $\text{SiO}_2$ ,  $\text{Al}_2\text{O}_3$ ,  $\text{HfO}_2$  and Au) and working principle of deposition methods (RF magnetron sputtering and electron beam evaporation) used in this work are discussed. Finally, various characterization techniques such as X-ray diffraction (XRD), Rutherford backscattering spectrometry (RBS), atomic force microscopy (AFM), transmission electron microscopy (TEM), electrical characterization (I-V and C-V) and X-ray photoelectron spectroscopy (XPS) are also explained.

**Chapter 4:** This chapter is divided into two sections:

**4a) Growth and optimization of  $\text{HfO}_2$  thin films**

**4b) Charge storage characteristic of Au nanocrystals in  $\text{HfO}_2$  tunneling and blocking layers**

**4a) Growth and optimization of  $\text{HfO}_2$  thin films**

In this section, the effects of annealing temperature on hafnia thin films prepared by RF sputtering have been discussed. Thin films of hafnium oxide were deposited onto p-type Si substrates and annealed at different temperatures in air atmosphere to understand the effect of annealing temperature on the structural, morphological, compositional and electrical properties. This work correlates stoichiometry, surface roughness and crystallinity for better electrical application. This work is published by A. Vinod *et. al.* in *Vacuum 155 (2018) 339–344*.

**4b) Charge storage characteristic of Au nanocrystals in  $\text{HfO}_2$  tunneling and blocking layers**

In this section, the fabrication and characterization of Au charge trapping layer between two hafnium oxide tunneling and blocking layers are discussed. The aim of this work is to investigate the role of annealing temperature on charge storage characteristics of Au NCs with  $\text{HfO}_2$  tunneling and blocking layers. The structural, compositional and electrical properties of the trilayer structure are drastically affected by the annealing temperature. This work is published in *Superlattices and Microstructures* by Arun Vinod,

*Mahendra Singh Rathore, Srinivasa Rao Nelamarri in Superlattices and Microstructures 120 (2018) 616-628.*

### **Chapter 5: Electrical and compositional properties of SiO<sub>2</sub>/Au/SiO<sub>2</sub> trilayer structure**

In this chapter, electrical and compositional properties of SiO<sub>2</sub>/Au/SiO<sub>2</sub> for nonvolatile memory application are investigated. The blocking (20 nm) and tunneling oxide (10nm) layers were deposited using RF magnetron sputtering and the charge trapping layer of Au (3nm) was deposited using electron beam evaporation. The aim of this study is to fabricate Au charge trapping layer sandwiched between SiO<sub>2</sub> tunneling and blocking layers and to understand the effect of annealing temperature on various characteristics of trilayer structure. This work is published by *Arun Vinod, Mahendra Singh Rathore, Srinivasa Rao Nelamarri in Applied Physics A 124 (2018) 548.*

### **Chapter 6: Fabrication and characterization of Al<sub>2</sub>O<sub>3</sub>/Au/Al<sub>2</sub>O<sub>3</sub> for nonvolatile memory application**

This chapter demonstrates the structural, electrical and compositional properties of Au NCs embedded between Al<sub>2</sub>O<sub>3</sub> tunneling and blocking layers. The aim of this study is to fabricate and understand various properties Al<sub>2</sub>O<sub>3</sub>/Au/Al<sub>2</sub>O<sub>3</sub> trilayer structure.

### **Chapter 7: Conclusions and future work plan**

In conclusion, the present thesis work demonstrates the effect of annealing temperature on nonvolatile memory device structures such as HfO<sub>2</sub>/Au/HfO<sub>2</sub>, SiO<sub>2</sub>/Au/SiO<sub>2</sub> and Al<sub>2</sub>O<sub>3</sub>/Au/Al<sub>2</sub>O<sub>3</sub>. The role of annealing temperature on structural, electrical and compositional properties was systematically investigated. The charge storage behaviour of Au NCs embedded in various oxide layers with annealing temperature is confirmed with memory window. This chapter also gives an outlook on the future aspects of the work to be carried out along the same direction.

# Chapter 2

## *Literature Review*

## 2.1 Introduction

In recent years, the growth and widespread of technology led to an increased demand for memories with high speed, density storage, reliability and low power consumption [25]. Because of device size scalability, alternative dielectric materials capable of replacing  $\text{SiO}_2$  in memory devices are sought [26]. High dielectric oxide in replacement of  $\text{SiO}_2$  helps in the reduction of leakage current and can improve the memory performance [16]. Furthermore, the memory performance of the device is increased using NCs [27]. Si NCs attained great importance in nonvolatile memory device as compared to conventional nonvolatile memories [27]. Si NCs were replaced by Ge NCs due to their superior properties related memory characteristics [28]. Recently, metal NCs (esp. Au NCs) are preferred more than semiconductor counterparts in nonvolatile memory application for achieving better work function engineering, high density of states, etc [29]. This chapter presents an overview of research work that was reported for the fabrication and characterization of various nonvolatile memory structures.

### 2.1.1 Semiconductor nanocrystal based memories

Fabrication and characterization of Si nanocrystal memory device with  $\text{HfO}_2$  tunneling and blocking oxide layers using CVD were reported for the first time by Lee et. al. Si NCs were grown on  $\text{HfO}_2$  tunneling layer at  $600^\circ\text{C}$ . Si NCs formation on  $\text{HfO}_2$  and  $\text{SiO}_2$  layer under similar growth conditions were compared. It was reported that more denser and smaller Si NCs were formed in  $\text{HfO}_2$  layer than in  $\text{SiO}_2$  layers and the observation indicated that  $\text{HfO}_2$  provides more reaction centres for Si NCs formation than  $\text{SiO}_2$  [30].

The influence of Si NCs on the electrical property of  $\text{SiO}_2/\text{SiO}_x/\text{SiO}_2$  multilayer stack was reported by Lu et. al. Si NCs were prepared using high temperature annealing by varying the oxygen concentration from 0.9 to 1.63 in  $\text{SiO}_x/\text{SiO}_2$  multilayer structure. For the fabrication of  $\text{SiO}_2/\text{SiO}_x/\text{SiO}_2$  multilayer stack,  $\text{SiO}_2$  tunneling oxide layer was deposited prior to the deposition of  $\text{SiO}_x$  layer by evaporation of SiO powder under different oxygen pressures. The multilayer structure was completed by depositing  $\text{SiO}_2$  control oxide and annealed at  $1100^\circ\text{C}$  in  $\text{N}_2$  atmosphere to form Si NCs in  $\text{SiO}_2$  matrix. The charge trapping, storing and de-trapping to and from Si NCs were observed in the C-V hysteresis curve. The

results indicate that oxygen pressure is one of the influential parameters for attaining nanocrystal density, which plays a crucial role in charge storage behaviour of the multilayer structure [31].

The effect of annealing environment on the structural and electrical properties of Si NCs embedded SiO<sub>2</sub> was reported by Normand et. al. Si ions were implanted on SiO<sub>2</sub> thin films to a dose of  $2 \times 10^{16}$  ions/cm<sup>2</sup> with an energy of 1keV. The samples were annealed at various environments such as N<sub>2</sub> and N<sub>2</sub> + O<sub>2</sub>. It was observed that the samples annealed in N<sub>2</sub> and O<sub>2</sub> environment exhibit better flat band voltage shift than samples annealed in pure N<sub>2</sub> environment. This increase in flat band voltage is reported due to the enhancement of overall oxide quality and the increased control oxide thickness. Improvement in electrical behaviour of samples annealed in N<sub>2</sub> and O<sub>2</sub> environment was observed for current-voltage characteristics. The study demonstrates that electrical characteristics of nonvolatile memory devices can be improved with low energy Si ion implantation and annealing in diluted oxygen environment [32].

The characteristics and performance of Si nanocrystal based nonvolatile device with thin and thick tunneling oxide were investigated. The SiO<sub>2</sub> tunneling oxide was thermally grown and Si ions were implanted into SiO<sub>2</sub> tunneling layer. Additional SiO<sub>2</sub> (blocking) layer was deposited using low pressure chemical vapour deposition and the structure was annealed at 1000°C to induce nanocrystal formation in N<sub>2</sub> ambient. Charge trapping behaviour due to Si NCs was observed from C-V curve. Results showed that the structure with thin tunneling oxide shows better writing/erasing time than thicker oxide [33].

S. Choi et. al proposed fabrication of charge trapping layer of SiN with Si NCs. The purpose of incorporating Si NCs was to increase the trap density. Si ions were implanted on Si rich SiN layer using low energy Si plasma immersion ion implantation and the formation of Si NCs at 1000°C was confirmed using secondary ion mass spectroscopy (SIMS). C-V measurements of three devices with different charge trapping layers such as Si rich SiN, SiN, and Si NCs in SiN were compared to understand memory characteristics. Larger C-V curve was obtained for devices incorporating SiN with Si NCs [34].

The effect of additional oxidation on Si NC based memory was studied by Garrido et. al. Si ions were implanted at room temperature on SiO<sub>2</sub> layer and the structure was annealed to form NCs. Additional oxidation was performed in oxygen ambient to understand the

effect of additional oxidation process on memory characteristics. Decrease in memory effect due to additional oxidation was reported. It was observed that the reduction in memory window is due to various reasons such as growth of additional oxide layer, decrease in nanocrystal size and density [35].

The electrical properties of Ge NCs embedded SiO<sub>2</sub> were reported by Kanoun et. al. SiO<sub>2</sub> tunnelling layer was thermally grown on p-type Si substrate. Ge NCs were grown on SiO<sub>2</sub> layer using low pressure chemical vapor deposition. After Ge nanocrystal formation, a thick control oxide layer of high temperature oxide was deposited. To understand the electrical properties of the structure, tunnel oxide thickness was varied, and thickness of control oxide and Ge nanocrystal formation were optimized and kept constant. C-V characteristics of various devices with charging and discharging effects were compared. It was observed that the voltage shift is higher for samples with thicker SiO<sub>2</sub> tunneling oxide and the charging effects reduce the current density of nonvolatile memory structures [36].

Memory effects of Ge NCs in HfAlO tunneling and blocking oxides were investigated. The influence of Ge nanocrystal density, thickness of tunneling and blocking layers and oxygen partial pressure effects on charge storage characteristics was studied. A composite target containing HfO<sub>2</sub> and Al<sub>2</sub>O<sub>3</sub> was used as a target for the deposition of HfAlO tunneling oxide by PLD. Ge NCs were deposited on tunneling oxide layer at 600°C. Subsequently, after the deposition of the HfAlO control oxide, the structure was annealed at 800°C in N<sub>2</sub> ambient to reduce the defects in dielectric layers. High frequency C-V measurements of the samples showed memory window indicating strong charging effects of Ge NCs [37].

Trilayer structure with Ge nanocrystal in HfAlO for memory application was fabricated using co-sputtering. Ge NCs were chosen due to its excellent chemical stability with respect to Hf-based dielectric oxides and HfAlO was selected due to its robustness at high temperature and high dielectric value. The structure was fabricated by co-sputtering of HfO<sub>2</sub>, Al<sub>2</sub>O<sub>3</sub> and Ge. The films were annealed at 500, 700 and 950°C in N<sub>2</sub> ambient. The results indicated that at high temperature annealing, GeO<sub>2</sub> spontaneously reduced to Ge to form NCs and excess Hf oxidized into HfO<sub>2</sub>. C-V characterization showed a memory window of 2.2V. The comparison of results from reference and device samples confirmed memory effects resulted from Ge NCs [38].

Ge NCs embedded in SiON layer as charge storage element for nonvolatile memory application were proposed. Tunneling oxide was grown on p-type Si substrate using dry oxidation. To form Ge NCs embedded in SiON layers thin films of silicon germanium nitride, silicon germanium, and silicon nitride were deposited on tunneling oxide. Blocking layer was formed by the oxidization of deposited a-Si layer. During blocking oxide formation SiGe-based layer was also oxidized to form Ge NCs at 900°C. To compare the memory effects of various layers and Ge NCs, three different structures with and without Ge NCs such as metal/Oxide/SiON/GeNCs/SiON/Oxide/Si, metal/Oxide/SiON/Oxide/Si and metal/Oxide/GeNCs/Oxide/Si were fabricated. Results indicated that for voltage sweep of  $\pm 5V$ , Ge NCs embedded SiON structures exhibit better memory window than SiON trapping layer and Ge embedded in SiO<sub>2</sub> structures, respectively [39].

Phenomena of charging and discharging of Ge NCs fabricated by low pressure chemical vapor deposition was investigated. Possibility of electron and hole storage was reported by applying positive and negative voltage. The discharge kinetics related to leakage of stored charge in Ge NCs have also been explained. It was found that the discharge kinetics of electrons are much faster than hole leakage for the same device with same experimental conditions. The study confirms the potentiality of Ge NCs for p-type MOS memory application [40].

The above literature review demonstrates about various limitations of conventional memory consisting of a floating layer. Si NCs (as charge storage layer) were introduced as an alternative solution to overcome the above problem. However, further studies were carried out to replace nanocrystals of Si by Ge to improve the nonvolatile memory.

### **2.1.2 Au nanocrystal based memories**

Nonvolatile memory behaviour of Au NCs embedded in SiO<sub>2</sub> tunneling and Al<sub>2</sub>O<sub>3</sub> blocking layers was reported by C. C. Wang et. al. Au NCs were selected as trapping layer due to low process temperature, high work function, chemical stability and ease of fabrication. Here, the sandwich structure of SiO<sub>2</sub>/Au/Al<sub>2</sub>O<sub>3</sub> was deposited using a combination of three different deposition methods. For the deposition of SiO<sub>2</sub> tunneling

layer dry oxidation process was used. RF magnetron sputtering and atomic layer deposition (ALD) were used to deposit Au and Al<sub>2</sub>O<sub>3</sub> gate oxide layers. To transform Au layer into Au NCs, the samples were annealed at 600°C for 3 min in N<sub>2</sub> environment. The hysteresis loop with a flat band voltage shift of 9V for a voltage sweep of ±6V was obtained in the C-V curve that indicated significant charge storage effect of Au NCs [23].

The charge storage characteristics of chemically synthesized (CS) and vacuum deposited (VD) Au nanoparticles are reported. The chemical synthesis has an advantage in the formation of uniform nanoparticles while vacuum deposited process followed by annealing process has the advantage of ease of nanoparticle formation. SiO<sub>2</sub> tunneling oxide was thermally grown on Si and SiO<sub>2</sub> blocking layer was deposited using plasma enhanced chemical vapor deposition. The charge storage behaviour of two different structures with Au nanoparticles (CS and VD) has been investigated. Memory with Au nanoparticles prepared by VD exhibited better memory window as compared to memory with CS Au nanoparticles [41].

Sargentis et. al. compared the electrical behaviour of Au and Pt nanoparticle based nonvolatile memory structures. Au and Pt were deposited on thermally grown SiO<sub>2</sub> tunneling layer. The nanoparticles of Au and Pt were formed during the e-gun deposition without annealing. Thick blocking layer of HfO<sub>2</sub> was deposited without breaking the chamber vacuum. The use of HfO<sub>2</sub> layer as blocking layer has various advantages such as reduction in low operating voltage of the device and prevention of diffusion of Au in the tunneling and blocking oxides. To study possible hysteresis effect, the C-V measurements were performed from inversion to accumulation region and vice versa. The devices with Au nanoparticles showed better device performance in comparison to devices with Pt nanoparticles [42].

The potential application of Au NCs together with high dielectric oxide for advanced complimentary metal-oxide semiconductor was studied by Chan et. al. Trilayer structure with Au in HfAlO was fabricated using pulsed laser deposition and Au NCs were formed by annealing at 300 and 500°C. High dielectric oxide was selected as tunneling and control oxide due to its asymmetric band, dielectric constant ~~value~~ and thermal stability in programming and retention modes. TEM images indicate interface layer formation between Si and tunneling layer due to oxygen diffusion. The charge injection from the substrate to



NCs was observed in the hysteresis loop. Significant voltage shift with a definite memory window of 10V for a sweep voltage of  $\pm 12\text{V}$  was reported. It was found that high density and small size of Au NCs result in high memory window [43].

Nanofloating gate memory with  $\text{SiO}_x\text{N}_y/\text{Au}/\text{SiO}_x\text{N}_y$  was fabricated using sputtering method. The trilayer structure was annealed at  $800^\circ\text{C}$  to remove surface defects formed between the metal and insulator. Significant voltage shift due to the charging effects of Au NCs was reported. For a gate bias of  $\pm 10\text{V}$ , larger threshold voltage shift of 2.5V was observed between writing and erasing states. The work confirmed nonvolatile memory device application of Au NCs [44].

The memory performance of Au nanocrystal-based structure was studied by R. Tang et. al. After the deposition Au layer on  $\text{SiO}_2$  by sputtering, the structure was annealed at  $600^\circ\text{C}$  in  $\text{N}_2$  to form Au NCs. Then, blocking layer of  $\text{HfO}_2$  film was deposited by electron beam evaporation and the structure was characterized using XPS, TEM and electrical measurements. Memory performance of the structure degraded due to electron leakage from Au NCs through oxygen related vacancy in  $\text{HfO}_2$  blocking layer. Memory window of 1V for a sweep voltage of  $\pm 2\text{V}$ , low program/erase voltage and retention performance indicate the promising nonvolatile application of Au NCs [45].

Charging characteristics of metal oxide semiconductor capacitor structure with various metals such as Au, Co and Ni were investigated by Guan et. al.  $\text{SiO}_2$  tunneling layer was thermally grown on Si. Metal layer was deposited using electron beam evaporation and rapid thermal annealing process in  $\text{N}_2$  ambient was induced for the formation of NCs. The influence of process parameters on the formation of metal NCs was investigated. It was found that Au NCs showed promising results such as density, uniformity and size as compared to Co and Ni nanocrystal formation at  $600^\circ\text{C}$  and electron beam evaporation method together with RTA is an effective method for the formation of high quality Au NCs. Charging and discharging effects of the structure were observed for hysteresis loop with a memory window of 4.5V for a sweep voltage of  $\pm 16\text{V}$  and confirm the potentiality of Au nanocrystal-based structures for nonvolatile memory application [46].

V. Mikhelashvili et. al. proposed and demonstrated Au nanocrystal based nonvolatile memory with  $\text{HfO}_2$  tunneling and blocking layers. Tunneling  $\text{HfO}_2$  layer was deposited on

p-type silicon substrate using ALD. Thin layer of Au was annealed (RTA) at 600°C in N<sub>2</sub> atmosphere to form Au NCs. Finally, the capacitor structure was formed by depositing a blocking HfO<sub>2</sub> layer using ALD. Hysteresis loop from C-V measurements indicates charging effects from electrons and holes. Large memory window of 9.25V was reported for a voltage sweep of ±7V and confirmed the charge storage role of Au NCs [24].

To study the charge storage characteristics, a sandwich structure of SiO<sub>2</sub>/Au/SiO<sub>2</sub> was fabricated on p-type Si. Thin tunneling SiO<sub>2</sub> layer was deposited using dry oxidation process. Subsequently, Au and blocking layers were deposited using RF magnetron sputtering at room temperature with low power. The specimens were annealed in N<sub>2</sub> atmosphere at 600°C to form well-separated Au NCs. Hysteresis loop was obtained from bidirectionally sweeping C-V curve from accumulation to inversion regions and it indicated charge storage effects of nanocrystal embedded SiO<sub>2</sub> layers. The hysteresis loop exhibited a significant memory window even at low operating voltage of 2V [47].

The thermal annealing effects on electrical characteristics of HfO<sub>2</sub>/Au/HfO<sub>2</sub> structure was investigated by Feng et. al. The simple method for the fabrication of the high dielectric isolated metal cluster array using ALD and thermal evaporation was proposed. It was reported that the electrical property of the sandwich structure was greatly affected by annealing temperature. Thermal annealing resulted in formation of Au islands or clusters in HfO<sub>2</sub> films and the properties of HfO<sub>2</sub> were drastically affected by annealing temperature. Even though, annealing resulted in removal of defects in the blocking layer it deteriorated the blocking property of HfO<sub>2</sub> due to crystallization [48].

The structural and electrical properties of laser annealed Au NCs embedded in oxide layers were reported. The trilayer structure was fabricated on n-type Si substrate by thermally grown SiO<sub>2</sub> tunneling layer. Subsequently, Au layer was deposited on the tunneling layer using RF sputtering and was exposed to laser annealing for the formation of Au NCs. Finally, the blocking layer of Y<sub>2</sub>O<sub>3</sub> was deposited using RF sputtering. The memory window obtained indicates the formation of Au NCs and the experimental results conclude by suggesting laser annealing as a promising technique for nanocrystal formation in future device applications [49].

From the above literature, it is observed that metal nanocrystals show significant memory characteristics than semiconductor nanocrystals and hence metal nanocrystals have attracted significant interest for nonvolatile memory application. Many researchers have fabricated Au based trilayer structure using various methods or combination of different deposition techniques. But, no detailed study prevails to correlate the method of deposition (esp. using RF magnetron sputtering and electron beam evaporation) and effect of annealing temperature to understand charge storage characteristics of these structures.

## 2.2 Research gap

NCs embedded in different oxide layers have potential application in science and engineering. The scaling down of the memory structure constituted many problems. The possible solution is to increase the charge storage capacity of the structure using high dielectric oxides as a replacement of  $\text{SiO}_2$  and to use metal NCs. The use of high dielectric oxide material for nonvolatile memory has advantage in memory device due to its thermal stability, dielectric constant, reduction in operating voltages and prevention of diffusion of metal in tunneling and blocking layers. Meanwhile, Au NCs based nonvolatile memory possess high density of states, enhance electric field, better work function engineering and deep potential well that enhances carrier confinement. Thus, the aim of present thesis is to investigate the effect of annealing temperature on the structural, electrical and compositional properties of  $\text{HfO}_2/\text{Au}/\text{HfO}_2$ ,  $\text{SiO}_2/\text{Au}/\text{SiO}_2$  and  $\text{Al}_2\text{O}_3/\text{Au}/\text{Al}_2\text{O}_3$  structures fabricated by a combination of two different deposition methods such as RF magnetron sputtering and e-beam evaporation in detail.

## 2.3 Objective of thesis

- To understand the charge storage characteristics of Au nanocrystals with  $\text{HfO}_2$  tunneling and blocking layers.
- To investigate the effect of annealing on the electrical and compositional properties of  $\text{SiO}_2/\text{Au}/\text{SiO}_2$  trilayer structure.
- To fabricate and understand the properties of  $\text{Al}_2\text{O}_3/\text{Au}/\text{Al}_2\text{O}_3$  structure for nonvolatile memory application.



# Chapter 3

## *Materials and Methods*

### 3.1. Introduction

Over the past few years, nonvolatile memory structures with Au NCs have been explored with great interest. The use of various oxides as a replacement for SiO<sub>2</sub> tunneling and blocking layers and comparison of electrical properties with conventional structures has been reported in the present work. This chapter is divided into two sections. The first section deals on the description of various materials used. The second section is based on different deposition methods and characterization techniques.

### 3.2. Materials

In the present thesis, various materials such as SiO<sub>2</sub>, Al<sub>2</sub>O<sub>3</sub>, HfO<sub>2</sub> and Au have been used. The dielectric oxides (SiO<sub>2</sub>, Al<sub>2</sub>O<sub>3</sub> and HfO<sub>2</sub>) were used as tunneling and blocking oxide layers and Au was used as trapping layer for the fabrication of trilayer structure.

#### 3.2.1 Silicon dioxide (SiO<sub>2</sub>)

SiO<sub>2</sub>, is also known as silica, has many interesting physical properties. It exhibits both amorphous and crystalline phase. Amorphous SiO<sub>2</sub> finds application in electronic devices as gate dielectric material [50,51]. SiO<sub>2</sub> is also used as an anti-reflection coating due to its good optical property [52]. The refractive index and dielectric constant of SiO<sub>2</sub> thin films are around 1.4 and 4, respectively [53]. SiO<sub>2</sub> has high band gap around 9 eV [54], melting point (~1700°C) and chemical stability.

#### 3.2.2 Aluminium oxide (Al<sub>2</sub>O<sub>3</sub>)

Al<sub>2</sub>O<sub>3</sub> is commonly known as alumina and has interesting physical, thermal and chemical properties. Crystalline Al<sub>2</sub>O<sub>3</sub> forms phases such as corundum ( $\alpha$ ), cubic ( $\gamma$  &  $\eta$ ), monoclinic ( $\theta$ ), etc [55]. Natural crystalline alumina forms corundum structure. Al<sub>2</sub>O<sub>3</sub> has melting point around 2100°C and is kinetically and thermodynamically stable. Amorphous Al<sub>2</sub>O<sub>3</sub> is useful for the solution of leakage problems in electronic devices. The large band gap

(9 eV), dielectric constant (5.5) and insulating property make  $\text{Al}_2\text{O}_3$  a prominent material in replacement of  $\text{SiO}_2$  [56].

### **3.2.3 Hafnium oxide ( $\text{HfO}_2$ )**

Hafnium oxide or hafnia is considered as a capable material of replacing  $\text{SiO}_2$  gate dielectric oxide due to their physical and electrical properties [57,58]. But the key problem in implementation of  $\text{HfO}_2$  as gate dielectric is its low crystallization temperature.  $\text{HfO}_2$  exhibits monoclinic, tetragonal, cubic and orthorhombic crystal structures [59–61].  $\text{HfO}_2$  has high dielectric constant (25), band gap (5.5 eV) and good optical properties [56,62].

### **3.2.4 Gold (Au)**

Gold is one of the transition metals, which is the noblest metal among other noble metals [63]. The density of gold is  $19.3 \text{ g/cm}^3$  and its melting and boiling point are  $\sim 1064$  and  $\sim 2850^\circ\text{C}$ , respectively. Gold is an excellent conductor of electricity and exhibits face centered cubic crystal structure. Gold nanoparticles have attracted great research interest due to their potential application in optics, electronics, nanoelectronics, medicine, etc [64,65]. Gold NCs are used in memory application due to its high work function (5.1), ease of synthesis, low process temperature, chemical stability, restricts from oxidation and reactions with dielectric layers [23,24]. The integration of Au NCs with various oxides ( $\text{HfO}_2$ ,  $\text{SiO}_2$  and  $\text{Al}_2\text{O}_3$ ) acting as tunneling and blocking layers and to understand the charge storage characteristics with annealing temperature are of great interest from a basic and applied perspective.

## **3.3 Deposition methods**

### **3.3.1. RF magnetron sputtering**

Sputtering is an efficient physical vapor deposition technique used to deposit high quality thin films. In sputtering process, atoms are ejected from a solid target material by the bombardment of energetic ions [66,67]. The process of the ejection of target atoms is by the

momentum transfer between the incoming energetic ions and the target atoms. The ejected atoms are settled on the substrates at an optimized distance from the target materials. Mostly, argon is used as sputtering gas for the formation of plasma inside the chamber. The solid target material is connected to the cathode and the substrate holder to the anode. The plasma is maintained in between the target and the substrate. Atoms of argon gas near the target collide with the energetic electrons from the cathode, results the formation of  $\text{Ar}^+$  ions. These  $\text{Ar}^+$  ions strike the target surface and the atoms from target are ejected from the surface by the cascade process. The number of atoms ejected from the surface of target to the number of incidence of ions is termed as sputtering yield. The yield depends on various factors such as the type of target atom, binding energy of the target atoms, incident ion energy, angle of incidence of ions and the relative mass of ions and atoms. Schematic mechanism of sputtering is shown in figure 3.1 [68].

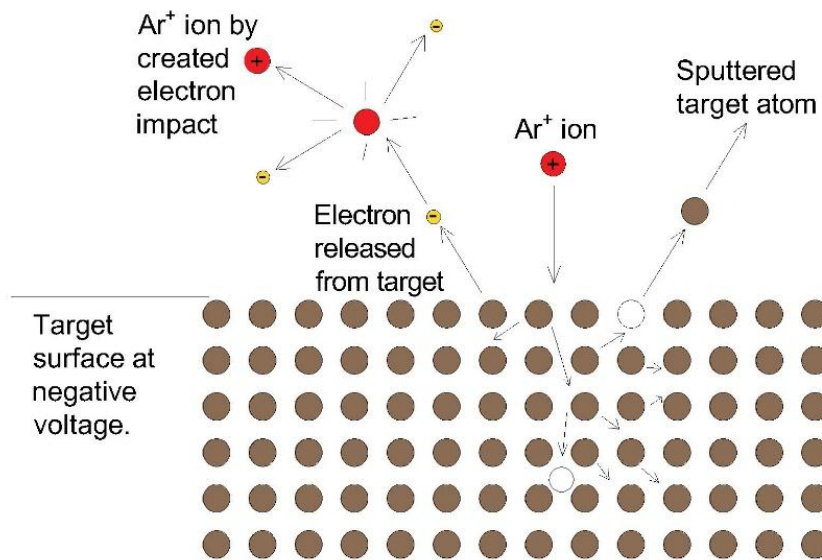


Figure 3.1 Schematic mechanism of sputtering

The sputtering techniques are further classified into different categories depending on their functions. They are direct current (usually used for coating metals), radio frequency (used for coating insulators to avoid charge build-up), magnetron sputtering (used to confine electrons using strong electric and magnetic fields for better deposition) and reactive sputtering (uses reactive gases and chemical reaction for the deposition of thin films) [69].



On sputtering of insulating materials, the positive ions (say Ar) are attracted towards the cathode and eventually neutralized after interacting with the electrons near the surface of the target. The neutralization of ions stops further attraction of the ions making it unfeasible for the further bombardment of ions. Thus, direct current (DC) sputtering is mainly used for the deposition of metal targets and has the demerit that insulator materials cannot be sputtered. Therefore, insulator can be deposited using radio frequency (RF) sputtering. Here, by alternating the potential, the charge neutralization on the surface of the target can be cleaned up. By capacitive coupling, RF power (frequency 13.56MHz) is transferred from cathode through the insulating material at higher frequencies. During the positive half cycle, due to higher mobility of the electrons than the positive ions, more number of electrons reach towards the insulating target by giving it negative bias. For negative half cycles, the sputtering of the targets due to ion bombardment continues [70].

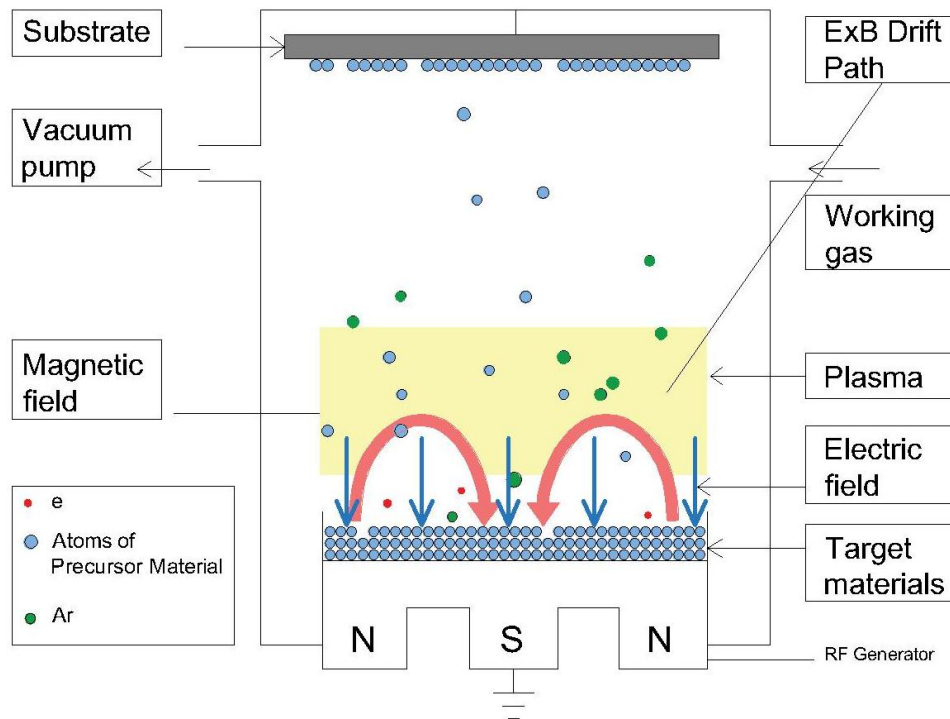


Figure 3.2 Schematic diagram of RF magnetron sputtering

In RF magnetron sputtering, a strong magnetic field is used to confine the plasma near the surface of target material to increase the sputter yield. Due to the magnetic field, electrons experience a force and follow the helical path around the magnetic field lines. The effective path length of the electrons is then increased and causing more collision with the neutral gaseous atoms lead to the higher deposition rate. Figure 3.2 shows the schematic diagram of RF magnetron sputtering [71].

In the present thesis work, RF magnetron sputtering is used to deposit various oxide layers such as SiO<sub>2</sub>, Al<sub>2</sub>O<sub>3</sub> and HfO<sub>2</sub> as tunneling and blocking layer for nonvolatile memory application.

### **3.3.2 Electron beam evaporation**

Electron beam evaporation is one form of physical vapour deposition which uses electrons to evaporate a target material under vacuum for the deposition of thin films [72] and schematic diagram of E-beam evaporation system is shown in figure 3.3 [73]. Physical vapour deposition has three basic stages for thin film deposition. Firstly, the target material is vaporized in vacuum using heat transfer or gaseous plasma. The second stage is the transportation of the vaporised material to the substrates. Thirdly, the vaporized material condenses to form thin films. The basic working principle of the electron beam evaporation is also the same. Here, energetic electron beam is used to concentrate energy on a very small area of a target material. When the electrons are focused on the material, electrons transfer its kinetic energy to the material via thermal energy so that the material get vaporized. Under high vacuum condition, the vaporized material is transferred from the source to substrate. Finally, the vapours bond to the substrates via condensation leading to the growth and deposition of the thin film. The advantages of electron beam evaporation method include the deposition of high purity films, less contamination from the crucible and deposition of more than one material at a time.

A typical electron beam system consists of coating chamber, vacuum pumps, vacuum gauges, electron beam gun and a crystal monitor. Deposition of thin films under vacuum environments has mainly two reasons such as to keep the films from reactive gases and to maintain better mean free path. The vacuum environment helps in limited collision between the vapor and the gas molecules. This helps in the propagation or transportation of vapor molecules in straight line paths.

To produce vacuum environment, a rotary and diffusion pumps are used. The rotary pump has a rotor, stator and a vane. The gas is pumped out from the chamber by compressing the gas by the combined working of the oil filled rotor- stator assembly. The rotary pump helps to create a vacuum pressure up to 10<sup>-2</sup> or 10<sup>-3</sup> mbar (low vacuum). But for better thin film deposition, reduction in particle density in the chamber is an utmost requirement so that the mean free path of the particles is long. High vacuum in the deposition chamber is

inevitable for providing the means to reduce the presence of undesired atoms, molecules and contaminants and to increase the mean free path of the particles. Here, in the present work, high vacuum (around  $10^{-6}$  mbar) is achieved by using a diffusion pump backed by rotary pump. The diffusion pump works on the gas diffusion principle to create high vacuum. The silicone oil in the diffusion pump is heated to its boiling point and is vaporized. These oil molecules will transfer its momentum to the particles and traps the air at the bottom of the pump. This creates a low pressure at the top side and a high pressure at the bottom side of the pump. The high pressure at the bottom side is removed or pumped out using a rotary pump. To measure low vacuum, pirani gauge is used whereas a penning gauge helps to measure high vacuum. Pirani gauge is basically a thermal conductivity gauge in which the conductivity of the surrounding medium is correlated to the pressure using a bridge circuit. Penning gauge is a cold cathode ionization gauge with a tungsten wire anode and an outer cylinder of the gauge as cathode. The gas discharge is generated by applying high voltage (through current limiting resistors) between the anode and the cathode and the resulting ion current is calibrated with respect to the pressure of the gas for pressure measurement.

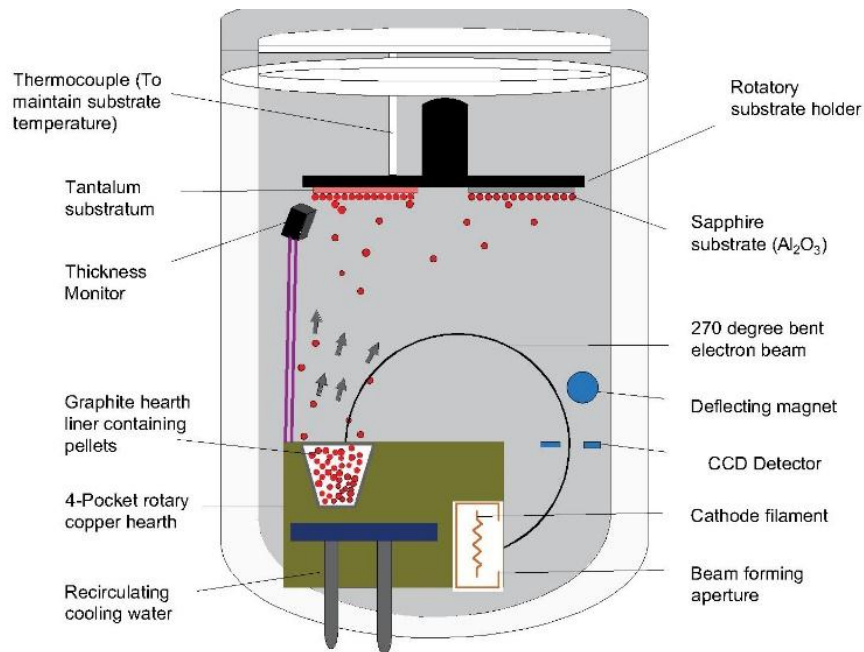


Figure 3.3 Schematic diagram of electron beam evaporation system

In the present thesis work, electron beam evaporation technique is used to deposit Au thin film as a charge trapping layer for trilayer structure and Al deposited as metal and back contacts for trilayer structure fabrication.

### 3.4 Thermal annealing

Annealing is a process in which the physical or chemical properties of a material is altered by heat treatment method. Most of the furnace atmosphere basically contain air which have oxygen, moistures and carbon dioxides. During annealing, the materials can interact with unwanted gases that are present and can alter their properties. Thus, selection of an atmosphere is essential for annealing [74]. An atmosphere is selected in such a way that the materials surface chemistry will be preserved and prevents oxidation. Nitrogen atmosphere is preferred for semiconductor processing as nitrogen is easily available and restricts unwanted chemical reactions.

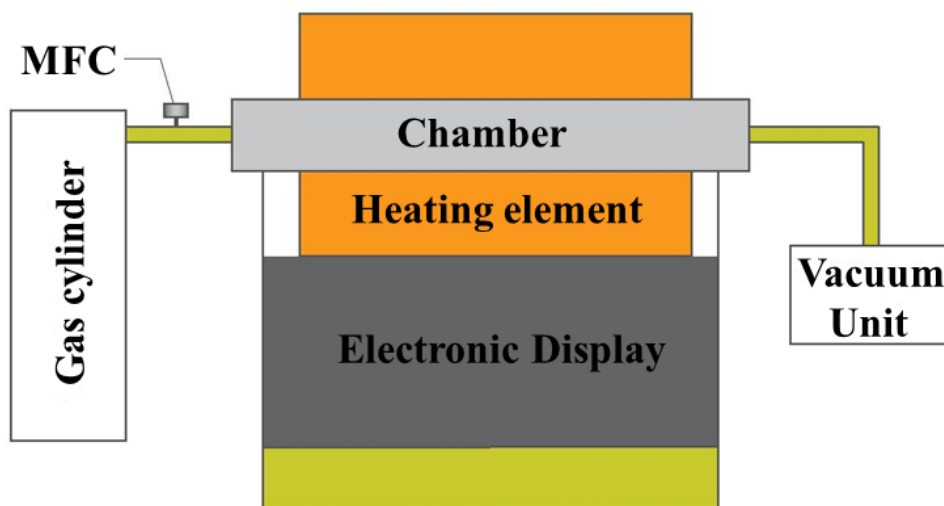


Figure 3.4 Typical vacuum furnace system

A typical vacuum furnace consists of a furnace chamber, heating element, a vacuum system, mass flow controllers (MFCs) and electronic displays as shown in figure 3.4. Usually, the heating element used to heat the furnace chamber is a kanthal wire or coil. By using the vacuum pump the air atmosphere inside the furnace chamber is pumped out and nitrogen (or needed atmosphere) is introduced to the chamber using a mass flow controller.

Here in the present experiment, to form Au NCs and to understand the effect of annealing temperature on memory characteristics of various trilayer structure, annealing was performed. The trilayer structures were annealed in nitrogen atmosphere at 650°C, 750°C and 850°C for 60 min with a ramp rate of 10°C/min.

## 3.5 Characterization techniques

### 3.5.1 Raman spectroscopy

Raman spectroscopy is one of the vibrational spectroscopic techniques used to obtain information regarding the structure, symmetry, electronic environment and bonding of the molecules [75,76]. When light is incident on matter/ molecule, it may undergo elastic or inelastic scattering. In an elastic scattering process, the energy of the incident light will be the same as that of the scattered light. This scattering is known as Rayleigh scattering. In inelastic scattering process, the energy of the scattering light is altered with respect to the incident light. This scattering is also known as Raman scattering. There are mainly two types are Raman scattering viz., anti-stokes and stokes. The anti-stokes Raman scattering occurs when the frequency of the scattered light is greater than that of the incident light. In stokes Raman scattering, the frequency of the scattered light is less than that of the incident light. In both Stokes and Anti-Stokes scattering, the difference between the incident energy and the emitted energy of the light is equal to the transition energy for the molecule. This change in energy gives the information about various modes, symmetry and bonding of the samples.

Raman spectrometer mainly consists of a source, optical setup and a detector as shown in figure 3.5 [75]. Mostly, the source consists of laser that is used to excite the molecules of the sample. The laser beam after passing through the optical setup is focused onto the sample. The optical arrangement basically consists of a dichromatic mirror, microscopic objectives, filters, pin holes and focusing lenses. Here, the laser beam incidents on the sample, most of the photons are scattered with the same frequency as of incident photons (i.e, Rayleigh scattering). While a small number of photons are scattered with a shift in frequency from the incident photons. The shift in frequency arises due to the interaction of incident photons with the molecules of the target. The shift in frequency gives the information about the various phonon modes of the sample. The laser beam from the sample is finally detected by the detector using a charge coupled device (CCD) camera to produce the Raman spectrum.

In the present work, the confocal micro-Raman spectrometer using a solid-state laser operating at 532 nm, at Materials Research Centre (MRC), MNIT Jaipur, is used to investigate the modes in HfO<sub>2</sub> thin films.

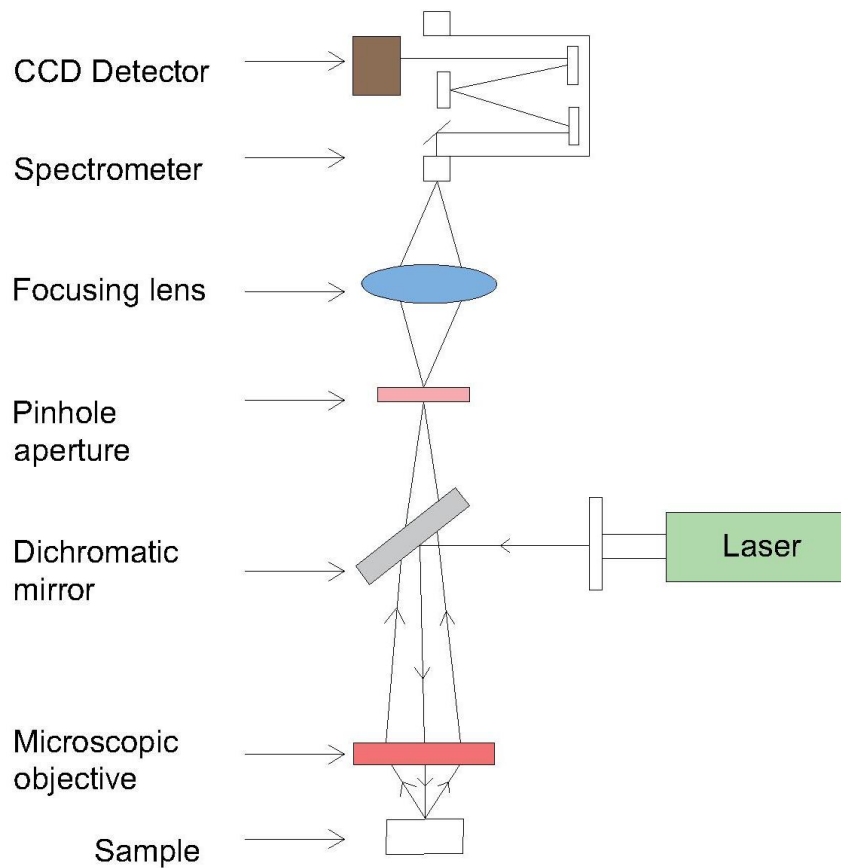


Figure 3.5 Schematic diagram of Raman spectrometer

### 3.5.2 Transmission electron microscopy

Transmission electron microscope is an electron microscope that uses high energetic electrons to understand the objects on a very fine scale [77]. It is used to observe features such as the morphology, crystal structure, dislocations and grain boundaries of a specimen. When a high energetic electron strikes through thin film specimen which is thin enough to transmit the incident electrons, various interactions can occur between the electrons and the specimen (atoms). In TEM, some of the electrons may emerge out from the sample without any interaction with the specimen. These type of incident electrons that are transmitted through the thin specimen without any interaction are known as unscattered electrons. Meanwhile, some of the electrons interact with the specimen without any loss of energy but undergo scattering. These electrons are known as elastic scattered electrons. If the incident electron loses its energy with scattering, it is inelastic electron scattering.

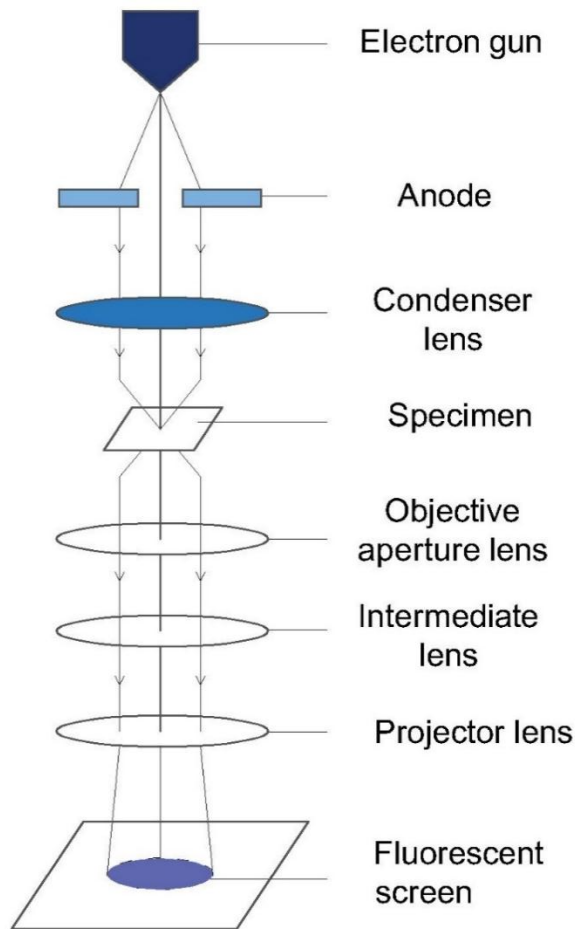


Figure 3.6 Schematic illustration of TEM

TEM basically consists of a source, condenser lens, condenser aperture, objective lens, objective aperture, projector lens and a screen [78] and is illustrated in figure 3.6. A tungsten filament or  $\text{LaB}_6$  is usually used to generate electron beams. A condenser lens is mainly used to focus the electron beam and a condenser aperture helps in filtering out unwanted scattered electrons before the beam is focused on the specimen. From the specimen, the transmitted beams are focused by an objective lens into an image. The objective and selected apertures are used to enhance contrast and to observe the periodic diffraction pattern of the specimen. Projected lens is used to project the beams to a phosphor screen.

The image mode and diffraction mode are the two operation modes associated with the TEM. The image mode is further subdivided as bright field, dark field and high resolution. The three modes differ in the way in which an objective aperture is used in the back focal plane. In the diffraction mode, the diffraction patterns are obtained by focusing the diffracted beams using an objective lens.

TEM is equipped with energy dispersive X-ray analysis (EDX) facility. EDX is used for elemental identification or chemical characterization of samples [77]. During EDX analysis, electron beam knocks out some inner core electrons from the specimen. Because of this vacancy, another electron from the outer most shell jumps to the vacant position by giving up some of its energy as X-rays. The electron shell and identity of elements could be identified by measuring or detecting the energy of X-ray emitted. EDX has basically four main components such as source (usually electron beam or X-ray), detector (Li drifted Si crystal), amplifiers and multichannel analyser (MCA).

In this present work, High Resolution Transmission Electron Microscope (Make: FEI Tecnai-T20) at MRC, MNIT Jaipur was used to confirm the formation Au nanocrystals. ImageJ software was used for the estimation of nanocrystals per unit area from TEM image.

### **3.5.3 Atomic force microscopy**

Atomic force microscopy (AFM) is the characterization technique that is used for the investigation about surface features, physical properties and materials performance [79]. AFM is a very powerful technique invented by Binnig, Quate and Gerber in 1986 [80]. AFM was invented as the modification of scanning tunneling microscope (STM) which limited its application mostly for the surface features of conductive samples in vacuum. AFM is a versatile technique that is capable of investigating surface topology of insulators as well as conductors on an atomic scale [81]. Recently developed AFM instruments are capable of recording measurements at different temperature scale in air or fluid environment rather than vacuum and can obtain information from biological and polymeric samples in their native state.

AFM consists of a light source (laser), photo detector, piezo electric scanner, cantilever and a feedback electronics as shown in figure 3.7 [82]. The cantilever tip is fabricated using silicon nitride  $\text{Si}_3\text{N}_4$  or silicon (Si) of the order of nanometer size with a sharp tip at the end which acts as the interaction probe. The top surface of the cantilever is polished with reflective thin film layer, usually with gold (Au).

In AFM, a fine sharp tip of the order of nanometer scale is attached to end of the cantilever and is subjected close to a surface of the sample and a deflection is produced by cantilever due to the Van der Waal's force between the tip and the atoms of the sample due to



Hooke's law. The cantilever can be moved in X-Y direction to scan the whole surface of the sample. The sample surface roughness causes deflection of the tip during the scanning process. With the movement or deflection of cantilever, the laser reflected from the top of the cantilever is detected by the photo sensitive diode (PSD). PSD consists of diodes and is divided into four parts as shown in the figure 3.7 and it records the signals from the two halves of the photo diode. A feedback mechanism is also used to keep the tip to sample distance constant.

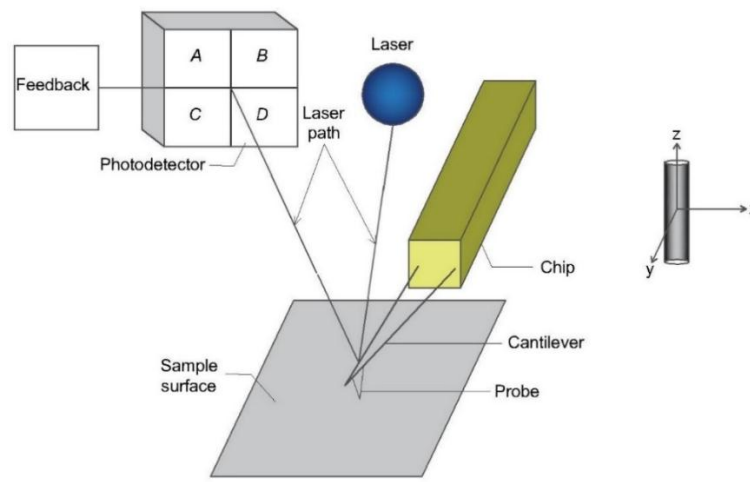


Figure 3.7 Schematic diagram of basic AFM setup.

AFM works in three different operational modes depending on the probe approaches:

1. Contact mode
2. Non-contact mode
3. Tapping (Intermittent contact) mode

Contact mode is basically used for imaging hard and smooth surface. In this mode, tip is always in contact with the surface by which a repulsive force act between tip and the sample. It can provide the sharp image of the surface with high resolution. But sometimes due to high force, the sample may deform. Therefore, soft samples are imaged under tapping mode or non-contact mode. In tapping mode, cantilever tip oscillates at or close to the resonant frequency. Due to the interaction of tip to the sample, the amplitude of the oscillation is modified. The change in amplitude with respect to external reference oscillation then provide the topographic information about the sample characterization. In non-contact mode, the tip is oscillating with very small amplitude as in tapping mode and has no direct

contact with the sample. The interaction between the tip and the sample is long range Van der Waal attraction.

In the present work, the surface topography and roughness of the films were analyzed using Bruker atomic force microscope facility available at MRC, MNIT Jaipur. For the analysis of AFM images, nanoscope analysis software was used.

### **3.5.4 X-ray photoelectron spectroscopy**

X-ray photoelectron spectroscopy (XPS), also known as electron spectroscopy for chemical analysis (ESCA), is a surface analysing technique that uses soft X-rays to examine the core levels within a material [83–85]. The basic principle of this spectroscopy is dependent on the photoelectric effect. The incident soft X-ray is used to irradiate and ionize the atom by ejection of an electron. The kinetic energy of the electron depends on the incident X-ray energy and the binding energy of the electron. Each element present in a material can be easily identified as it produces the characteristic sets of peaks at a specific binding energy [77]. The measurement of binding energy leads to the elemental identification and the chemical state of the element. The spectra are obtained by measuring the kinetic energy of the emitted rays from 1-10 nm top layer from the material.

XPS basically consist of the X-ray source, ion gun, energy analyser, detector, data acquisition system and a vacuum system as shown in figure 3.8 [86]. XPS mostly uses Mg  $K\alpha$  or Al  $K\alpha$  radiations with energies 1253.6 and 1486.6 eV as the source. The electrons emitted from the specimen are focused to the analyser using an electron optics which has an electrostatic and magnetic lens. Hemispherical energy analyser disperses the electrons with respect to their kinetic energies and it contain two concentric hemispherical electrodes (outer and inner hemispheres) kept at different potentials. The energy resolution of the instrument depends on full width half maxima (FWHM) of the source, line width of the photoelectron emission and the energy resolution of the analyser. Finally, the dispersed electrons are detected by a group of detectors such as discrete dynode, channeltrons and multichannel detectors. The data acquisition system acquires and stores the data. The entire characterization set-up needs internal ultra high vacuum (UHV) environment for obtaining the maximum electron counts. The UHV is reached/ obtained using turbo molecular pump with rotary pump assistance.

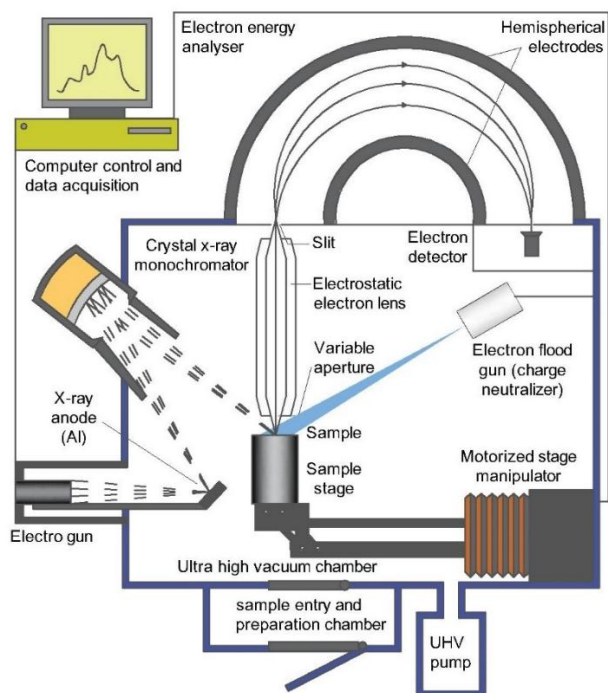


Figure 3.8 Schematic diagram of XPS

In the present thesis work, XPS spectra was obtained using an Omicron ESCA+ X-ray Photo Spectrometer from Oxford Instrument Germany with a monochromatic Al  $K\alpha$  ( $h\nu=1486.6$  eV) X-ray radiation at MRC, MNIT Jaipur. For the analysis of XPS results CasaXPS software was used.

### 3.5.5 X-ray diffraction

X-ray diffraction (XRD) is a non-contact and non-destructive technique used to understand the crystalline phases, different polymeric forms and the structural properties of the materials [77]. This measurement offers accurate results, which cannot be replaced by any techniques in crystalline, partially crystalline and amorphous materials. The intensities produced by the materials of a particular sample gives quantitative and precise information about the crystal structures, unit cell parameters, crystallite size, strain, epitaxy and defect structure.

Crystal structures are made up of a series of planes of atoms in which each plane is spaced with a distance  $d_{hkl}$  with each other. But various atomic planes in a crystal can be resolved with different d-spacing. For distinguishing different planes there is a coordinate

system introduced by William Hallows Miller called Miller indices [87]. Using the Miller indices, we can uniquely identify any atomic plane and crystal structure. If the distance between two planes is denoted by  $d_{hkl}$ , for a cubic system the d-spacing is given by:

$$d_{hkl} = \frac{a}{\sqrt{h^2 + k^2 + l^2}}$$

where  $a$  is the lattice constant of the crystal. When the X-rays are scattered from atoms of target material, the X-rays interfere constructively, and diffraction peak is observed. The constructive interference condition to occur according to Bragg's law ( $\theta_B$ ) is given by [88]:

$$n\lambda = 2d_{hkl}\sin\theta_B$$

where,  $\theta_B$  is the angle between the incident X-ray beam and the atomic planes. For observing the diffraction pattern, the detector should be at an angle twice to the incident angle  $\theta_B$  and the orientation must be in such a way that, the normal to the diffracting plane must be coplanar with the incident and diffracted X-rays.

X-ray diffractometer consists of three essential components:

1. X-ray tube
2. Sample holder
3. X-ray detector

X-rays are generated in the cathode ray tube (CRT) by the bombardment of energetic electrons on the target materials. The most widely used laboratory X-ray tube uses a copper anode, but cobalt and molybdenum are also popular. Electrons are produced by heating the filament (thermionic emission process) and are accelerated by applying high potential voltage. The generated X-rays are collimated using a filter (foils or crystal monitors) to produce monochromatic radiations, directed onto the specimens. Slits, crystal monochromator, X-ray mirror are the main components used in collimator for obtaining good focused sharp beam. The diffracted X-rays from the specimen in the range of  $2\theta$  angles are then detected. The intensity of the diffracted X-rays, from the crystalline planes at the different orientation, is recorded by the detector. The constructive interference pattern is occurred by impinging the X-rays and a particular intensity is recorded for a preferred orientation. A detector traces the diffracted X-ray signals, process them and convert signal

into counts which displays as output on the monitor screen. The schematic diagram of a typical X-ray diffractometer is shown in figure 3.9. In the present study, the crystallographic information of trilayer structures is obtained using Panalytical X-Pert Pro X-ray diffractometer using Cu-K<sub>α</sub> radiation source with the wavelength of 1.54 Å at MRC, MNIT Jaipur.

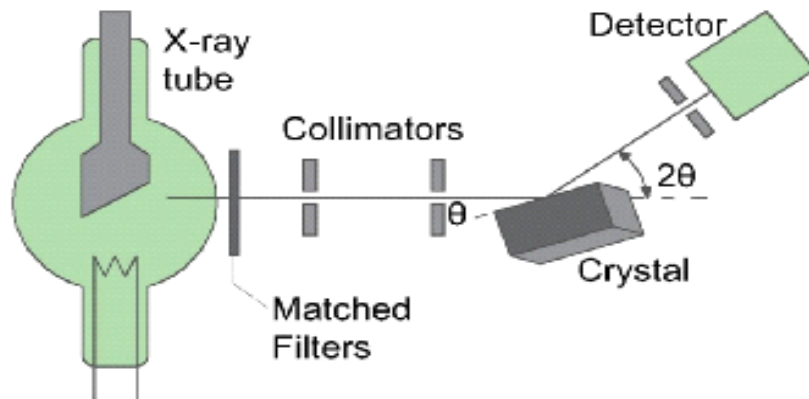


Figure 3.9 Schematic diagram of X-ray diffractometer

### 3.5.6 Rutherford backscattering spectrometry

Rutherford backscattering spectrometry (RBS) is one of the ion beam analysis methods used to investigate the composition and thickness of films. Here, in RBS, energetic ion beams having energy in the range 1 to 4 MeV are impinged on the target or the specimen and the backscattered projectiles are detected by sensitive solid-state detector [78,89]. The energy distribution of backscattered ions that are detected by detector help in determining compositional properties of the target material. This method is a non-destructive technique and finds application in various fields of science and technology [90]. Generally, RBS is used to understand the nature of impurities and various corrosion related phenomena in metallurgical engineering. Whereas, the growth mechanisms and related diffusion phenomena is studied in solid state physics. But, in surface science, RBS helps to understand the trace impurity percentage, atomic transport, gettering (process of removal of impurities or defects) and related adsorption mechanisms. For electrochemical application, backscattering spectrometry is one of the essential methods to understand anodic oxidation mechanism and passivity of a specimen. In semiconductor device physics application, the diffusion profiles,

implanted ion species location and layer thickness are key subjects of RBS analysis [90,91]. The basic principle of Rutherford backscattering spectrometry is based on the kinematics for binary collision. Here, an incident alpha particle loses its energy due to the interaction with a specimen and is backscattered.

The energy loss mechanism for the incident alpha particle happens mainly by two processes. Firstly, the particle loses its energy while they pass through the target material and the materials stopping power is a factor that influences energy loss. Secondly, the incident particle loses its energy via collision with the target atoms. The energy loss is due to the transfer of momentum between the incident particle and the target atoms and is highly dependent on masses of the projectile atoms. If  $E_0$  is the energy of alpha particle with mass  $M_1$  interacts with a target of mass  $M_2$  and is scattered by an angle  $\theta$  with an energy  $E_1$ . Then, the ratio of the scattered particles energy to the incident particle energy is kinematic factor (K) and is given as [77]:

$$K = \frac{E_1}{E_0}$$

The RBS set-up mainly consists of an accelerator, collimators, detector, multichannel analyser, ultra-high vacuum scattering chamber and electronic modules for data processing and acquisition as shown in figure 3.10 [92]. The first and essential component to produce high energetic projectiles is an ion source. The ions produced from the ion source are then accelerated through a high voltage gradient and the electrons in the ions are stripped using a stripper foil to produce positive ions in an accelerator. The positive ions are passed through an analyser magnet and is collimated using a collimator before it reaches the scattering chamber. In scattering chamber, the beam falls on the target and the backscattered ions are detected using a solid-state detector. The signals obtained are amplified using a pre-amplifier and amplifier until it reaches the multi-channel analyser. The obtained spectrum is fitted using RUMP simulation [93]. In the present work, RBS measurements of films are performed using  $\alpha$ -particle of energy 2 MeV using pelletron accelerator (RBS-400 Model) facility at IUAC, New Delhi.

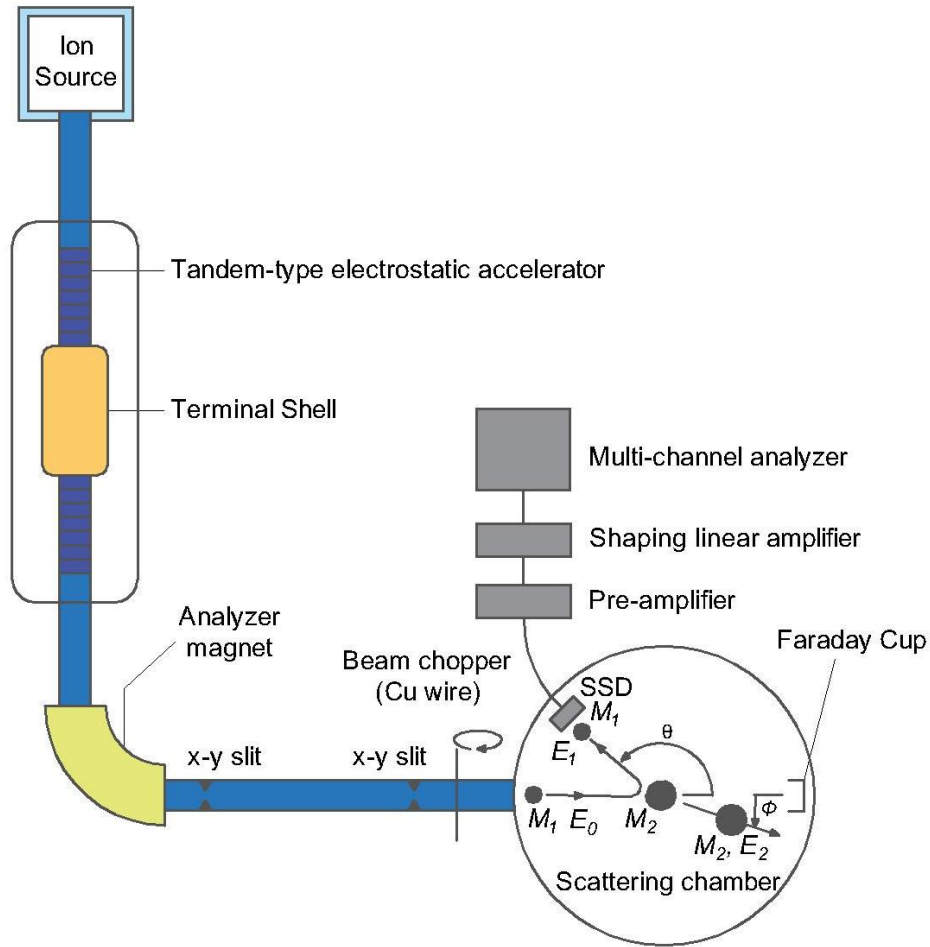


Figure 3.10 Schematic illustration of RBS experimental setup

### 3.5.7 Electrical characterization

Electrical characterizations are widely used in semiconductor industries and research labs for testing and evaluating new materials, devices and circuits. The combined use of advanced test methodologies, instrumentation and apt software help engineers and scientists to derive numerous electrical parameters. Capacitance-voltage and current-voltage measurements are the electrical measurements used to study the quality, reliability and performance of devices.

For MOS capacitors, C-V curve is recorded by applying a direct current (DC) bias voltage across the capacitor and making the measurement with an alternating current (AC). The DC bias voltage applied helps the device to sweep across accumulation, depletion and

inversion regions. In accumulation region, majority carriers accumulate near the interface region between the insulator and the semiconductor with strong DC voltage. The majority carriers are pushed away from the interface with a decrease in DC voltage creating a depletion region. The reversal of polarity results in minimum capacitance as the charge carriers are pushed further away from the dielectric oxide layer and forms inversion region.

In the present thesis, the leakage characteristics and memory window of trilayer structures were characterized using current-voltage and capacitance-voltage measurements. The electrical characterizations were performed using Agilent B1500A Semiconductor Device Analyzer at MNCF, IISc. Bangalore.



# **Chapter 4**

## **Synthesis and characterization of Au nanocrystals in HfO<sub>2</sub> tunneling and blocking layers**

## 4.1 Growth and optimization of HfO<sub>2</sub> thin films

### 4.1.1 Introduction

In recent years, the demand for low cost, faster and reliable electronic devices with high efficiency has attracted considerable attention. For decades, the silicon industry relied on SiO<sub>2</sub> gate dielectric until the scaling down of the dielectric has reached both its technological and theoretical limits [94,95]. Further shrinkage of SiO<sub>2</sub> gate dielectric thickness restrained due to permittivity and electron tunneling effect [96]. Due to the aforementioned difficulties, an alternative replacement for SiO<sub>2</sub> gate material has gained great interest. Among various dielectric materials such as Al<sub>2</sub>O<sub>3</sub>, ZrO<sub>2</sub>, HfO<sub>2</sub>, La<sub>2</sub>O<sub>3</sub>, SrO, and Y<sub>2</sub>O<sub>3</sub>, hafnium oxide has received significant focus due to its thermodynamical stability, reasonable energy gap, excellent electrical properties and high dielectric constant [97]. Moreover, the unique combination of structural, optical and electrical properties of HfO<sub>2</sub> films is used for various electronics and optoelectronics applications.

In optoelectronic applications, hafnium oxide thin films are very useful for anti-reflection coating in optical waveguide devices to reduce the Fresnel loss [98]. HfO<sub>2</sub> thin films are also being used as protective coating for electrical applications due to the hydrophobic effectiveness for outdoor insulators [99]. Moreover, in the electrical application, the presence of large conduction band offset in HfO<sub>2</sub> with respect to Si helps to attain lower leakage current at expected operational voltages [100,101]. The electrical properties such as capacitance and leakage current density of HfO<sub>2</sub> thin films drastically change with annealing [102]. For industrial application, low temperature annealing is required in the production process and HfO<sub>2</sub> thin films undergo phase transition from amorphous to crystalline even at low temperatures [103]. The formation of grain boundary due to crystallization, increases the leakage current and degrades the device performance [104]. Thus, the growth of high purity, quality and stoichiometry thin films and modulation of their properties under various conditions are of great interest for solid-state devices and communication. This attracts huge demand for the growth and optimization of high-quality HfO<sub>2</sub> thin films.

There are various physical and chemical methods employed to grow HfO<sub>2</sub> thin films such as electron beam evaporation, reactive dc sputtering, RF magnetron sputtering, metal-

organic molecular beam epitaxy and atomic layer deposition [105–110]. RF magnetron sputtering has various advantages like less wastage of the material, high adhesion of films and excellent uniformity with good packing density as compared to other methods. Recently, Das et. al. had reported the utmost importance of high-quality HfO<sub>2</sub> thin films and its incorporation into a low dimensional semiconductor technology [111]. Nam et. al. and He et. al. report the formation of stoichiometric HfO<sub>2</sub> thin films at high temperature annealing [59,112]. The variation in electrical and structural properties of HfO<sub>2</sub> based MOS structure with low surface roughness was studied by Khairnar and Mahajan [105]. This study shows that there is an utmost need to correlate stoichiometry, surface roughness and crystallinity for better electrical application. Our work aims at the systematic and detailed study of the growth and optimization of RF magnetron sputtered HfO<sub>2</sub> thin films and the correlation of the effects of annealing temperature (200, 400 and 600°C) in air atmosphere on the stoichiometry, surface roughness and crystallinity of HfO<sub>2</sub> thin films for various applications from a basic and applied scientific perspective.

#### **4.1.2 Experimental details**

Hafnium oxide thin films were deposited by RF magnetron sputtering method onto a p-type silicon (100) substrates with resistivity of 1-10 Ωcm. The substrates were thoroughly cleaned by standard Radio Corporation of America (RCA) I and II process before deposition [113]. For sputtering, HfO<sub>2</sub> target purchased from ACI Alloys, USA of purity 99.999% (5N) was used. The target was placed in a 2-inch holder, at a distance 10 cm from the substrates. Initially, the chamber was evacuated to a high vacuum pressure of  $6 \times 10^{-6}$  mbar using a rotary assisted turbo pump. The working pressure was maintained at  $3 \times 10^{-3}$  mbar by introducing high purity Ar gas (99.99%) into the chamber using mass flow controller. The Ar flow rate and RF power were kept constant (20 sccm and 100W) during deposition. Prior to deposition, the target was pre-sputtered for 10 min to remove surface contamination, if any, present. The substrate holder was rotated at low rpm to get uniform films, and the thickness of the film was around 25 nm as measured by a digital thickness monitor (DTM). After the deposition, annealing of the samples was carried out using a muffle furnace in air at different temperatures viz. 200, 400 and 600°C for 30 min with a ramp rate of 10°C/min. For electrical measurements, Al contacts with diameter ~1 mm and thickness around 250 nm were deposited using electron beam evaporation.

Raman spectra of the films were obtained using confocal micro-Raman spectrometer, which incorporates a solid-state laser of 532 nm. The structure of the films was evaluated using PANalytical X`pert Powder X-ray diffractometer with Cu K $\alpha$  radiation (1.54Å). The surface morphology of the films was studied using Bruker atomic force microscope. The chemical states and composition of films were examined using X-ray photoelectron spectroscopy (XPS) with a monochromatic Al K $\alpha$  ( $h\nu=1486.6$  eV) X-ray radiation under a base pressure of  $6\times 10^{-10}$  mbar using an Omicron Nanotechnology (ESCA+) from Oxford Instruments. The electrical measurements were carried out using B1500A Semiconductor Device Analyzer with frequency 1MHz at room temperature.

### 4.1.3 Results and discussion

The Raman spectra of as-deposited and annealed HfO<sub>2</sub> thin films in the range of 120 to 600 cm<sup>-1</sup> are depicted in figure 4.1. The broad peak around 150 cm<sup>-1</sup> for the films annealed at 200°C indicates the amorphous nature of the hafnia films. The peaks around 302 and 520 cm<sup>-1</sup> correspond to acoustic and optical phonon modes of Si substrates [114,115]. For samples annealed at 600°C, the origin of a new peak at 147 cm<sup>-1</sup> is observed, which is attributed to the A<sub>g</sub> mode in HfO<sub>2</sub> monoclinic structure. It is evident from the spectra that crystallinity increases with an increase in annealing temperature and there is a phase transformation from amorphous to crystalline structure at high temperature. Theoretical analysis predicts that for monoclinic structures, there are 36 phonon modes present, out of which 18 (9A<sub>g</sub> + 9B<sub>g</sub>) are Raman active modes, 15 are IR active modes and other three are zero-frequency translation modes [116]. In addition, the modes of HfO<sub>2</sub> have been studied by Zhou et. al. [117] using density functional perturbation theory. The results obtained are in good agreement with the reported phonon modes of monoclinic structure [116–120]. The bands occurred in the range of 130-300 cm<sup>-1</sup> are mainly due to Hf-Hf vibrations [120].

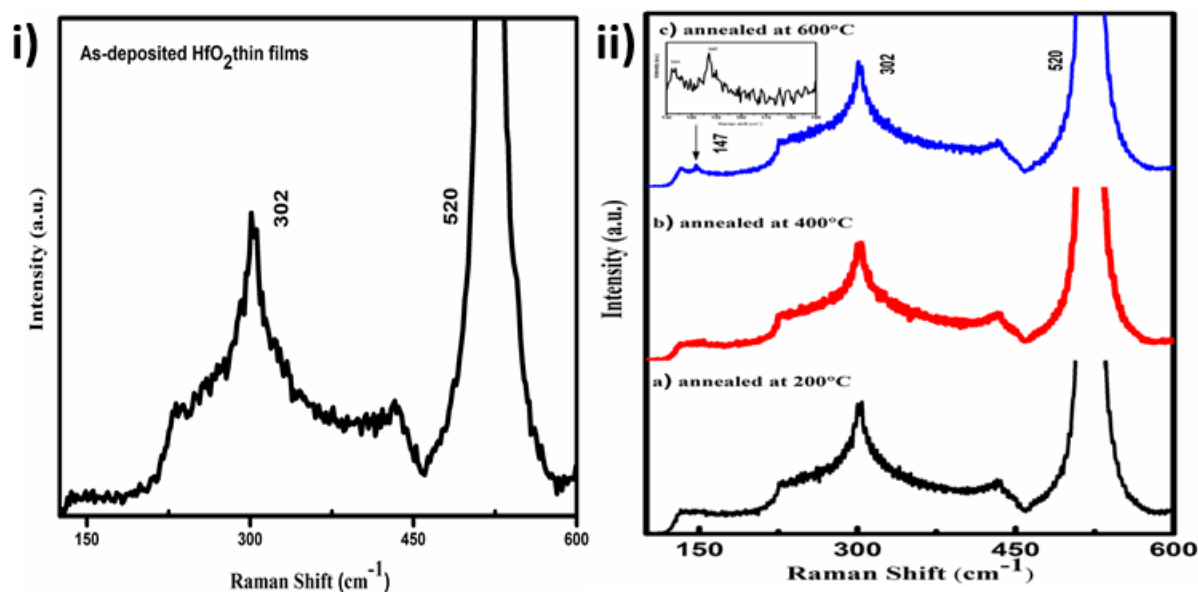


Figure 4.1 Raman spectra of HfO<sub>2</sub> thin films i) as-deposited and ii) annealed at a) 200°C b) 400°C c) 600°C.

XRD patterns of the pristine and annealed films are shown in 4.2. The XRD spectra of the as-deposited and films annealed up to 400°C reveal amorphous nature. A phase transition from amorphous to crystalline was observed for films annealed at 600°C. The phase transition could be due to the attainment of required activation energy in the form of temperature for rearrangement of atoms leading to crystallization of films [10]. The films annealed at 600°C exhibit monoclinic phase of HfO<sub>2</sub> with polycrystalline nature as evident from ( $\bar{1}11$ ), (111), (002), (200) and (102) planes [121]. The crystallite size is calculated using Scherrer formula [88] and it is found to be around 17 nm.

The surface morphology of the as-deposited and annealed films is presented in figure 4.3. The rms roughness of pristine and annealed films up to 400°C is around 0.20 nm. The images indicate that films are smooth, uniform and high-quality without any cracks, which make them suitable for the possible optoelectronic application. Further, it is observed that the surface roughness increased for the films annealed at 600°C. The increase in roughness could be due to the agglomeration of smaller grains to form bigger grains.

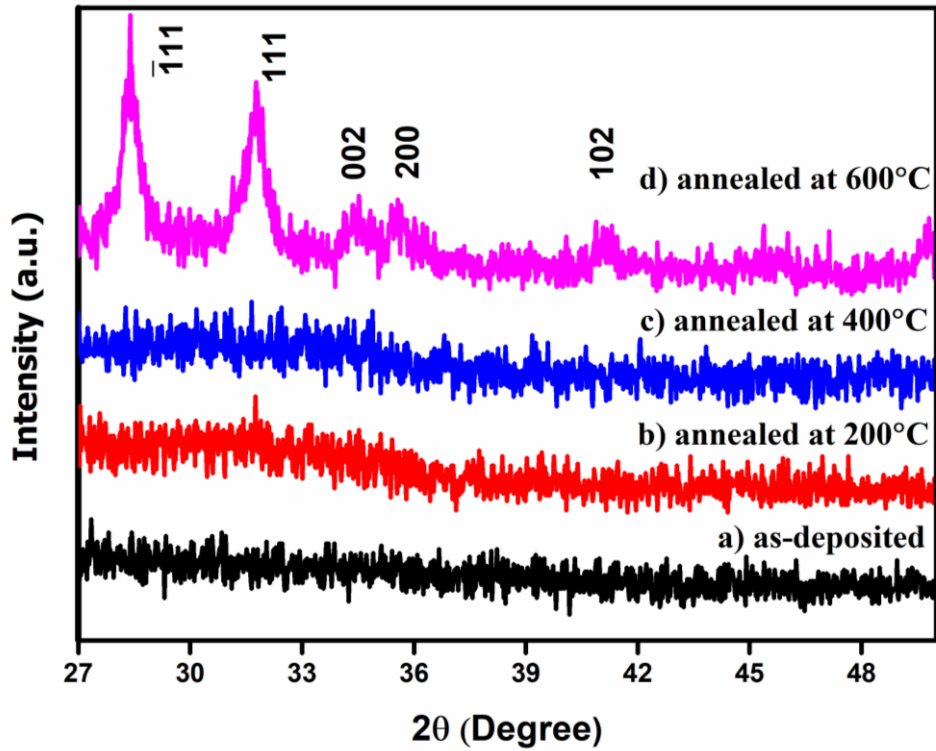


Figure 4.2 X-ray diffraction pattern of as-deposited and annealed HfO<sub>2</sub> thin films

To understand more about the surface symmetry distribution and spike of statistical distribution, two parameters such as skewness and kurtosis of the thin films were studied using nanoscope analysis software. The skewness and kurtosis refer to the third and fourth moments of roughness distribution function and both parameters are dimensionless quantities [122,123].

Table 1. The roughness, kurtosis and skewness values of the pristine and annealed HfO<sub>2</sub> thin films

Sl. No.	Sample	Roughness	Skewness	Kurtosis
1	As-deposited	0.21	-0.92	14.50
2	200°C	0.20	0.20	8.5
3	400°C	0.19	0.07	3.01
4	600°C	0.52	-0.22	3.99

For a gaussian distribution, the local maxima at a certain height under and over the mean line will be equal to the local minima, the kurtosis and skewness values are 3 and 0. A negative skewness represents that the film surface is with enormous local maxima whereas the positive skewness indicates the film surface with larger number of local minima above the mean as compared to the gaussian (skewness = 0). When compared to gaussian distribution (kurtosis = 3), the surface with a high kurtosis has enormous local minima above the mean but for a surface with high number of local maxima has low kurtosis [123,124]. The roughness, kurtosis and skewness value of the films are given in Table 1. The negative value of skewness signifies topological surfaces with a plateau-like structure and positive value implies surfaces without plateau. The high kurtosis and positive skewness values result in a lower static coefficient of friction. A negative skewness value results in a deviation in gaussian distribution. The above results indicate that the films may find potential applications in tribology [125–128].

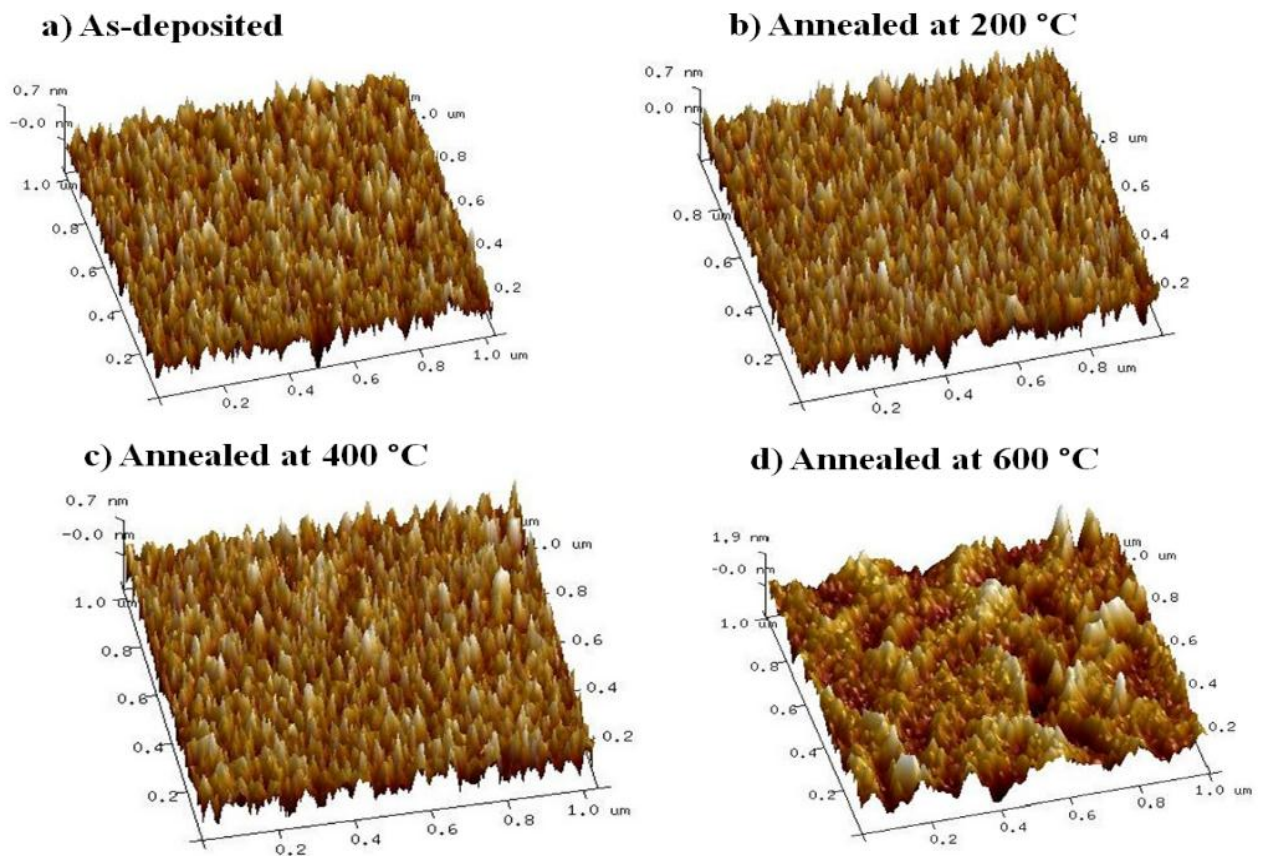


Figure 4.3 Surface morphology of as-deposited and annealed HfO<sub>2</sub> thin films

XPS spectra of HfO<sub>2</sub> thin films annealed at different temperatures recorded in the spectral range of 0 to 1100 eV are shown in figure 4.4. All the spectra were calibrated by adjusting C 1s peak at 284.8 eV. The identification of chemical composition of the thin films was capacitated by the peak positions in XPS spectra. It is evident from the graph that no other trace element except hafnium, oxygen and carbon are present. The core elemental spectra corresponding to 4f peaks of Hf along with their spin-orbit splitting values were analyzed (shown in figure 4.5). The feature peaks in the range of 16-19 eV stipulate the formation of Hf-O bonding in HfO<sub>2</sub> [129]. The spin-orbit splitting values (1.7 eV) match well with the previous reports. The binding energy of Hf 4f<sub>7/2</sub> and Hf 4f<sub>5/2</sub> related to the Hf-O bond in HfO<sub>2</sub> shifted to higher binding energies with annealing. The shift in binding energy suggests the existence of the electric field, charge transfer effect, environmental charge density or hybridization [130]. In the present work, the binding energy shift could be due to charge transfer related to the bond formation of hafnium oxide, sub-oxides that might have resulted an increase in potential experienced by the core electron that leads to a binding energy shift.

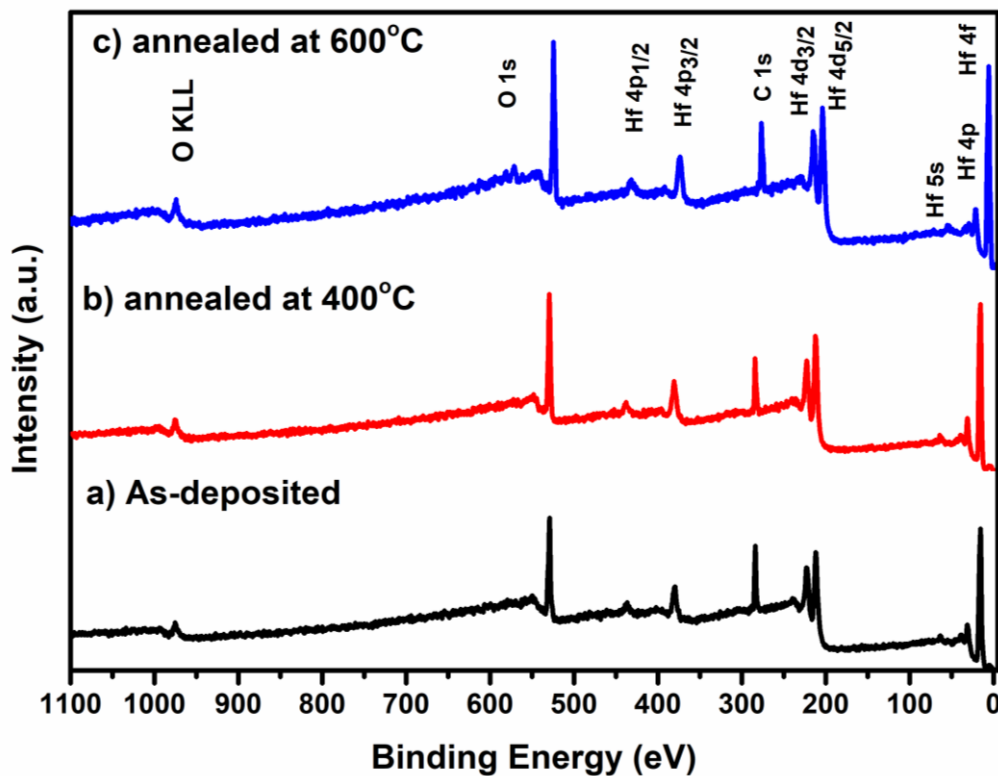


Figure 4.4 Survey XPS spectra of as-deposited and annealed HfO<sub>2</sub> thin films



The O/Hf relative concentration of the as-deposited thin films reveals almost stoichiometry (1.96:1). The deconvolution of Hf 4f peak at 16.2 eV and 17.9 eV indicates the formation of  $4f_{7/2}$  and  $4f_{5/2}$  corresponding to Hf 4f in hafnium oxide as-deposited films. The spectrum also suggests a small visible sub-peak towards the lower binding energy. This may be due to the presence of Hf-Hf bond and suggests oxygen vacancies or defects in  $\text{HfO}_2$  thin films [45,131]. For annealed films, the shoulder peak shifts toward the higher binding energy values. This may be attributed to the formation of hafnium sub-oxide resulted from the interaction of the hafnium metal with the oxygen [132,133]. The result of annealed films also suggests formation of hafnium-rich hafnium oxide and various interactions leading to sub-oxides formation. The bond formation of hafnium oxide, sub-oxides and their change could have resulted an increase in potential experienced by the core electron that leads to a binding energy shift [134].

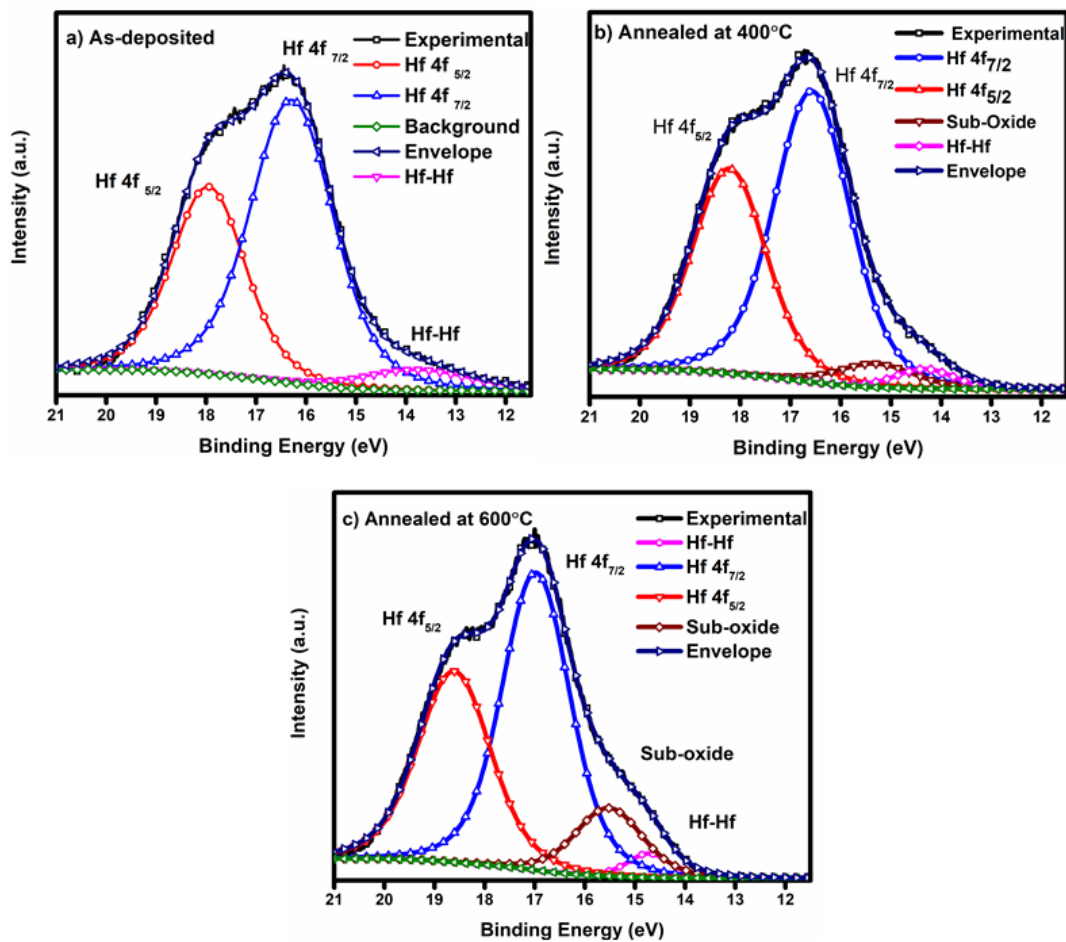


Figure 4.5 Core elemental XPS spectra of Hf 4f regions of as-deposited and annealed  $\text{HfO}_2$  thin films

Current-voltage characteristics of as-deposited and annealed films at 600°C are shown in figure 4.6. The annealed films show more leakage current than compared to the as-deposited films. The crystallization of the films with annealing causes increase in leakage current due to leakage paths [135–137]. The asymmetric nature of I-V curve in the accumulation and inversion bias is observed in the figure 4.6. This indicates that the leakage current under the substrate injection is lower than that under the gate injection at the same absolute voltage value [138,139].

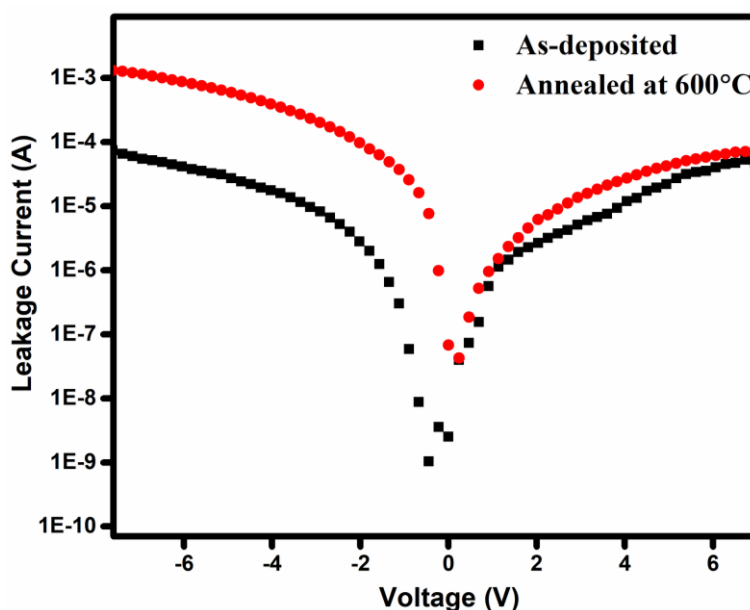


Figure 4.6 I-V characteristics of as-deposited and annealed HfO<sub>2</sub> thin film

Therefore, the growth process of the thin films may not only occur during the deposition but also later stages of post deposition annealing. The effect of annealing caused phase transition from amorphous to monoclinic structure. The crystalline films can increase the leakage current whereas an amorphous film restricts current leakage [140]. The AFM images reveal that the amorphous films are smooth than crystalline films. Thus, the amorphous thin film finds promising electronic application due to less current leakage rather than crystalline films [141,142].

In summary, HfO<sub>2</sub> thin films have been grown by RF magnetron sputtering on Si substrates. The effects of annealing temperature on structural, morphological, compositional and electrical properties were systematically investigated. Raman analysis reveals the

occurrence of phase transformation at high temperature. X-ray diffraction pattern confirms the formation of monoclinic structure. AFM images show that the amorphous films are of high-quality, which are smooth and crack free. Variation in kurtosis and skewness values reflect the potential tribological applications of the films. XPS spectra suggest shift in binding energy with annealing temperatures. Electrical measurements suggest the increase in leakage current with crystallization. The amorphous films exhibit better morphological, compositional and electrical properties than annealed crystalline films and these films are useful for electronic applications. It could be concluded that the annealing temperature strongly effects the structural, compositional and electrical properties of the films.

## **4.2 b) Charge storage characteristic of Au nanocrystals in HfO<sub>2</sub> tunneling and blocking layers**

### **4.2.1 Introduction**

Recently, nonvolatile memory (NVM) has attracted considerable attention due to the huge demand for faster, reliable and high capacity devices. An increase in data retention performance is achieved, especially in the programming efficiency of the device, by the introduction of high dielectric material rather than SiO<sub>2</sub> [24]. The occurrence of smaller conduction band as well as valance band offsets as compared to SiO<sub>2</sub> has enabled the performance of high-k materials in lower operating voltages [143,144]. Out of various high-k materials, HfO<sub>2</sub> is known to form better interface with Si and has better bandgap and dielectric constant [48]. Recently, floating gate memory devices have attracted wide interest for nonvolatile structures due to their retention time and low operating voltages. The improvement in memory performance can be achieved through the integration of semiconductor or metal NCs with high-k dielectric materials [25,145].

Particularly, metal nanoparticles possess large density of states and are preferred over semiconductor NCs due to their ability to enhance the electric field and provide better work-function engineering [146]. Among various metals, gold has gained considerable attention as it is non-toxic, easy to synthesize, has high density of states, large work function (5.1 eV), which creates deep potential well that enhance carrier confinement [147]. Au NCs as charge

storage nodes in various oxide matrices with better performance and retention time were reported [23,148–150].

Various techniques are employed for the synthesis of Au nanoparticles including electron-cyclotron-resonance plasma sputtering method, atom beam co-sputtering, chemical method, electron beam evaporation [151–154]. The properties of NCs memory are influenced by the size, shape and configuration of the NCs [155]. Moreover, NCs separation play an important role in the charge loss rate of the storage and retention behaviour of device. If the NCs are adjacent, it may act as a discharging path and degrade the charge storage and retention properties of the nonvolatile memory [146]. Thus, synthesis of Au NCs with uniformity and assembling them into a well-ordered matrix is most challenging. The use of insulating layer ( $\text{HfO}_2$ ) helps in attaining the necessary separation between adjacent NCs by preventing agglomeration [156,157].

There are various physical and chemical methods are employed for the fabrication of nonvolatile memory devices. The advantages of oxide deposition using RF magnetron sputtering include less wastage of the material, high adhesion of films and excellent uniformity with good packing density [158]. For the deposition of metal charge trap layer, electron beam evaporation method has merits in the deposition of material with high purity as there is a direct transfer of energy to the source via electron beams, simplicity, large area deposition and better control of deposition rate [159].

The main objective of the present investigation is to fabricate trilayer structure  $\text{HfO}_2/\text{Au}/\text{HfO}_2$  and to understand the effect of annealing temperature on various characteristics. Therefore, the trilayer structure of  $\text{HfO}_2/\text{Au}/\text{HfO}_2$  was deposited on Si substrate and further annealed at various temperatures for the formation of NCs. However, to the best of our knowledge, the combined use of RF sputtering and e-beam evaporation for the fabrication of  $\text{HfO}_2/\text{Au}/\text{HfO}_2$  trilayer structure has not been reported. Figure 4.7 shows the schematic diagram of the formation of the nonvolatile memory structure.

#### **4.2.2 Experimental details**

The nonvolatile memory trilayer structure was fabricated on p-type silicon substrates. Prior to the deposition, the substrates were thoroughly cleaned by Radio Corporation of

America (RCA) I and II processes [113] and HF was used for the removal of native oxide layer. The tunneling and blocking oxide layers of  $\text{HfO}_2$  were deposited by RF magnetron sputtering method with target-substrate distance (5cm), base pressure ( $6 \times 10^{-6}$  mbar, working pressure ( $3 \times 10^{-3}$  mbar), Ar flow rate (20 sccm) and RF power (100W). The target was pre-sputtered for 10 min to remove surface contamination and native oxides prior to the deposition. The substrate holder was rotated at low rpm (2) to obtain uniform thickness of the films [59] and the thickness of tunneling oxide was around 10 nm and blocking oxide was 20 nm as measured by a DTM. The Au layer of 5 nm was deposited using electron beam evaporation. The basic NVM structure with  $\text{HfO}_2$  tunneling and blocking layers is schematically illustrated in the figure 4.7. After the deposition, annealing of the samples was carried out for 60 min in nitrogen environment at  $650^\circ\text{C}$ ,  $750^\circ\text{C}$  and  $850^\circ\text{C}$  with a ramp rate of  $10^\circ\text{C}/\text{min}$ .

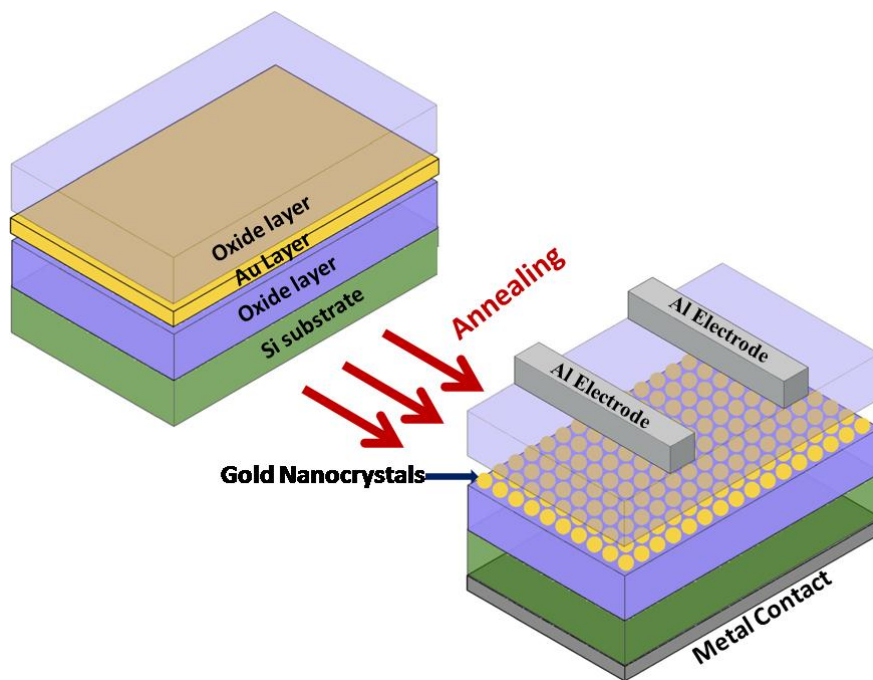


Figure 4.7 Schematic illustration of NVM structure.

### 4.2.3 Results and discussion

X-ray diffraction spectra of pristine and annealed  $\text{HfO}_2/\text{Au}/\text{HfO}_2$  nonvolatile memory structures are shown in figure 4.8. There is no peak observed in spectra of as-deposited

sample, which indicates that as grown films were amorphous. After annealing at a temperature greater than 650°C, HfO<sub>2</sub> films exhibit a monoclinic crystalline phase with the presence of predominate ( $\bar{1}11$ ), (111) and (200) planes. It is evident from the spectra that the orientation is predominant in the (111) rather than ( $\bar{1}11$ ) plane. The growth of the thin film in a preferred orientation is dominated by the minimization of total free energy. This could be explained by the migration of atoms towards the plane with lower surface energy. The basic crystal growth mechanism indicates that the growth of a crystal face is favoured by the crystal orientation. At preferred growth conditions, a growth competition may rise among differently oriented crystals. This may give rise to fast and slow growth rates of various preferred orientations. This competition will lead to an orientation selection and texture growth [160].

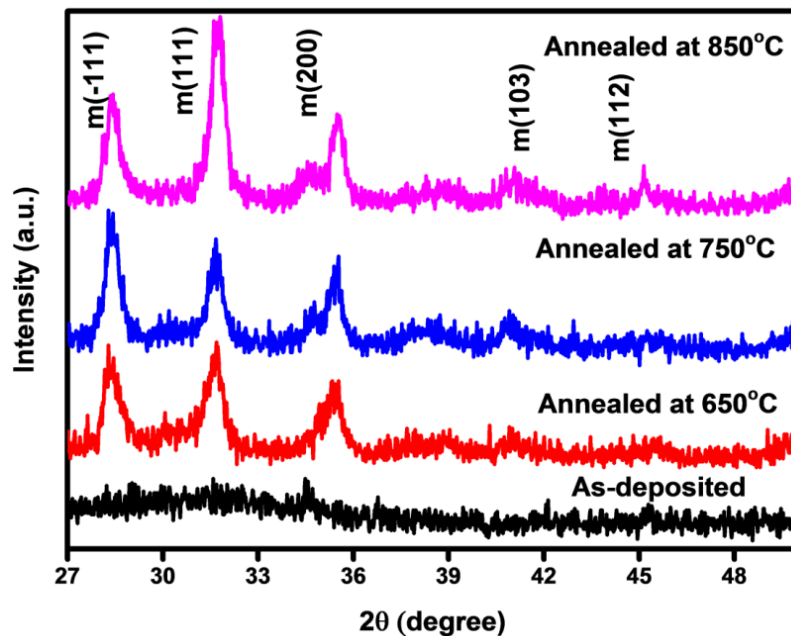


Figure 4.8 XRD pattern of NVM structure before and after annealing.

The Au/HfO<sub>2</sub> films deposited on carbon coated Ni TEM grids were annealed at 850°C. The TEM micrographs and elemental image mapping through STEM-EDX are shown in figure 4.9. The density of the Au NCs is around  $1 \times 10^{11} / \text{cm}^2$ . The HR-TEM image of Au points to the nanocrystal formation with a lattice spacing  $\sim 2.36 \text{ \AA}$  which corresponds to (111) plane. The polycrystalline diffraction rings indicate the formation of monoclinic HfO<sub>2</sub> as that of XRD. The presence of Au (white dots in STEM image and red in EDX image) along with Hf and O are also confirmed using STEM-EDX mapping shown in figure 4.9(e-h).



The surface morphology of the blocking layer using AFM for the as-deposited and annealed samples at different temperatures is presented in figure 4.10. The as-deposited sample images show rms roughness of around 0.6 nm indicating that the films are smooth, uniform and high-quality without any deformation.

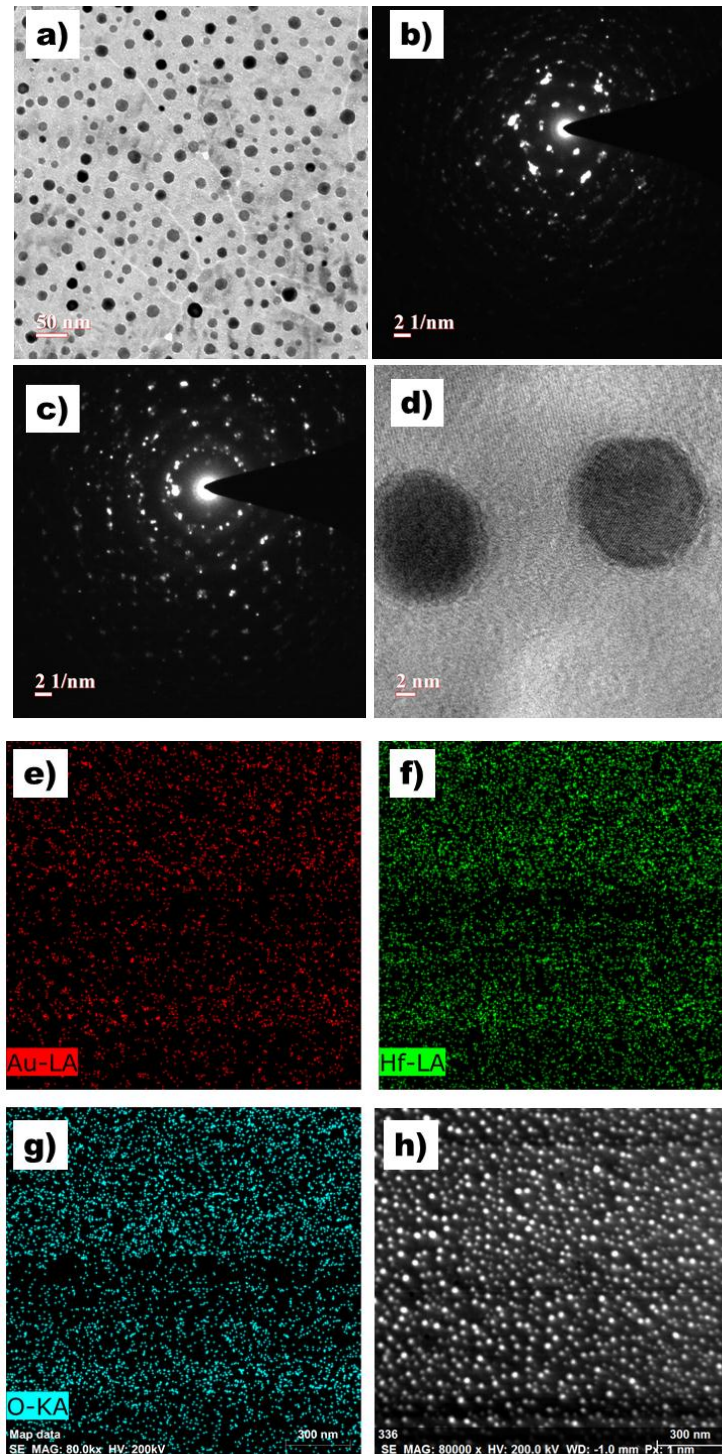


Figure 4.9 a) TEM images of Au in HfO<sub>2</sub> and SAED pattern of b) HfO<sub>2</sub> & c) Au d) typical HR image of Au nanocrystals (e-f) EDX mapping images and h) STEM image of Au.

The AFM images of the as-deposited and annealed films (blocking layer) indicate that the surface roughness increases as the films undergo transition from amorphous to crystalline. This could be due to the temperature assisted growth mechanism exhibited by the films. As the temperature is increased (650°C), the atoms attain activation energy and favours atomic mobility on the film surface resulting in re-orientation. The re-orientation of atoms on the surface due to the aggregation of small grains leading to the growth of larger grains might have resulted in an increase in roughness [10]. Further increase in temperature (850°C) results in the decrease in roughness. This could be attributed to the increase in atomic mobility, at high temperature, resulting in the easy attainment of equilibrium position by the fast-moving atoms [9].

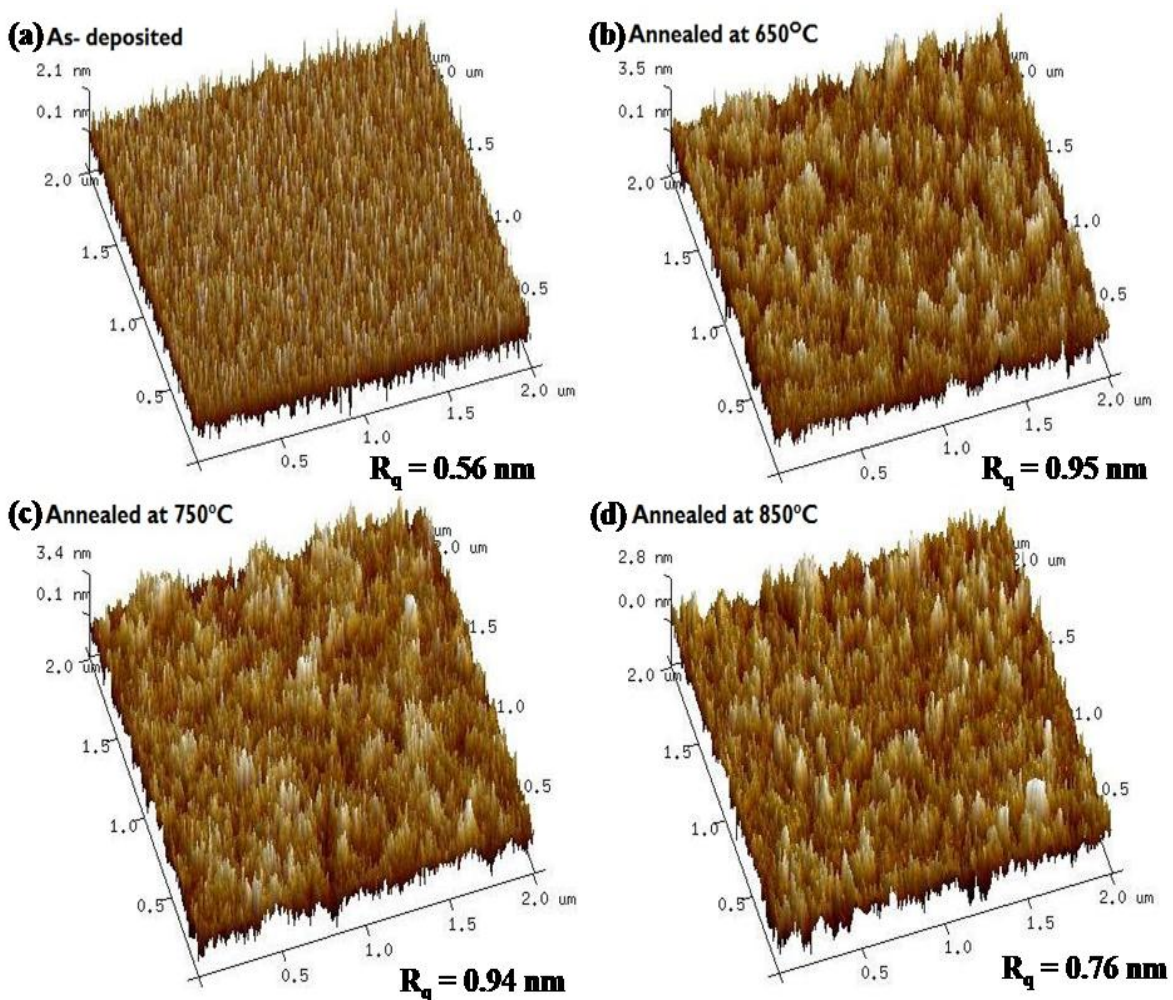


Figure 4.10 Surface morphology of HfO<sub>2</sub> blocking layer a) as-deposited b) annealed at 650°C c) annealed at 750°C and d) annealed at 850°C.



Figures 4.11-4.13 present the XPS spectra obtained from various layers of the nonvolatile memory structure. The peaks of all layers are calibrated from C 1s peak at 284.8 eV. The presence of C 1s peak arose due to the adsorbed environmental carbon. The core elemental spectra corresponding to 4f peaks of Hf along with their spin-orbit splitting values were analyzed for the blocking layer (fig 4.11). XPS spectra of the pristine as well as the annealed samples indicate the peaks at 16-19 eV with a spin-orbit splitting values (1.7 eV) that confirms the formation of Hf-O bonding in HfO<sub>2</sub> [161]. In addition, the spectra indicate significant shift in binding energy of HfO<sub>2</sub> in comparison of samples with and without annealing. The pristine samples reveal the presence of a sub-peak between 15-16 eV due to the formation of sub-oxide peak of hafnium [162,163]. An increase in the sub-oxide percentage with thermal annealing is evident from the deconvoluted spectra. Furthermore, the increase in temperature (850°C) results in the out-diffusion of oxygen, which results in an additional peak around 13 eV that corresponds to Hf-Hf peak [45].

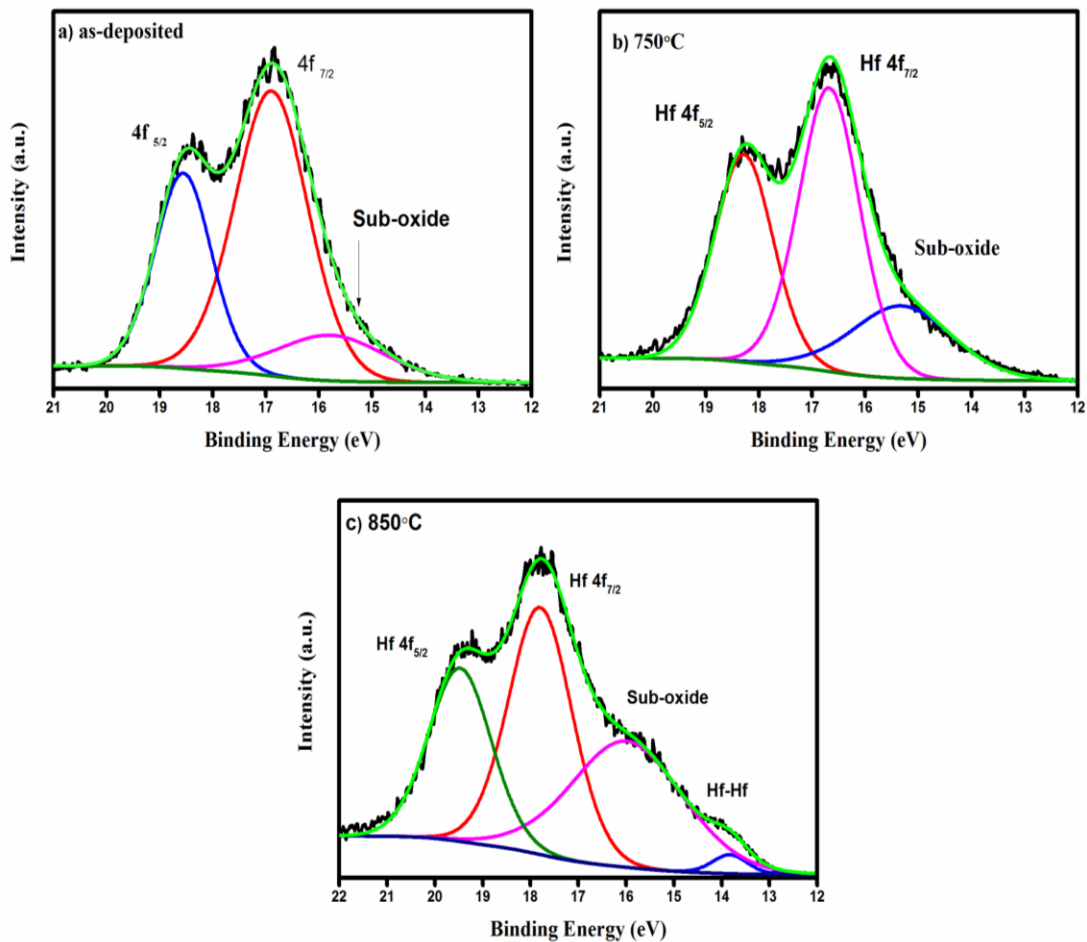


Figure 4.11 Core elemental XPS spectra of Hf blocking layer of NVM structure a) as-deposited b) annealed at 750°C and c) annealed at 850°C.

The XPS spectra obtained for the Au layer is presented in figure 4.12. The obtained results of Au 4f peaks are at 84 and 87.7 eV with difference in binding energy 3.7 eV. Other than the expected feature peak, emergence of two other peaks such as metallic gold (83 and 86 eV) [164,165] and gold oxide (85 and 89 eV) is observed [166]. The samples annealed at 750°C indicate a slight shift in the peak towards higher binding energies at 84.3 and 88 eV due to the formation of Au nanocrystals [167]. On the other hand, the peak at 83 eV completely disappears at 850°C indicating an increase in nanocrystals.

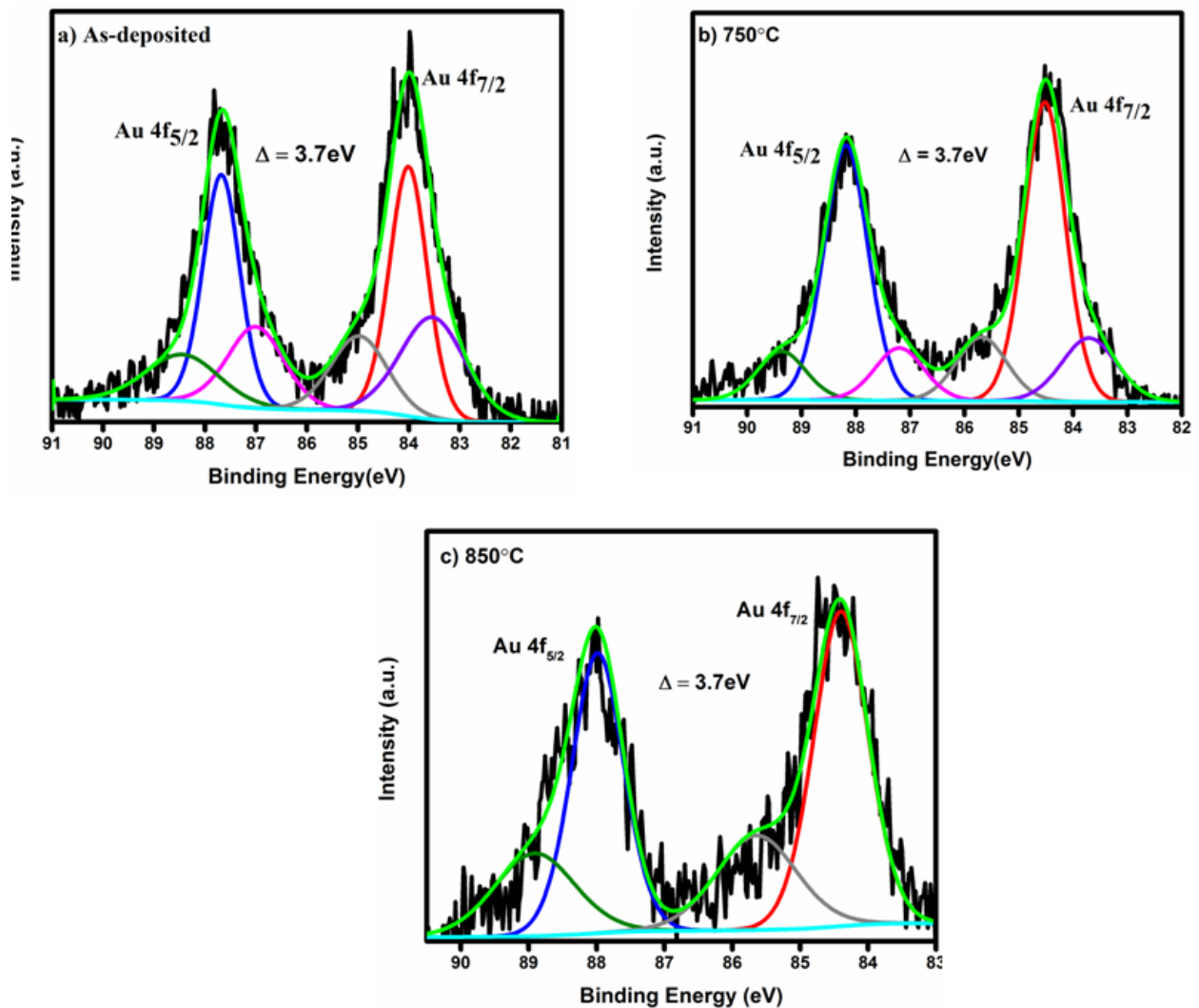


Figure 4.12 Core elemental XPS spectra of Au charge trapping layer of NVM structure a) as-deposited and annealed at b) 750°C and c) 850°C.

Figure 4.13 shows the core elemental spectra of the tunneling layer of the NVM structures. The hafnia 4f peak positions in the spectra indicate the possible formation of HfO<sub>2</sub>. The spin-orbital splitting of 4f<sub>5/2</sub> and 4f<sub>7/2</sub> is 1.7 eV. The as-deposited films show not

only the existence of  $\text{HfO}_2$  but also silicides, sub-oxides and silicates [162,163,168–171]. High temperature annealing at  $750^\circ\text{C}$  shows the reduction of sub-oxides concentration and shift of silicates to higher binding energy reveals the formation of stronger hafnium silicates bonds. When the temperature is further increased to  $850^\circ\text{C}$ , the deconvoluted images suggest possible occurrence of hafnium silicide doublets and it is evident from the spectra that stronger hafnium silicates have been formed due to the shoulder peak around 22 eV. Higher binding energy shift of silicates indicates the formation of passivated traps. This passivated trap may result in improved leakage property of the device [172].

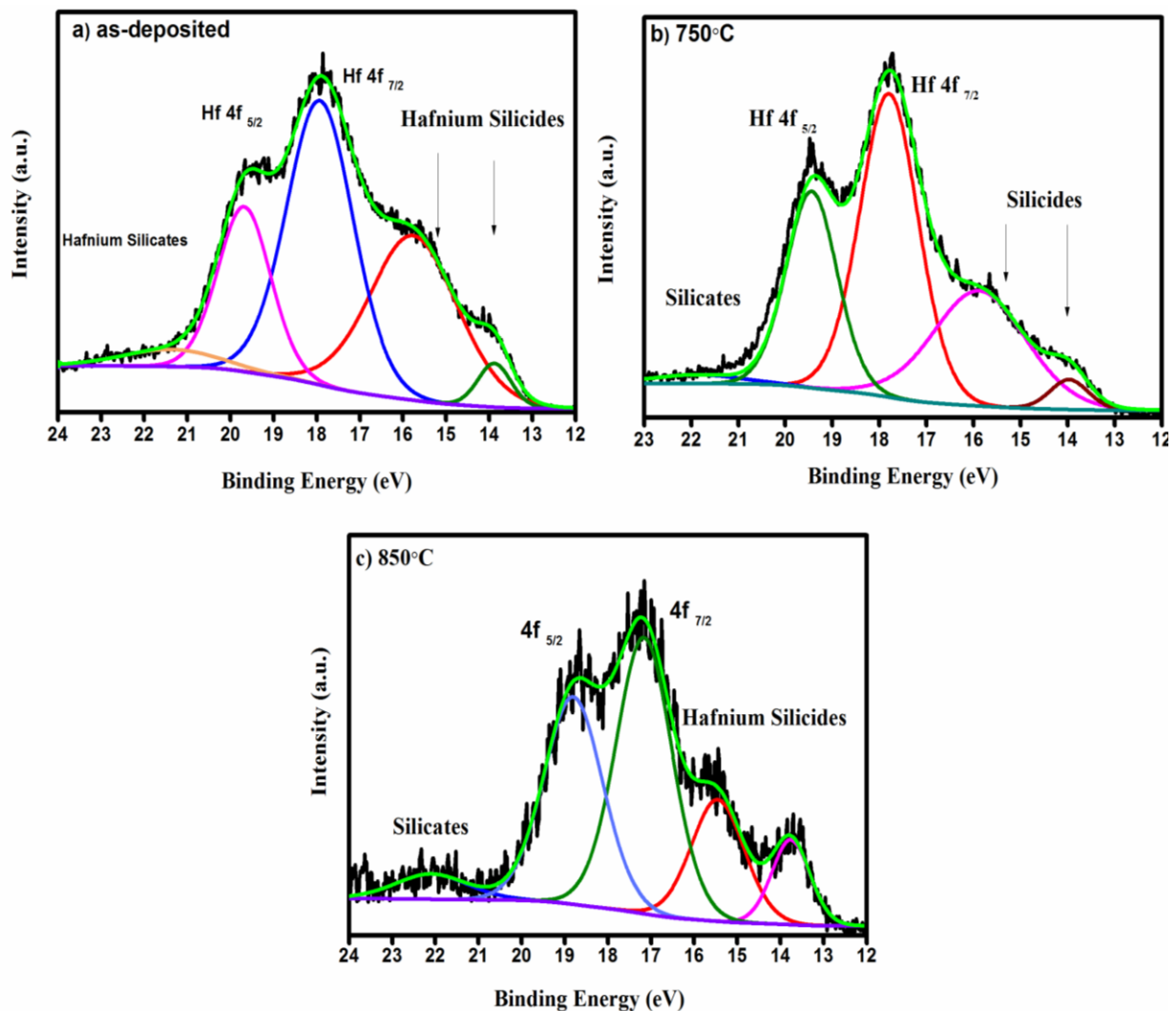


Figure 4.13 Core elemental XPS spectra of  $\text{HfO}_2$  tunneling layer of NVM structure a) as-deposited and annealed at b)  $750^\circ\text{C}$  and c)  $850^\circ\text{C}$ .

The RBS spectrum of sample annealed at  $850^\circ\text{C}$  presented in figure 4.14 shows the presence of Hf, O and Au. The diffusion of the  $\text{HfO}_2$  layers has been observed after thermal

annealing in the spectrum. The possibility of inter-diffusion and silicate formation is also confirmed through XPS spectra. The total thickness of the trilayer structure is estimated and found to be ~37 nm (considering the bulk densities).

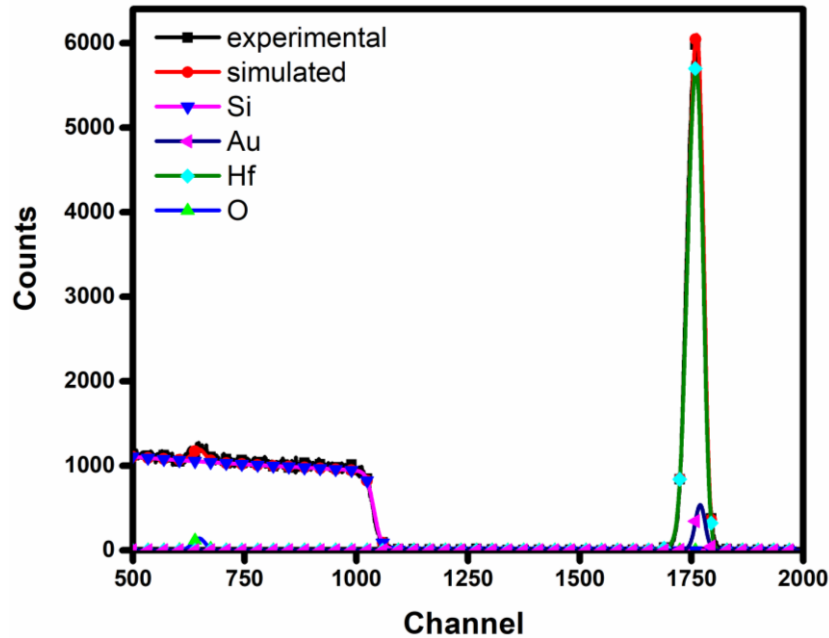


Figure 4.14 Rutherford backscattering spectra of NVM structure annealed at 850°C.

To understand the electrical behaviour of the structure, I-V measurements have been carried out and the characteristics are shown in figure 4.15. The low leakage value of the as-deposited structure indicates the excellent insulating behaviour of HfO<sub>2</sub> layer. The I-V characteristics show that at 750°C annealing the leakage properties of the trilayer structure decrease as compared to the pristine ones. The increase in leakage current is due to the crystallization [103,135,137] and grain growth of the HfO<sub>2</sub> thin films with annealing as indicated by XRD and AFM. Moreover, the interface states and defects might have also increased the leakage current density at high temperature annealing (here 750°C) [23]. Further annealing at 850°C results in decrease in the leakage current as compared to 750°C. This could be due to the significant role played by the increased Au nanocrystals formation as suggested by the XPS spectra. Either the injection and storage of carriers into the Au nanocrystals is prevented by the coulomb blockade effect or it could be due to the external electric field compensating the internal electric field in the nanocrystals by the charge stored [173].

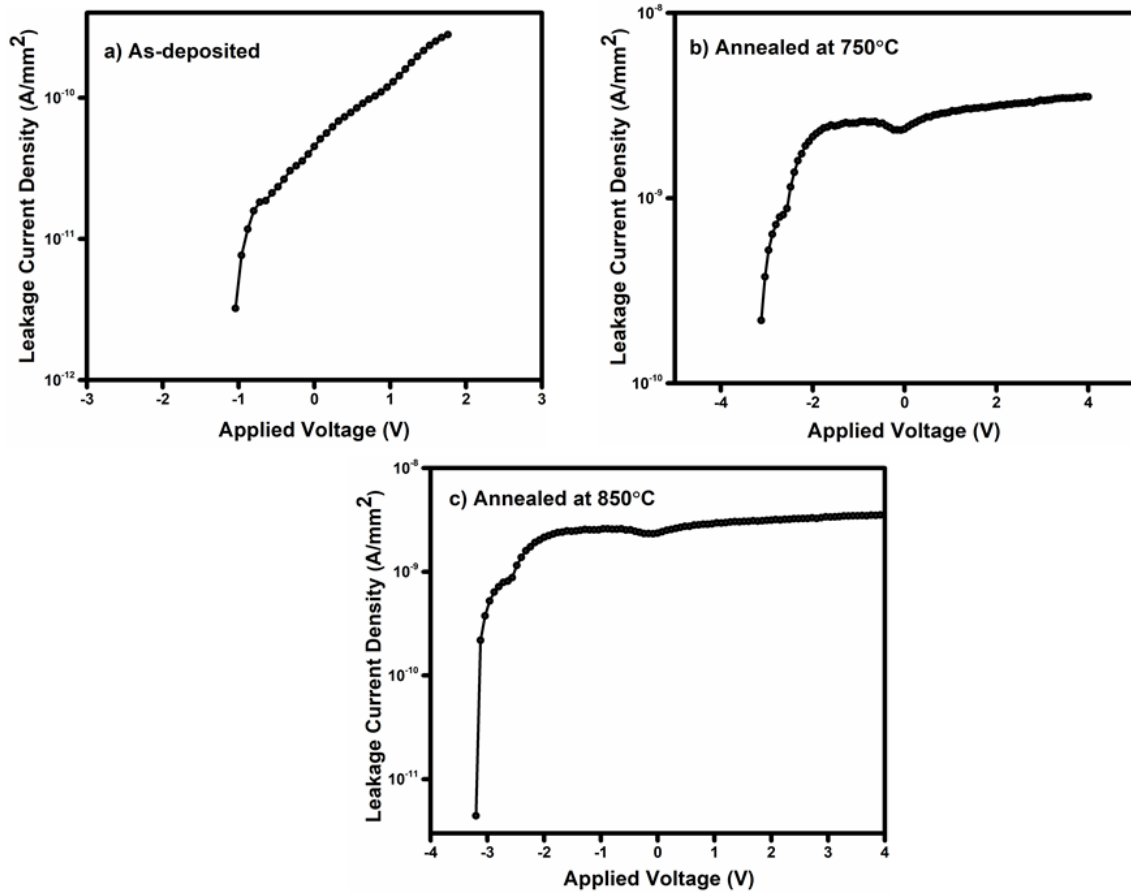


Figure 4.15 Leakage current versus applied voltage for as-deposited and annealed NVM structure

The high frequency (1MHz) C-V curve after bidirectional sweeps for different voltages for sample annealed at 850°C is shown in figure 4.16. The C-V curve implies the hole as well as electron trapping effects in the trilayer structure for nonvolatile memory application. When the negative bias voltage is applied, the hole tunneling happens through the tunneling layers from the substrate whereas with the forward bias voltage electron tunneling occurs. This, in turn, creates a deep inversion and accumulation regions. The similar clockwise and anticlockwise hysteresis characteristics with large memory window indicate the charge storage behaviour arising due to the Au NCs [23,24]. The C-V curve of the reference sample (HfO<sub>2</sub> only) without Au NCs exhibit negligible hysteresis as compared to the sample with Au NCs annealed at 850°C. Thus, hysteresis loop confirms the significant role of Au NCs in charge storage behaviour of the trilayer structure.

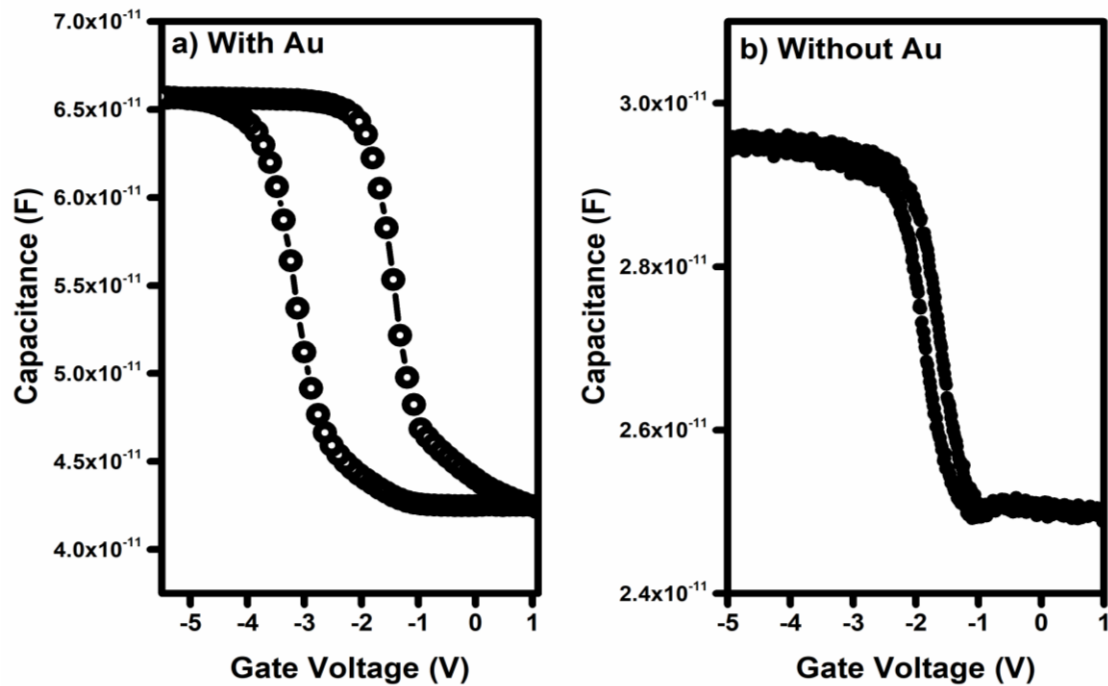


Figure 4.16 The capacitance-voltage curve of a) trilayer capacitor with Au nanocrystals and b) reference sample ( $\text{HfO}_2$  only) without Au nanocrystals annealed at  $850^\circ\text{C}$ .

#### 4.2.4 Summary

In summary, Au nanocrystals based hafnium oxide stack layer was fabricated for nonvolatile memory application. TEM image indicates the formation of Au nanocrystals. The deconvoluted spectra of XPS shows the formation of hafnium oxide with sub-oxides, silicides and silicate. XPS of Au layer suggests the formation of Au nanocrystals. RBS was used to estimate the thickness of annealed trilayer structure. The I-V measurements indicate that annealing results in a variation of the leakage properties. C-V hysteresis curve confirms the significant role of Au nanocrystals in charge storage characteristics and it shows the charge accumulation as well as inversion properties. This study demonstrates the structural, morphological and electrical properties of  $\text{HfO}_2/\text{Au}/\text{HfO}_2$  stack layer and the role of Au nanocrystals in the charge storage behaviour of nonvolatile memory device structures.

# **Chapter 5**

## **Electrical and compositional properties of SiO<sub>2</sub>/Au/SiO<sub>2</sub> trilayer structure**

## 5.1 Introduction

During recent years, the semiconductor storage device technology has witnessed the boom in big data, cloud computing and electronic gadgets [44]. The increased demand for nonvolatile memory with high density, low power consumption, high speed communication and better reliability have led the silicon industry to rescale the dimensions of the gate dielectric oxide [25]. The scaling down of oxide layers has increased the leakage current leading to the degradation of device performance. Predominant gate dielectric material ( $\text{SiO}_2$ ) has been gradually replaced by alternative dielectric materials with high dielectric constant, large bandgap, low interface state density and good thermal stability for better device performance [26,59]. One of the alternate approaches other than scaling  $\text{SiO}_2$  is to use floating nodes [174,175]. The two main methods in this approach are nitride floating gates and NC storage nodes. In nanocrystal floating gate approach, the conventional floating gate is replaced by NCs. The utilization of NCs in floating gate reduces the charge loss, increases write-erase speed and lowers operating voltage [176]. The NCs memory can be further classified as metal and semiconductor NCs. Among them, the metal NCs are more advantageous than semiconductor NCs in nonvolatile memory devices due to high density of states, better three-dimensional electric field enhancement and high work-function engineering. The metal nanoparticles play a significant role in charge storage capability and characteristic reproducibility for nonvolatile devices [177]. The high density of states provided by the metal NCs help in enhanced charge storage.

Researchers have used various methods to fabricate NVM device. Chan et. al. fabricated Au NC based floating gate memory structure with  $\text{HfAlO}$  as tunneling and blocking layers using pulsed laser deposition. For the growth of Au NCs, the device was annealed at various temperatures and obtained a memory window up to 10V with a voltage sweep  $\pm 12\text{V}$  [43]. Similarly, the memory capacitor behaviour of Au NCs in  $\text{HfO}_2$  tunneling and blocking layers was reported. The oxide layers were deposited using Atomic layer deposition (ALD) and very large hysteresis window of 9.25V for a sweep of  $\pm 7\text{V}$  was observed [24]. Moreover, for  $\text{SiO}_2$  tunneling and  $\text{HfO}_2$  blocking layer deposited using ALD with Au NCs exhibited a window of 12.6V at  $\pm 12\text{V}$  [178]. The promising potential application of Au NCs in low programming/ erasing voltage with a memory window of 1V at  $\pm 2\text{V}$  was reported. The device structure was fabricated using a combination of various



methods such as RTA, sputtering and e-beam evaporation [45]. The charge localization effects of Au nonvolatile structure with thermal annealing were investigated by F. Xang et al. The device structure was fabricated by ALD for oxide deposition and e-beam for Au deposition [48]. The method of deposition and the annealing temperature play a crucial role on various properties of device structure. Therefore, it is very important to understand the effect of annealing temperature on the trilayer structure from basic and applied point of view. Here, in this experiment RF magnetron sputtering was used for the deposition of oxide layers and electron beam evaporation for the deposition of Au charge trapping layer. However, no systematic reports are available on the fabrication of SiO<sub>2</sub>/Au/SiO<sub>2</sub> trilayer structure using RF magnetron sputtering and electron beam evaporation and the effects of annealing temperature. Therefore, an extensive investigation is utmost required to correlate the performance with fabrication methods and annealing temperature.

The present study aims at the fabrication of Au charge trapping layer sandwiched between SiO<sub>2</sub> tunneling and blocking layers and to understand the effect of annealing temperature on various characteristics of trilayer structure. For this purpose, the SiO<sub>2</sub>/Au/SiO<sub>2</sub> trilayer was deposited on Si substrate and further annealed at various temperatures for the formation of NCs.

## 5.2 Experimental details

In the present work, nonvolatile memory trilayer structure with Au charge trapping layer was fabricated on p-type silicon (100) substrate with resistivity of 1-10 Ωcm. The Si wafers were cleaned using RCA I and II process to remove organic and inorganic residues from the surface. To remove the native oxide, the substrates were treated with dilute hydrofluoric solution. The base vacuum of  $6 \times 10^{-6}$  mbar was achieved using a rotary assisted turbo pump prior to the deposition. After pre-sputtering of target for 10 min, tunneling layer of 10 nm of SiO<sub>2</sub> was deposited using RF magnetron sputtering. For the deposition of trapping layer, an Au layer of 3 nm was deposited using electron beam evaporation. Finally, a thick layer of SiO<sub>2</sub> with a thickness of 20 nm was also deposited using RF magnetron sputtering for the fabrication of the trilayer structure. The schematic illustration of SiO<sub>2</sub>/Au/SiO<sub>2</sub> trilayer structure is shown in figure 5.1. To form Au NCs, the thermal annealing of the structure was carried out in N<sub>2</sub> environment at various temperatures (650,750

and 850°C) for an hour with a ramp rate of 10°C/min. For measuring the electrical properties of the trilayer structure, top Al electrodes with a diameter ~1 mm and thickness 250 nm were deposited using electron beam evaporation. To understand the formation of NCs, SiO<sub>2</sub> tunneling layer with thickness of 10 nm was deposited using RF magnetron sputtering on Ni TEM grid. Subsequently, a thin layer of 3 nm Au was deposited using electron beam evaporation on SiO<sub>2</sub> layer and was annealed at 850°C for an hour in N<sub>2</sub> environment. These samples were characterized using TEM to confirm the formation of Au NCs.

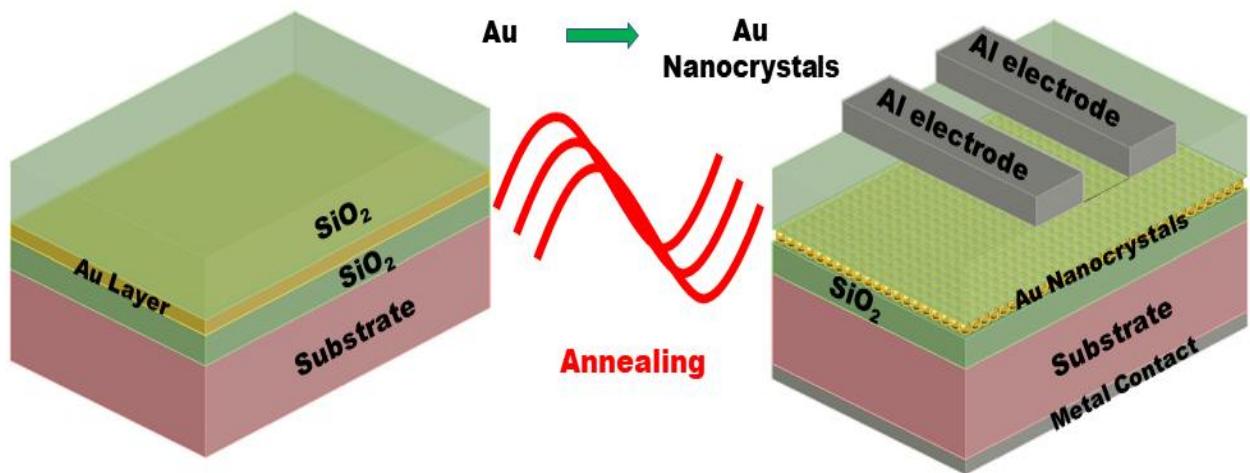


Figure 5.1 Schematic illustration of SiO<sub>2</sub>/Au/SiO<sub>2</sub> NVM structure.

### 5.3 Results and discussion

TEM images of Au/SiO<sub>2</sub> annealed at 850°C are shown in figure 5.2. Figure 5.2a presents TEM micrographs of Au NCs in SiO<sub>2</sub>. The density of Au NCs is around  $1.1 \times 10^{11}/\text{cm}^2$ . The selected area electron diffraction pattern (SAED) of Au is presented in figure 5.2b. The HRTEM image (shown in figure 5.2c) confirms the formation of Au NCs. Moreover, in figure 5.3, the STEM image also confirms the presence of Au particle either as white dots or as red dots in EDX mapping along with Si and oxygen.

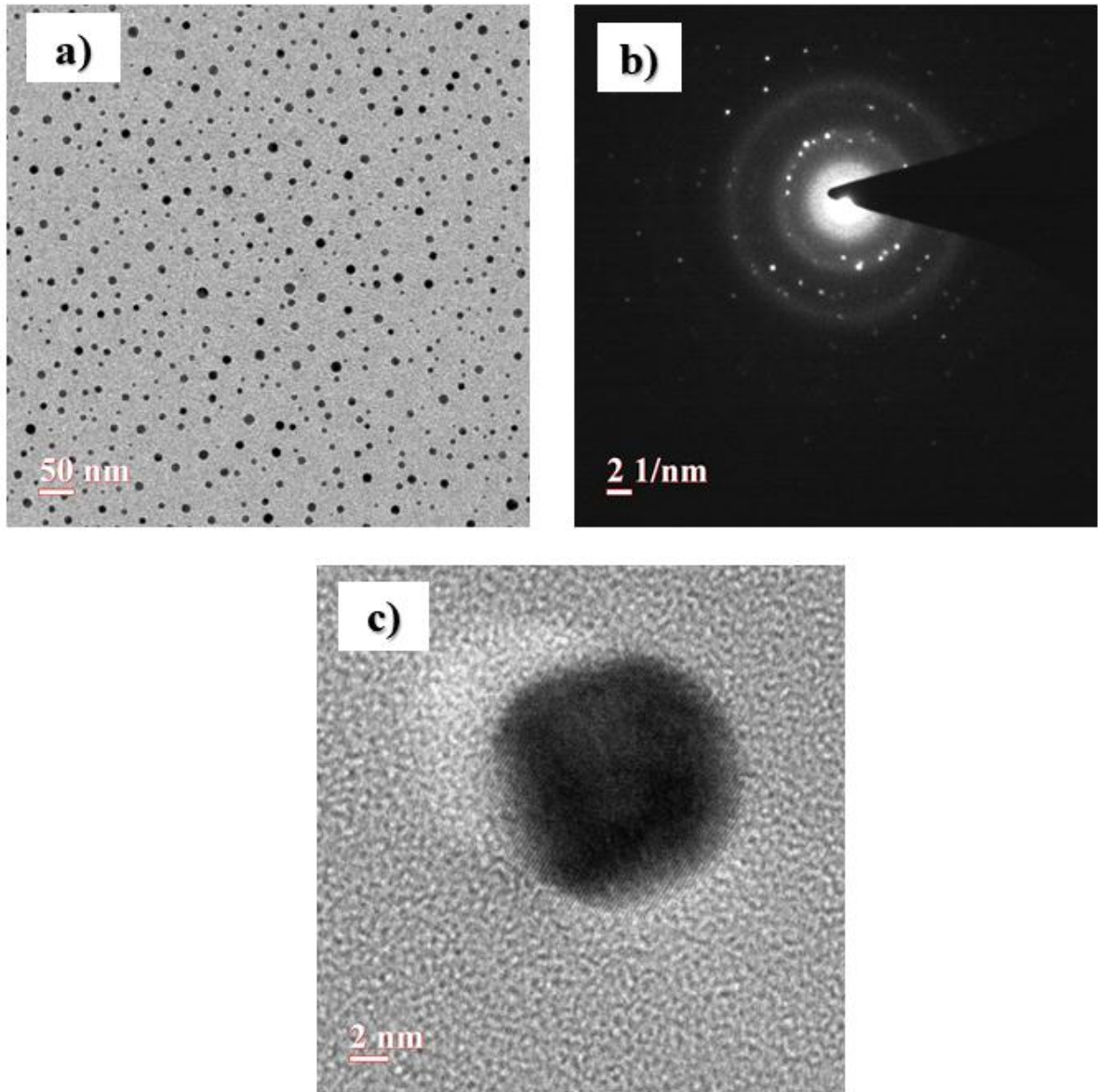


Figure 5.2 a) TEM images of Au in SiO<sub>2</sub> b) Au SAED pattern c) HRTEM image of Au nanocrystal in SiO<sub>2</sub> annealed at 850°C.

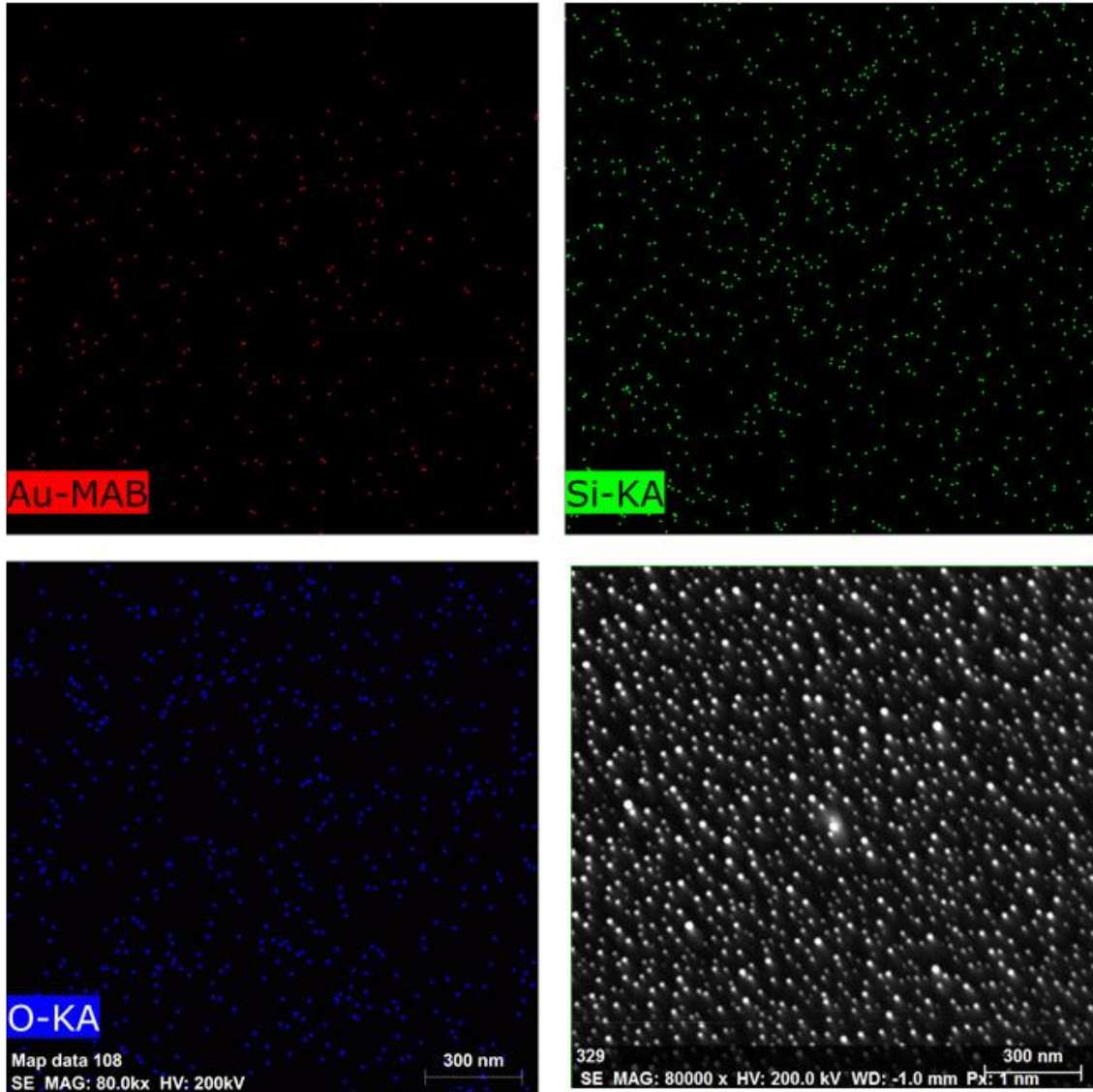


Figure 5.3 STEM – EDX mapping image of Au, Si and O

The surface morphology of the blocking layer was studied using AFM. Figure 5.4 shows the AFM images of as-deposited and annealed samples at different temperatures in the scan range of  $1 \times 1 \mu\text{m}^2$ . The root mean square roughness ( $R_{\text{rms}}$ ) of the as-deposited and annealed samples at  $650^\circ\text{C}$ ,  $750^\circ\text{C}$  and  $850^\circ\text{C}$  are estimated to be 1.08, 0.92, 0.99 and 0.93 nm, respectively. The absence of visible pores, cracks and voids in as-deposited blocking layer indicates tightly packed atomic arrangement. This shows that the films are well-deposited [179] and RF magnetron sputtering is good to be employed for oxides depositions. The peak to valley roughness for the as-deposited and annealed samples are 8.5, 5.4, 7.0 and 6.9 nm, respectively. It is reported that when the peak to valley roughness increases the leakage



current also increases [180]. The peak to valley roughness of the samples annealed at 650°C is decreased as compared to pristine ones. Further increase in the annealing temperature results in the increase in the peak to valley roughness as compared to samples annealed at 650°C. This could be due to the rearrangement of atoms on the surface by attaining sufficient thermal energy.

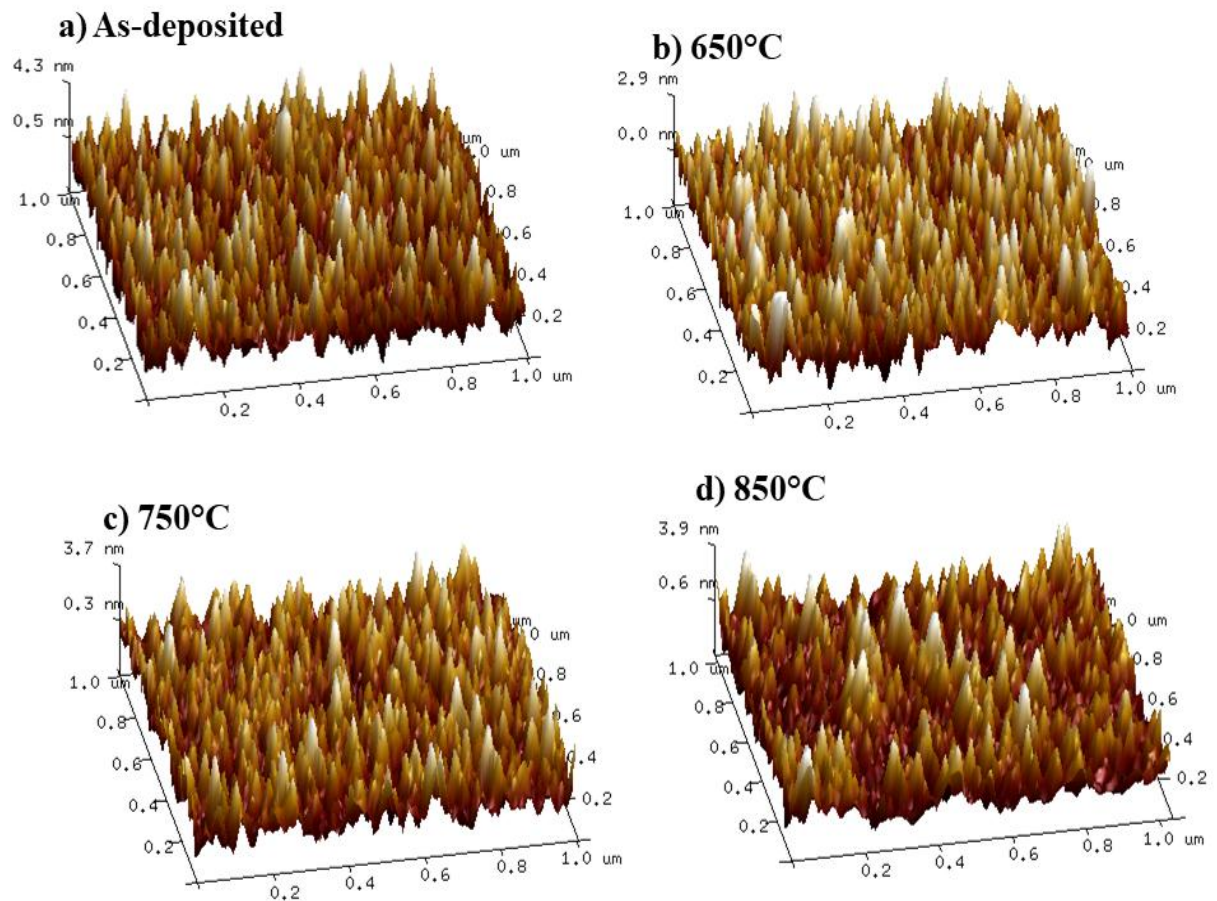


Figure 5.4 Surface morphology of blocking layer before and after annealing.

RBS measurements were done to understand the presence of elements and to estimate thickness of trilayer structure. The RBS spectrum of the nonvolatile structure annealed at 850°C is presented in figure 5.5. The spectrum clearly shows the presence of O, Si and Au. The thickness of the trilayer structure is determined by fitting the experimentally obtained spectrum (black) with simulated spectrum (red). The spectrum reveals the inter-diffusion, which is also evident from XPS spectra as shown in figure 5.9-5.11. The total thickness of the trilayer structure is estimated and found to be ~38 nm by considering the bulk densities.

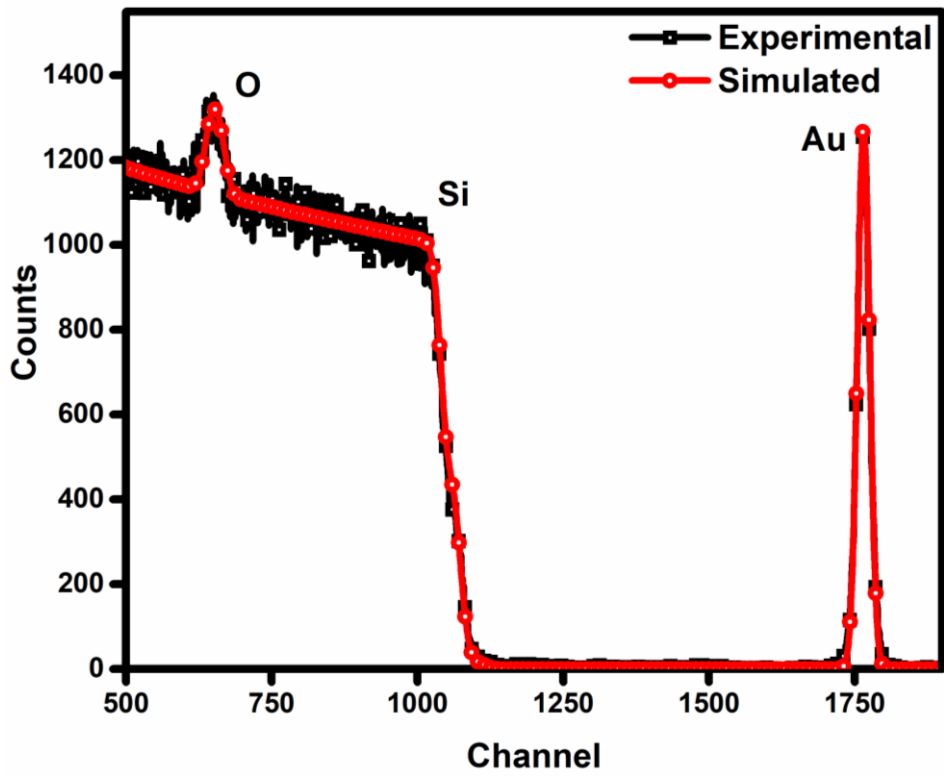


Figure 5.5 Rutherford backscattering spectrum of SiO<sub>2</sub>/Au/SiO<sub>2</sub> structure annealed at 850°C.

The XRD pattern of trilayer structure is shown in figure 5.6. Amorphous nature of SiO<sub>2</sub> is evident from the XRD pattern.

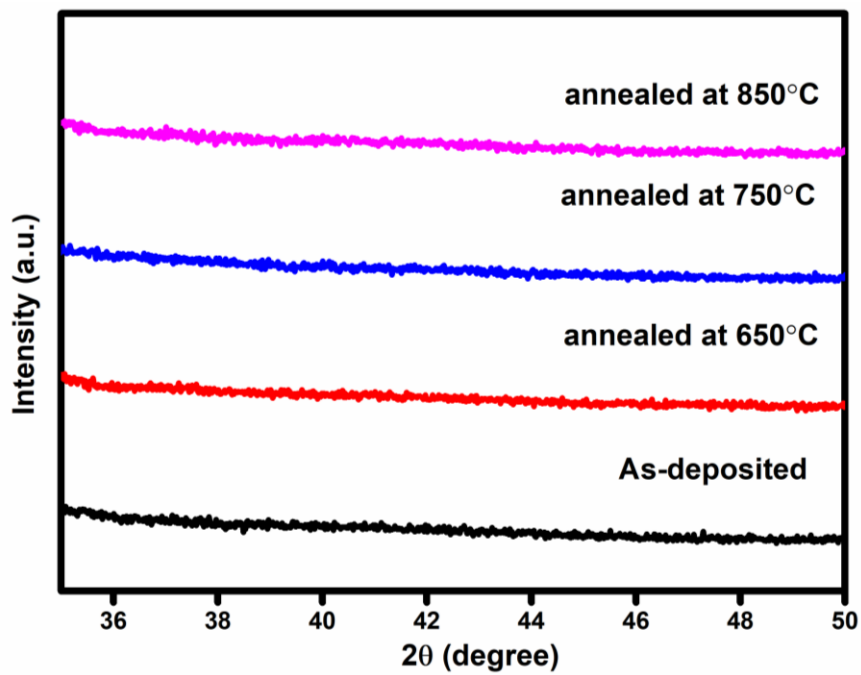


Figure 5.6: XRD pattern of trilayer structure

Figure 5.7 shows the I-V relation of NVM structure under different annealing temperatures. The reverse and forward current was measured by scanning the voltage from -6 to +6V. A variation in leakage current with annealing is visible from the I-V measurement. The leakage current values for as-deposited and annealed samples at 1V are compared. The annealed samples show significant decrease in leakage current as compared to the pristine ones. The decrease in leakage current with high temperature annealing may be due to Au nanocrystal formation [23]. This reduction might have resulted either from the carriers injected into the NCs or by the blocking of external electric field by the internal electric field of the charge stored in the Au NCs. The as-deposited and annealed structures show a variation in current minima values from 0V. This shift in leakage current value from 0V is due to the charge storage [23,181,182]. The variation in the current minima values may be attributed to the formation of NCs with annealing. It is also reported that the NCs play a crucial role in nonvolatile memory behaviour [155].

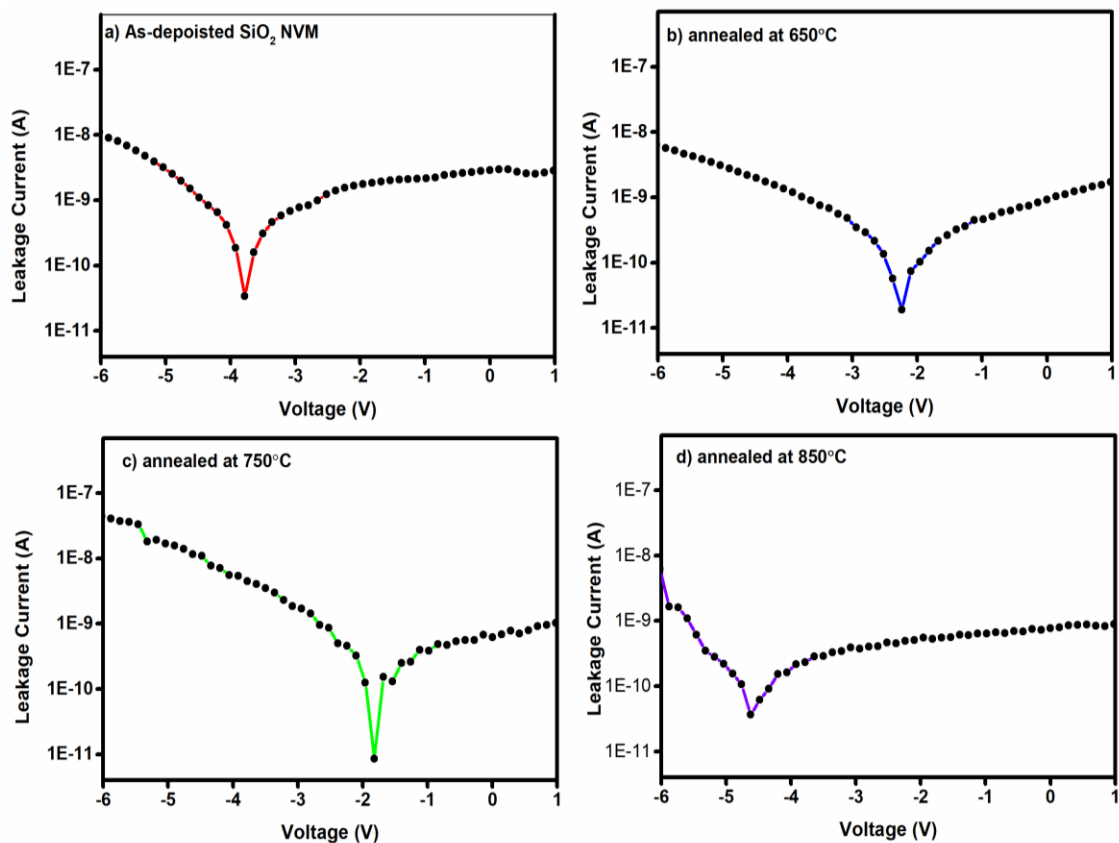


Figure 5.7 Leakage current - voltage characteristics of trilayer structure before and after annealing

The charge storage characteristics of nonvolatile memory structure with Au NCs annealed at 850°C analysed by typical high frequency (1MHz) C-V measurement at room temperature are presented in figure 5.8. The gate voltage is swept from negative to positive region and vice versa in the range of 7V. Hence, the capacitor structure is swept across accumulation and inversion regions. This counter-clockwise hysteresis curve indicates the injection of the charges from the substrate into the NCs and vice versa. The deviation from ideal condition is observed in the hysteresis curve as the centre comes around -3V rather than 0V. The main reasons for the deviation are the difference in work function between the metal electrode and the silicon and the immobile charges existing in the oxide layers [46]. The presence of accumulation and inversion regions in the hysteresis curve could be explained with respect to the voltage applied. When a positive voltage is applied, electrons will be ejected into the Au NCs from the Si substrate (electron charging). On the other hand, when negative voltage is applied, holes will be injected into the NCs (hole charging). Here, in the present experiment, the memory window obtained is around 2V. The hysteresis curve confirms the significant role of Au NCs in the charge storage behaviour of the capacitor structure.

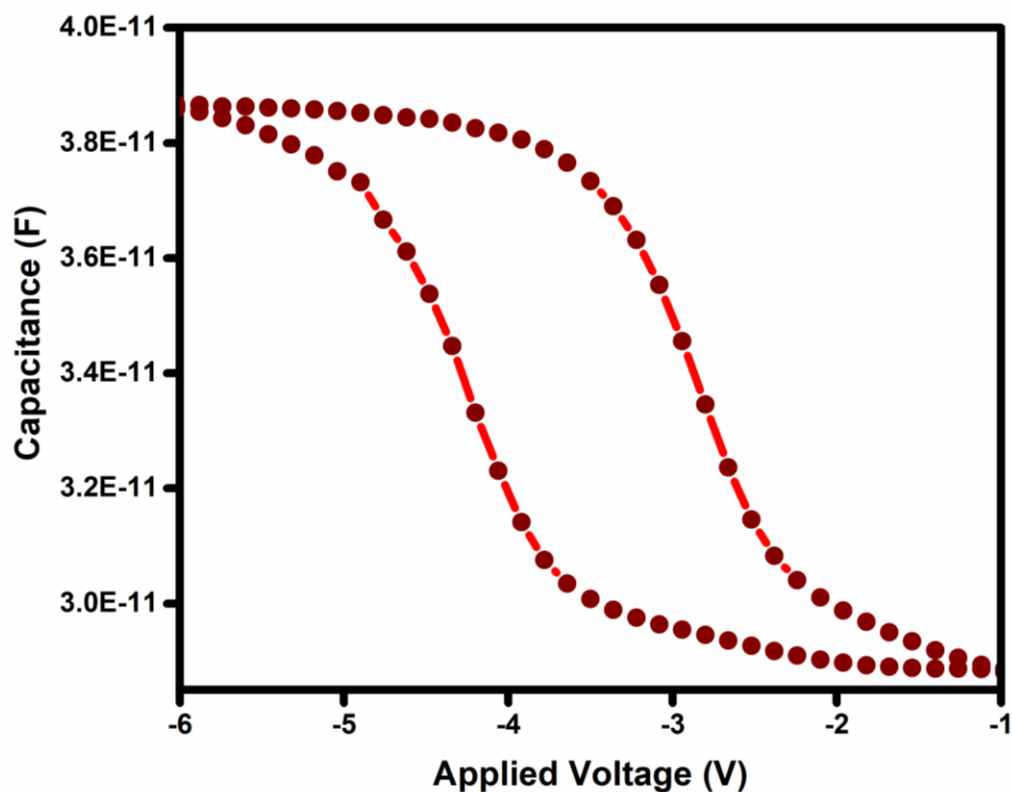


Figure 5.8 C-V hysteresis of NVM structure with Au nanocrystals in SiO<sub>2</sub> tunneling and blocking layers



Further understanding of the elemental composition of the NVM structures was obtained using XPS (figures 5.9-5.11). The peaks of all layers are calibrated from C 1s peak at 284.8 eV. The blocking layer of the as-deposited sample indicates the binding energy of Si 2p is at 103.5 eV. This shows the formation of SiO<sub>2</sub> [183]. Meanwhile, in addition to the major 4f peak, the Au spectra indicate two more sub-peaks. The 4f peak of gold is around 84 eV and 87.7 eV with a difference in binding energy around 3.7 eV, whereas the sub-peaks around 83 and 87 eV represent the presence of metallic/bulk Au particle [184–186]. The shoulder peak at higher binding energy is related to the oxidation of Au [166]. On the other hand, the Au spectra of the samples annealed at 750°C show slight shift towards higher binding energy around 84.3 eV indicating the formation of Au nanocrystals [167]. This could be attributed to the shift in fermi level with respect to the shrinkage of the particles. The disappearance of metallic peak in the spectra compliments the nanocrystals formation. No variation for Si 2p peak of blocking layer has been noticed but the tunneling layer shows an additional peak of SiO at 101.8 eV. Almost similar features in blocking, trapping and tunneling layer are observed for the films annealed at 850°C with a small shift towards lower binding energy due to annealing.

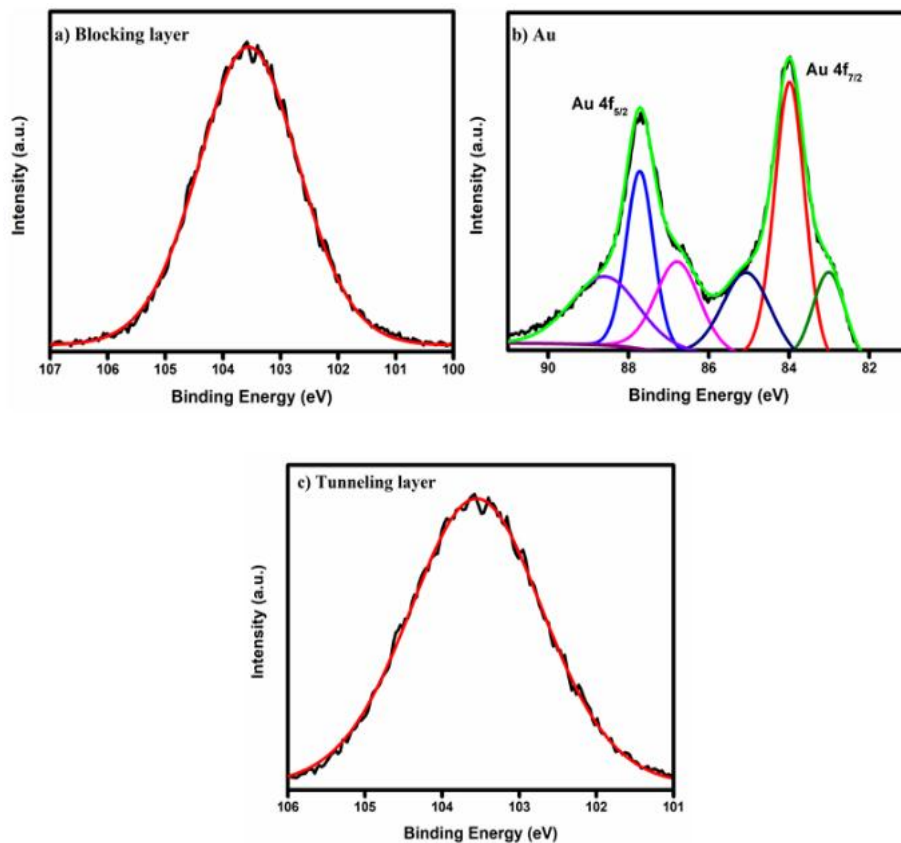


Figure 5.9 XPS spectra of as-deposited blocking, trapping and tunneling layers.

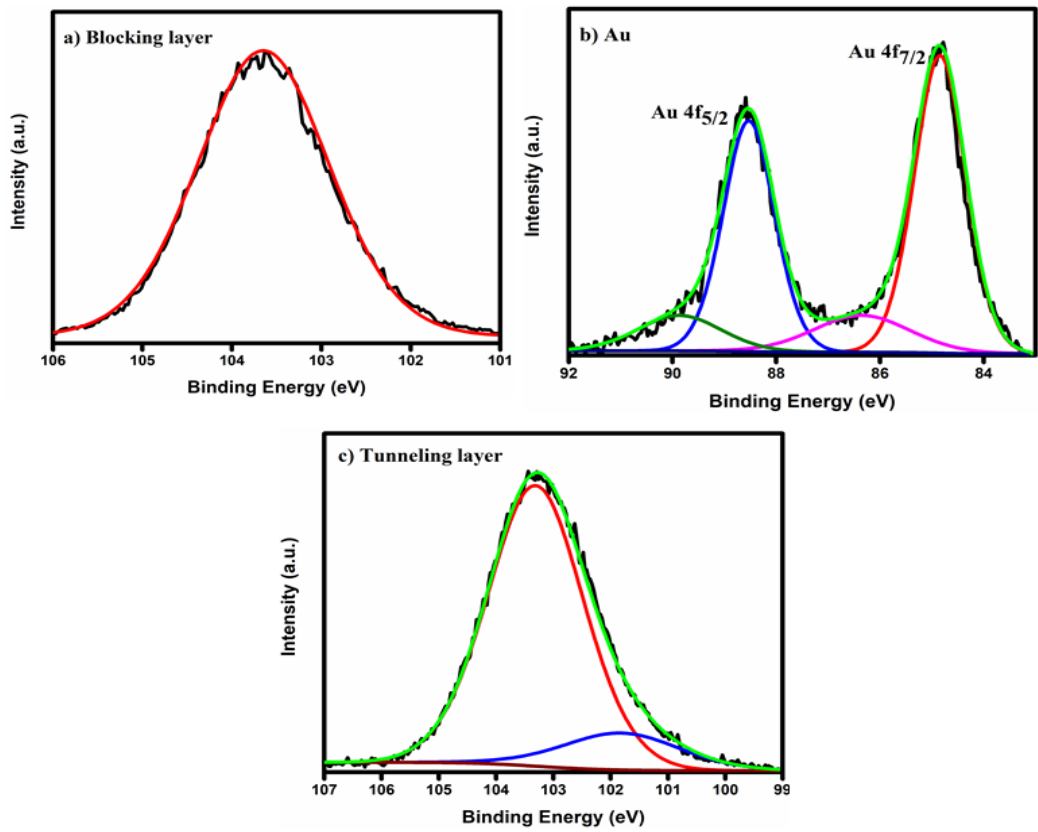


Figure 5.10 XPS spectra of blocking, trapping and tunneling layers annealed at 750°C.

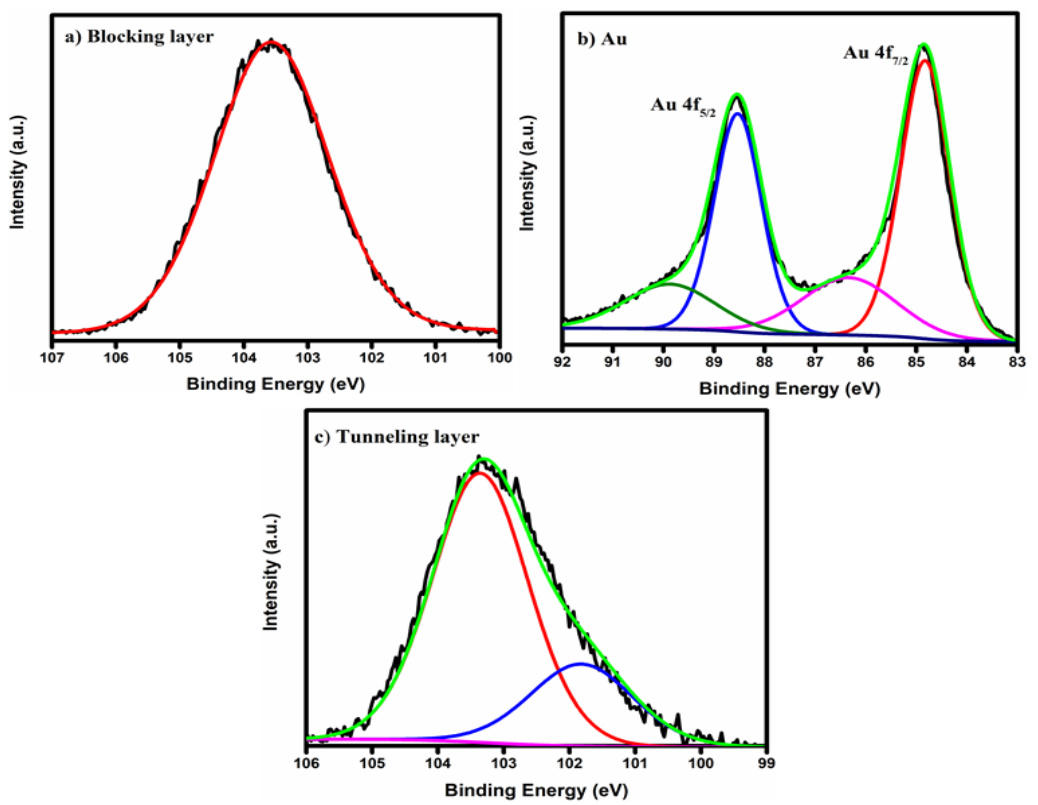


Figure 5.11 XPS spectra of blocking, trapping and tunneling layers annealed at 850°C.

## 5.4 Summary

In summary, this work demonstrates the effect of annealing temperature on SiO<sub>2</sub>/Au/SiO<sub>2</sub> trilayer structure. The nonvolatile memory device structure was fabricated using RF magnetron sputtering and electron beam evaporation on Si substrates. TEM images indicate Au nanocrystal formation with annealing. The total thickness of the trilayer structure is estimated with RBS. XPS spectra of annealed samples confirm the formation of Au nanocrystals. The I-V measurements show a decrease in leakage current with Au nanocrystal formation. The memory window of 2V shows the charge storage capability of Au nanocrystals. Thus, this work confirms the role of Au nanocrystals in charge storage behaviour at high temperature annealing and the effect of annealing temperature on structural and electrical properties of trilayer structure.



# **Chapter 6**

## **Fabrication and characterization of $\text{Al}_2\text{O}_3/\text{Au}/\text{Al}_2\text{O}_3$ for nonvolatile memory application**

## 6.1 Introduction

In recent years, metal NCs embedded in oxide layers have been widely studied for nonvolatile memory applications [45]. Nanocrystal based memory devices show better charge storage characteristics and allows scaling down of tunneling oxide as compared to conventional nonvolatile memory devices. Further improvement of memory performance can be obtained through the integration of metal NCs with high dielectric oxide materials. The use of high dielectric oxide as replacement of SiO<sub>2</sub> dielectric oxide material increases device performance [15]. In the previous chapters, systematic study on the effects of annealing on Au NCs in HfO<sub>2</sub> and SiO<sub>2</sub> based tunneling and blocking layers have been investigated. The aim of this study is to fabricate and characterize Al<sub>2</sub>O<sub>3</sub>/Au/Al<sub>2</sub>O<sub>3</sub> trilayer structure for nonvolatile memory application and to understand the effect of annealing temperature on various properties of the trilayer structure.

## 6.2 Experimental details

In the present study, the trilayer structure was fabricated onto a p-type Si substrate using RF magnetron sputtering and electron beam evaporation techniques. Prior to the deposition, the substrates were cleaned using standard RCA methods and immersed in HF solution for the removal of native oxides. A thin tunneling layer (10 nm) of Al<sub>2</sub>O<sub>3</sub> was deposited onto the Si substrates. During the deposition, the base and the working pressures were  $6 \times 10^{-6}$  and  $3 \times 10^{-3}$  mbar, respectively. High purity Ar and oxygen gases were introduced into the chamber. Flow rate of Ar and Oxygen were kept constant throughout the deposition at 7 and 14 sccm, respectively. The RF power and source-substrate distance were kept at 100W and 5cm. For trapping layer, Au layer of 3 nm was deposited using electron beam evaporation. Finally, Al<sub>2</sub>O<sub>3</sub> with a thickness of 20 nm was also deposited using RF magnetron sputtering for the fabrication of the trilayer structure. The schematic illustration of the trilayer structure with Al<sub>2</sub>O<sub>3</sub> acting as tunneling and blocking layers with Au NCs is shown in figure 6.1. To form Au NCs, the thermal annealing of the structure was carried out in N<sub>2</sub> environment at 650,750 and 850°C for an hour with a ramp rate of 10°C/min. The top electrodes of Al with diameter around 1 mm and thickness 250 nm were deposited using electron beam evaporation. For TEM analysis, Al<sub>2</sub>O<sub>3</sub> tunneling layer with thickness of 10 nm was deposited using RF magnetron sputtering on Ni TEM grid. Subsequently, a thin layer of

3 nm Au was deposited using electron beam evaporation on  $\text{Al}_2\text{O}_3$  layer and was annealed at  $850^\circ\text{C}$  for an hour in  $\text{N}_2$  environment. These samples were characterized using TEM to confirm the formation of NCs.

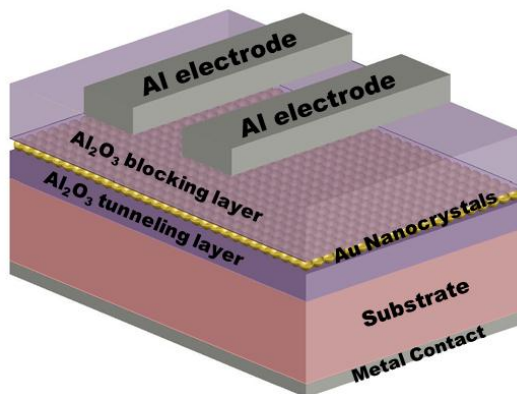


Figure 6.1 Schematic illustration of Au nanocrystals sandwiched between  $\text{Al}_2\text{O}_3$  tunneling and blocking layers

### 6.3 Results and discussion:

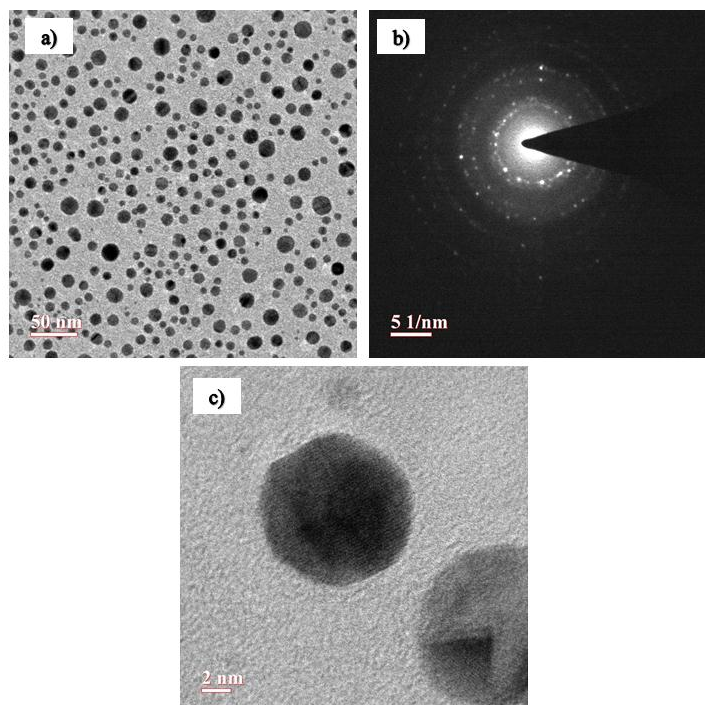


Figure 6.2 a) TEM images of Au in  $\text{Al}_2\text{O}_3$  b) SAED pattern of Au and c) HR image of Au nanocrystals

Figure 6.2a shows the TEM micrograph of Au NCs in Al<sub>2</sub>O<sub>3</sub>. The density of Au NCs is around  $2.68 \times 10^{11}/\text{cm}^2$ . The selected area electron diffraction (SAED) pattern of Au is presented in fig. 6.2b. The HR-TEM image in fig. 6.2c confirms the formation of Au NCs.

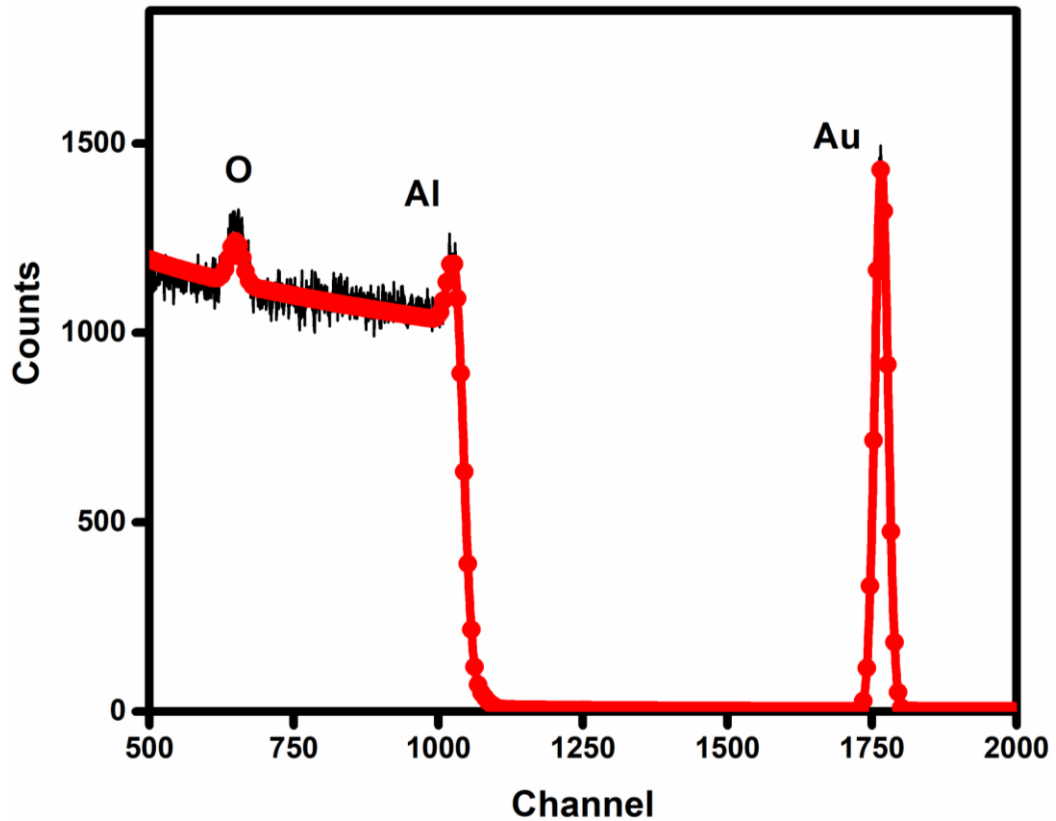


Figure 6.3 Rutherford backscattering spectrum of Al<sub>2</sub>O<sub>3</sub>/Au/Al<sub>2</sub>O<sub>3</sub> annealed at 850°C

Figure 6.3 shows the RBS spectrum of trilayer structure annealed at 850°C. The thickness of the trilayer structure estimated by RBS spectra is around 37 nm. The peaks of various elements corresponding to O, Al and Au are detected in the RBS measurement.

The X-ray diffraction pattern of the as-deposited and annealed structures is shown in figure 6.4. The amorphous nature of as-deposited and annealed Al<sub>2</sub>O<sub>3</sub> films is reported [187–190] and is evident from diffraction pattern.



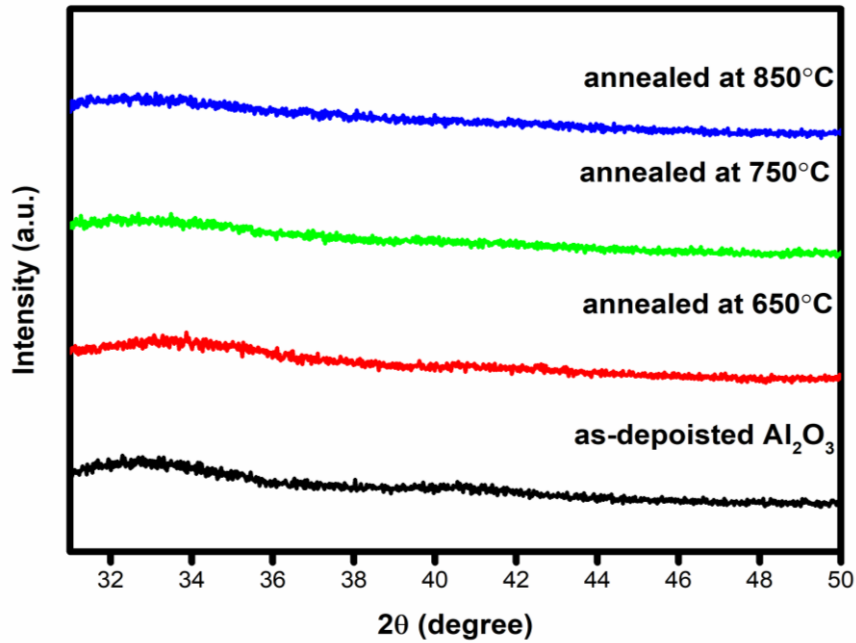


Figure 6.4 XRD pattern of as-deposited and annealed NVM structure

To understand the leakage characteristics of trilayer structure current-voltage measurements were carried out and it is presented in the figure 6.5. The forward and reverse characteristics of the structure before and after annealing were carried out in the range from -6 to +6V and the measurement was performed at room temperature. The leakage current values for as-deposited and annealed samples at 0.5 V are compared. The graphs show a variation in leakage current with annealing. As compared to the as-deposited samples the annealed ones show decrease in leakage current. The formation of Au NCs at high temperature could have resulted in the decrease in the leakage current. This reduction might have resulted either from the carriers injected into the NCs or by the blocking of external electric field by the internal electric field of the charge stored in the Au NCs. Similar behaviour of reduction in leakage current with annealing for nonvolatile structures due to Au NCs formation for nonvolatile structures with HfO<sub>2</sub> and SiO<sub>2</sub> tunneling and blocking layers were also reported [191,192]. The current minima values of the pristine and annealed structures show a variation from 0 V that can be attributed to the charge storage [192]. The formation of NCs plays a crucial role in nonvolatile memory behaviour and the different current minima values obtained in the present study is attributed to the formation of NCs with annealing.

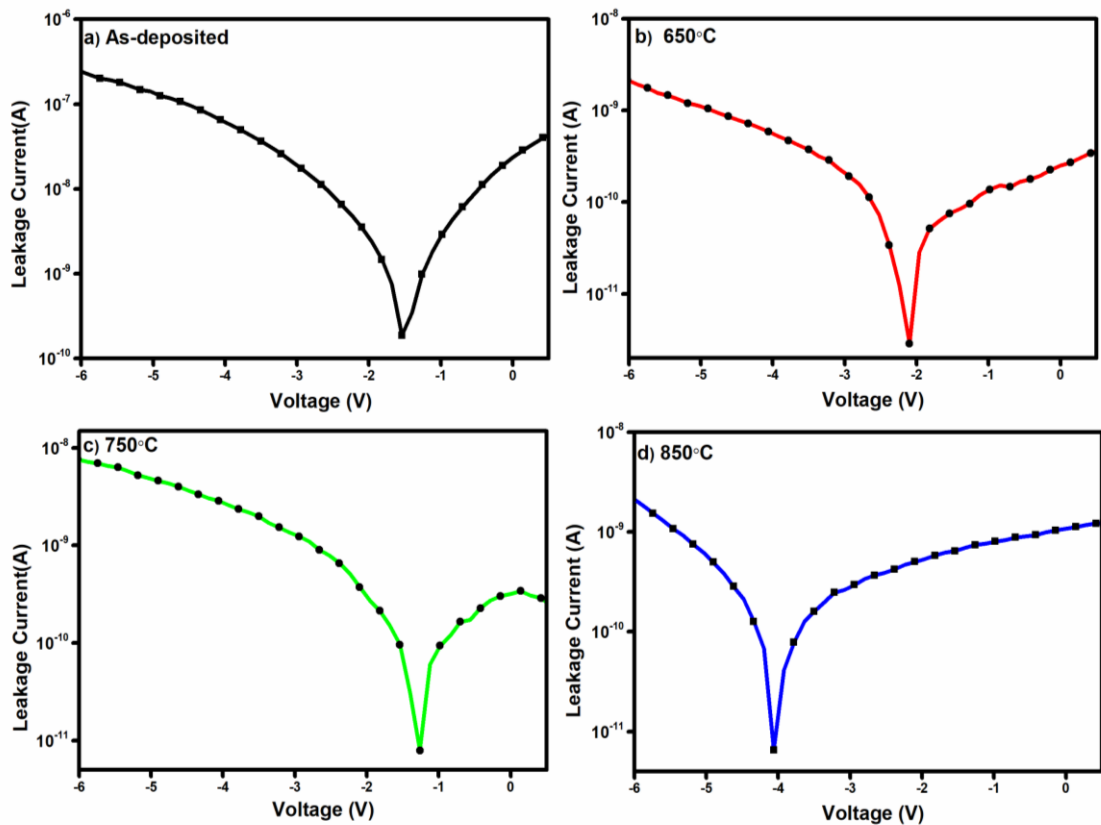


Figure 6.5 Leakage current–voltage characteristics of  $\text{Al}_2\text{O}_3/\text{Au}/\text{Al}_2\text{O}_3$  structure before and after annealing

The charge storage characteristics of  $\text{Al}_2\text{O}_3/\text{Au}/\text{Al}_2\text{O}_3$  structure annealed at  $850^\circ\text{C}$  analysed by high frequency  $C-V$  measurement at room temperature are presented in figure 6.6. The gate voltage was swept over  $\pm 7$  V. The obtained  $C-V$  curve indicates the injection of the charges from the NCs to the substrates and vice versa. It is observed that the centre of the hysteresis curve comes around  $-1$  V rather than  $0$  V, which is a deviation from the ideal conditions. This could be due to the difference in work function between the metal electrode and the silicon and the immobile charges existing in the oxide layers. The obtained hysteresis curve with accumulation and inversion regions shows the charge storage behaviour of Au NCs and could be explained with respect to the voltage applied [191,192]. Electrons from the substrates are ejected into the Au NCs during positive voltage and holes will be injected into the NCs with negative voltage. This injection of electrons or hole leads to a voltage shift (memory window). Here, in the present experiment, the memory window obtained is around  $3.9$  V. In comparison with the other two trilayer structures (i.e.,  $\text{HfO}_2/\text{Au}/\text{HfO}_2$  and  $\text{SiO}_2/\text{Au}/\text{SiO}_2$ ), this trilayer structure shows better memory window. The hysteresis loop

confirms the significant role of Au NCs in the charge storage behaviour of the trilayer structure.

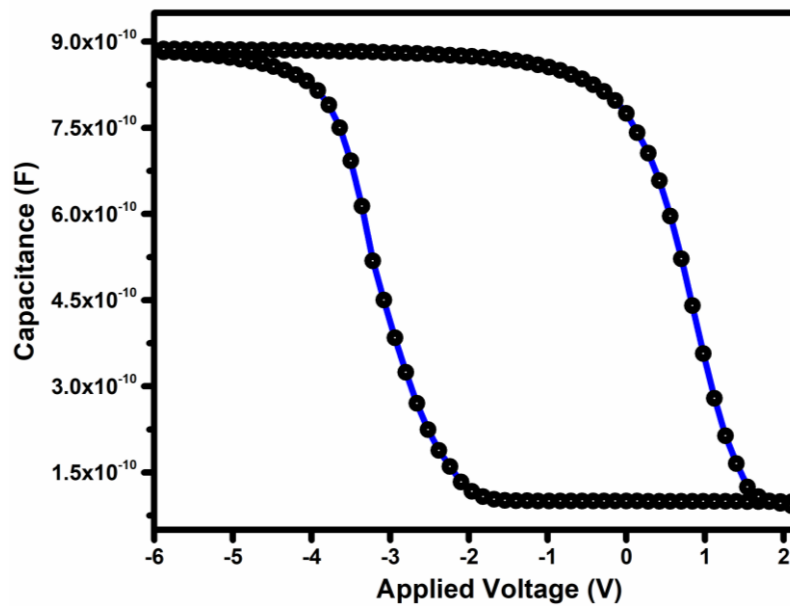


Figure 6.6 C–V hysteresis of NVM structure with Au nanocrystals annealed at 850°C

To understand the elemental composition and electronic state of various layers of the nonvolatile memory structure, XPS was used and the spectra of NVM structures before and after annealing are presented in figures 6.7-6.9. The peaks of all layers are calibrated from C 1s peak at 284.8 eV.

The XPS spectra of the as-deposited nonvolatile memory structure is shown in figure 6.7. The as-deposited blocking layer shows strong Al peak characteristic of Al<sub>2</sub>O<sub>3</sub>. The figure indicates that a single peak is used to fit the Al 2p peak suggesting Al is present in the film as Al<sub>2</sub>O<sub>3</sub> without any suboxides. The formation of Al<sub>2</sub>O<sub>3</sub> was confirmed by Al 2p peak around 74 eV and it is in good agreement with previous reported values [189,193]. In figure 6.7b, the results of Au suggest that Au 4f peaks are at 84 and 87.7 eV with difference in binding energy 3.7 eV. The shoulder peak appeared at higher binding energy is related to the oxidation of Au [166].

On the other hand, the XPS spectra of annealed trilayer structure at 750°C are shown in figure 6.8. The small shift of Al 2p peak towards higher binding energy with annealing is observed. The formation of Al rich Al<sub>2</sub>O<sub>3</sub> could be ruled out as there are no peaks around 72.7 eV and only a single fit is used to fit Al 2p peak. It is also mentioned in literature about the formation of Al<sub>2</sub>O<sub>3</sub> at higher binding energy around 75 eV [194]. Au spectra of the

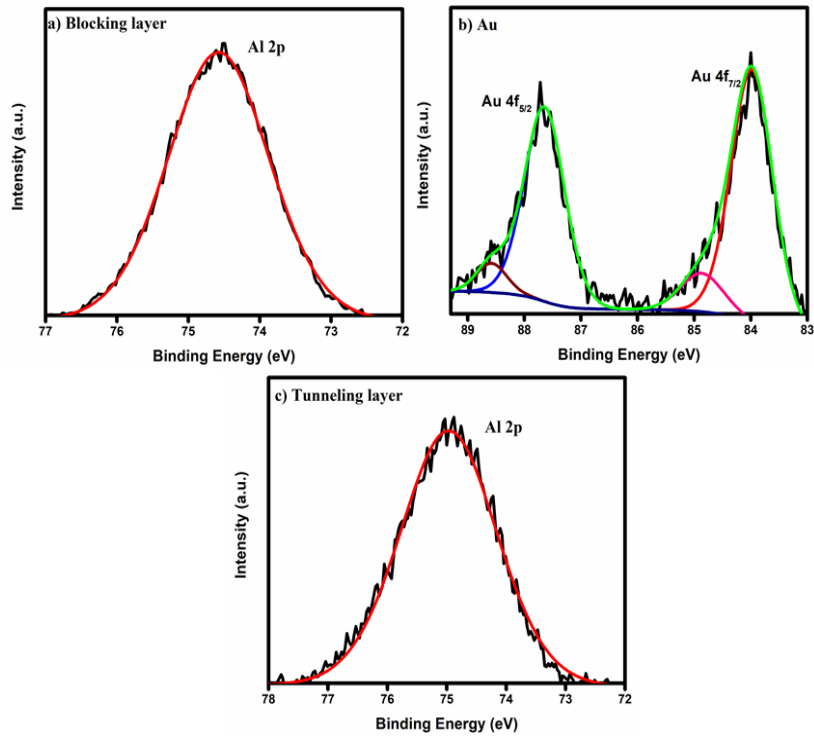


Figure 6.7 XPS spectra of blocking, trapping and tunneling layers of as-deposited  $\text{Al}_2\text{O}_3/\text{Au}/\text{Al}_2\text{O}_3$  trilayer structure

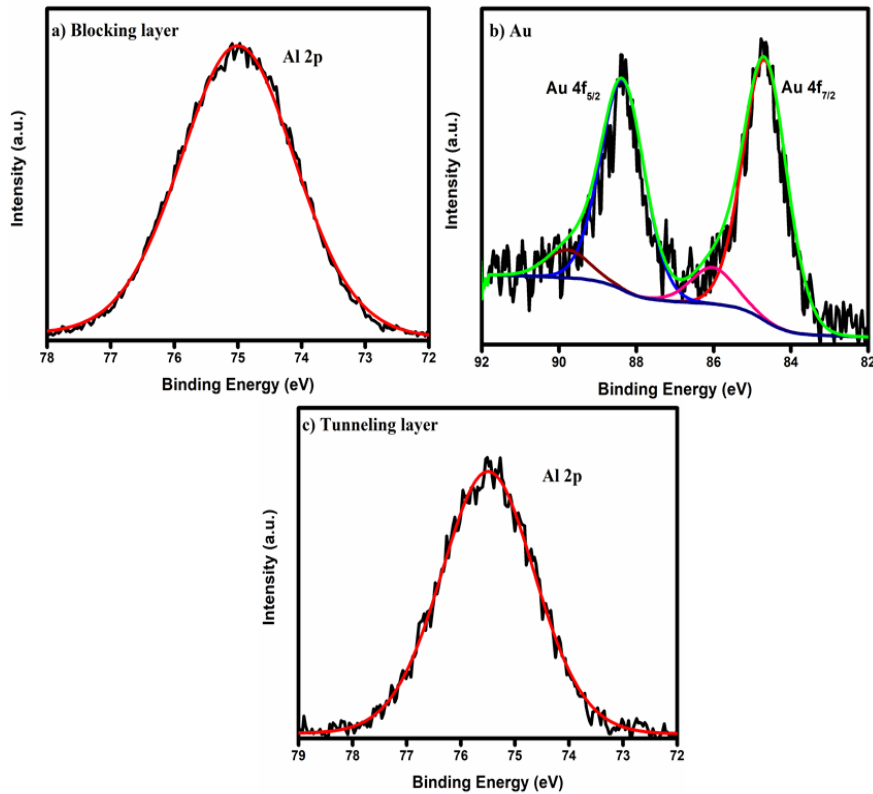


Figure 6.8 XPS spectra of blocking, trapping and tunneling layers of  $\text{Al}_2\text{O}_3/\text{Au}/\text{Al}_2\text{O}_3$  trilayer structure annealed at 750°C

samples annealed at 750°C show slight shift towards higher binding energy around 84.3 eV confirms the formation of Au nanocrystals [167,191,192]. Almost similar behaviour in blocking, trapping and tunneling layer is observed for samples annealed at 850°C (shown in figure 6.9) with a minor shift in binding energy.

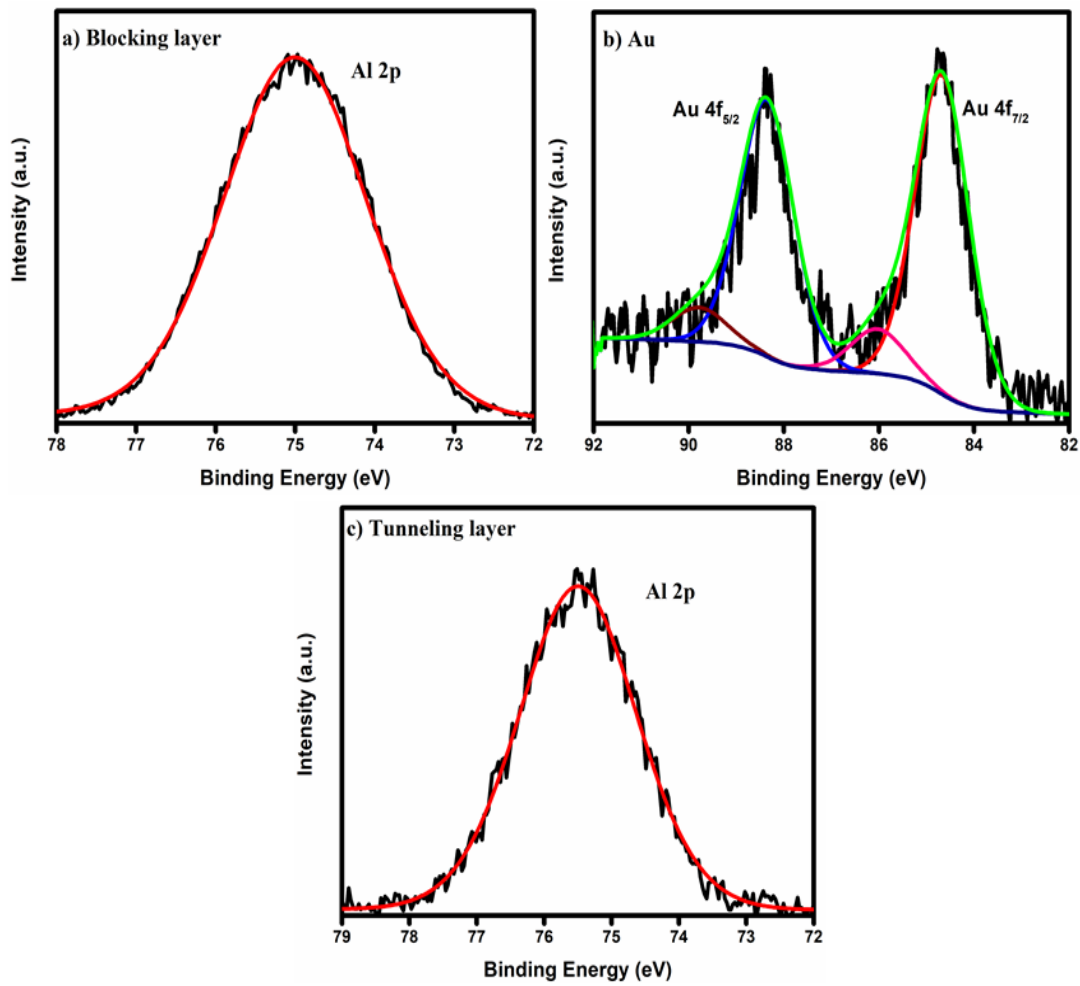


Figure 6.9 XPS spectra of blocking, trapping and tunneling layers of Al<sub>2</sub>O<sub>3</sub>/Au/Al<sub>2</sub>O<sub>3</sub> trilayer structure annealed at 850°C

## 6.4 Summary

Nonvolatile memory structure with Au nanocrystals embedded in  $\text{Al}_2\text{O}_3$  tunneling and blocking layers has been fabricated on silicon substrate. The effects of annealing on electrical and compositional properties of  $\text{Al}_2\text{O}_3/\text{Au}/\text{Al}_2\text{O}_3$  trilayer structure were investigated. TEM images show the formation of Au nanocrystals. The thickness of the trilayer structure is estimated using RBS. I-V curve shows a variation in leakage characteristics with annealing. C-V confirms the significant role played by Au nanocrystals in charge storage behaviour. XPS results of tunneling and blocking oxide layers show  $\text{Al}_2\text{O}_3$  formation and it also confirms the formation of Au nanocrystals with annealing.

# **Chapter 7**

## **Conclusions and Future work plan**





## 7.1 Conclusions of thesis work

The present thesis investigates the effects of annealing temperature on Au NCs in various dielectric oxides for nonvolatile memory applications. The overall conclusions of the present study are summarized as follows:

The trilayer structures such as  $\text{HfO}_2/\text{Au}/\text{HfO}_2$ ,  $\text{SiO}_2/\text{Au}/\text{SiO}_2$  and  $\text{Al}_2\text{O}_3/\text{Au}/\text{Al}_2\text{O}_3$  were fabricated using RF magnetron sputtering and electron beam evaporation on Si substrates and were annealed at various temperatures. TEM images indicate Au nanocrystal formation with annealing. The total thickness of the trilayer structures is estimated using RBS. XPS spectra of annealed trilayer structures confirm the formation of Au NCs. The I-V measurements show a decrease in leakage current with Au nanocrystal formation. The memory window shows the charge storage capability of Au NCs. Thus, this work confirms the role of Au NCs in charge storage behaviour at high temperature annealing.

The advantages and limitations of Au NCs with various blocking and tunneling layers for nonvolatile memory application have been investigated and reported in detail. Among various Au NCs based nonvolatile memory structures,  $\text{Al}_2\text{O}_3/\text{Au}/\text{Al}_2\text{O}_3$  trilayer structure shows promising memory effects. The reasons for the increase in memory window in  $\text{Al}_2\text{O}_3/\text{Au}/\text{Al}_2\text{O}_3$  trilayer structures are due to amorphous nature of  $\text{Al}_2\text{O}_3$  (as crystalline nature leads to leakage path formation as in  $\text{HfO}_2$ ), the absence of interfacial layer formation, high dielectric constant (as compared to  $\text{SiO}_2$ ) and the density of Au NCs.

## 7.2 Scope of future work

There are many possibilities and queries arising from the present work, therefore, we would like to extend the work by considering the following points in future:

- Systematic investigation of electrical characteristics of these structures is required.
- Detailed study is needed to correlate the shift in binding energy of XPS spectra with nanocrystal size
- It is proposed to understand various charging/discharging mechanisms across various layers of the trilayer structures and it is required to understand the effects of oxide layers on the growth of Au NCs with annealing temperature.
- It is also very important to study the charge storage characteristics of Au NCs with different combinations of tunneling and blocking oxides.



## References

- [1] R. Karpagam, S. Gopalakrishnan, M. Natarajan, B. Ramesh Babu, *Scientometrics* 89 (2011) 501–522.
- [2] *Nanoscience and Nanotechnologies: Opportunities and Uncertainties*, Royal Society, 2004.
- [3] Guozhong Cao, *Nanostructures and Nanomaterials: Synthesis, Properties, and Applications*, Imperial College Press, London, 2004.
- [4] S.S. Su, I. Chang, in: *Commer. Nanotechnologies—A Case Study Approach*, Springer International Publishing, Cham, 2018, pp. 15–29.
- [5] C. Buzea, I.I. Pacheco, K. Robbie, *Biointerphases* 2 (2007) MR17-MR71.
- [6] J.N. Tiwari, R.N. Tiwari, K.S. Kim, *Prog. Mater. Sci.* 57 (2012) 724–803.
- [7] V.V. Pokropivny, V.V. Skorokhod, *Mater. Sci. Eng. C* 27 (2007) 990–993.
- [8] H. Gleiter, *Acta Mater.* 48 (2000) 1–29.
- [9] M.S. Rathore, A. Vinod, R. Angalakurthi, A.P. Pathak, F. Singh, S.K. Thatikonda, S.R. Nelamarri, *Appl. Phys. A* 123 (2017) 708.
- [10] A. Vinod, M.S. Rathore, T. Santhosh Kumar, D. Pamu, A.P. Pathak, N. Srinivasa Rao, *Radiat. Eff. Defects Solids* 172 (2017) 81–89.
- [11] M.S. Shekhawat, M.C. Rao, *Int. J. Mod. Phys. Conf. Ser.* 22 (2013) 576–582.
- [12] J. Meena, S. Sze, U. Chand, T.-Y. Tseng, *Nanoscale Res. Lett.* 9 (2014) 526.
- [13] M. Bohr, R. Chau, T. Ghani, K. Mistry, *IEEE Spectr.* 44 (2007) 29–35.
- [14] Peter M., Zeitzoff, Howard R. Huff, Robert W. Murto, Mark I. Gardner, George A. Brown, *Solid State Technol.* 46 (2003) 43.
- [15] J. Robertson, *Reports Prog. Phys.* 69 (2006) 327–396.
- [16] J. Robertson, *Eur. Phys. J. Appl. Phys.* 28 (2004) 265–291.
- [17] C. Zhao, C.Z. Zhao, S. Taylor, P. Chalker, *Materials (Basel)*. 7 (2014) 5117–5145.
- [18] C.H. Lee, S.H. Hur, Y.C. Shin, J.H. Choi, D.G. Park, K. Kim, *Appl. Phys. Lett.* 86 (2005) 152908.
- [19] J. De Blauwe, *IEEE Trans. Nanotechnol.* 1 (2002) 72–77.
- [20] R. Bez, E. Camerlenghi, A. Modelli, A. Visconti, *Proc. IEEE* 91 (2003) 489–502.
- [21] S. Tiwari, F. Rana, H. Hanafi, A. Hartstein, E.F. Crabbé, K. Chan, *Appl. Phys. Lett.* 68 (1996) 1377–1379.
- [22] Z. Liu, C. Lee, V. Narayanan, G. Pei, E.C. Kan, *IEEE Trans. Electron Devices* 49

- (2002) 1614–1622.
- [23] C.C. Wang, Y.K. Chiou, C.H. Chang, J.Y. Tseng, L.J. Wu, C.Y. Chen, T.B. Wu, *J. Phys. D. Appl. Phys.* 40 (2007) 1673–1677.
- [24] V. Mikhelashvili, B. Meyler, S. Yoffis, J. Salzman, M. Garbrecht, T. Cohen-Hyams, W.D. Kaplan, G. Eisenstein, *Appl. Phys. Lett.* 95 (2009) 023104.
- [25] J.S. Lee, *Electron. Mater. Lett.* 7 (2011) 175–183.
- [26] J. Robertson, R.M. Wallace, *Mater. Sci. Eng. R Reports* 88 (2015) 1–41.
- [27] R. Tang, K. Huang, H. Lai, C. Li, Z. Wu, J. Kang, *Nanoscale Res. Lett.* 8 (2013) 368.
- [28] Ya Chin King, Tsu Jae King, Chenming Hu, *IEEE Trans. Electron Devices* 48 (2001) 696–700.
- [29] P.H. Yeh, L.J. Chen, P.T. Liu, D.Y. Wang, T.C. Chang, *Electrochim. Acta* 52 (2007) 2920–2926.
- [30] Jong Jin Lee, Xuguang Wang, Weiping Bai, Nan Lu, Dim Lee Kwong, *IEEE Trans. Electron Devices* 50 (2003) 2067–2072.
- [31] T.Z. Lu, M. Alexe, R. Scholz, V. Talalaev, R.J. Zhang, M. Zacharias, *J. Appl. Phys.* 100 (2006) 014310.
- [32] P. Normand, E. Kapetanakis, P. Dimitrakis, D. Tsoukalas, K. Beltsios, N. Cherkashin, C. Bonafos, G. Benassayag, H. Coffin, A. Claverie, V. Soncini, A. Agarwal, M. Ameen, *Appl. Phys. Lett.* 83 (2003) 168–170.
- [33] C.Y. Ng, T.P. Chen, D. Sreeduth, Q. Chen, L. Ding, A. Du, *Thin Solid Films* 504 (2006) 25–27.
- [34] S. Choi, H. Yang, M. Chang, S. Baek, H. Hwang, S. Jeon, J. Kim, C. Kim, *Appl. Phys. Lett.* 86 (2005) 251901.
- [35] B. Garrido, S. Cheylan, O. González Varona, A. Pérez Rodríguez, J.R. Morante, *Appl. Phys. Lett.* 82 (2003) 4818–4820.
- [36] M. Kanoun, A. Souifi, T. Baron, F. Mazen, *Appl. Phys. Lett.* 84 (2004) 5079–5081.
- [37] P.F. Lee, X.B. Lu, J.Y. Dai, H.L.W. Chan, E. Jelenkovic, K.Y. Tong, *Nanotechnology* 17 (2006) 1202–1206.
- [38] Y.Q. Wang, J.H. Chen, W.J. Yoo, Y. C. Yeo, S. J. Kim, R. Gupta, Z.Y.L. Tan, D. L. Kwong, A.Y. Du, N. Balasubramanian, *Appl. Phys. Lett.* 84 (2004) 5407–5409.
- [39] C.H. Tu, T.C. Chang, P.T. Liu, H.C. Liu, S.M. Sze, C.Y. Chang, *Appl. Phys. Lett.* 89 (2006) 162105.
- [40] M. Kanoun, C. Busseret, A. Poncet, A. Souifi, T. Baron, E. Gautier, *Solid. State. Electron.* 50 (2006) 1310–1314.

- [41] J.C. Wang, C.H. Liao, C.T. Lin, R.D. Chang, L.C. Chang, C.I. Wu, J.H. Chang, *Curr. Appl. Phys.* 15 (2015) 535–540.
- [42] C. Sargentis, K. Giannakopoulos, A. Travlos, P. Normand, D. Tsamakis, *Superlattices Microstruct.* 44 (2008) 483–488.
- [43] K.C. Chan, P.F. Lee, J.Y. Dai, *Appl. Phys. Lett.* 92 (2008) 223105.
- [44] D.U. Lee, M.S. Lee, J.-H. Kim, E.K. Kim, H.-M. Koo, W.-J. Cho, W.M. Kim, *Appl. Phys. Lett.* 90 (2007) 093514.
- [45] R. Tang, K. Huang, H. Lai, C. Li, Z. Wu, J. Kang, *Nanoscale Res. Lett.* 8 (2013) 368.
- [46] W. Guan, S. Long, M. Liu, Z. Li, Y. Hu, Q. Liu, *J. Phys. D: Appl. Phys.* 40 (2007) 2754–2758.
- [47] C.C. Wang, J.Y. Tseng, T.B. Wu, L.J. Wu, C.S. Liang, J.M. Wu, *J. Appl. Phys.* 99 (2006) 026102.
- [48] X. Feng, S. Dong, H. Wong, D. Yu, K.L. Pey, K. Shubhakar, W.S. Lau, *Microelectron. Reliab.* 61 (2016) 78–81.
- [49] L. Kastanis, J.L. Spear, C. Sargentis, N. Konofaos, D. Tsamakis, D.C. Koutsogeorgis, E.K. Evangelou, *Solid. State. Electron.* 148 (2018) 63–69.
- [50] M. Vishwas, K. Narasimha Rao, A.R. Phani, K.V. Arjuna Gowda, R.P.S. Chakradhar, *Spectrochim. Acta Part A Mol. Biomol. Spectrosc.* 78 (2011) 695–699.
- [51] G. Pacchioni, L. Skuja, D.L. Griscom, *Defects in SiO<sub>2</sub> and Related Dielectrics: Science and Technology*, Springer Netherlands, Dordrecht, 2000.
- [52] W.F. Wu, B.S. Chiou, *Appl. Surf. Sci.* 115 (1997) 96–102.
- [53] K.A. Vorotilov, E.V. Orlova, V.I. Petrovsky, *Thin Solid Films* 209 (1992) 188–194.
- [54] A. Barranco, F. Yubero, J.P. Espinós, P. Groening, A.R. González-Elipe, *J. Appl. Phys.* 97 (2005) 113714.
- [55] P.S. Santos, H.S. Santos, S.P. Toledo, *Mater. Res.* 3 (2000) 104–114.
- [56] J. Robertson, *J. Vac. Sci. Technol. B Microelectron. Nanom. Struct. Process. Meas. Phenom.* 18 (2000) 1785.
- [57] W.E. Fu, B.C. He, Y.Q. Chang, *Thin Solid Films* 544 (2013) 212–217.
- [58] P.M. Tirmali, A.G. Khairnar, B.N. Joshi, A.M. Mahajan, *Solid. State. Electron.* 62 (2011) 44–47.
- [59] S.W. Nam, J.H. Yoo, S. Nam, H.J. Choi, D. Lee, D.H. Ko, J.H. Moon, J.H. Ku, S. Choi, *J. Non. Cryst. Solids* 303 (2002) 139–143.
- [60] R. Terki, G. Bertrand, H. Aourag, C. Coddet, *Mater. Lett.* 62 (2008) 1484–1486.
- [61] M. Balog, M. Schieber, M. Michman, S. Patai, *Thin Solid Films* 41 (1977) 247–259.

- [62] S.S. Lin, C.S. Liao, *Ceram. Int.* 39 (2013) 353–358.
- [63] B. Hammer, J.K. Norskov, *Nature* 376 (1995) 238–240.
- [64] M. Das, K.H. Shim, S.S.A. An, D.K. Yi, *Toxicol. Environ. Health Sci.* 3 (2011) 193–205.
- [65] I. Venditti, *Materials (Basel)*. 10 (2017) 97.
- [66] P. Sigmund, *Phys. Rev.* 184 (1969) 383–416.
- [67] S. Swann, *Phys. Technol.* 19 (1988) 67–75.
- [68] M. M. Abdelrahman, *J. Phys. Sci. Appl.* 5 (2015).
- [69] Q. Wei, *Surface Modification of Textiles*, CRC Press, 2009.
- [70] S.H. Kiyotaka Wasa, *Handbook of Sputter Deposition Technology*, Noyes Publications, New Jersey, 1992.
- [71] R. Bosco, J. Van Den Beucken, S. Leeuwenburgh, J. Jansen, *Coatings* 2 (2012) 95–119.
- [72] Y. Lin, C. Xin, *Advanced Nano Deposition Methods*, First Edition, Chemical Industry Press, 2016.
- [73] K. Vijayalakshmi, D. Sivaraj, *Analyst* 141 (2016) 6149–6159.
- [74] Y. V. Deshmukh, *Industrial Heating : Principles, Techniques, Materials, Applications, and Design*, First Edition, Taylor & Francis, Boca Raton, 2005.
- [75] R.S. Das, Y.K. Agrawal, *Vib. Spectrosc.* 57 (2011) 163–176.
- [76] C.V. Raman, K. S. Krishnan, *Nature* 121 (1928) 501–502.
- [77] C.R. Brundle, C.A. Evans, S. Wilson, *Encyclopedia of Materials Characterization : Surfaces, Interfaces, Thin Films*, Butterworth-Heinemann, 1992.
- [78] D.J. O'Connor, B. Sexton, R.C. Smart, *Surface Analysis Methods in Materials Science*, 1st editio, Springer-Verlag Berlin Heidelberg, New York, 1992.
- [79] W.R. Bowen, N. Hilal, *Atomic Force Microscopy in Process Engineering : Introduction to AFM for Improved Processes and Products*, First Edition, Butterworth-Heinemann, 2009.
- [80] G. Binnig, C.F. Quate, C. Gerber, *Phys. Rev. Lett.* 56 (1986) 930–933.
- [81] A. Méndez Vilas, J. Díaz, *Modern Research and Educational Topics in Microscopy*, First Edition, Formatex, 2007.
- [82] D. Guo, G. Xie, J. Luo, *J. Phys. D. Appl. Phys.* 47 (2014) 013001.
- [83] P. Van der Heide, *X-Ray Photoelectron Spectroscopy : An Introduction to Principles and Practices*, First Edition, John Wiley & Sons, Inc., New Jersey, 2012.
- [84] K. Siegbahn, *J. Electron Spectros. Relat. Phenomena* 5 (1974) 3–97.

- [85] E. Korin, N. Froumin, S. Cohen, *ACS Biomater. Sci. Eng.* 3 (2017) 882–889.
- [86] Malgorzata Kot, In-Operando Hard X-Ray Photoelectron Spectroscopy Study on the Resistive Switching Physics of HfO<sub>2</sub> Based RRAM, Brandenburg University of Technology Cottbus, Senftenberg.
- [87] H.D. Deas, *Centaurus* 6 (1959) 129–148.
- [88] B. D. Cullity, *Elements of X-Ray Diffraction*, Second Edition, Addison-Wesley Publ. Company, Massachusetts, 1978.
- [89] G. Friedbacher, H. (Henning) Bubert, *Surface and Thin Film Analysis: A Compendium of Principles, Instrumentation, and Applications*, Wiley-VCH, 2011.
- [90] J. Perrière, *Vacuum* 37 (1987) 429–432.
- [91] K. Saravanan, R. Krishnan, S.H. Hsieh, H.T. Wang, Y.F. Wang, W.F. Pong, K. Asokan, D.K. Avasthi, D. Kanjilal, *RSC Adv.* 5 (2015) 40813–40819.
- [92] D. Sekiba, in: *Compend. Surf. Interface Anal.*, Springer Singapore, Singapore, 2018, pp. 539–543.
- [93] L.R. Doolittle, *Nucl. Instruments Methods Phys. Res. Sect. B Beam Interact. with Mater. Atoms* 9 (1985) 344–351.
- [94] H. Iwai, S. Ohmi, *Microelectron. Reliab.* 42 (2002) 465–491.
- [95] H. Wong, V.A. Gritsenko, *Microelectron. Reliab.* 42 (2002) 597–605.
- [96] M. Vargas, N.R. Murphy, C.V. Ramana, *Opt. Mater. (Amst.)* 37 (2014) 621–628.
- [97] S. Rudenja, A. Minko, D.A. Buchanan, *Appl. Surf. Sci.* 257 (2010) 17–21.
- [98] Y. Wang, Z. Lin, X. Cheng, H. Xiao, F. Zhang, S. Zou, *Appl. Surf. Sci.* 228 (2004) 93–99.
- [99] V. Dave, P. Dubey, H.O. Gupta, R. Chandra, *Thin Solid Films* 549 (2013) 2–7.
- [100] G. He, L. Zhu, Z. Sun, Q. Wan, L. Zhang, *Prog. Mater. Sci.* 56 (2011) 475–572.
- [101] G. He, Z. Sun, G. Li, L. Zhang, *Crit. Rev. Solid State Mater. Sci.* 37 (2012) 131–157.
- [102] F. Zhang, G. Liu, A. Liu, B. Shin, F. Shan, *Ceram. Int.* 41 (2015) 13218–13223.
- [103] J.W. Zhang, G. He, H.S. Chen, J. Gao, X.F. Chen, P. Jin, D.Q. Xiao, R. Ma, M. Liu, Z.Q. Sun, *J. Alloys Compd.* 647 (2015) 1054–1060.
- [104] W.-E. Fu, Y.-Q. Chang, *Appl. Surf. Sci.* 257 (2011) 7436–7442.
- [105] A.G. Khairnar, A.M. Mahajan, *Solid State Sci.* 15 (2013) 24–28.
- [106] Q. Du, W. Wang, S. Li, D. Zhang, W. Zheng, *Thin Solid Films* 608 (2016) 21–25.
- [107] C.T. Tsai, T.C. Chang, P.T. Liu, P.Y. Yang, Y.C. Kuo, K.T. Kin, P.L. Chang, F.S. Huang, *Appl. Phys. Lett.* 91 (2007) 012109.
- [108] P. Kondaiah, H. Shaik, G. Mohan Rao, *Electron. Mater. Lett.* 11 (2015) 592–600.

- [109] T.H. Moon, M.H. Ham, J.M. Myoung, *Appl. Phys. Lett.* 86 (2005) 102903.
- [110] J. Gope, Vandana, N. Batra, J. Panigrahi, R. Singh, K.K. Maurya, R. Srivastava, P.K. Singh, *Appl. Surf. Sci.* 357 (2015) 635–642.
- [111] K.C. Das, S.P. Ghosh, N. Tripathy, D.H. Kim, T.I. Lee, J.M. Myoung, J.P. Kar, *Ceram. Int.* 42 (2016) 138–145.
- [112] G. He, M. Liu, L.Q. Zhu, M. Chang, Q. Fang, L.D. Zhang, *Surf. Sci.* 576 (2005) 67–75.
- [113] W. Kern, *J. Electrochem. Soc.* 137 (1990) 1887.
- [114] A. Diaz Cano, S. Jiménez Sandoval, Y. Vorobiev, F. Rodriguez Melgarejo, T. V Torchynska, *Nanotechnology* 21 (2010) 134016.
- [115] A. Zwick, R. Carles, *Phys. Rev. B* 48 (1993) 6024–6032.
- [116] T. Tan, Z. Liu, H. Lu, W. Liu, H. Tian, *Opt. Mater. (Amst)*. 32 (2010) 432–435.
- [117] B. Zhou, H. Shi, X.D. Zhang, Q. Su, Z.Y. Jiang, *J. Phys. D: Appl. Phys.* 47 (2014) 115502.
- [118] A. Jayaraman, S.Y. Wang, S.K. Sharma, L.C. Ming, *Phys. Rev. B* 48 (1993) 9205–9211.
- [119] M.A. Krebs, R.A. Condrate, *J. Am. Ceram. Soc.* 65 (1982) c144–c145.
- [120] A. Ramadoss, K. Krishnamoorthy, S.J. Kim, *Mater. Res. Bull.* 47 (2012) 2680–2684.
- [121] C.T. Kuo, R. Kwor, K.M. Jones, *Thin Solid Films* 213 (1992) 257–264.
- [122] J. Liu, X. Jiang, X. Huang, S. Wu, *Fuel* 89 (2010) 3884–3891.
- [123] B. Bhushan, *Introduction to Tribology*, Second Edition, Wiley, New York, 2013.
- [124] L. Raghavan, P.A. Joy, B.V. Vijaykumar, R.V. Ramanujan, M.R. Anantharaman, *Nucl. Instruments Methods Phys. Res. Sect. B Beam Interact. with Mater. Atoms* 396 (2017) 68–74.
- [125] K. Joy, L.V. Maneeshya, J.K. Thomas, P.V. Thomas, *Thin Solid Films* 520 (2012) 2683–2688.
- [126] K. Holmberg, A. Mathews, *Thin Solid Films* 253 (1994) 173–178.
- [127] M. Sedlaček, B. Podgornik, J. Vižintin, *Tribol. Int.* 48 (2012) 102–112.
- [128] N. Tayebi, A.A. Polycarpou, *Tribol. Int.* 37 (2004) 491–505.
- [129] N. Zhan, M.C. Poon, C.W. Kok, K.L. Ng, H. Wong, *J. Electrochem. Soc.* 150 (2003) F200–F202.
- [130] M.S. Kim, Y.D. Ko, M. Yun, J.H. Hong, M.C. Jeong, J.M. Myoung, I. Yun, *Mater. Sci. Eng. B* 123 (2005) 20–30.
- [131] B. Chen, R. Jha, V. Misra, *IEEE Electron Device Lett.* 27 (2006) 731–733.



- [132] C. Morant, L. Galán, J.M. Sanz, *Surf. Interface Anal.* 16 (1990) 304–308.
- [133] M. Copel, R.P. Pezzi, D. Neumayer, P. Jamison, *Appl. Phys. Lett.* 88 (2006) 2004–2007.
- [134] P.S. Bagus, F. Illas, G. Pacchioni, F. Parmigiani, *J. Electron Spectros. Relat. Phenomena* 100 (1999) 215–236.
- [135] P. Jin, G. He, D. Xiao, J. Gao, M. Liu, J. Lv, Y. Liu, M. Zhang, P. Wang, Z. Sun, *Ceram. Int.* 42 (2016) 6761–6769.
- [136] S.W. Jeong, H.J. Lee, K.S. Kim, M.T. You, Y. Roh, T. Noguchi, W. Xianyu, J. Jung, *Thin Solid Films* 515 (2006) 526–530.
- [137] R. Ma, M. Liu, G. He, M. Fang, G. Shang, J. Zhang, X. Chen, J. Gao, G. Fei, L. Zhang, *J. Alloys Compd.* 646 (2015) 310–314.
- [138] Z. Xu, M. Houssa, S. De Gendt, M. Heyns, *Appl. Phys. Lett.* 80 (2002) 1975–1977.
- [139] T. Yu, C.G. Jin, Y.J. Dong, D. Cao, L.J. Zhuge, X.M. Wu, *Mater. Sci. Semicond. Process.* 16 (2013) 1321–1327.
- [140] H. Ikeda, T. Goto, M. Sakashita, A. Sakai, S. Zaima, Y. Yasuda, *Jpn. J. Appl. Phys.* 42 (2003) 1949–1953.
- [141] C.-H. Lin, Y. Kuo, *J. Electrochem. Soc.* 158 (2011) G162.
- [142] H. Ikeda, S. Goto, K. Honda, M. Sakashita, A. Sakai, S. Zaima, Y. Yasuda, *Jpn. J. Appl. Phys.* 41 (2002) 2476–2479.
- [143] X. Feng, S. Dong, H. Wong, D. Yu, K.L. Pey, K. Shubhakar, W.S. Lau, *Microelectron. Reliab.* 61 (2016) 78–81.
- [144] H. Wong, H. Iwai, *Microelectron. Eng.* 138 (2015) 57–76.
- [145] M. Nath, A. Roy, *Phys. B Condens. Matter* 482 (2016) 43–50.
- [146] Q. Wang, R. Jia, W. Guan, W. Li, Q. Liu, Y. Hu, S. Long, B. Chen, M. Liu, T. Ye, W. Lu, L. Jiang, *J. Phys. D: Appl. Phys.* 41 (2008) 035109.
- [147] S.A. Ng, K.A. Razak, K.Y. Cheong, K.C. Aw, *Thin Solid Films* 615 (2016) 84–90.
- [148] W.L. Leong, P.S. Lee, A. Lohani, Y.M. Lam, T. Chen, S. Zhang, A. Dodabalapur, S. G. Mhaisalkar, *Adv. Mater.* 20 (2008) 2325–2331.
- [149] Y.-S. Lo, K.-C. Liu, J.-Y. Wu, C.-H. Hou, T.-B. Wu, *Appl. Phys. Lett.* 93 (2008) 132907.
- [150] Y. Che, Y. Zhang, X. Cao, X. Song, M. Cao, H. Dai, J. Yang, G. Zhang, J. Yao, *Appl. Phys. Lett.* 109 (2016) 013106.
- [151] S. Horikoshi, N. Matsumoto, Y. Omata, T. Kato, *J. Appl. Phys.* 115 (2014) 193506.
- [152] Y.K. Mishra, S. Mohapatra, R. Singhal, D.K. Avasthi, D.C. Agarwal, S.B. Ogale,

- Appl. Phys. Lett. 92 (2008) 043107.
- [153] F. Schulz, T. Homolka, N.G. Bastús, V. Puentes, H. Weller, T. Vossmeier, Langmuir 30 (2014) 10779–10784.
- [154] A. Kossoy, V. Merk, D. Simakov, K. Leosson, S. Kéna-Cohen, S.A. Maier, Adv. Opt. Mater. 3 (2015) 71–77.
- [155] T.C. Chang, F.Y. Jian, S.C. Chen, Y.T. Tsai, Mater. Today 14 (2011) 608–615.
- [156] Y.K. Mishra, V.S.K. Chakravadhanula, V. Hrkac, S. Jebril, D.C. Agarwal, S. Mohapatra, D.K. Avasthi, L. Kienle, R. Adelung, J. Appl. Phys. 112 (2012) 064308.
- [157] V.S.K. Chakravadhanula, Y.K. Mishra, V.G. Kotnur, D.K. Avasthi, T. Strunskus, V. Zaporotchenko, D. Fink, L. Kienle, F. Faupel, Beilstein J. Nanotechnol. 5 (2014) 1419–1431.
- [158] S. Maidul Haque, P.R. Sagdeo, S. Balaji, K. Sridhar, S. Kumar, D. Bhattacharyya, D. Bhattacharyya, N.K. Sahoo, J. Vac. Sci. Technol. B, Nanotechnol. Microelectron. Mater. Process. Meas. Phenom. 32 (2014) 03D104.
- [159] I.S. Kim, E.K. Jeong, D.Y. Kim, M. Kumar, S.Y. Choi, Appl. Surf. Sci. 255 (2009) 4011–4014.
- [160] A. van der Drift, Philips Res. Reports 22 (1967) 267–288.
- [161] N. Zhan, M.C. Poon, C.W. Kok, K.L. Ng, H. Wong, J. Electrochem. Soc. 150 (2003) F200.
- [162] O.M. Orlov, G.J. Krasnikov, V.A. Gritsenko, V.N. Kruchinin, T. V. Perevalov, V.S. Aliev, D.R. Islamov, I.P. Prosvirin, ECS Trans. 69 (2015) 237–241.
- [163] A.R. Chourasia, J.L. Hickman, R.L. Miller, G.A. Nixon, M.A. Seabolt, Int. J. Spectrosc. 2009 (2009) 1–6.
- [164] L. Zhang, R. Persaud, T.E. Madey, Phys. Rev. B 56 (1997) 10549–10557.
- [165] J. Xin, D. Cheng, L. Zhang, K. Lin, H. Fan, Y. Wang, C. Xia, Int. J. Mol. Sci. 14 (2013) 21676–21688.
- [166] S. Gaur, J.T. Miller, D. Stellwagen, A. Sanampudi, C.S.S.R. Kumar, J.J. Spivey, Phys. Chem. Chem. Phys. 14 (2012) 1627–1634.
- [167] R.K. Gupta, D.Y. Kusuma, P.S. Lee, M.P. Srinivasan, ACS Appl. Mater. Interfaces 3 (2011) 4619–4625.
- [168] Y. Senzaki, S. Park, H. Chatham, L. Bartholomew, W. Nieveen, J. Vac. Sci. Technol. A Vacuum, Surfaces, Film. 22 (2004) 1175–1181.
- [169] G.D. Wilk, R.M. Wallace, J.M. Anthony, J. Appl. Phys. 87 (2000) 484–492.
- [170] S.J. Wang, P.C. Lim, A.C.H. Huan, C.L. Liu, J.W. Chai, S.Y. Chow, J.S. Pan, Q. Li,

- C.K. Ong, *Appl. Phys. Lett.* 82 (2003) 2047–2049.
- [171] T.P. Smirnova, L.V. Yakovkina, V.N. Kitchai, V.V. Kaichev, Y.V. Shubin, N.B. Morozova, K.V. Zherikova, *J. Phys. Chem. Solids* 69 (2008) 685–687.
- [172] Y.P. Gong, A.D. Li, X. Qian, C. Zhao, D. Wu, *J. Phys. D. Appl. Phys.* 42 (2009) 015405.
- [173] D. Panda, A. Dhar, S.K. Ray, *Semicond. Sci. Technol.* 24 (2009) 115020.
- [174] S.N. Keeney, *Proc. Electrochem. Soc* (n.d.) 151–158.
- [175] J. De Blauwe, *IEEE Trans. Nanotechnol.* 1 (2002) 72–77.
- [176] K. Das, M. NandaGoswami, R. Mahapatra, G.S. Kar, A. Dhar, H.N. Acharya, S. Maikap, J.-H. Lee, S.K. Ray, *Appl. Phys. Lett.* 84 (2004) 1386–1388.
- [177] J.S. Lee, *Gold Bull.* 43 (2010) 189–199.
- [178] V. Mikhelashvili, B. Meyler, S. Yofis, Y. Shneider, A. Zeidler, M. Garbrecht, T. Cohen-Hyams, W.D. Kaplan, M. Lisiansky, Y. Roizin, J. Salzman, G. Eisenstein, *Appl. Phys. Lett.* 98 (2011) 212902.
- [179] Z.Y. Wang, R.J. Zhang, H.L. Lu, X. Chen, Y. Sun, Y. Zhang, Y.F. Wei, J.P. Xu, S.Y. Wang, Y.X. Zheng, L.Y. Chen, *Nanoscale Res. Lett.* 10 (2015) 46.
- [180] Y.H. Tak, K.B. Kim, H.G. Park, K.H. Lee, J.R. Lee, *Thin Solid Films* 411 (2002) 12–16.
- [181] V. Mikhelashvili, B. Meyler, S. Yofis, J. Salzman, M. Garbrecht, T. Cohen-Hyams, W.D. Kaplan, G. Eisenstein, *J. Electrochem. Soc.* 157 (2010) H463.
- [182] S. Duguay, S. Burignat, P. Kern, J.J. Grob, A. Souifi, A. Slaoui, *Semicond. Sci. Technol.* 22 (2007) 837–842.
- [183] F.J. Himpsel, F.R. McFeely, A. Taleb-Ibrahimi, J.A. Yarmoff, G. Hollinger, *Phys. Rev. B* 38 (1988) 6084–6096.
- [184] M.T. Camci, B. Ulgut, C. Kocabas, S. Suzer, *ACS Omega* 2 (2017) 478–486.
- [185] M.K. Bayazit, S.A. Hodge, A.J. Clancy, R. Menzel, S. Chen, M.S.P. Shaffer, *Chem. Commun.* 52 (2016) 1934–1937.
- [186] D.Y.C. Leung, X. Fu, D. Ye, H. Huang, *Kinet. Catal.* 53 (2012) 239–246.
- [187] O. Zywitzki, K. Goedicke, H. Morgner, *Surf. Coatings Technol.* 151–152 (2002) 14–20.
- [188] J.A. García Valenzuela, R. Rivera, A.B. Morales Vilches, L.G. Gerling, A. Caballero, J.M. Asensi, C. Voz, J. Bertomeu, J. Andreu, *Thin Solid Films* 619 (2016) 288–296.
- [189] S. Prasanna, H. Shaik, G. Mohan Rao, Vandana, P.K. Singh, S. Jayakumar, R. Balasundaraprabhu, *Mater. Technol.* 29 (2014) 83–89.

- [190] S. Jakschik, U. Schroeder, T. Hecht, M. Gutsche, H. Seidl, J.W. Bartha, *Thin Solid Films* 425 (2003) 216–220.
- [191] A. Vinod, M.S. Rathore, S.R. Nelamarri, *Superlattices Microstruct.* 120 (2018) 616–628.
- [192] A. Vinod, M.S. Rathore, S.R. Nelamarri, *Appl. Phys. A* 124 (2018) 548.
- [193] J.L. Hodgkinson, D.W. Sheel, H.M. Yates, M.E. Pemble, *Plasma Process. Polym.* 3 (2006) 597–605.
- [194] Z. Liu, T.P. Chen, Y. Liu, Z.H. Cen, S. Zhu, M. Yang, J.I. Wong, Y. Bin Li, S. Zhang, *IEEE Trans. Electron Devices* 58 (2011) 33–38.

***Appendix- A***  
***List of Publications***

### **List of Publications from thesis work**

1. Arun Vinod, Mahendra Singh Rathore, Srinivasa Rao Nelamarri, “Role of annealing temperature on charge storage characteristics of Au nanocrystals with HfO<sub>2</sub> tunneling and blocking layers”, Superlattices and Microstructures, 120 (2018) 616.
2. Arun Vinod, Mahendra Singh Rathore, N Srinivasa Rao, “Effects of annealing on quality and stoichiometry of HfO<sub>2</sub> thin films grown by RF magnetron sputtering”, Vacuum, 155 (2018) 339.
3. Arun Vinod, Mahendra Singh Rathore, Srinivasa Rao Nelamarri, “Investigation of electrical and compositional properties of SiO<sub>2</sub>/Au/SiO<sub>2</sub> for nonvolatile memory application”, Applied Physics A, 124 (2018) 548.

### **List of Publications from other contributed work**

1. Arun Vinod, Mahendra Singh Rathore, T. Santhosh Kumar, D. Pamu, A. P. Pathak, N Srinivasa Rao, “Ion beam induced modification of structural and optical properties of MgTiO<sub>3</sub> nanocrystalline thin films”, Radiation Effects & Defects in Solids, 172 (2017) 81.
2. T. Santhosh Kumar, Arun Vinod, Mahendra Singh Rathore, A.P. Pathak, Fouran Singh, D. Pamu, N. Srinivasa Rao, “Effects of high-energy ion-beam irradiation on structural and optical properties of (Mg<sub>0.95</sub>Co<sub>0.05</sub>)TiO<sub>3</sub> thin films”, Radiation Effects and Defects in Solids, 173 (2018) 128.
3. Mahendra Singh Rathore, Arun Vinod, A. Rambabu, A. P. Pathak, Fouran Singh, T. Santhosh Kumar, N. Srinivasa Rao, “Ion beam modification of structural and optical properties of GeO<sub>2</sub> thin films deposited at various substrate temperatures using pulsed laser deposition”, Applied Physics A, 123 (2017) 708.
4. Mahendra Singh Rathore, Arun Vinod, N. Srinivasa Rao, “Effects of annealing temperature on structural, optical and electrical properties of Ge nanocrystals embedded in GeO<sub>x</sub> matrix” Macromolecular Symposia, 376 (2017) 1700024.
5. Mahendra Singh Rathore, Arun Vinod, N. Srinivasa Rao, “Structural and Optical Properties of GeO<sub>2</sub> Thin Films Prepared by E-Beam Evaporation”, Advanced Science Letters, 22 (2016) 3798.

*Appendix B*  
*Research Articles*



# Investigation of electrical and compositional properties of SiO<sub>2</sub>/Au/SiO<sub>2</sub> for nonvolatile memory application

Arun Vinod<sup>1</sup> · Mahendra Singh Rathore<sup>1</sup> · Srinivasa Rao Nelamarri<sup>1</sup>

Received: 12 April 2018 / Accepted: 9 July 2018  
© Springer-Verlag GmbH Germany, part of Springer Nature 2018

## Abstract

In this work, the effects of annealing temperature on the compositional, morphological and electrical properties of SiO<sub>2</sub>/Au/SiO<sub>2</sub> trilayer structure are investigated. SiO<sub>2</sub> and Au layers were deposited using RF magnetron sputtering and e-beam evaporation techniques, respectively. Transmission electron microscopic images reveal the formation of Au nanocrystals. Atomic force micrographs show the variation in surface roughness with annealing temperature. Rutherford backscattering spectroscopy was employed to estimate the thickness of the trilayer structure. X-ray photoelectron spectroscopy results indicate the formation of Au nanocrystal and SiO<sub>2</sub> tunneling and blocking layers. The hysteresis curve indicates the role of Au nanocrystals in charge storage characteristics of the device structure.

## 1 Introduction

During recent years, the semiconductor storage device technology has witnessed the boom in big data, cloud computing and electronic gadgets [1]. The increased demand for non-volatile memory with high density, low power consumption, high speed communication and better reliability have led the silicon industry to rescale the dimensions of the gate dielectric oxide [2]. The scaling down of oxide layers has increased the leakage current leading to the degradation of device performance. Predominant gate dielectric material (SiO<sub>2</sub>) has been gradually replaced by alternative dielectric materials with high dielectric constant, large bandgap, low interface state density and good thermal stability for better device performance [3, 4]. One of the alternate approaches other than scaling SiO<sub>2</sub> is to use floating nodes [5, 6]. The two main methods in this approach are Nitride floating gates and nanocrystal (NC) storage nodes. In nanocrystal floating gate approach, the conventional floating gate is replaced by nanocrystals. The utilization of nanocrystals in floating gate reduces the charge loss, increases write-erase speed and lowers operating voltage [7]. The nanocrystals memory can be further classified as metal, semiconductor and high dielectric nanocrystals. Among them, the metal nanocrystals

are more advantageous than semiconductor nanocrystal in nonvolatile memory devices due to high density of states, better three-dimensional electric field enhancement and high work-function engineering. The metal nanoparticles play a significant role in charge storage capability and characteristic reproducibility for nonvolatile devices [8]. The high density of states provided by the metal nanocrystals helps in enhanced charge storage.

Researchers have used various methods to fabricate non-volatile memory (NVM) device. Chan et al. fabricated Au NC based floating gate memory structure with HfAlO as tunneling and blocking layers using pulsed laser deposition. For the growth of Au NCs, the device was annealed at various temperatures and obtained a memory window up to 10 V with a voltage sweep  $\pm 12$  V [9]. Similarly, the memory capacitor behaviour of Au NCs in HfO<sub>2</sub> tunneling and blocking layers was reported. The oxide layers were deposited using Atomic layer deposition (ALD) and very large hysteresis window of 9.25 V for a sweep of  $\pm 7$  V was observed [10]. Moreover, for SiO<sub>2</sub> tunneling and HfO<sub>2</sub> blocking layer deposited using ALD with Au NCs exhibited a window of 12.6 V at  $\pm 12$  V [11]. The promising potential application of Au NCs in low programming/erasing voltage with a memory window of 1 V at  $\pm 2$  V was reported. The device structure was fabricated using a combination of various deposition methods such as RTA, sputtering and e-beam evaporation [12]. The charge localization effects of Au nonvolatile structure with thermal annealing was investigated by F. Xang et al. The device structure was fabricated by ALD for oxide

✉ Srinivasa Rao Nelamarri  
srnelamarri.phy@mmit.ac.in

<sup>1</sup> Department of Physics, Malaviya National Institute of Technology Jaipur, J L N Marg, Jaipur 302017, India



deposition and e-beam for Au deposition [13]. The method of deposition and the annealing temperature play a crucial role on various properties of device structure. Therefore, it is very important to understand the effect of annealing temperature on the trilayer structure from basic and applied point of view. Here, in this experiment RF magnetron sputtering was used for the deposition of oxide layers and electron beam evaporation for the deposition of Au charge trapping layer. However, no systematic reports are available on the fabrication of  $\text{SiO}_2/\text{Au}/\text{SiO}_2$  trilayer structure using RF magnetron sputtering and electron beam evaporation and the effects of annealing temperature. Therefore, an extensive investigation is utmost required to correlate the device performance with fabrication methods and effects of annealing temperature.

The present study aims at the fabrication of Au charge trapping layer sandwiched between  $\text{SiO}_2$  tunneling and blocking layers and to understand the effect of annealing temperature on various characteristics of trilayer structure. For this purpose, the  $\text{SiO}_2/\text{Au}/\text{SiO}_2$  trilayer was deposited on Si substrate and further annealed at various temperatures for the formation of nanocrystals.

## 2 Experimental procedure

In the present experiment, nonvolatile memory device structure with Au charge trapping layer was fabricated on p-type silicon (100) substrate with resistivity of 1–10  $\Omega\text{cm}$ . The Si wafers were cleaned using RCA I and II process to remove organic and inorganic residues from the surface. To remove the native oxide, the substrates were treated with dilute hydrofluoric solution. The base vacuum of  $6 \times 10^{-6}$  mbar was achieved using a rotary assisted turbo pump prior to the deposition. After pre-sputtering the target for 10 min, tunneling layer of 10 nm of  $\text{SiO}_2$  was deposited using RF magnetron sputtering. For the deposition of trapping layer, an Au layer of 3 nm

was deposited using electron beam evaporation. Finally, a thick layer of  $\text{SiO}_2$  with a thickness of 20 nm was also deposited using RF magnetron sputtering for the fabrication of the trilayer structure. The schematic illustration of  $\text{SiO}_2/\text{Au}/\text{SiO}_2$  trilayer structure is shown in Fig. 1. To form Au nanocrystals, the thermal annealing of the structure was carried out in  $\text{N}_2$  environment at various temperatures (650, 750 and 850  $^\circ\text{C}$ ) for an hour with a ramp rate of 10  $^\circ\text{C}/\text{min}$ .

To understand the formation of nanocrystals,  $\text{SiO}_2$  tunneling layer with thickness of 10 nm was deposited using RF magnetron sputtering on Ni TEM grid. Subsequently, a thin layer of 3 nm Au was deposited using electron beam evaporation on  $\text{SiO}_2$  layer and was annealed at 850  $^\circ\text{C}$  for an hour in  $\text{N}_2$  environment. These samples were characterized using transmission electron microscopy (TEM) to confirm the formation of nanocrystals. The topographical features of the blocking layer have been obtained by the atomic force microscopy (Bruker) at room temperature. Rutherford backscattering spectroscopy (RBS) measurements were carried out using 2 MeV He ion beam from 1.7 MV Pelletron Accelerator at Inter-University Acceleration Centre (IUAC), New Delhi, to identify the presence of various elements and to estimate the thickness of the trilayer structure. The obtained spectrum is fitted using Rutherford Universal Simulation Program (RUMP) simulation [14]. For measuring the electrical properties of the device structure, top Al electrode with a diameter  $\sim 1$  mm and thickness 250 nm was deposited using electron beam evaporation. For the ohmic contact formation, Al with a thickness of 250 nm was deposited on the back of the p-Si substrate using electron beam evaporation. The electrical measurements were carried out using Agilent Device Analyzer B1500A at room temperature. The elemental composition of the trilayer structures has been analysed by the X-ray photoelectron spectroscopy (XPS) with Al  $K\alpha$  ( $h\nu = 1486.6$  eV) source.

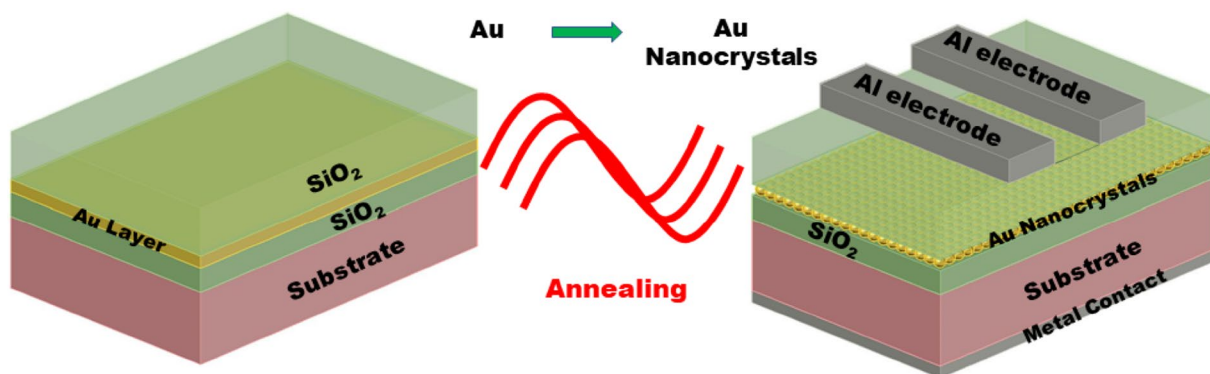


Fig. 1 Schematic illustration of  $\text{SiO}_2/\text{Au}/\text{SiO}_2$  NVM structure

### 3 Results and discussion

TEM images of Au/SiO<sub>2</sub> annealed at 850 °C are shown in Fig. 2. Figure 2a presents TEM micrographs of Au nanocrystals in SiO<sub>2</sub>. The density of Au nanocrystals is around  $1.1 \times 10^{11}/\text{cm}^2$ . The selected area electron diffraction pattern (SAED) of Au is presented in Fig. 2b. The HRTEM image (shown in Fig. 2c) confirms the formation of Au nanocrystals.

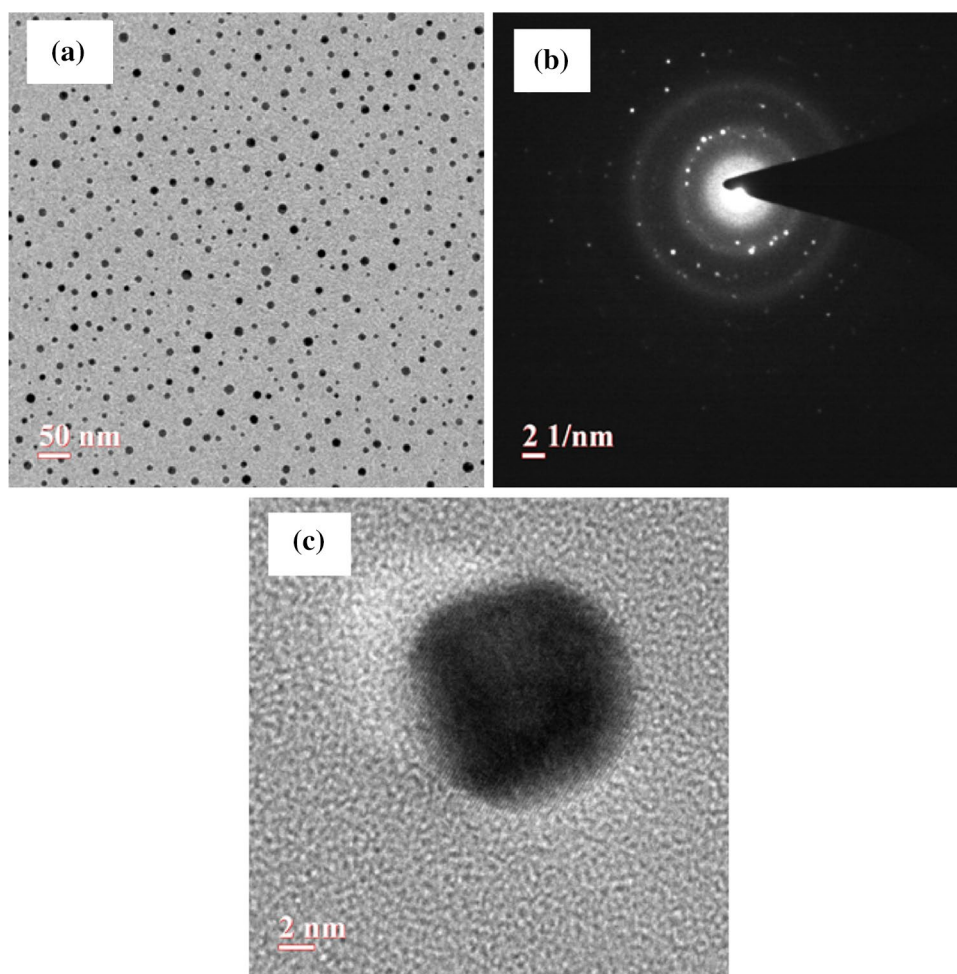
The surface morphology of the blocking layer was studied using AFM. Figure 3 shows the AFM images of as-deposited and annealed samples at different temperatures in the scan range of  $1 \times 1 \mu\text{m}$ . The root mean square roughness ( $R_{\text{rms}}$ ) of the as-deposited and annealed samples at 650, 750 and 850 °C are estimated to be 1.08, 0.92, 0.99 and 0.93 nm, respectively. The absence of visible pores, cracks and voids in as-deposited blocking layer indicates tightly packed atomic arrangement. This shows that the films are well-deposited [15] and RF magnetron sputtering is good to be employed for oxides depositions. The peak to valley roughness for the as-deposited and annealed

samples are 8.5, 5.4, 7.0 and 6.9 nm, respectively. It is reported that when the peak to valley roughness increases the leakage current also increases [16]. The peak to valley roughness of the samples annealed at 650 °C is decreased as compared to pristine ones. Further increase in the annealing temperature results in the increase in the peak to valley roughness as compared to samples annealed at 650 °C. This could be due to the rearrangement of atoms on the surface by attaining sufficient thermal energy.

RBS measurements were done to understand the presence of elements and to estimate the thickness of trilayer structure. The RBS spectrum of the nonvolatile structure annealed at 850 °C is presented in Fig. 4. The spectrum clearly shows the presence of O, Si and Au. The thickness of the trilayer structure is determined by fitting the experimentally obtained spectrum (black) with simulated spectrum (red). The spectrum reveals the inter-diffusion, which is also evident from XPS spectra as shown in Figs. 7, 8 and 9. The total thickness of the trilayer structure is estimated and found to be  $\sim 38$  nm by considering the bulk densities.

Figure 5 shows the current–voltage relation of NVM structure under different annealing temperatures. The reverse

**Fig. 2** a TEM micrograph of Au in SiO<sub>2</sub>, b Au SAED pattern, c HRTEM image of Au in SiO<sub>2</sub> annealed at 850 °C



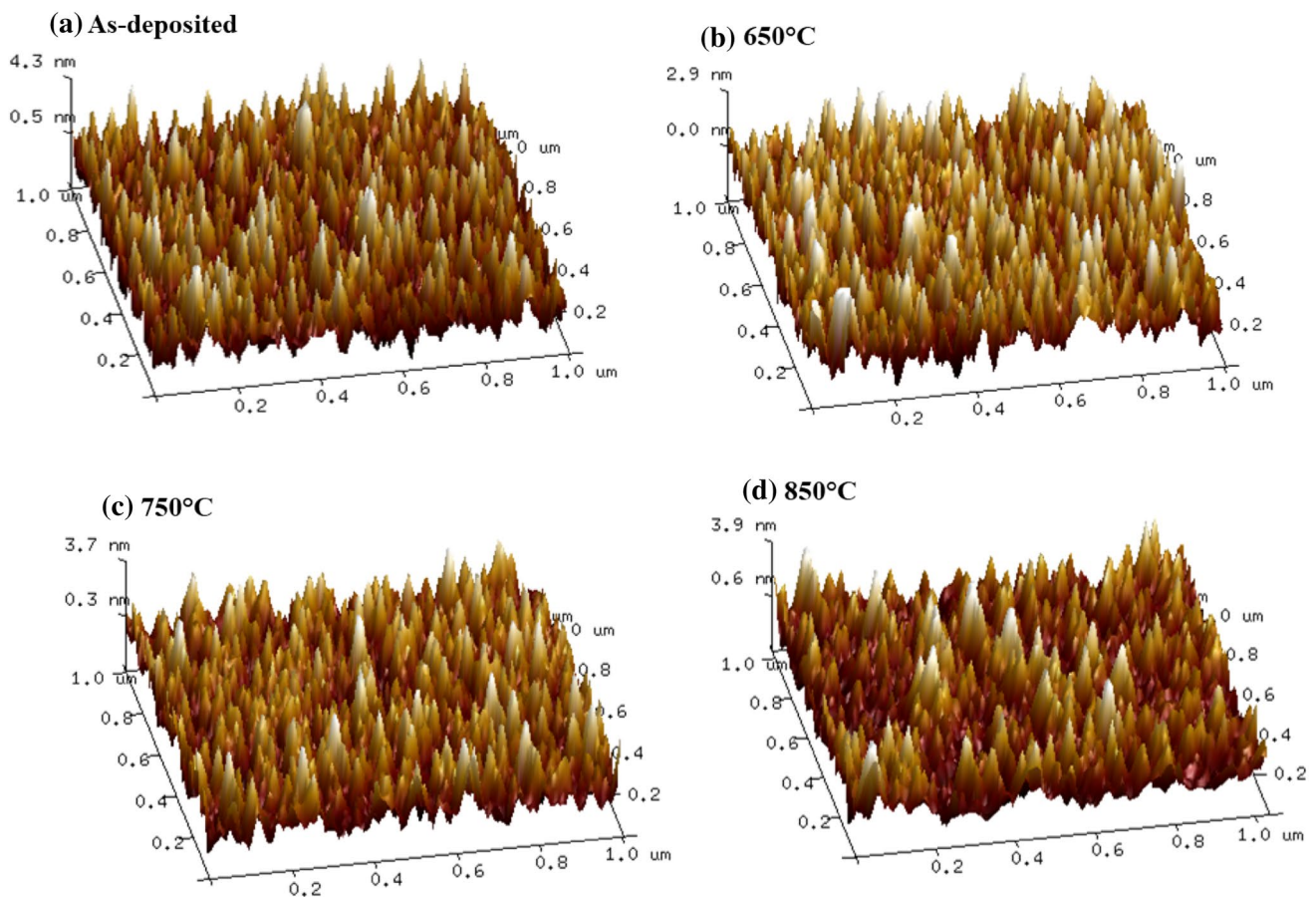


**Fig. 3** The surface morphologies of blocking layer before and after annealing

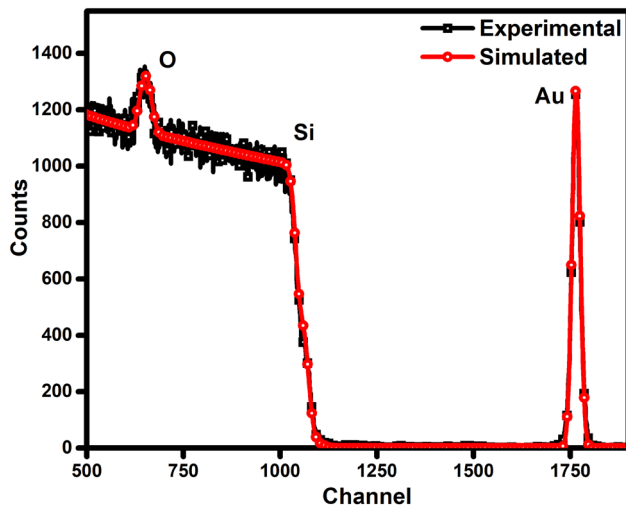


**Fig. 4** Rutherford backscattering spectrum of  $\text{SiO}_2/\text{Au}/\text{SiO}_2$  structure annealed at 850 °C

and forward current were measured by scanning the voltage from  $-6$  to  $+6$  V. A variation in leakage current with annealing is visible from the I–V measurement. The leakage current values for as-deposited and annealed samples at 1 V are compared. The annealed samples show significant decrease in leakage current as compared to the pristine ones. The decrease in leakage current with high temperature annealing may be due to Au nanocrystal formation [17]. This reduction might have resulted either from the carriers injected into the nanocrystals or by the blocking of external electric field by the internal electric field of the charge stored in the Au nanocrystals. The as-deposited and annealed structures show a variation in current minima values from 0 V. This shift in leakage current value from 0 V is due to the charge storage [17–19]. The variation in the current minima values may be attributed to the formation of nanocrystals with annealing. It is also reported that the formation of nanocrystals plays a crucial role in nonvolatile memory behaviour [20].

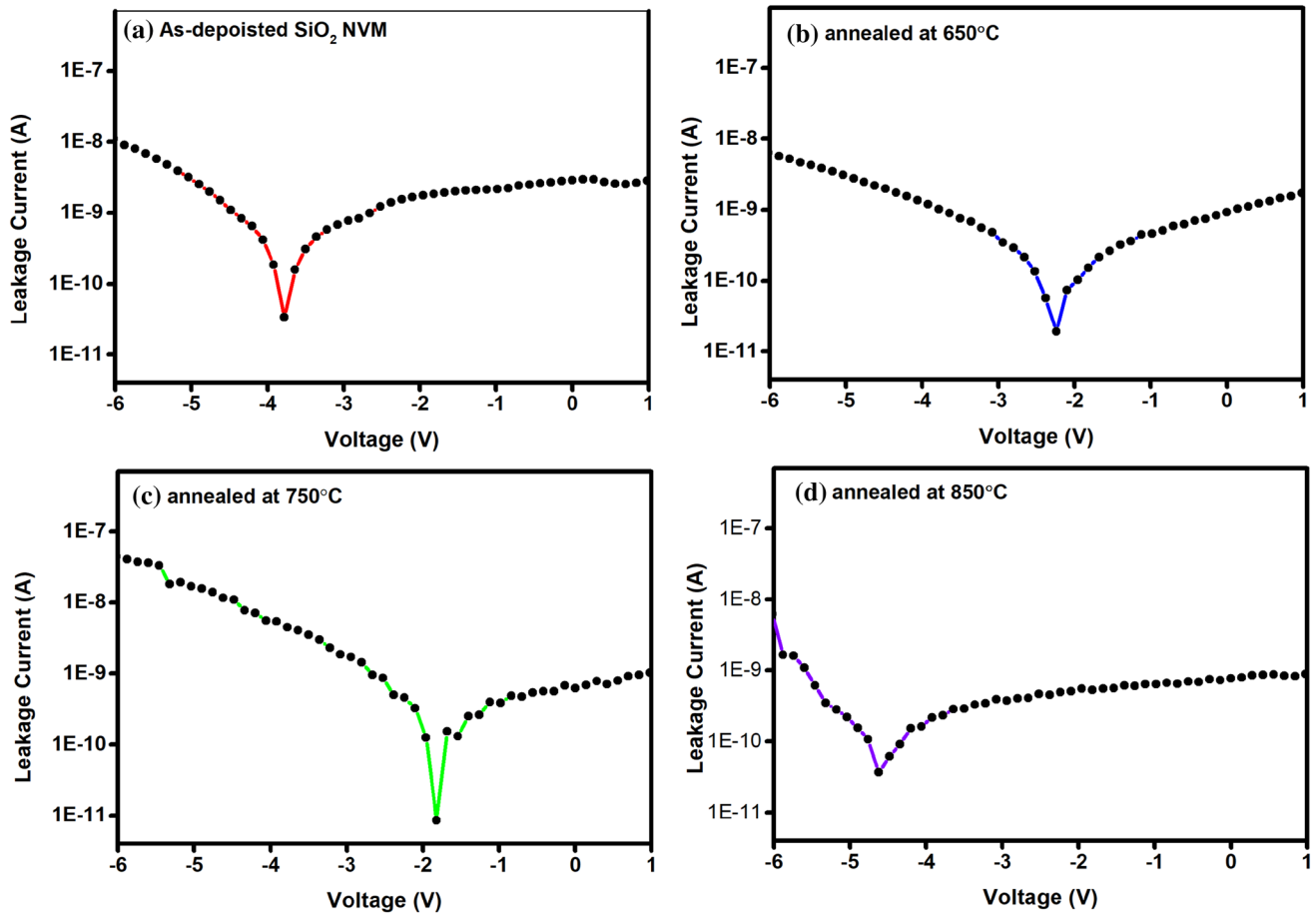


Fig. 5 Leakage current–voltage characteristics of trilayer structure before and after annealing

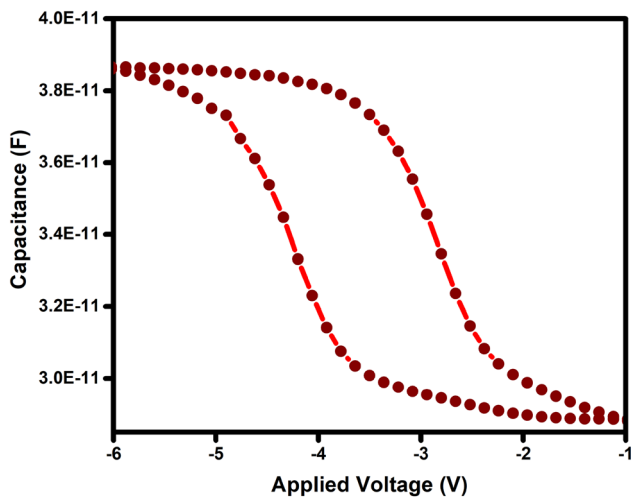


Fig. 6 C–V hysteresis of NVM structure with Au nanocrystals in SiO<sub>2</sub> tunneling and blocking layers

The charge storage characteristics of nonvolatile structure with Au nanocrystals at 850 °C analysed by typical high frequency (1 MHz) capacitance–voltage (C–V) measurement at room temperature are presented in Fig. 6. The gate voltage is swept from negative to positive region and vice versa in the range of 7 V. Hence, the capacitor structure is swept across accumulation and inversion regions. This counter-clockwise hysteresis curve indicates the injection of the charges from the substrate into the nanocrystals and vice versa. The deviation from ideal condition is observed in the hysteresis curve as the centre comes around  $-3$  V rather than 0 V. The main reasons for the deviation are the difference in work function between the metal electrode and the silicon and the immobile charges existing in the oxide layers [21]. The presence of accumulation and inversion regions in the hysteresis curve could be explained with respect to the voltage applied. When a positive voltage is applied, electrons will be



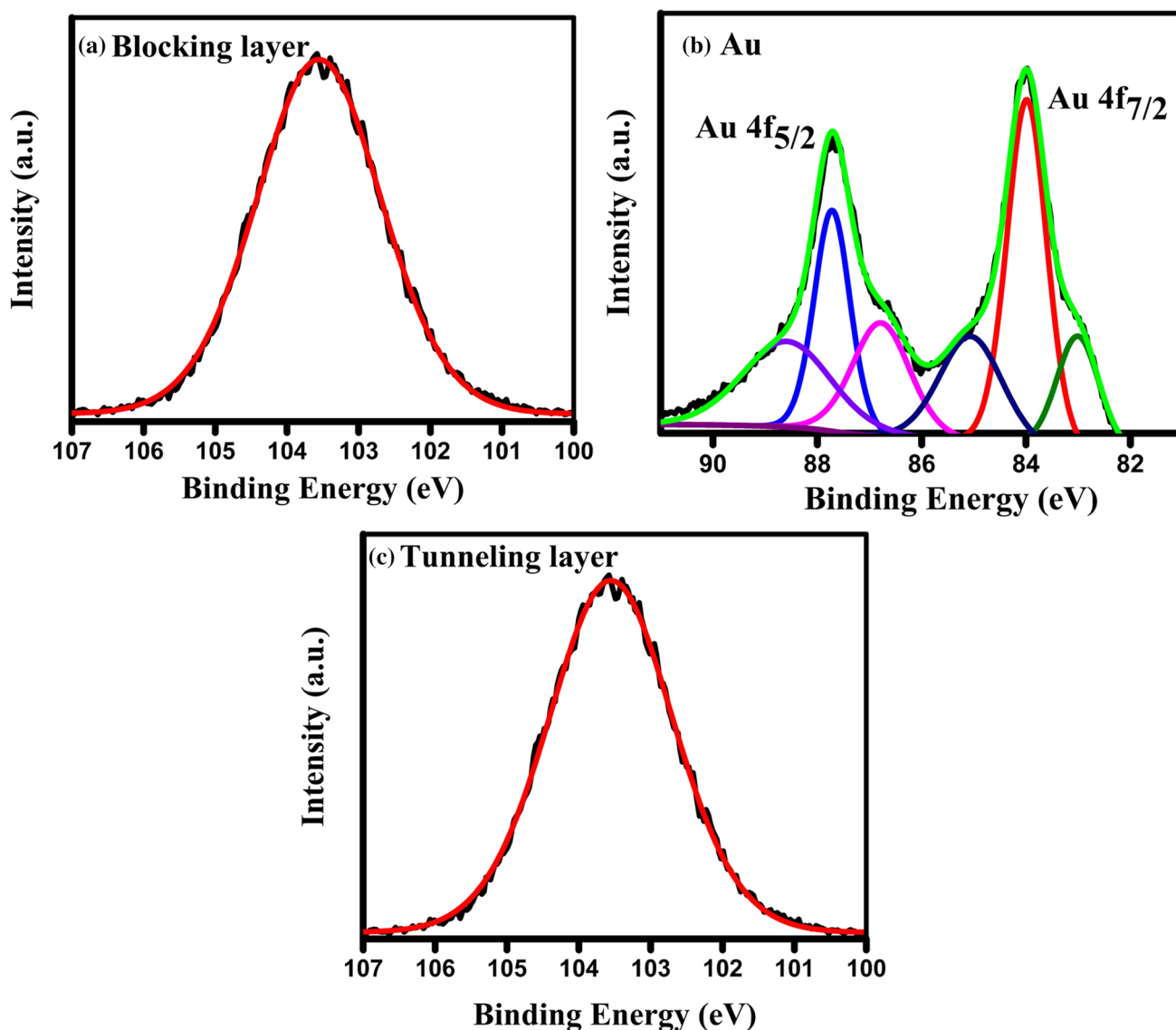
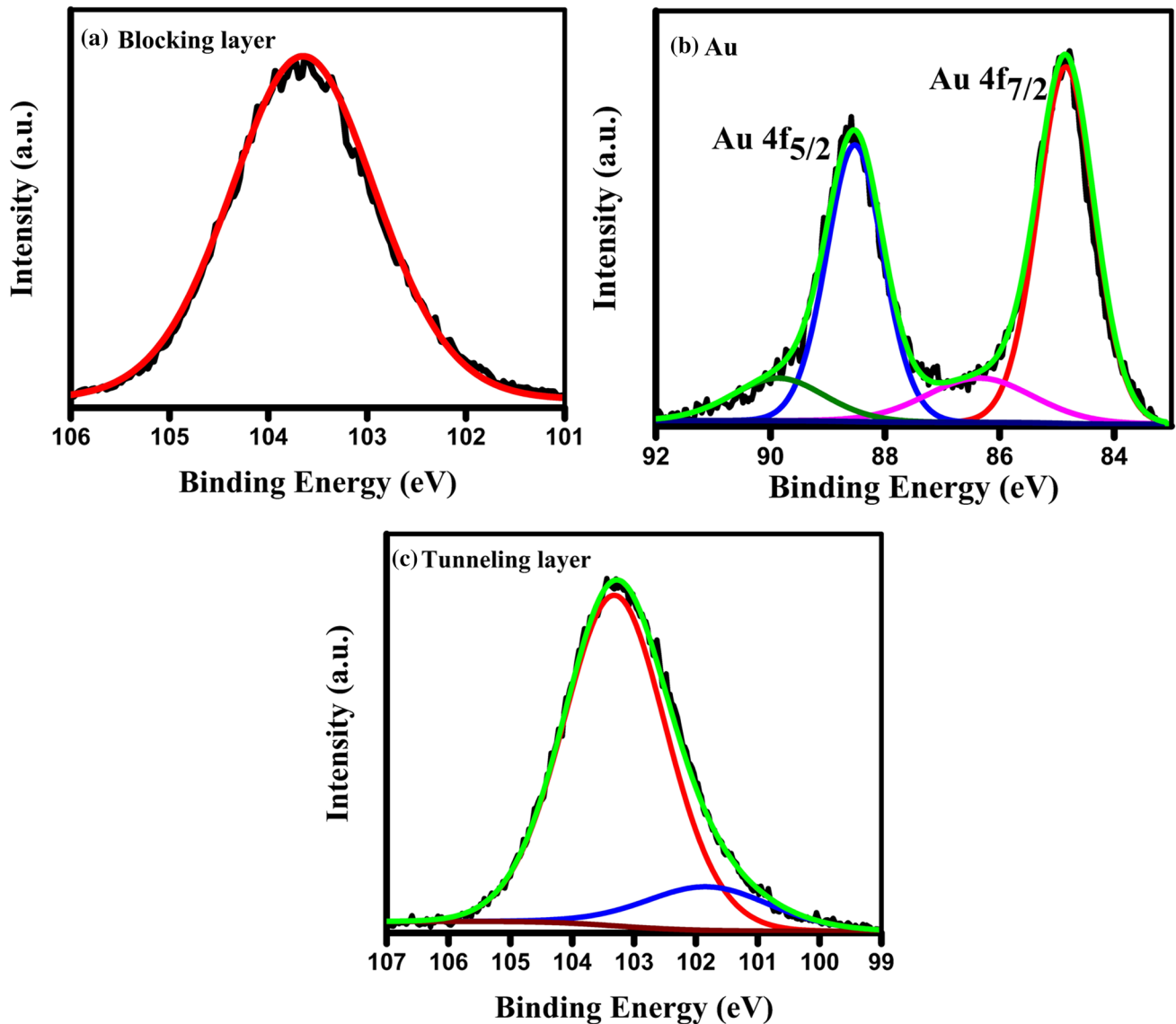


Fig. 7 XPS spectra of as-deposited blocking, trapping and tunneling layer

ejected into the Au nanocrystals from the Si substrate (electron charging). On the other hand, when negative voltage is applied, holes will be injected into the nanocrystals (hole charging). Here, in the present experiment, the memory window obtained is around 2 V with a net charge trapped to be estimated as  $1.59 \times 10^{12}/\text{cm}^2$ . The hysteresis curve confirms the significant role of Au nanocrystals in the charge storage behaviour of the capacitor structure.

Further understanding of the elemental composition of the NVM structures was obtained using XPS (Figs. 7, 8, 9). The peaks of all layers are calibrated from C 1s peak at 284.8 eV. The blocking layer of the as-deposited sample indicates the binding energy of Si 2p is at 103.5 eV. This shows the formation of SiO<sub>2</sub> [22]. Meanwhile, in addition to the major 4f peak, the Au spectra indicates two more

sub-peaks. The 4f peak of gold is around 84 and 87.7 eV with a difference in binding energy around 3.7 eV, whereas the sub-peaks around 83 and 87 eV represent the presence of metallic/bulk Au particle [23–25]. The shoulder peak at higher binding energy is related to the oxidation of Au [26]. On the other hand, the Au spectra of the samples annealed at 750 °C show slight shift towards higher binding energy around 84.3 eV indicating the formation of Au nanocrystals [27]. This could be attributed to the shift in fermi level with respect to the shrinkage of the particles. The disappearance of metallic peak in the spectra compliments the nanocrystals formation. No variation for Si 2p peak of blocking layer has been noticed but the tunneling layer shows an additional peak of SiO at 101.8 eV. Almost similar features in blocking, trapping and tunneling layer are observed for the films



**Fig. 8** XPS spectra of blocking, trapping and tunneling layer annealed at 750 °C

annealed at 850 °C with a small shift towards lower binding energy due to annealing.

## 4 Conclusions

In conclusion, this work demonstrates the effect of annealing temperature on SiO<sub>2</sub>/Au/SiO<sub>2</sub> trilayer structure. The nonvolatile memory device structure was fabricated using RF magnetron sputtering and electron beam evaporation

on Si substrates. TEM images indicate Au nanocrystal formation with annealing. The total thickness of the trilayer structure is estimated with RBS. XPS spectra of annealed samples confirm the formation of Au nanocrystals. The I–V measurements show a decrease in leakage current with Au nanocrystal formation. The memory window of 2 V shows the charge storage capability of Au nanocrystals. Thus, this work confirms the role of Au nanocrystals in charge storage behaviour at high temperature annealing.

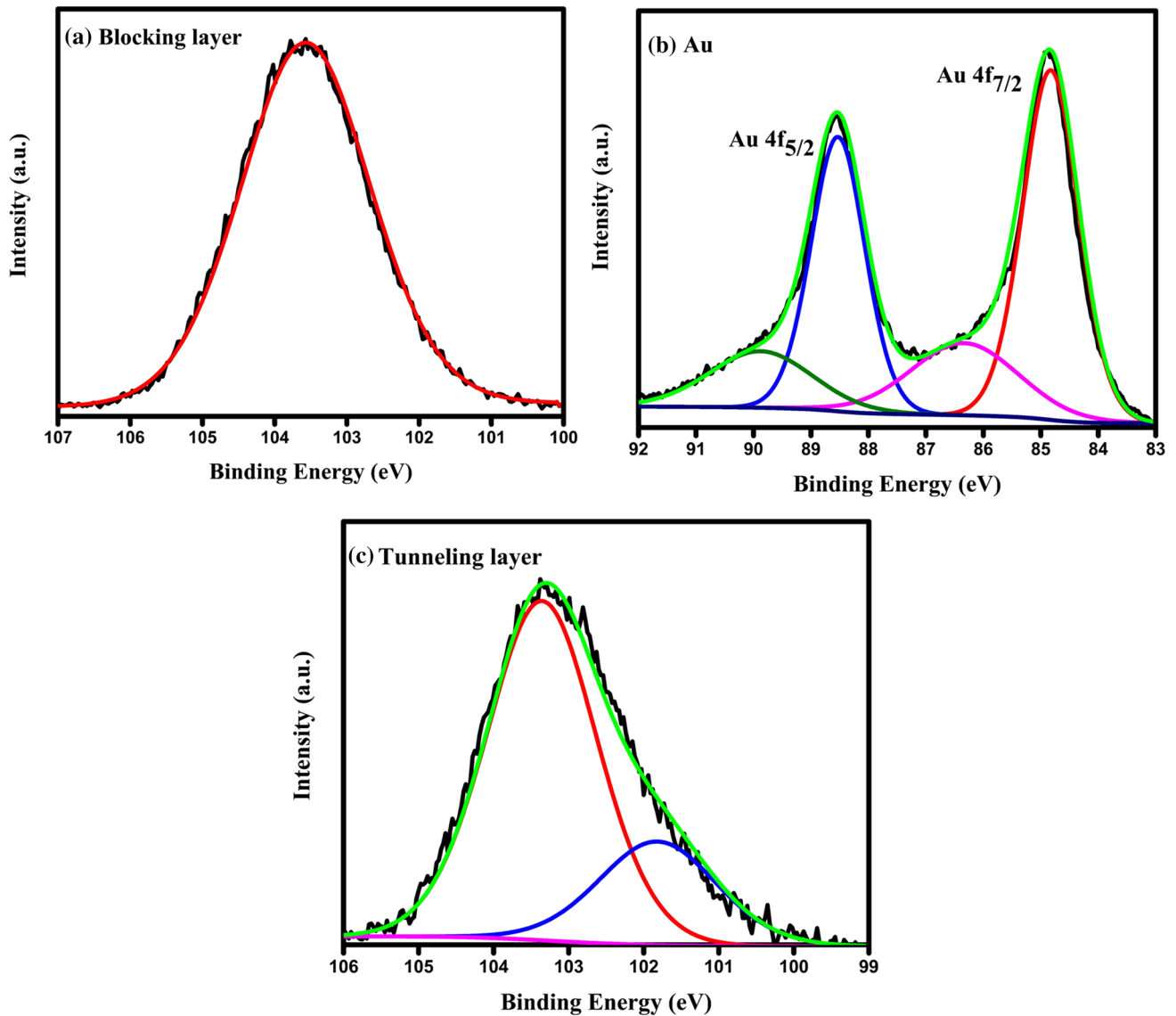


**Fig. 9** XPS spectra of blocking, trapping and tunneling layer annealed at 850 °C

**Acknowledgements** This work was financially supported by SERB, New Delhi (Project no. SR/FTP/PS-101/2013) and authors acknowledge the support of Sunil Ojha, Scientist, Inter-University Accelerator Centre, New Delhi for RBS measurements and fruitful discussions. Authors are grateful to MNCF, IISc, Bangalore and MRC, MNIT Jaipur for providing necessary characterization facilities.

## References

1. D.U. Lee, M.S. Lee, J.H. Kim, E.K. Kim, H.-M. Koo, W.J. Cho, W.M. Kim, *Appl. Phys. Lett.* **90**, 093514 (2007)
2. J.S. Lee, *Electron. Mater. Lett.* **7**, 175–183 (2011)
3. S.W. Nam, J.H. Yoo, S. Nam, H.J. Choi, D. Lee, D.H. Ko, J.H. Moon, J.-H. Ku, S. Choi, *J. NonCryst. Solids* **303**, 139–143 (2002)
4. J. Robertson, R.M. Wallace, *Mater. Sci. Eng. R* **88**, 1–41 (2015)
5. S.N. Keeney, *Proc. Electrochem. Soc.* **4**, 151–158 (2004)
6. J.De Blaauwe, *IEEE Trans. Nanotechnol.* **1**, 72–77 (2002)
7. K. Das, M. NandaGoswami, R. Mahapatra, G.S. Kar, A. Dhar, H.N. Acharya, J.H. Lee, S.K. Ray, *Appl. Phys. Lett.* **84**, 1386 (2004)
8. J.S. Lee, *Gold Bull.* **43**, 189 (2010)
9. K.C. Chan, P.F. Lee, J.Y. Dai, *Appl. Phys. Lett.* **92**, 223105 (2008)
10. V. Mikhelashvili, B. Meyler, S. Yoffis, J. Salzman, M. Garbrecht, T. Cohen-Hyams, W.D. Kaplan, G. Eisenstein, *Appl. Phys. Lett.* **95**, 023104 (2009)
11. V. Mikhelashvili, B. Meyler, S. Yofis, Y. Shneider, A. Zeidler, M. Garbrecht, T. Cohen Hyams, W.D. Kaplan, M. Lisiansky, Y. Roizin, J. Salzman, G. Eisenstein, *Appl. Phys. Lett.* **98**, 212902 (2011)
12. R. Tang, K. Huang, H. Lai, C. Li, Z. Wu, J. Kang, *Nanoscale Res. Lett.* **8**, 368 (2013)
13. X. Feng, S. Dong, H. Wong, D. Yu, K.L. Pey, K. Shubhakar, W.S. Lau, *Microelectron. Reliab.* **61**, 78–81 (2016)
14. L.R. Doolittle, *Nucl. Instrum. Methods Phys. Res. Sect. B* **9**, 344–351 (1985)

15. Z.-Y. Wang, R.J. Zhang, H.-L. Lu, X. Chen, Y. Sun, Y. Zhang, Y.-F. Wei, J.-P. Xu, S.-Y. Wang, Y.-X. Zheng, L.-Y. Chen, *Nanoscale Res. Lett.* **10**, 46 (2015)
16. Y.-H. Tak, K.B. Kim, H.G. Park, K.H. Lee, J.R. Lee, *Thin Solid Films* **411**, 12–16 (2002)
17. C.C. Wang, Y.K. Chiou, C.H. Chang, J.Y. Tseng, L.J. Wu, C.Y. Chen, T.B. Wu, *J. Phys. D Appl. Phys.* **40**, 1673–1677 (2007)
18. S. Duguay, S. Burignat, P. Kern, J.J. Grob, A. Souifi, A. Slaoui, *Semicond. Sci. Technol.* **22**, 837–842 (2007)
19. V. Mikhelashvili, B. Meyler, S. Yofis, J. Salzman, M. Garbrecht, T. Cohen Hyams, W.D. Kaplan, G. Eisenstein, *J. Electrochem. Soc.* **157**, H463–H469 (2010)
20. T.C. Chang, F.Y. Jian, S.C. Chen, Y.T. Tsai, *Mater. Today* **14**, 608–615 (2011)
21. W. Guan, S. Long, M. Liu, Z. Li, Y. Hu, Q. Liu, *J. Phys. D Appl. Phys.* **40**, 2754–2758 (2007)
22. F.J. Himpsel, F.R. McFeely, A. Taleb-Ibrahimi, J.A. Yarmoff, G. Hollinger, *Phys. Rev. B* **38**, 6084–6096 (1988)
23. M.T. Camci, B.U.C. Kocabas, S. Suzer, *ACS Omega* **2**, 478–486 (2017)
24. M.K. Bayazit, S.A. Hodge, A.J. Clancy, R. Menzel, S. Chen, M.S.P. Shaffer, *Chem. Commun.* **52**, 1934–1937 (2016)
25. D.Y.C. Leung, F. Xianliang, Y. Daiqi, H. Haibao, *Kinet. Catal.* **53**, 239–246 (2012)
26. S. Gaur, J.T. Miller, D. Stellwagen, A. Sanampudi, C.S.S.R. Kumar, J.J. Spivey, *Phys. Chem. Chem. Phys.* **14**, 1627–1634 (2012)
27. R.K. Gupta, D.Y. Kusuma, P.S. Lee, M.P. Srinivasan, *ACS Appl. Mater. Interfaces* **3**, 4619–4625 (2011)





# Role of annealing temperature on charge storage characteristics of Au nanocrystals with HfO<sub>2</sub> tunneling and blocking layers

Arun Vinod, Mahendra Singh Rathore, Srinivasa Rao Nelamarri\*

Department of Physics, Malaviya National Institute of Technology Jaipur, J L N Marg, Jaipur 302017, India

## ARTICLE INFO

### Article history:

Received 16 March 2018  
Received in revised form 24 April 2018  
Accepted 27 April 2018  
Available online 2 May 2018

### Keywords:

Nonvolatile memory  
Nanocrystals  
High-k dielectric  
Annealing  
XPS  
RBS

## ABSTRACT

In this paper, we demonstrate the fabrication and charge storage characteristics of Au nanocrystals located between two hafnium oxide films acting as the tunneling and blocking layers serving as nonvolatile memory structure. The structure, composition and electrical properties of the device are drastically affected by annealing temperature. The inter-diffusion and stoichiometric changes of various layers are investigated using X-ray Photoelectron Spectroscopy and Rutherford Backscattering Spectroscopy. Electrical measurements show an improvement in leakage characteristics with annealing. The C-V hysteresis loop with and without Au nanocrystals are compared to understand charge storage behavior of the device structures. The occurrence of well-defined hysteresis loop with Au nanocrystals indicates significant role of Au nanocrystals in charge storage characteristics of the device.

© 2018 Elsevier Ltd. All rights reserved.

## 1. Introduction

Recently, non-volatile memory (NVM) has attracted considerable attention due to the huge demand for faster, reliable and high capacity devices. An increase in data retention performance is achieved, especially in the programming efficiency of the device, by the introduction of high dielectric material rather than SiO<sub>2</sub> [1]. The occurrence of smaller conduction band as well as valance band offsets has enabled the performance of high-k materials in lower operating voltages. Out of various high-k materials, HfO<sub>2</sub> is known to form better interface with Si and has better bandgap and dielectric value [2]. Recently, floating gate memory devices have attracted wide interest for nonvolatile structures due to their retention time and low operating voltages. The improvement in memory performance can be achieved through the integration of semiconductor or metal nanocrystals (NCs) with high-k dielectric materials [3,4].

Particularly, metal nanoparticles have been reported to possess large density of states and are preferred over its semiconductor counterparts due to their ability to enhance the electric field and provide better work-function engineering [5]. Among various metals, gold has gained considerable attention as it is non-toxic, easy to synthesize, has high density of states, large work function (5.1eV), which creates deep potential well that enhance carrier confinement [6]. Au nanocrystals as charge storage nodes in various oxide matrices with better performance and retention time were reported [7–10]. The performance of nonvolatile memory device depends on two main factors such as high density and uniformity of

\* Corresponding author.

E-mail address: [snelamarri.phy@mnit.ac.in](mailto:snelamarri.phy@mnit.ac.in) (S.R. Nelamarri).

nanoparticles. The former helps in better charge storage capability, while the latter is essential for the device characteristics reproducibility [11].

Various techniques are employed for the synthesis of Au nanoparticles including electron-cyclotron-resonance plasma sputtering method, atom beam co-sputtering, chemical method, electron beam evaporation, etc. [12–15]. The nanocrystal memory properties are influenced by the size, shape and configuration of the nanocrystals [16]. Moreover, nanocrystals separation play an important role in the charge loss rate of the storage and retention behaviour of the device. If the nanocrystals are adjacent, it may act as a discharging path and degrade the charge storage and retention properties of the nonvolatile memory [5]. Thus, synthesis of Au nanocrystals with uniformity and assembling them into a well-ordered matrix is most challenging. The use of insulating layer ( $\text{HfO}_2$ ) helps in attaining the necessary separation between adjacent nanocrystals by preventing agglomeration [17,18].

There are various physical and chemical methods employed for the fabrication of non-volatile memory devices. The advantages of oxide deposition using RF magnetron sputtering include less wastage of the material, high adhesion of films and excellent uniformity with good packing density [19]. For the deposition of metal charge trap layer, electron beam evaporation method has merits in the deposition of material with high purity as there is a direct transfer of energy to the source via electron beams, simplicity, large area deposition and better control of deposition rate [20].

The main objective of the present investigation is to fabricate trilayer structure  $\text{HfO}_2/\text{Au}/\text{HfO}_2$  and to understand the effect of annealing temperature on device characteristics of Au nanocrystals. For this purpose, the trilayer structure of  $\text{HfO}_2/\text{Au}/\text{HfO}_2$  was deposited on Si substrate and further annealed at various temperatures for the formation of nanocrystals. However, to the best of our knowledge, the combined use of RF sputtering and e-beam evaporation for the fabrication of  $\text{HfO}_2/\text{Au}/\text{HfO}_2$  trilayer structure has not been reported. Fig. 1 shows the schematic diagram of the formation of the nonvolatile memory structure.

## 2. Experimental details

The non-volatile memory device structure was fabricated on p-type silicon substrates of 1–10  $\Omega\text{cm}$  resistivity. Prior to the deposition, the substrates were thoroughly cleaned by standard Radio Corporation of America (RCA) I and II process [21] and HF was used for the removal of native oxide layer. The tunneling and blocking oxide layers of  $\text{HfO}_2$  were deposited by RF magnetron sputtering method with target-substrate distance (5 cm), base pressure ( $6 \times 10^{-6}$  mbar, working pressure ( $3 \times 10^{-3}$  mbar), Ar flow rate (20sccm) and RF power (100 W). The target was pre-sputtered for 10 min to remove surface contamination and native oxides prior to the deposition. The substrate holder was rotated at low rpm (2) to obtain uniform thickness of the films [22] and the thickness of tunneling oxide was around 10 nm and blocking oxide was 20 nm as measured

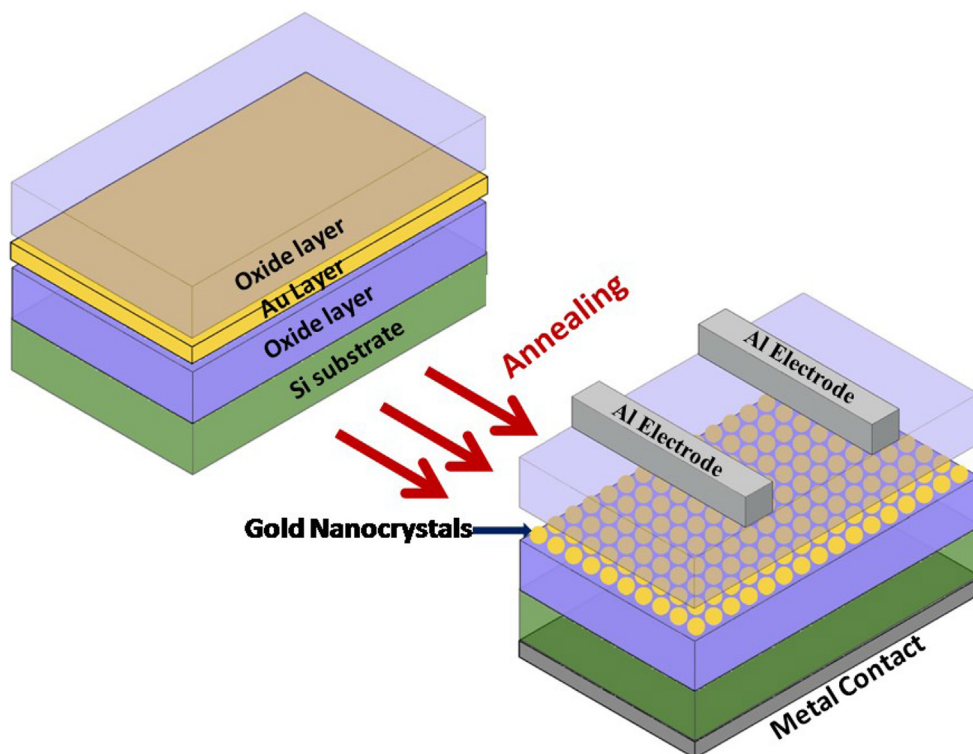


Fig. 1. Schematic illustration of the formation of NVM structure.

by a digital thickness monitor (DTM). The Au layer of 5 nm was deposited using electron beam evaporation. The basic structure of NVM device with  $\text{HfO}_2$  tunneling and blocking layer is schematically illustrated in the Fig. 1. After the deposition, annealing of the samples was carried out for 60 min in nitrogen environment at 650 °C, 750 °C and 850 °C with a ramp rate of 10 °C/min.

The structure of the films was evaluated using X-ray diffractometer with  $\text{CuK}_\alpha$  radiation (1.5406 Å). The surface morphology of the films was studied using a Bruker atomic force microscopy in ScanAsyst mode and the root mean square roughness ( $R_q$ ) is determined using NanoScope Analysis software. High Resolution Transmission Electron Microscopy (Make: FEI Tecnai-T20) was used to confirm the formation Au nanocrystals. The Au (charge trap layer of 5 nm)/ $\text{HfO}_2$  (tunneling layer of 10 nm) films were deposited on carbon coated Ni TEM grids and subsequently were annealed at 850 °C to study the formation and size distribution of Au nanocrystals. The chemical states and composition of the structures were examined using X-ray photoelectron spectroscopy (XPS) with a monochromatic Al  $\text{K}_\alpha$  ( $h\nu = 1486.6\text{eV}$ ) X-ray radiation using an Omicron ESCA + X-ray Photo Spectrometer from Oxford Instrument Germany. The electrical characterizations such as I-V and C-V were performed using Agilent B1500A Semiconductor Device Analyzer. Rutherford Backscattering Spectroscopy (RBS) measurements were performed with 2 MeV  $\text{He}^+$  ions at Inter- University Acceleration Centre (IUAC), New Delhi using 1.7 MV Tandem accelerator facility. Analysis of RBS data has been done using Rutherford Universal Simulation Program (RUMP) to estimate the composition and thickness of each layer [23].

### 3. Results and discussion

X-ray diffraction spectra of pristine and annealed  $\text{HfO}_2/\text{Au}/\text{HfO}_2$  nonvolatile memory structures are shown in Fig. 2. There is no peak observed in spectra of as-deposited sample, which indicates that as-grown films were amorphous. After annealing at a temperature greater than 650 °C,  $\text{HfO}_2$  films exhibit a monoclinic crystalline phase with the presence of predominate ( $\bar{1}\bar{1}1$ ), (111) and (200) planes. It is evident from the spectra that the orientation is predominant in the (111) rather than ( $\bar{1}\bar{1}1$ ) plane. The growth of the thin film in a preferred orientation is dominated by the minimization of total free energy. This could be explained by the migration of atoms towards the plane with lower surface energy [24]. The basic crystal growth mechanism indicates that the growth of a crystal face is favoured by the crystal orientation. At preferred growth conditions, a growth competition may rise among differently oriented crystals. This may give rise to fast and slow growth rates of various preferred orientations. This competition will lead to an orientation selection and texture growth [25,26].

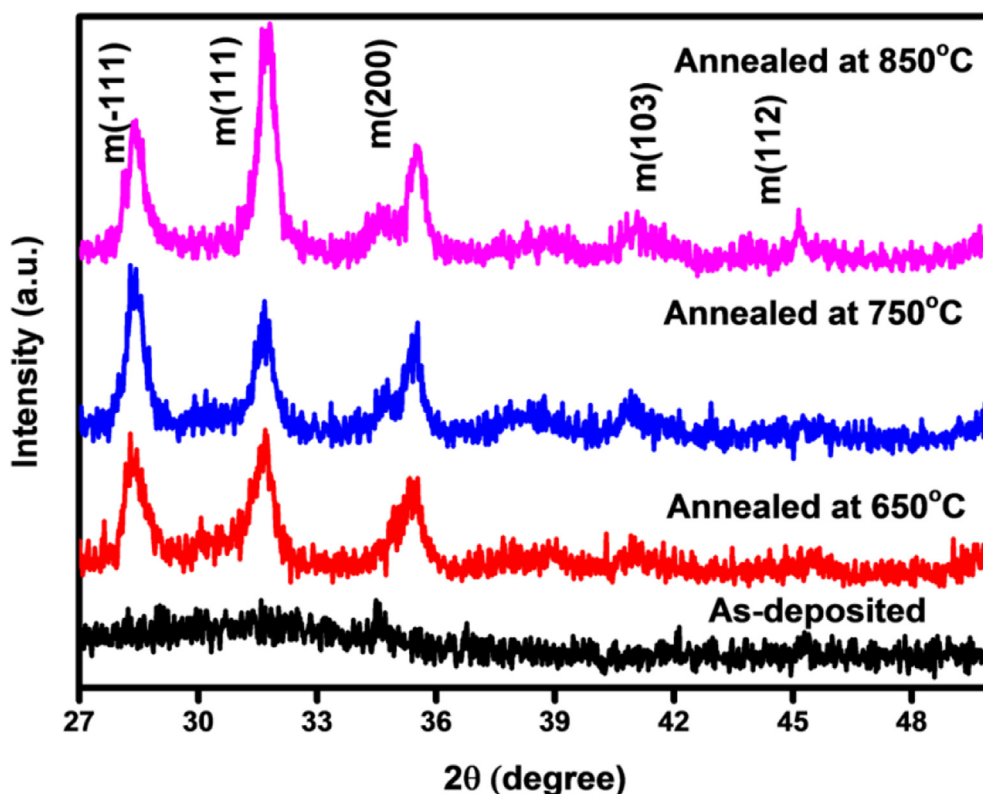
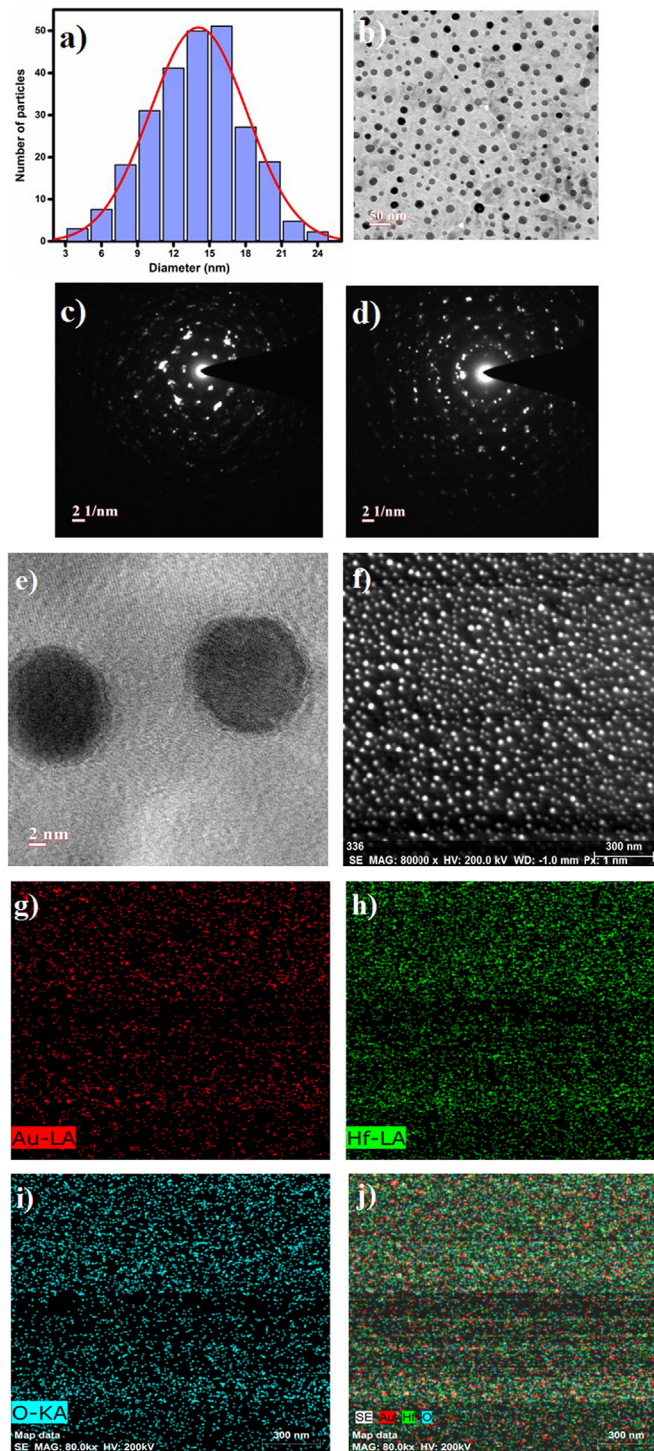


Fig. 2. XRD spectra of NVM structure before and after annealing.

The Au/HfO<sub>2</sub> films deposited on carbon coated Ni TEM grids were annealed at 850 °C and the particle size distribution, the TEM micrographs and elemental image mapping through STEM-EDX are shown in Fig. 3. The size distribution particle histogram for Au nanocrystals indicates that the particles are spherical in nature and are nearly uniform in size. The average core diameter of the crystals calculated by Gaussian fitting and found to be  $14 \pm 0.5$  nm. The average areal density of the Au nano-



**Fig. 3.** a) The histogram of Au nanoparticles b) TEM graphics of Au nanoparticles in HfO<sub>2</sub> and SAED pattern of c) HfO<sub>2</sub> & d) Au e) typical HR image of Au nanoparticles with EDX mapping images (f–j).



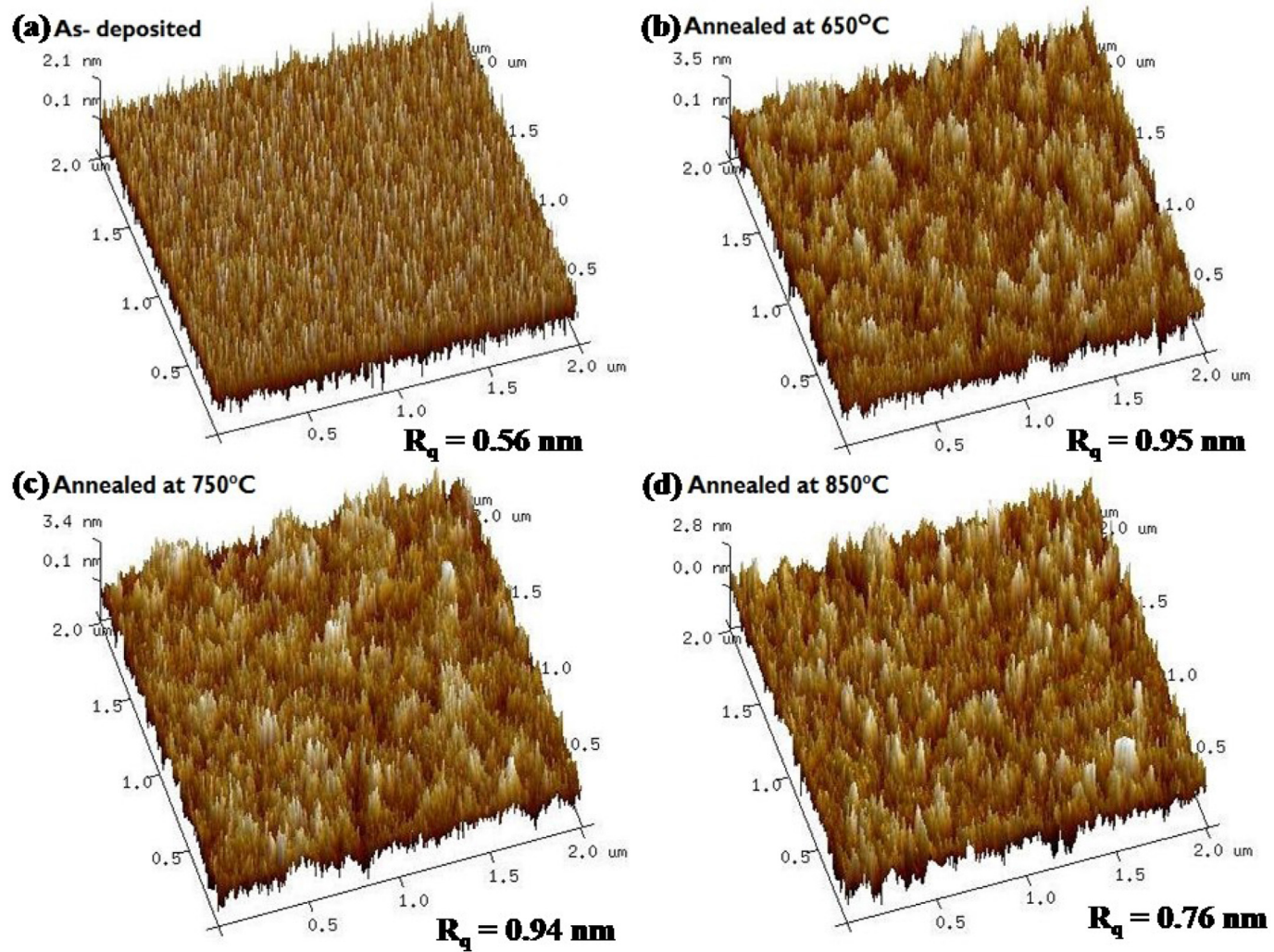


Fig. 4. The surface morphologies of HfO<sub>2</sub> blocking layer a) as-deposited b) annealed at 650 °C c) annealed at 750 °C and d) annealed at 850 °C.

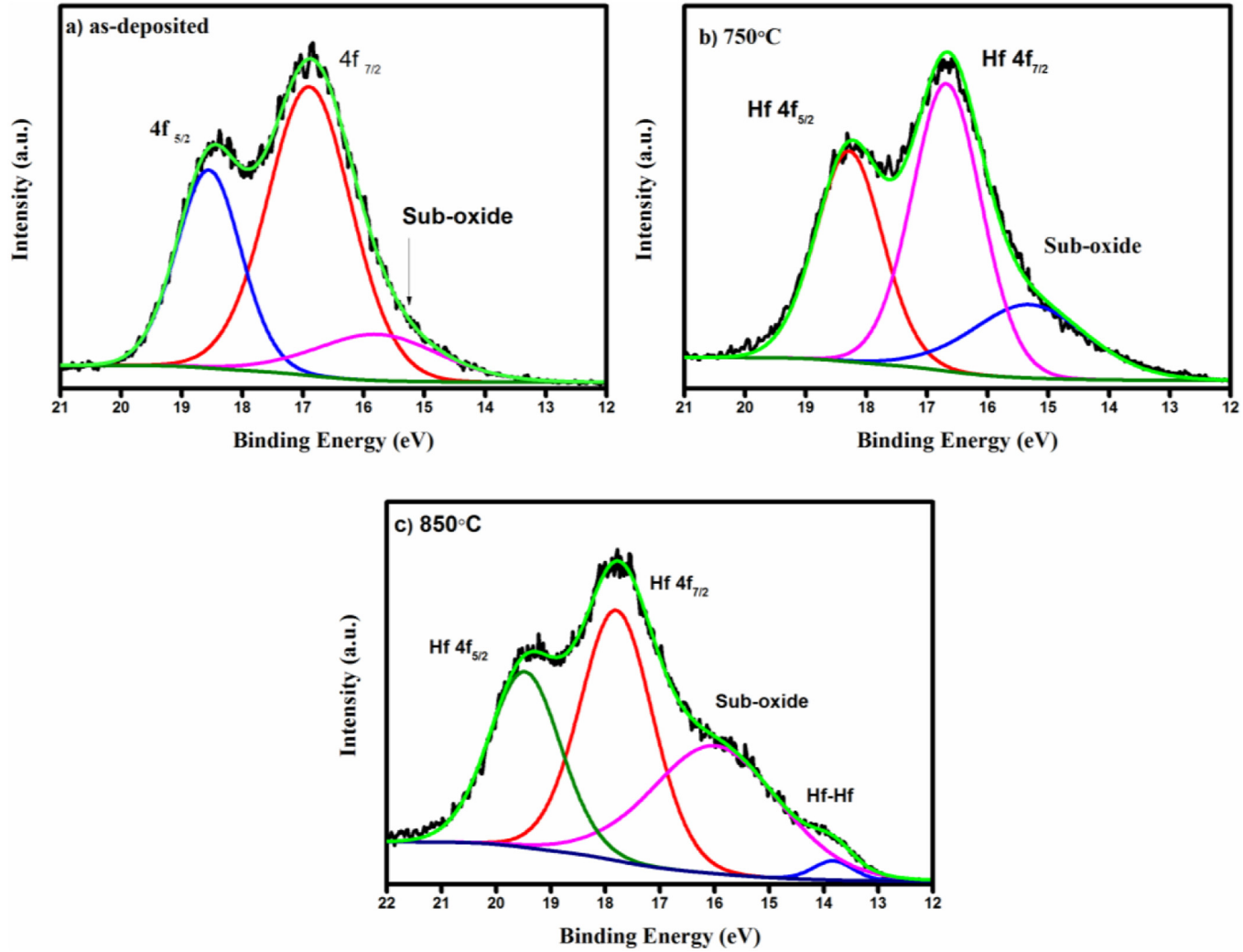


Fig. 5. The core elemental XPS spectra of Hf blocking layer of NVM structure a) as-deposited b) annealed at 750 °C and c) annealed at 850 °C.

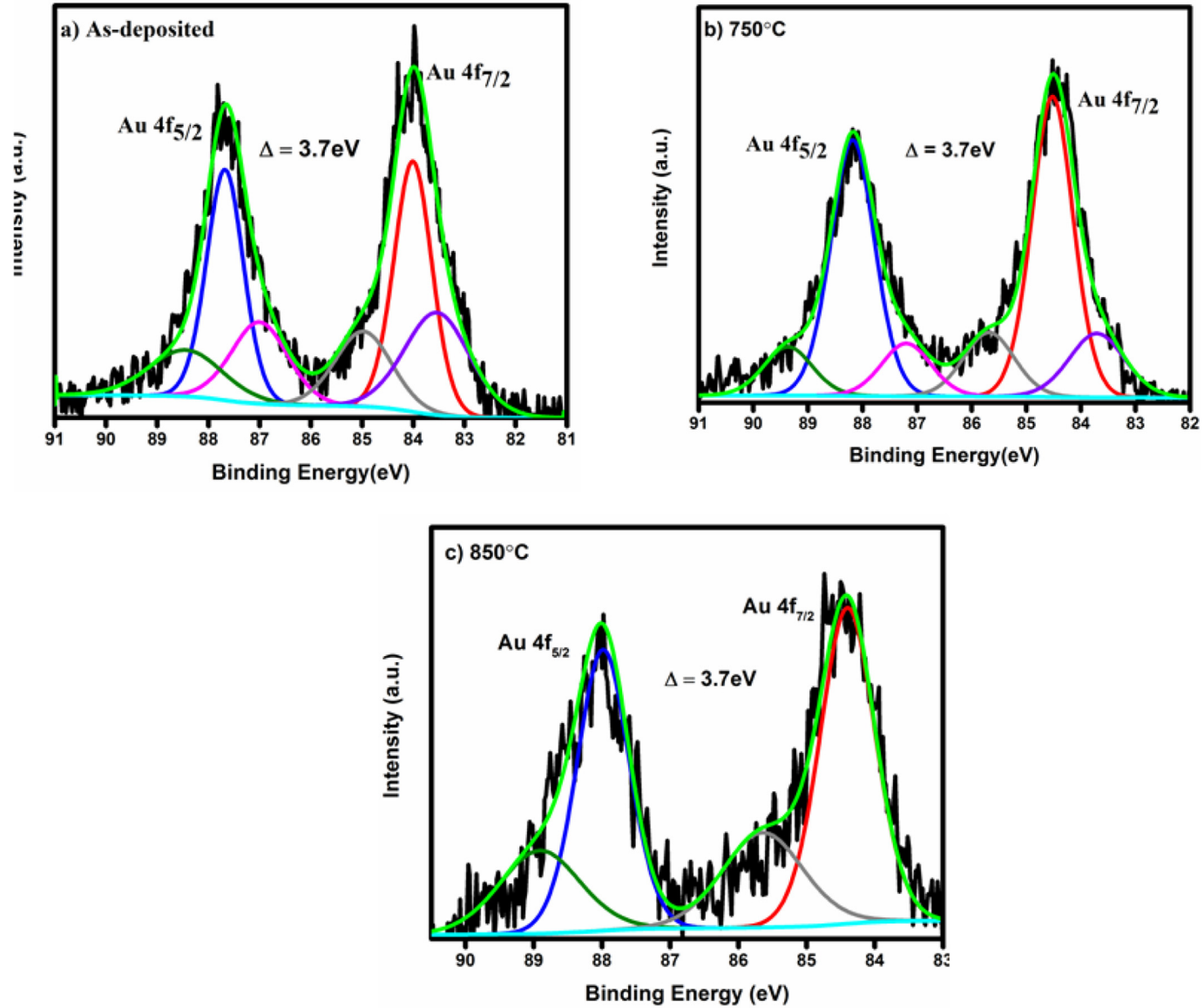


Fig. 6. The core elemental XPS spectra of Au charge trapping layer of NVM structure a) as-deposited and annealed at b) 750 °C and c) 850 °C.

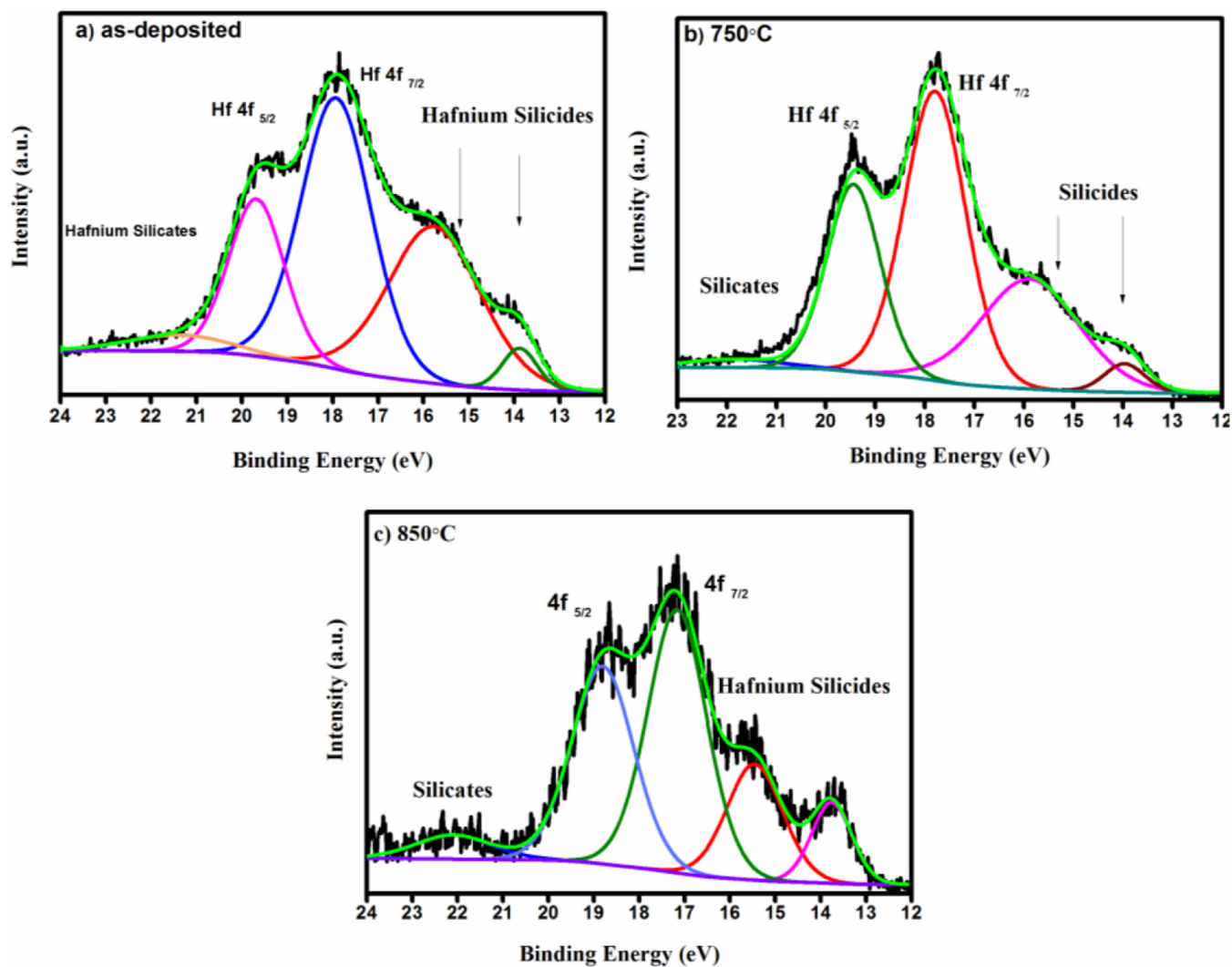


Fig. 7. The core elemental XPS spectra of HfO<sub>2</sub> tunneling layer of NVM structure a) as-deposited and annealed at b) 750 °C and c) 850 °C.



particles has also been estimated by TEM image and found to be  $1 \times 10^{11} / \text{cm}^2$ . The HR-TEM image of Au points to the nanocrystal formation with a lattice spacing  $\sim 2.36 \text{ \AA}$  which corresponds to (111) plane. The polycrystalline diffraction rings indicate the formation of monoclinic  $\text{HfO}_2$  as that of XRD. The presence of Au nanoparticles (white dots in STEM image and red in EDX image) along with Hf and O are also confirmed using STEM-EDX mapping shown in Fig. 3(f–j).

The surface morphology of the blocking layer using AFM for the as-deposited and annealed samples at different temperatures is presented in Fig. 4. The as-deposited sample images show rms roughness of around 0.6 nm indicating that the films are smooth, uniform and high-quality without any deformation, which makes them apt for the possible electronic and optoelectronic applications [27,28].

The AFM images of the as-deposited and annealed films (blocking layer) indicate that the surface roughness increases as the films undergo transition from amorphous to crystalline. This could be due to the temperature assisted growth mechanism exhibited by the films. As the temperature is increased ( $650^\circ\text{C}$ ), the atoms attain activation energy and favours atomic mobility on the film surface resulting in re-orientation. The re-orientation of atoms on the surface due to the aggregation of small crystallites leading to the growth of larger grains might have resulted in an increase in roughness and grain density [29]. Further increase in temperature ( $850^\circ\text{C}$ ) results in the decrease in roughness. This could be attributed to the increase in atomic mobility, at high temperature, resulting in the easy attainment of equilibrium position by the fast-moving atoms [30].

Figs. 5–7 present the XPS spectra obtained from various layers of the nonvolatile memory structure. The peaks of all layers are calibrated from C 1s peak at 284.8eV. The presence of C 1s peak arose due to the adsorbed environmental carbon. The core elemental spectra corresponding to 4f peaks of Hf along with their spin-orbit splitting values were analyzed for the blocking layer (Fig. 5). XPS spectra of the pristine as well as the annealed samples indicate the peaks at 16–19 eV with a spin-orbit splitting values (1.7eV) that confirms the formation of Hf-O bonding in  $\text{HfO}_2$  [31]. In addition, the spectra indicate significant shift in binding energy of  $\text{HfO}_2$  in comparison of samples with and without annealing. The pristine samples reveal the presence of a sub-peak between 15 and 16 eV due to the formation of sub-oxide peak of hafnium [32,33]. An increase in the sub-oxide percentage with thermal annealing is evident from the deconvoluted spectra. Furthermore, the increase in temperature ( $850^\circ\text{C}$ ) results in the out-diffusion of oxygen, which results in an additional peak around 13eV that corresponds to Hf-Hf peak [34].

The XPS spectra obtained for the Au layer is presented in Fig. 6. The obtained results of Au 4f peaks are at 84 and 87.7eV with difference in binding energy 3.7eV. Other than the expected feature peak, emergence of two other peaks such as metallic gold (83 and 86eV) [35,36] and gold oxide (85 and 89eV) is observed [37]. The samples annealed at  $750^\circ\text{C}$  indicate a slight shift in the peak towards higher binding energies at 84.3 and 88eV due to the formation of Au nanocrystals [11]. On the other hand, the peak at 83eV completely disappears at  $850^\circ\text{C}$  indicating an increase in nanoparticles.

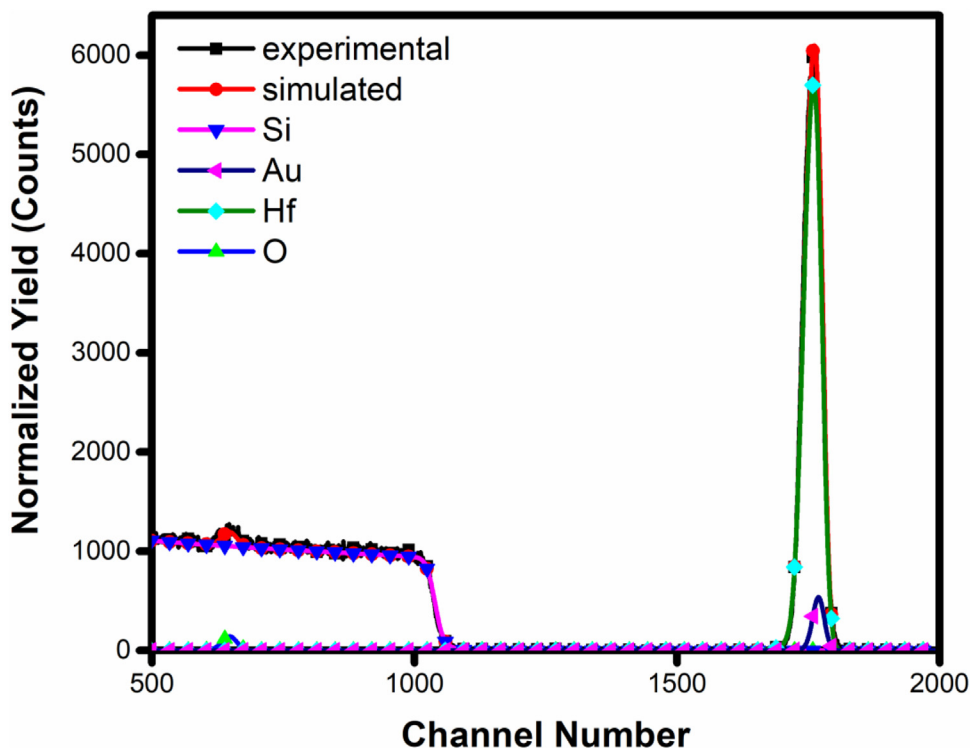


Fig. 8. Rutherford backscattering spectra of NVM structure annealed at  $850^\circ\text{C}$ .

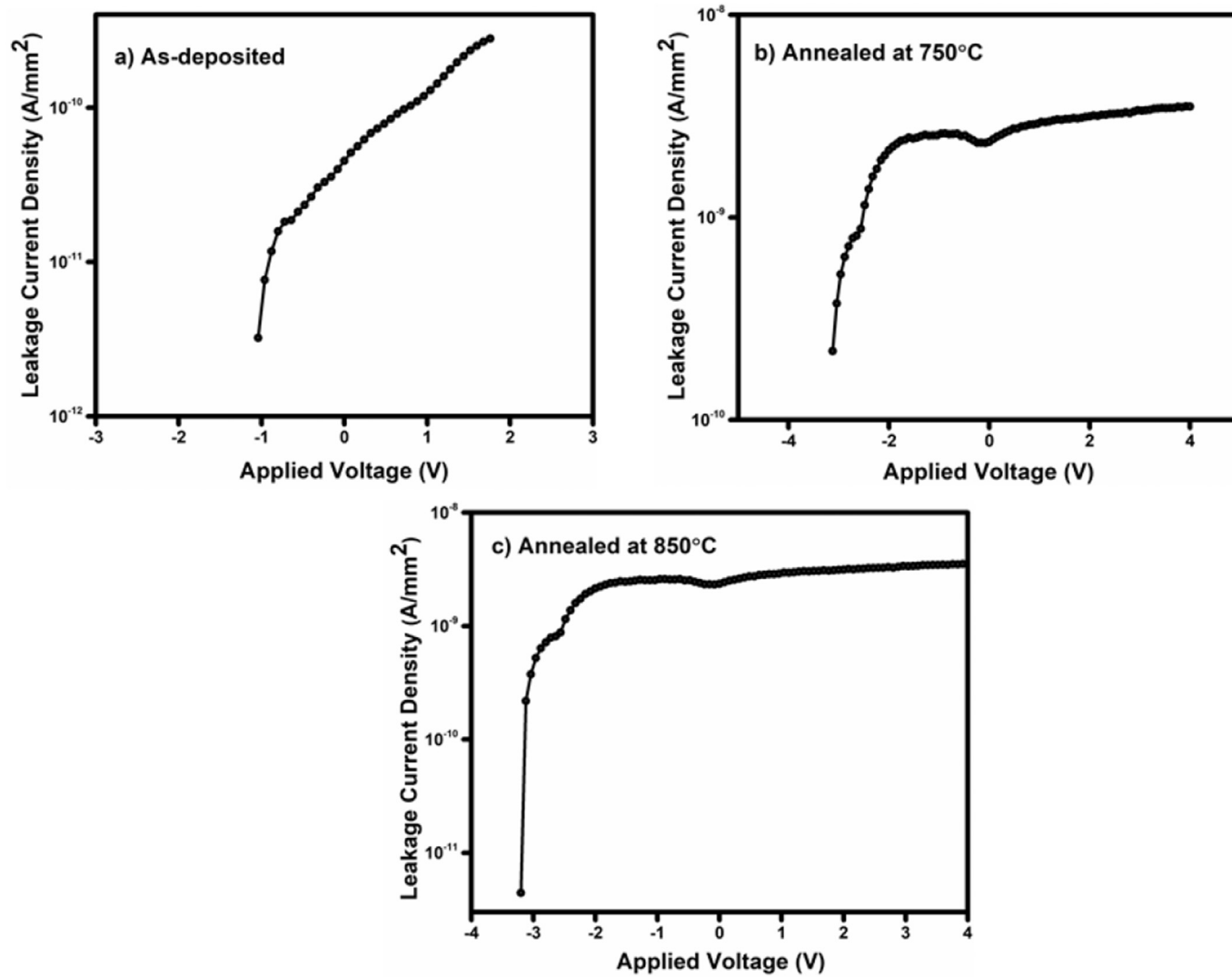


Fig. 9. Leakage current versus applied voltage for as-deposited and annealed NVM structure.

Fig. 7 shows the core elemental spectra of the tunneling layer of the NVM structures. The Hf 4f peak positions in the spectra indicate the possible formation of HfO<sub>2</sub>. The spin-orbital splitting of 4f<sub>5/2</sub> and 4f<sub>7/2</sub> is  $1.7 \pm 0.1$  eV. The as-deposited films show not only the existence of HfO<sub>2</sub> but also silicides, sub-oxides and silicates [32,33,38–41]. High temperature annealing at 750 °C shows the reduction of sub-oxides concentration and shift of silicates to higher binding energy reveals the formation of stronger hafnium silicates bonds. When the temperature is further increased to 850 °C, the deconvoluted images suggest possible occurrence of hafnium silicide doublets and it is evident from the spectra that stronger hafnium silicate have been formed due to the shoulder peak around 22eV. Higher binding energy shift of silicates indicates the formation of passivated traps. This passivated trap may result in improved leakage property of the device [42].

The RBS spectrum of sample annealed at 850 °C presented in Fig. 8 clearly shows the presence of Hf, O and Au. The thickness and atomic concentration of the elements have been estimated. The diffusion of the HfO<sub>2</sub> layers has been observed after thermal annealing in the spectrum. The possibility of inter-diffusion and silicate formation of tunneling layer is also evident from the spectrum and is calculated using RUMP. The total thickness of the trilayer structure is estimated and found to be ~37 nm (considering the bulk densities).

To understand the electrical behaviour of the device, current density-voltage (J-V) measurements have been carried out and the characteristics are shown in Fig. 9. The low leakage value of the as-deposited structure indicates the excellent insulating behaviour of HfO<sub>2</sub> layer. The J-V characteristics show that at 750 °C annealing the leakage properties of the device decrease as compared to the pristine ones. The increase in leakage current is due to the crystallization and grain growth of the HfO<sub>2</sub> thin films with annealing as indicated by XRD and AFM [43,44]. Moreover, the interface states and defects might have also increased the leakage current density at high temperature annealing (here 750 °C) [45,46]. Further annealing at 850 °C results in decrease in the leakage current as compared to 750 °C. This could be due to the significant role played by the increased Au nanocrystal formation as suggested by the XPS spectra. Either the injection and storage of carriers into the Au nanocrystals is prevented by the Coulomb blockade effect or it could be due to the external electric field compensating the internal electric field in the nanocrystals by the charge stored [47].

The high frequency (1 MHz) Capacitance –Voltage curve after bidirectional sweeps for different voltages for sample annealed at 850 °C is shown in Fig. 10. The C-V curve implies the hole trapping as well as electron trapping effects in the nonvolatile memory device. When the negative bias voltage is applied, the hole tunneling happens through the tunneling layers from the substrate whereas with the forward bias voltage electron tunneling occurs. This, in turn, creates deep inversion and accumulation regions. The similar clockwise and anticlockwise hysteresis characteristics with large memory window indicate the charge storage behaviour arising due to the Au nanocrystals [47,48]. The C-V curve of the reference sample (HfO<sub>2</sub> only) without Au nanocrystals exhibit negligible hysteresis as compared to the sample with Au nanocrystals

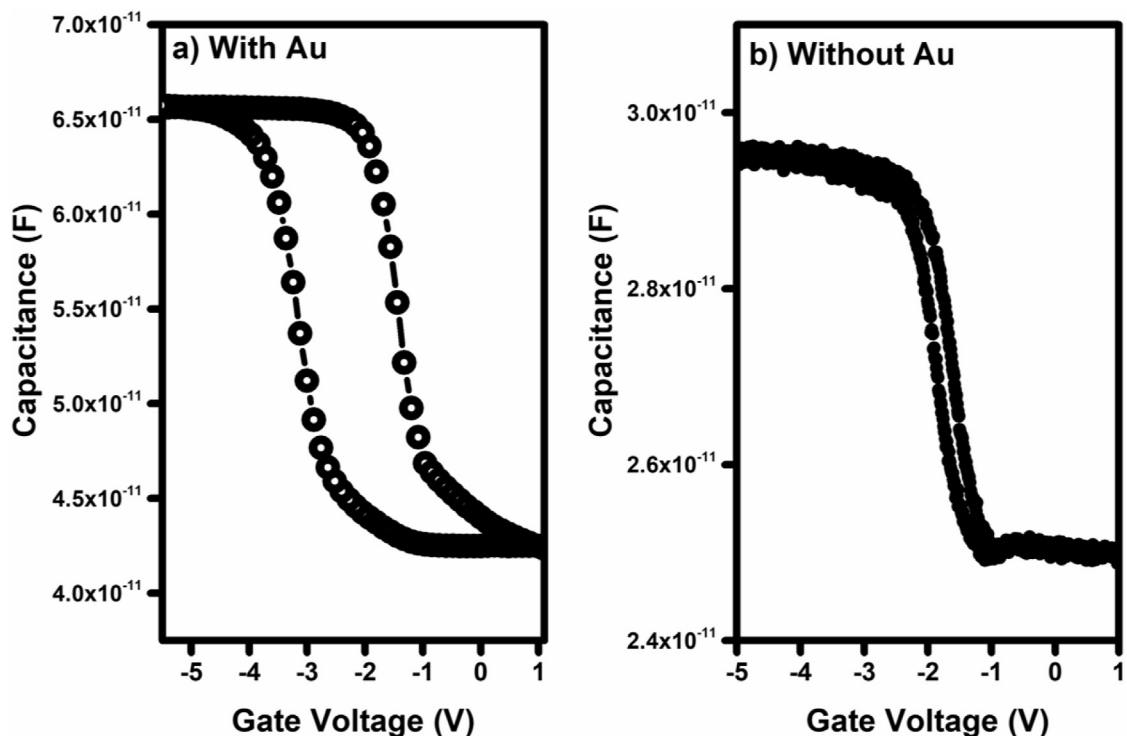


Fig. 10. The capacitance-voltage curve of a) trilayer capacitor with Au nanocrystals and b) reference sample (HfO<sub>2</sub> only) without Au nanocrystals annealed at 850 °C.

annealed at 850 °C. Thus, hysteresis loop confirms the significant role of Au nanocrystals in charge storage behaviour of the device structure with charge trapped density estimated as  $2.6 \times 10^{12}/\text{cm}^2$ .

#### 4. Conclusions

In summary, Au nanocrystal based hafnium oxide stack layer for nonvolatile memory device was fabricated. The XRD results show preferred orientation growth of the hafnium oxide films. TEM image indicates the formation of Au nanocrystals with average areal density of  $1 \times 10^{11}/\text{cm}^2$ . The deconvoluted spectra of XPS indicate the formation of hafnium oxide with sub-oxides, silicides and silicate. XPS of Au layer suggests the formation of Au nanocrystals. The thickness of trilayer structure has been estimated using RBS. The I-V measurements indicate that annealing results in a variation of the leakage properties. C-V curve confirms the significant role of Au nanocrystals in charge storage characteristics and it shows the charge accumulation as well as inversion properties. The results of XPS, I-V and C-V indicate that device characteristic performance is improved at higher annealing temperature. This study demonstrates the structural, morphological and electrical properties of  $\text{HfO}_2/\text{Au}/\text{HfO}_2$  stack layer and the role of Au nanocrystals in the charge storage behavior of nonvolatile memory device structures.

#### Acknowledgments

This work was supported by DST-SERB, New Delhi (Project No: SR/FTP/PS-101/2013) and authors acknowledge MNCf, IISc, Bangalore and MRC, MNIT Jaipur for providing necessary characterization facilities. The authors would like to acknowledge Mr. Sunil Ojha, IUAC New Delhi for his help in RBS characterization and discussions.

#### References

- [1] V. Mikhelashvili, B. Meyler, S. Yoffis, J. Salzman, M. Garbrecht, T. Cohen-Hyams, W.D. Kaplan, G. Eisenstein, A nonvolatile memory capacitor based on Au nanocrystals with  $\text{HfO}_2$  tunneling and blocking layers, *Appl. Phys. Lett.* 95 (2009), 023104.
- [2] Xuan Feng, Shurong Dong, Hei Wong, Danqun Yu, K.L. Pey, K. Shubhakar, W.S. Lau, Effects of thermal annealing on the charge localization characteristics of  $\text{HfO}_2/\text{Au}/\text{HfO}_2$  stack, *Microelectron. Reliab.* 61 (2016) 78–81.
- [3] Jang Sik Lee, Review Paper: nano-floating gate memory devices, *Electronic Mater. Lett.* 7 (2011) 175–183.
- [4] Madhuchhanda Nath, Asim Roy, Interface and electrical properties of ultra-thin  $\text{HfO}_2$  film grown by radio frequency sputtering, *Physica B* 482 (2016) 43–50.
- [5] Qin Wang, Rui Jia, Weihua Guan, Weilong Li, Qi Liu, Yuan Hu, Shibing Long, Baoqin Chen, Ming Liu, Tianchun Ye, Wensheng Lu, Long Jiang, Comparison of discrete-storage nonvolatile memories: advantage of hybrid method for fabrication of Au nanocrystal nonvolatile memory, *J. Phys. D Appl. Phys.* 41 (2008), 035109.
- [6] S.A. Ng, K.A. Razak, K.Y. Cheong, K.C. Aw, Memory properties of Au nanoparticles prepared by tuning  $\text{HAuCl}_4$  concentration using low-temperature hydrothermal reaction, *Thin Solid Films* 615 (2016) 84–90.
- [7] Chen Chan Wang, Yan Kai Chiou, Che Hao Chang, Jiun Yi Tseng, Lin Jung Wu, Chun Yu Chen, Tai Bor Wu, Memory characteristics of Au nanocrystals embedded in metal-oxide-semiconductor structure by using atomic-layer-deposited  $\text{Al}_2\text{O}_3$  as control oxide, *J. Phys. D Appl. Phys.* 40 (2007) 1673–1677.
- [8] Wei Lin Leong, Pooi See Lee, Anup Lohani, Yeng Ming Lam, Tupei Chen, Sam Zhang, Ananth Dodabalapur, Subodh G. Mhaisalkar, Non-volatile organic memory applications enabled by in situ synthesis of gold nanoparticles in a self-assembled block copolymer, *Adv. Mater.* 20 (2008) 2325–2331.
- [9] Yun Shan Lo, Ke Chih Liu, Jyun Yi Wu, Cheng Hao Hou, Tai Bor Wu, Bandgap engineering of tunnel oxide with multi-stacked layers of  $\text{Al}_2\text{O}_3/\text{HfO}_2/\text{SiO}_2$  for Au-nanocrystal memory application, *Appl. Phys. Lett.* 93 (2008), 132907.
- [10] Yongli Che, Yating Zhang, Xiaolong Cao, Xiaoxian Song, Mingxuan Cao, Haitao Dai, Junbo Yang, Guizhong Zhang, Jianquan Yao, Ambipolar nonvolatile memory based on a quantum-dot transistor with a nanoscale floating gate, *Appl. Phys. Lett.* 109 (2016), 013106.
- [11] Raju Kumar Gupta, Damar Yoga Kusuma, P.S. Lee, M.P. Srinivasan, Covalent assembly of gold nanoparticles for nonvolatile memory applications, *ACS Appl. Mater. Interfaces* 3 (2011) 4619–4625.
- [12] S. Horikoshi, N. Matsumoto, Y. Omata, T. Kato, Growth of Au nanoparticle films and the effect of nanoparticle shape on plasmon peak wavelength, *J. Appl. Phys.* 115 (2014), 193506.
- [13] Y.K. Mishra, S. Mohapatra, R. Singhal, D.K. Avasthi, D.C. Agarwal, D.C. Agarwal, Au–ZnO: a tunable localized surface plasmonic nanocomposite, *Appl. Phys. Lett.* 92 (2008) 043107.
- [14] Florian Schulz, Torge Homolka, Neus G. Bastús, Víctor F. Puntes, Horst Weller, and Tobias Vossmeier, little adjustments significantly improve the turkevich synthesis of gold nanoparticles, *Langmuir* 30 (2014) 10779–10784.
- [15] Anna Kossov, Virginia Merk, Denis Simakov, Kristjan Leosson, Stephane Kena Cohen, Stefan A. Maier, Optical and structural properties of ultra-thin gold films, *Adv. Optical. Mater.* 3 (2015) 71–77.
- [16] Ting-Chang Chang, Fu-Yen Jian, Shih-Cheng Chen, Yu-Ting Tsai, Developments in nanocrystal memory, *Mater. Today* 14 (2011) 608–615.
- [17] Y.K. Mishra, V.S.K. Chakravadhanula, V. Hrkac, S. Jebirli, D.C. Agarwal, S. Mohapatra, D.K. Avasthi, L. Kienle, R. Adelun, Crystal growth behaviour in Au-ZnO nanocomposite under different annealing environments and photoswitchability, *J. Appl. Phys.* 112 (2012), 064308.
- [18] Venkata Sai Kiran Chakravadhanula, Yogendra Kumar Mishra, Venkata Girish Kotnur, Devesh Kumar Avasthi, Thomas Strunskus, Vladimir Zaporotchenko, Dietmar Fink, Lorenz Kienle, Franz Faupel, Microstructural and plasmonic modifications in Ag– $\text{TiO}_2$  and Au– $\text{TiO}_2$  nanocomposites through ion beam irradiation, *Beilstein J. Nanotechnol.* 5 (2014) 1419–1431.
- [19] Sk Moidul Haque, Pankaj R. Sagdeo, Shanmugam Balaji, Kalavathi Sridhar, Sanjiv Kumar, Debarati Bhattacharyya, Dibyendu Bhattacharyya, Naba K. Sahoo, Effect of substrate bias and oxygen partial pressure on properties of RF magnetron sputtered  $\text{HfO}_2$  thin films, *J. Vac. Sci. Technol., B* 32 (2014), 03D104.
- [20] In Soo Kim, Eun-Kyung Jeong, Do Yun Kim, Manoj Kumar, Se-Young Choi, Investigation of p-type behavior in Ag-doped ZnO thin films by E-beam evaporation, *Appl. Surf. Sci.* 255 (2009) 4011–4014.
- [21] Werner Kern, The evolution of silicon wafer cleaning technology, *J. Electrochem. Soc.* 137 (1990) 1887–1892.
- [22] Seok Woo Nam, Jung-Ho Yoo, Suheun Nam, Hyo-jick Choi, Dongwon Lee, Dae-Hong Ko, Joo Ho Moon, Ja Hum Ku, Siyoung Choi, Influence of annealing condition on the properties of sputtered hafnium oxide, *J. Non-Cryst. Solids* 303 (2002) 139–143.
- [23] L.R. Doolittle, Algorithms for the rapid simulation of rutherford backscattering spectra, *Nucl. Instrum. Methods Phys. Res., Sect. B* 9 (1985) 344–351.
- [24] Atif Mossad Ali, Adel A. Ismail, Rasha Najmy, Ali Al Hajry, Annealing effects on zinc oxide-silica films prepared by sol-gel technique for chemical sensing applications, *Thin Solid Films* 558 (2014) 378–384.
- [25] A. van der Drift, Evolutionary selection, a principle governing growth orientation in vapour-deposited layers, *Philips Res. Rep.* 22 (1967) 267–288.

- [26] Lin Cui, Gui Gen Wang, Hua Yu Zhang, Rui Sun, Xu Ping Kuang, Jie Cai Han, Effect of film thickness and annealing temperature on the structural and optical properties of ZnO thin films deposited on sapphire (0001) substrates by sol–gel. *Ceram. Int.* 39 (2013) 3261–3268.
- [27] Samuel P. Morgan Jr., Effect of surface roughness on eddy current losses at microwave frequencies, *J. Appl. Phys.* 20 (1949) 352–362.
- [28] Hyong Seo Yoon, Byeongho Park, Seong Chan Jun, Surface roughness effects on the frequency tuning performance of a nanoelectromechanical resonator, *Nanoscale Res. Lett.* 8 (2013) 270.
- [29] Arun Vinod, Mahendra Singh Rathore, T. Santhosh Kumar, D. Pamu, A.P. Pathak, N. Srinivasa Rao, Ion beam induced modification of structural and optical properties of MgTiO<sub>3</sub> nanocrystalline thin films, *Radiat. Eff. Defect Solid* 172 (2017) 81–89.
- [30] Mahendra Singh Rathore, Arun Vinod, Rambabu Angalakurthi, A.P. Pathak, Fouran Singh, Santhosh Kumar Thatikonda, Srinivasa Rao Nelamarri, Ion beam modification of structural and optical properties of GeO<sub>2</sub> thin films deposited at various substrate temperatures using pulsed laser deposition, *Appl. Phys. A* 123 (2017) 708.
- [31] Nian Zhan, M.C. Poon, C.W. Kok, K.L. Ng, Hei Wong, XPS study of the thermal instability of HfO<sub>2</sub> prepared by Hf sputtering in oxygen with RTA, *J. Electrochem. Soc.* 150 (2003) F200–F202.
- [32] O.M. Orlov, G. Ya Krasnikov, V.A. Gritsenko, V.N. Kruchinin, T.V. Perevalov, V. Sh Aliev, D.R. Islamov, I.P. Prosvirin, Nanoscale potential fluctuation in non-stoichiometric hafnium suboxides, *ECS Trans.* 69 (2015) 237–241.
- [33] A.R. Chourasia, J.L. Hickman, R.L. Miller, G.A. Nixon, M.A. Seabolt, X-ray photoemission study of the oxidation of hafnium, *Int. J. Spectrosc.* 2009 (2009) 1–6.
- [34] R. Tang, K. Huang, H. Lai, C. Li, Z. Wu, J. Kang, Charge storage characteristics of Au nanocrystal memory improved by the oxygen vacancy-reduced HfO<sub>2</sub> blocking layer, *Nanoscale Res. Lett.* 8 (2013) 368.
- [35] Lei Zhang, Rajendra Persaud, Theodore E. Madey, Ultrathin metal films on a metal oxide surface: growth of Au on TiO<sub>2</sub> (110), *Phys. Rev. B Condens. Matter* 56 (1997) 549–557.
- [36] Jia-ying Xin, Dan-dan Cheng, Lan-xuan Zhang, Kai Lin, Hong-chen Fan, Yan Wang, Chun-gu Xia, Methanobactin-mediated one-step, synthesis of gold nanoparticles, *Int. J. Mol. Sci.* 14 (2012) 21676–21688.
- [37] Sarthak Gaur, Jeffrey T. Miller, Daniel Stellwagen, Ashwin Sanampudi, Challa S.S.R. Kumard, James J. Spivey, Synthesis, characterization, and testing of supported Au catalysts prepared from atomically-tailored Au<sub>38</sub>(SC<sub>12</sub>H<sub>25</sub>)<sub>24</sub> clusters, *Phys. Chem. Chem. Phys.* 14 (2012) 1627–1634.
- [38] Yoshihide Senzaki, Seung Park, Hood Chatham, Lawrence Bartholomew, Wesley Nieveen, Atomic layer deposition of hafnium oxide and hafnium silicate thin films using liquid precursors and ozone, *J. Vac. Sci. Technol., A* 22 (2004) 1175–1181.
- [39] G.D. Wilk, R.M. Wallace, J.M. Anthony, Hafnium and zirconium silicates for advanced gate dielectrics, *J. Appl. Phys.* 87 (2000) 484–492.
- [40] S.J. Wang, P.C. Lim, A.C.H. Huan, C.L. Liu, J.W. Chai, S.Y. Chow, J.S. Pan, Q. Li, C.K. Ong, Reaction of SiO<sub>2</sub> with hafnium oxide in low oxygen pressure, *Appl. Phys. Lett.* 82 (2003) 2047–2049.
- [41] T.P. Smirnova, L.V. Yakovkina, V.N. Kitchai, V.V. Kaichev, Yu.V. Shubin, N.B. Morozova, K.V. Zherikova, Chemical vapor deposition and characterization of hafnium oxide film, *J. Phys. Chem. Solid.* 69 (2008) 685–687.
- [42] You Pin Gong, Ai-Dong Li, Xu Qian, Chao Zhao, Di Wu, Interfacial structure and electrical properties of ultrathin HfO<sub>2</sub> dielectric films on Si substrates by surface sol–gel method, *J. Phys. D Appl. Phys.* 42 (2009), 015405.
- [43] Peng Jin, Gang He, Dongqi Xiao, Juan Gao, Mao Liu, Jianguo Lv, Yanmei Liu, Miao Zhang, Peihong Wang, Zhaoqi Sun, Microstructure, optical, electrical properties, and leakage current transport mechanism of sol–gel-processed high-k HfO<sub>2</sub> gate dielectrics, *Ceram. Int.* 42 (2016) 6761–6769.
- [44] Rui Ma, Mao Liu, Gang He, Ming Fang, Guoliang Shang, Jiweng Zhang, Xuefei Chen, Juan Gao, Guangtao Fei, Lide Zhang, Effects of rapid thermal annealing on interfacial and electrical properties of Gd-doped HfO<sub>2</sub> high-k gate dielectrics, *J. Alloy. Comp.* 646 (2015) 310–314.
- [45] J.W. Zhang, G. He, H.S. Chen, J. Gao, X.F. Chen, P. Jin, D.Q. Xiao, R. Ma, M. Liu, Z.Q. Sun, Modulation of charge trapping and current-conduction mechanism of TiO<sub>2</sub>-doped HfO<sub>2</sub> gate dielectrics based MOS capacitors by annealing temperature, *J. Alloy. Comp.* 647 (2015) 1054–1060.
- [46] Chen Chan Wang, Yan Kai Chiu, Che Hao Chang, Jiun Yi Tseng, Lin Jung Wu, Chun Yu Chen, Tai Bor Wu, Memory characteristics of Au nanocrystals embedded in metal–oxide–semiconductor structure by using atomic-layer-deposited Al<sub>2</sub>O<sub>3</sub> as control oxide, *J. Phys. D Appl. Phys.* 40 (2007) 1673–1677.
- [47] Debashis Panda, Achintya Dhar, Samit K. Ray, Improved charge storage characteristics of the tetralayer non-volatile memory structure using nickel nanocrystal trapping layer, *Semicond. Sci. Technol.* 24 (2009), 115020.
- [48] V. Mikhelashvili, B. Meyler, S. Yofis, Y. Shneider, A. Zeidler, M. Garbrecht, T. Cohen-Hyams, W.D. Kaplan, M. Lisiansky, Y. Roizin, J. Salzman, G. Eisenstein, Nonvolatile low-voltage memory transistor based on SiO<sub>2</sub> tunneling and HfO<sub>2</sub> blocking layers with charge storage in Au nanocrystals, *Appl. Phys. Lett.* 98 (2011), 212902.



# Effects of annealing on quality and stoichiometry of HfO<sub>2</sub> thin films grown by RF magnetron sputtering



Arun Vinod, Mahendra Singh Rathore, N. Srinivasa Rao\*

Department of Physics, Malaviya National Institute of Technology Jaipur, J L N Marg, Jaipur, 302017, India

## ARTICLE INFO

### Keywords:

HfO<sub>2</sub> films  
Annealing  
XPS  
Leakage current  
Skewness  
Kurtosis

## ABSTRACT

In this paper, the effects of annealing temperature on HfO<sub>2</sub> thin films prepared by RF sputtering have been investigated. Thin films of hafnium oxide were deposited using sputtering onto p-type Si substrates and the pristine films were annealed at different temperatures in air atmosphere to obtain crystallinity. The Raman and XRD results of the as-deposited films show amorphous nature, whereas the annealed films at 600 °C results in crystallization. AFM was used to study the surface morphology of the films and to estimate the skewness, kurtosis and the roughness values. The core level orbitals of Hf 4f spectra of as-deposited films not only reveal the formation of hafnium rich hafnium oxide but also nearly stoichiometric composition of HfO<sub>2</sub> and exhibit a shift in binding energy with annealing. Electrical measurements of the films suggest that the leakage current is increased for crystalline films as compared to the as-deposited ones. The effects of annealing temperature on quality and stoichiometry of hafnia thin films and their possible applications are reported.

## 1. Introduction

In recent years, the demand for low cost, faster and reliable electronic devices with high efficiency has attracted considerable attention. For decades, the silicon industry relied on SiO<sub>2</sub> gate dielectric until the scaling down of the dielectric has reached both technological and theoretical limits [1,2]. Further shrinkage of SiO<sub>2</sub> gate dielectric thickness restrained due to permittivity and electron tunneling effect [3]. Due to the aforementioned difficulties, an alternative replacement for SiO<sub>2</sub> gate material has gained great interest. Among various dielectric materials such as Al<sub>2</sub>O<sub>3</sub>, ZrO<sub>2</sub>, La<sub>2</sub>O<sub>3</sub>, SrO, Y<sub>2</sub>O<sub>3</sub> and HfO<sub>2</sub>, hafnium oxide has received significant focus due to its thermodynamical stability, reasonable energy gap, excellent electrical properties and high dielectric constant [4]. Moreover, the unique combination of structural, optical and electrical properties of HfO<sub>2</sub> films is used for various electronics and optoelectronics applications.

In optoelectronic applications, hafnium oxide thin films are very useful for anti-reflection coating in optical waveguide devices to reduce the Fresnel loss [5]. HfO<sub>2</sub> thin films are also being used as protective coating for electrical applications due to the hydrophobic effectiveness for outdoor insulators [6]. Moreover, in the electrical application, the presence of large conduction band offset in HfO<sub>2</sub> helps to attain lower operational voltage and makes it suitable for low leakage current application. The electrical properties such as capacitance and leakage current density of HfO<sub>2</sub> thin films drastically change with annealing

[7]. For industrial application, low temperature annealing is required in the production process and HfO<sub>2</sub> thin films undergo phase transition from amorphous to crystalline even at low temperatures [8]. The formation of grain boundary due to crystallization, increases the leakage current and degrades the device performance [9]. Thus, the growth of high purity, quality and stoichiometry thin films and modulation of their properties under various conditions are of great interest for solid-state devices and communication. This attracts huge demand for the growth and optimization of high-quality HfO<sub>2</sub> thin films.

There are various physical and chemical methods employed to grow HfO<sub>2</sub> thin films such as electron beam evaporation, reactive dc sputtering, RF magnetron sputtering, metal-organic molecular beam epitaxy and atomic layer deposition [10–15]. RF magnetron sputtering has various advantages like less wastage of the material, high adhesion of films and excellent uniformity with good packing density as compared to other methods. Recently, Das et al. had reported the utmost importance of high-quality HfO<sub>2</sub> thin films and its incorporation into a low dimensional semiconductor technology [16]. Nam et al. and He et al. reports the formation of stoichiometric HfO<sub>2</sub> thin films at high temperature annealing [17,18]. The variation in electrical and structural properties of HfO<sub>2</sub> based MOS capacitance with low surface roughness was studied by Khairnar and Mahajan [10]. This study shows that there is an utmost need to correlate stoichiometry, surface roughness and crystallinity for better electrical application. Our work aims at the systematic and detailed study of the growth and optimization of RF

\* Corresponding author.

E-mail address: [snelamarri.phy@mnit.ac.in](mailto:snelamarri.phy@mnit.ac.in) (N. Srinivasa Rao).



magnetron sputtered  $\text{HfO}_2$  thin films and the correlation of the effects of annealing temperature (200, 400 and 600 °C) in air atmosphere on the stoichiometry, surface roughness and crystallinity of  $\text{HfO}_2$  thin films for various applications from a basic and applied scientific perspective.

## 2. Experimental details

Hafnium oxide thin films were deposited by RF magnetron sputtering method onto a p-type silicon (100) substrates with resistivity of 1–10  $\Omega\text{cm}$ . The substrates were thoroughly cleaned by standard Radio Corporation of America (RCA) I and II process before deposition. For sputtering,  $\text{HfO}_2$  target purchased from ACI Alloys, USA of purity 99.999% (5N) was used. The target was placed in a 2-inch holder, at a distance 10 cm from the substrates. Initially, the chamber was evacuated to a high vacuum pressure of  $6 \times 10^{-6}$  mbar using a rotary assisted turbo pump. The working pressure was maintained at  $3 \times 10^{-3}$  mbar by introducing high purity Ar gas (99.99%) into the chamber using mass flow controller. The Ar flow rate and RF power were kept constant (20 sccm and 100 W) during deposition. Prior to deposition, the target was pre-sputtered for 10 min to remove surface contamination, if any, present. The substrate holder was rotated at low rpm to get uniform films, and the thickness of the film was around 25 nm as measured by a digital thickness monitor (DTM). After the deposition, annealing of the samples was carried out using a muffle furnace in air at different temperatures viz. 200 °C, 400 °C and 600 °C for 30 min with a ramp rate of 10 °C/min.

Raman spectra of the films were obtained using confocal micro-Raman spectrometer, which incorporates a solid-state laser of 532 nm. The crystal structure and the orientation of the films have been investigated using PANalytical X'pert Powder X-ray diffractometer with  $\text{Cu K}\alpha$  radiation (1.5406 Å). The surface morphology of the films was studied using Bruker atomic force microscopy and the roughness, skewness and kurtosis values were estimated using NanoScope Analysis software. The chemical states and composition of films were examined using X-ray photoelectron spectroscopy (XPS) with a monochromatic  $\text{Al K}\alpha$  ( $h\nu = 1486.6\text{eV}$ ) X-ray radiation under a base pressure of  $6 \times 10^{-10}$  mbar using an Omicron Nanotechnology (ESCA+) from Oxford Instruments. For electrical measurements, Al contacts with diameter  $\sim 1$  mm and thickness around 250 nm were deposited using electron beam evaporation. The electrical measurements were carried out using B1500A Semiconductor Device Analyzer with frequency 1 MHz at room temperature.

## 3. Results and discussion

The Raman spectra of  $\text{HfO}_2$  thin films in the range of 120–600  $\text{cm}^{-1}$  are depicted in Fig. 1. The broad peak around 150  $\text{cm}^{-1}$  for the films annealed at 200 °C indicates the amorphous nature of the hafnia films. The peaks around 302 and 520  $\text{cm}^{-1}$  correspond to acoustic and optical phonon modes the Si substrates [19,20]. For samples annealed at 600 °C, the origin of a new peak at 147  $\text{cm}^{-1}$  is observed, which is attributed to the  $A_g$  mode in  $\text{HfO}_2$  monoclinic structure. It is evident from the spectra that crystallinity increases with an increase in annealing temperature and there is a phase transformation from amorphous to crystalline structure at high temperature. Theoretical analysis predicts that for monoclinic structures, there are 36 phonon modes present, out of which 18 ( $9A_g + 9B_g$ ) are Raman active modes, 15 are IR active modes and other three are zero-frequency translation modes [21]. In addition, the modes of  $\text{HfO}_2$  have been studied by Zhou et al. [22] using density functional perturbation theory. The results obtained are in good agreement with the reported phonon modes of monoclinic structures [21–25]. The bands occurred at 130–300  $\text{cm}^{-1}$  are mainly due to Hf-Hf vibrations [25].

XRD patterns of the pristine and annealed films are shown in Fig. 2. The XRD spectra of the as-deposited and films annealed upto 400 °C reveal amorphous nature. A phase transition from amorphous to

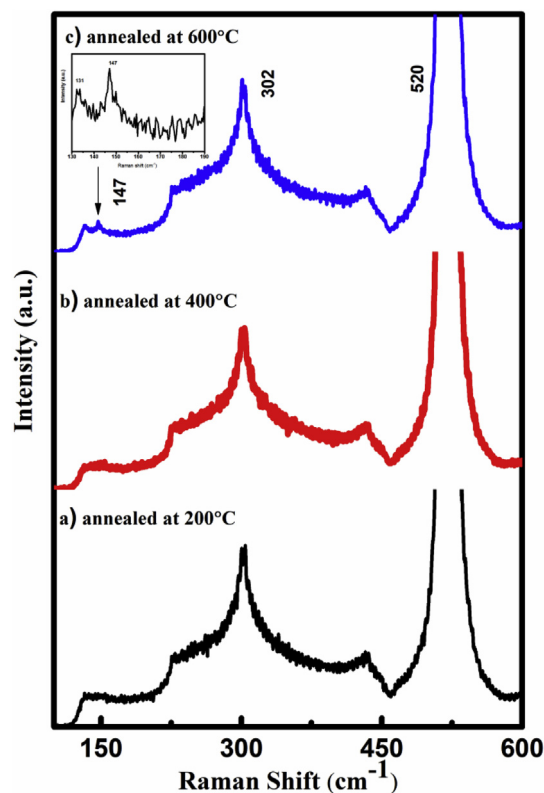


Fig. 1. Raman spectra of  $\text{HfO}_2$  thin films annealed at a) 200 °C b) 400 °C c) 600 °C.

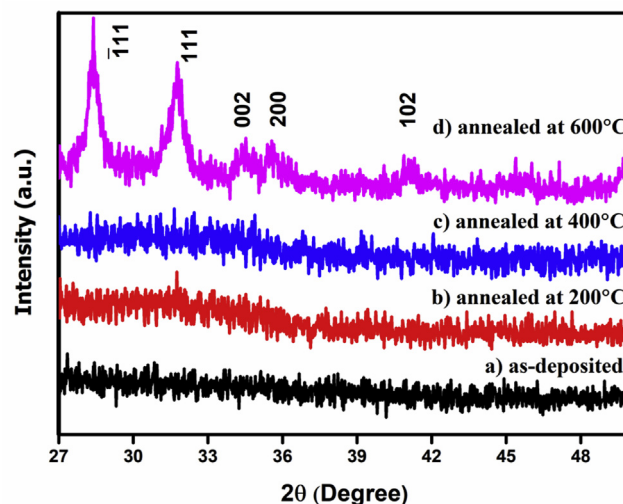


Fig. 2. X-ray diffraction pattern of as-deposited and annealed  $\text{HfO}_2$  thin films.

crystalline observed for films annealed at 600 °C. The phase transition could be due to the attainment of required activation energy in the form of temperature for rearrangement of atoms leading to crystallization of films [26]. The films annealed at 600 °C exhibit monoclinic phase of  $\text{HfO}_2$  with polycrystalline nature as evident from ( $\bar{1}11$ ), (111), (002), (200) and (102) planes [27]. The crystallite size is calculated using Scherrer formula [28] and it is found to be around 17 nm.

The surface morphology of the as-deposited and annealed films is presented in Fig. 3. AFM images show rms roughness of pristine and annealed films up to 400 °C is around 0.20 nm. The images indicate that films are smooth, uniform and high-quality without any cracks, which make them suitable for the possible optoelectronic application. Further,

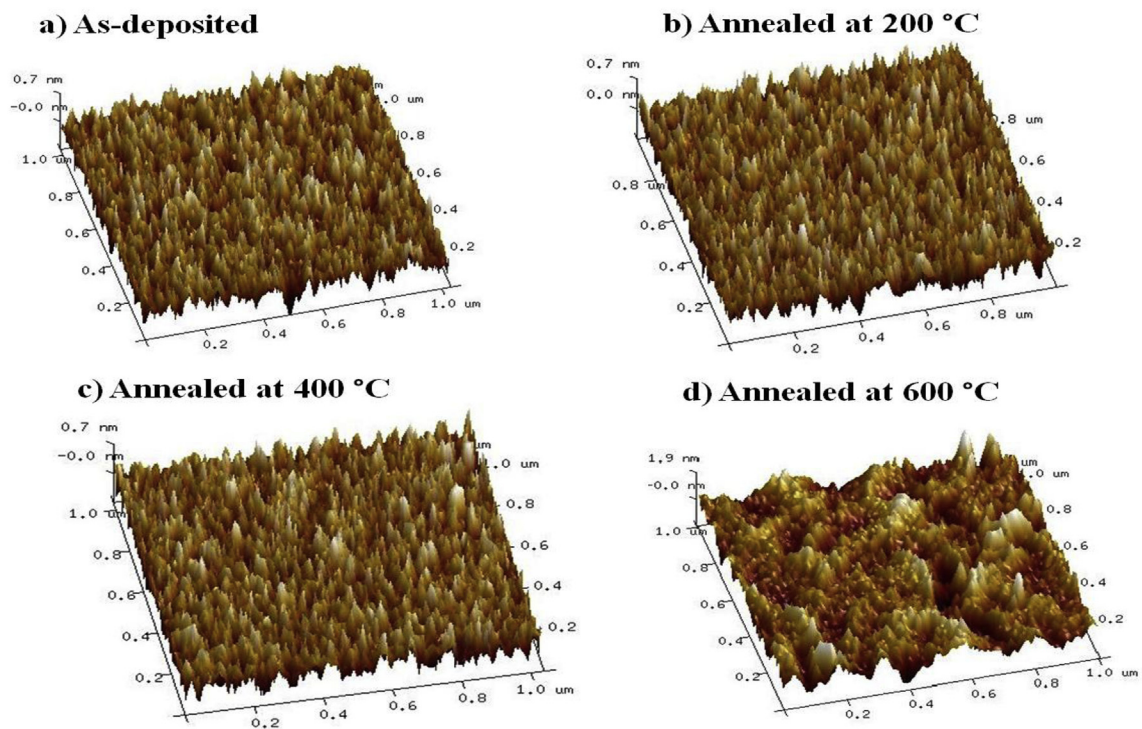


Fig. 3. The surface morphology of as-deposited and annealed HfO<sub>2</sub> thin films.

it is observed that the surface roughness increased for the films annealed at 600 °C. The increase in roughness could be due to the agglomeration of smaller grains to form bigger grains.

To understand more about the surface symmetry distribution and spike of statistical distribution, two parameters such as skewness and kurtosis of the thin films were studied. The skewness and kurtosis refer to the third and fourth moments of roughness distribution function and both parameters are dimensionless quantities.

The value of skewness  $S$  is obtained by the relation [29,30]:

$$S = \frac{1}{R_q^3 N} \sum_{j=1}^N Z_j^3 \quad (1)$$

where  $Z_j$  is height distribution and  $R_q$  is the root mean square roughness,  $R_q$  is calculated using

$$R_q = \left[ \frac{1}{N} \sum_{i=1}^N |Z_i - \bar{Z}|^2 \right]^{1/2} \quad (2)$$

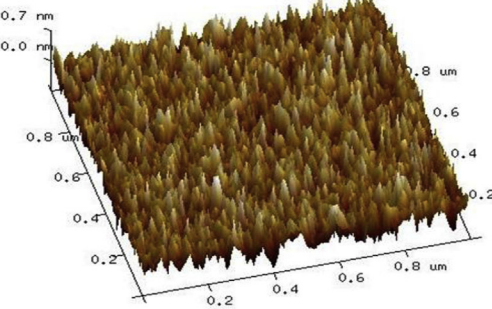
where  $N$  represents the number of surface height data, and  $\bar{Z}$  represents the mean height distance.

The value of kurtosis  $K$  is obtained by the relation [29,30]:

$$K = \frac{1}{R_q^4 N} \sum_{j=1}^N Z_j^4 \quad (3)$$

For a Gaussian distribution, the local maxima at a certain height under and over the mean line will be equal to the local minima, the kurtosis and skewness values are 3 and 0. A negative skewness represents that the film surface is with enormous local maxima whereas the positive skewness indicate the film surface with larger number of local minima above the mean as compared to the Gaussian (skewness = 0). When compared to Gaussian distribution (kurtosis = 3), the surface with a high kurtosis has enormous local minima above the mean but for a surface with high number of local maxima has low kurtosis [30,31]. The roughness, kurtosis and skewness value of the films are given in Table 1. The negative value of skewness signifies topological surfaces with a plateau-like structure and positive value implies

b) Annealed at 200 °C



d) Annealed at 600 °C

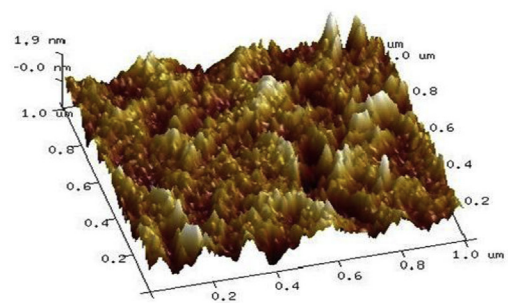


Table 1

The roughness, kurtosis and skewness values of the pristine and annealed HfO<sub>2</sub> thin films.

Sl. No	Sample	Roughness (nm)	Kurtosis	Skewness
1	As deposited	0.21	14.5	−0.92
2	Annealed at 200 °C	0.20	8.50	0.20
3	Annealed at 400 °C	0.19	3.01	0.07
4	Annealed at 600 °C	0.52	3.99	−0.22

surfaces without plateau. The high kurtosis value and positive skewness value surfaces result in a lower static coefficient of friction. A negative skewness value results in a deviation in Gaussian distribution. The above results indicate that the films may find potential applications in tribology [32–35].

XPS spectra of HfO<sub>2</sub> thin films annealed at different temperatures recorded in the spectral range of 0–1100 eV are shown in Fig. 4. All the spectra were calibrated by adjusting C 1s peak at 284.8 eV. The identification of chemical composition of the thin films was capacitated by the peak positions in XPS spectra. It is evident from the graph that no other trace element except hafnium, oxygen and carbon are present. The core elemental spectra corresponding to 4f peaks of Hf along with their spin-orbit splitting values were analyzed (shown in Fig. 5). The feature peaks in the range of 16–19 eV stipulate the formation of Hf-O bonding in HfO<sub>2</sub> [36]. The spin-orbit splitting values (1.7 eV) match well with the previous reports. The binding energy of Hf 4f<sub>7/2</sub> and Hf 4f<sub>5/2</sub> related to the Hf-O bond in HfO<sub>2</sub> shifted to higher binding energies with annealing. The shift in binding energy suggests the existence of the electric field, charge transfer effect, environmental charge density or hybridization [37].

The O/Hf relative concentration of the as-deposited thin films reveals almost stoichiometry (1.96:1). The deconvolution of Hf 4f peak at 16.2 eV and 17.9 eV indicate the formation of 4f<sub>7/2</sub> and 4f<sub>5/2</sub> corresponding to Hf 4f in hafnium oxide as-deposited films. The spectrum also suggests a small visible sub-peak towards the lower binding energy. This may be due to the presence of Hf-Hf bond and suggests oxygen



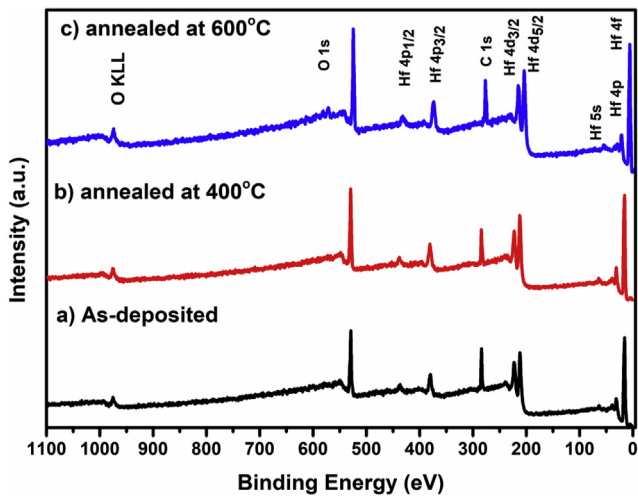


Fig. 4. The survey XPS spectra of as-deposited and annealed  $\text{HfO}_2$  thin films.

vacancies or defects in  $\text{HfO}_2$  thin films [38,39]. For annealed films, the shoulder peak shifts toward the higher binding energy values. This may be attributed to the formation of hafnium sub-oxide resulted from the interaction of the hafnium metal with the oxygen [40,41]. The result also suggests formation of hafnium-rich hafnium oxide and various interactions leading to sub-oxides formation. The bond formation of hafnium oxide, sub-oxides and their change could have resulted an increase in potential experienced by the core electron that leads to a

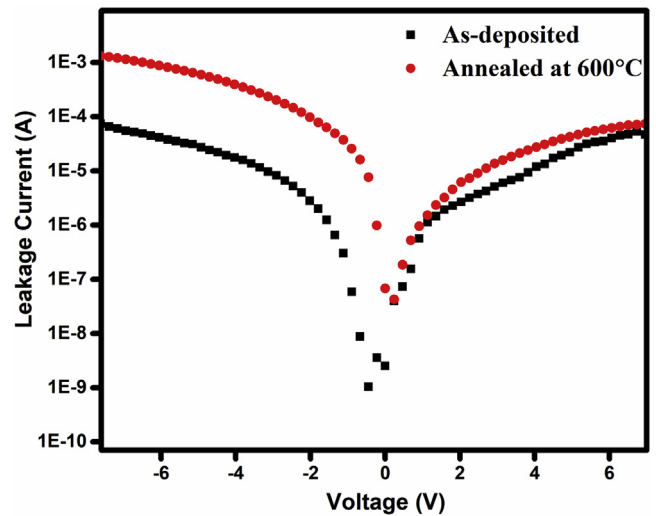


Fig. 6. I-V characteristics of as-deposited and annealed  $\text{HfO}_2$  thin film.

binding energy shift [42].

Current-Voltage characteristics of as-deposited and annealed films at 600 °C are shown in Fig. 6. The annealed films show more leakage current than compared to the as-deposited films. The crystallization of the films with annealing causes increase in leakage current due to leakage paths [43–45]. The asymmetric nature of I-V curve in the accumulation and inversion bias is observed in the Fig. 6. This indicates

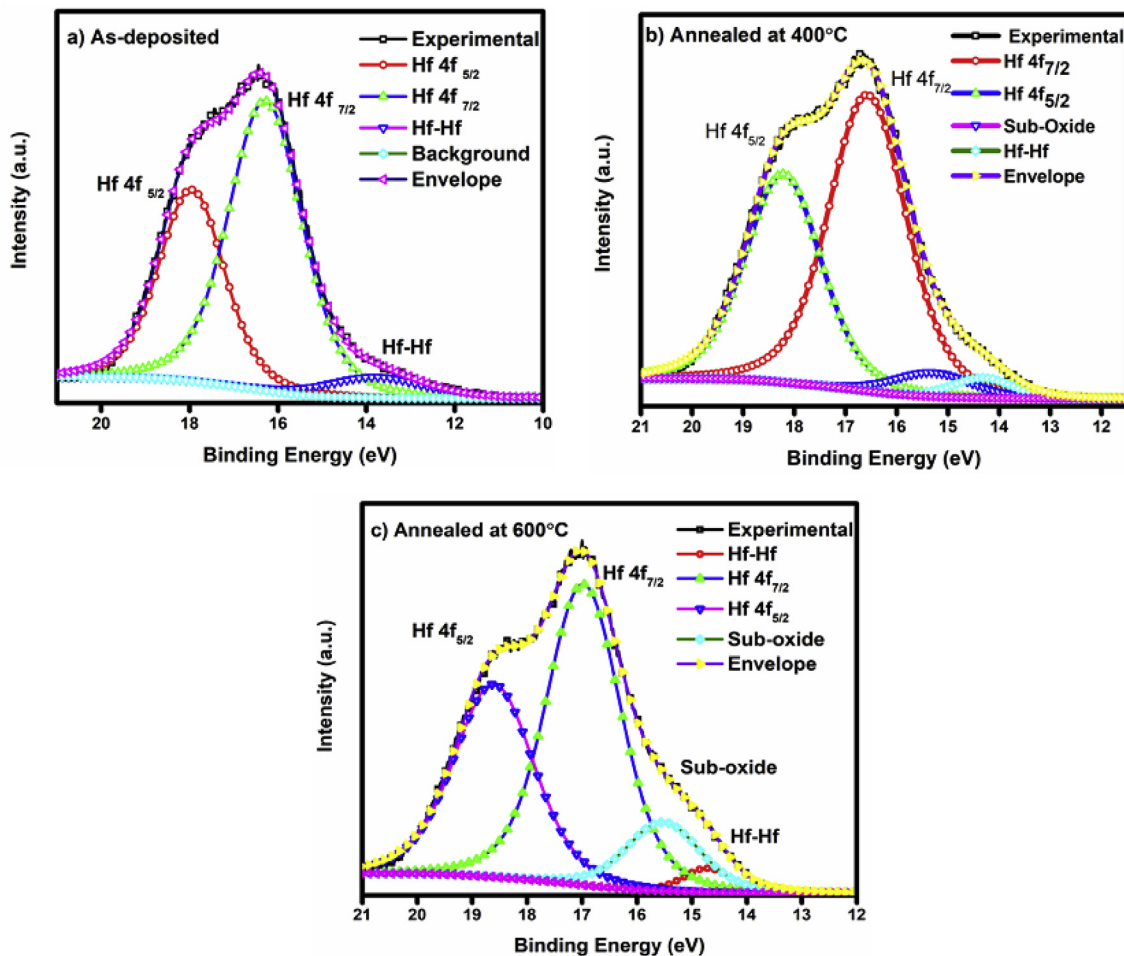


Fig. 5. The core elemental XPS spectra of Hf 4f regions of as-deposited and annealed  $\text{HfO}_2$  thin films.

that the leakage current under the substrate injection is lower than that under the gate injection at the same absolute voltage value [46,47].

Therefore, the growth process of the thin films may not only occur during the deposition but also with the later stages of post deposition annealing. The effect of annealing caused phase transition from amorphous to monoclinic structure. The crystalline films can increase the leakage current whereas an amorphous film restricts current leakage [48]. The AFM images reveal that the amorphous films are uniform than crystalline films. Thus, the amorphous thin film finds promising electronic application due to less current leakage rather than crystalline films [49,50].

#### 4. Conclusions

In summary,  $\text{HfO}_2$  thin films have been grown by RF magnetron sputtering on Si substrates. The effects of annealing temperature on structural, morphological, compositional and electrical properties were systematically investigated. The Raman analysis reveals the occurrence of phase transformation at high temperature. X-ray diffraction pattern confirms the formation of monoclinic structure. AFM images show that the amorphous films are of high-quality, which are smooth and crack free. Variation in kurtosis and skewness values reflect the potential tribological applications of the films. XPS spectra suggest shift in binding energy with annealing temperatures. Electrical measurements suggest the increase in leakage current with crystallization. The amorphous films exhibit better morphological, compositional and electrical properties than annealed crystalline films and these films are useful for electronic applications. It could be concluded that the annealing temperature strongly influence the structural, compositional and electrical properties of the films.

#### Acknowledgements

This work was supported by SERB, New Delhi (Project No: SR/FTP/PS-101/2013) and authors acknowledge MRC, MNIT Jaipur for the necessary experimental facilities.

#### References

- H. Iwai, S. Ohmi, Silicon integrated circuit technology from past to future, *Microelectron. Reliab.* 42 (2002) 465–491.
- H. Wong, V. a. Gritsenko, Defects in silicon oxynitride gate dielectric films, *Microelectron. Reliab.* 42 (2002) 597–605.
- M. Vargas, N.R. Murphy, C.V. Ramana, Structure and optical properties of nanocrystalline hafnium oxide thin films, *Opt. Mater.* 37 (2014) 621–628.
- S. Rudenja, A. Minko, D.A. Buchanan, Low-temperature deposition of stoichiometric  $\text{HfO}_2$  on silicon: analysis and quantification of the  $\text{HfO}_2/\text{Si}$  interface from electrical and XPS measurements, *Appl. Surf. Sci.* 257 (2010) 17–21.
- Y. Wang, Z. Lin, X. Cheng, H. Xiao, F. Zhang, S. Zou, Study of  $\text{HfO}_2$  thin films prepared by electron beam evaporation, *Appl. Surf. Sci.* 228 (2004) 93–99.
- V. Dave, P. Dubey, H.O. Gupta, R. Chandra, Influence of sputtering pressure on the structural, optical and hydrophobic properties of sputtered deposited  $\text{HfO}_2$  coatings, *Thin Solid Films* 549 (2013) 2–7.
- Feng Zhang, Guoxia Liu, Ao Liu, Byoungchul Shin, Fukai Shan, Solution-processed hafnium oxide dielectric thin films for thin-film transistors applications, *Ceram. Int.* 41 (2015) 13218–13223.
- J.W. Zhang, G. He, H.S. Chen, J. Gao, X.F. Chen, P. Jin, D.Q. Xiao, R. Ma, M. Liu, Z.Q. Sun, Modulation of charge trapping and current-conduction mechanism of  $\text{TiO}_2$ -doped  $\text{HfO}_2$  gate dielectrics based MOS capacitors by annealing temperature, *J. Alloy. Comp.* 647 (2015) 1054–1060.
- Wei En Fu, Yong Qing Chang, Layer structure variations of ultra-thin  $\text{HfO}_2$  films induced by post-deposition annealing, *Appl. Surf. Sci.* 257 (2011) 7436–7442.
- A.G. Khairnar, A.M. Mahajan, Effect of post-deposition annealing temperature on RF-Sputtered  $\text{HfO}_2$  thin film for advanced CMOS technology, *Solid State Sci.* 15 (2012) 24–28.
- Q. Du, W. Wang, S. Li, D. Zhang, W. Zheng, Effects of substrate temperature on the structural, optical and resistive switching properties of  $\text{HfO}_2$  films, *Thin Solid Films* 608 (2016) 21–25.
- C.T. Tsai, T.C. Chang, P.T. Liu, P.Y. Yang, Y.C. Kuo, K.T. Kin, P.L. Chang, F.S. Huang, Low-temperature method for enhancing sputter-deposited  $\text{HfO}_2$  films with complete oxidation, *Appl. Phys. Lett.* 91 (2007) 89–92.
- P. Kondaiah, H. Shaik, G.M. Rao, Studies on RF magnetron sputtered  $\text{HfO}_2$  thin films for microelectronic applications, *Electronic Materials Letters* 11 (2015) 592–600.
- T.-H. Moon, M.-H. Ham, J.-M. Myoung, Correlation of nanochemistry and electrical properties in  $\text{HfO}_2$  films grown by metalorganic molecular-beam epitaxy, *Appl. Phys. Lett.* 86 (2005) 102903.
- J. Gope, N. Batra, J. Panigrahi, R. Singh, K.K. Maurya, R. Srivastava, P.K. Singh, Silicon surface passivation using thin  $\text{HfO}_2$  films by atomic layer deposition, *Appl. Surf. Sci.* 357 (2015) 635–642.
- K.C. Das, S.P. Ghosh, N. Tripathy, D.H. Kim, T.I. Lee, J.M. Myoung, J.P. Kar, Evolution of microstructural and electrical properties of sputtered  $\text{HfO}_2$  ceramic thin films with RF power and substrate temperature, *Ceram. Int.* 42 (2016) 138–145.
- Seok-Woo Nam, Jung-Ho Yoo, Suheun Nam, Hyo-Jick Choi, Dongwon Lee, Dae-Hong Ko, Joo Ho Moon, Ja-Hum Ku, Siyoung Choi, Influence of annealing condition on the properties of sputtered hafnium oxide, *J. Non-Cryst. Solids* 303 (2002) 139–143.
- G. He, M. Liu, L.Q. Zhu, M. Chang, Q. Fang, L.D. Zhang, Effect of postdeposition annealing on the thermal stability and structural characteristics of sputtered  $\text{HfO}_2$  films on Si(100), *Surf. Sci.* 576 (2005) 67–75.
- D. Cano, S.J. Sandoval, Y. Vorobiev, F.R. Melgarejo, T.V. Torchynska, Peculiarities of Raman scattering in bioconjugated CdSe/ZnS quantum dots, *Nanotechnology* 21 (2010) 134016.
- A. Zwick, C. R. Multiple-order Raman scattering in crystalline and amorphous silicon, *Phys. Rev. B* 48 (1993) 6024–6032.
- T. Tan, Z. Liu, H. Lu, W. Liu, H. Tian, Structure and optical properties of  $\text{HfO}_2$  thin films on silicon after rapid thermal annealing, *Opt. Mater.* 32 (2010) 432–435.
- B. Zhou, H. Shi, X.D. Zhang, Q. Su, Z.Y. Jiang, The simulated vibrational spectra of  $\text{HfO}_2$  polymorphs, *J. Phys. D: Appl. Phys.* 47 (2014) 115502.
- A. Jayaraman, S.Y. Wang, S.K. Sharma, L.C. Ming, Pressure-induced phase transformations in  $\text{HfO}_2$  to 50 GPa studied by Raman spectroscopy, *Phys. Rev. B* 48 (1993) 9205–9211.
- M.A. Krebs, R.A. Condrate, Vibrational spectra of  $\text{HfO}_2\text{-ZrO}_2$  solid solutions, *J. Am. Ceram. Soc.* 65 (1982) c144–c145.
- A. Ramadoss, K. Krishnamoorthy, S.J. Kim, Novel synthesis of hafnium oxide nanoparticles by precipitation method and its characterization, *Mater. Res. Bull.* 47 (2012) 2680–2684.
- Arun Vinod, Mahendra Singh Rathore, T. Santhosh Kumar, D. Pamu, A.P. Pathak, N. Srinivasa Rao, Ion beam induced modification of structural and optical properties of  $\text{MgTiO}_3$  nanocrystalline thin films, *Radiat. Eff. Defect Solid* 172 (2017) 81–89.
- C.T. Kuo, R. Kwor, K.M. Jones, Study of sputtered  $\text{HfO}_2$  thin films on silicon, *Thin Solid Films* 213 (1992) 257–264.
- B.D. Cullity, Elements of X-ray Diffraction, First ed., Addison-Wesley Publishing Company, Inc., Massachusetts, 1956, p. 99.
- Jiaxun Liu, Xiumin Jiang, Xiangyong Huang, Shaohua Wu, Morphological characterization of super fine pulverized coal particle. Part 2. AFM investigation of single coal particle, *Fuel* 89 (2010) 3884–3891.
- B. Bhushan, Introduction to Tribology, second ed., Wiley, New York, 2013, pp. 17–30.
- Lisha Raghavan, P.A. Joy, B. Varma Vijaykumar, R.V. Ramanujan, M.R. Anantharaman, Defect induced modification of structural, topographical and magnetic properties of zinc ferrite thin films by swift heavy ion irradiation, *Nucl. Instrum. Meth. Phys. Res. B* 396 (2017) 68–74.
- K. Joy, L.V. Maneesha, J.K. Thomas, P.V. Thomas, Effect of sol concentration on the structural, morphological, optical and photoluminescence properties of zirconia thin films, *Thin Solid Films* 520 (2012) 2683–2688.
- K. Holmberg, A. Mathews, Coatings tribology: a concept, critical aspects and future directions, *Thin Solid Films* 253 (1994) 173–178.
- M. Sedlacek, B. Podgornik, J. Vižintin, Correlation between standard roughness parameters skewness and kurtosis and tribological behaviour of contact surfaces, *Tribol. Int.* 48 (2012) 102–112.
- N. Tayebi, A.A. Polycarpou, Modeling the effect of skewness and kurtosis on the static friction coefficient of rough surfaces, *Tribol. Int.* 37 (2004) 491–505.
- N. Zhan, M.C. Poon, C.W. Kok, K.L. Ng, H. Wong, XPS study of the thermal instability of  $\text{HfO}_2$  prepared by Hf sputtering in oxygen with RTA, *J. Electrochem. Soc.* 150 (2003) F200–F202.
- M.-S. Kim, Y.-D. Ko, M. Yun, J.-H. Hong, M.-C. Jeong, J.-M. Myoung, I. Yun, Characterization and process effects of  $\text{HfO}_2$  thin films grown by metal-organic molecular beam epitaxy, *Mater. Sci. Eng., B* 123 (2005) 20–30.
- R. Tang, K. Huang, H. Lai, C. Li, Z. Wu, J. Kang, Charge storage characteristics of Au nanocrystal memory improved by the oxygen vacancy-reduced  $\text{HfO}_2$  blocking layer, *Nanoscale Research Letters* 8 (2013) 368.
- B. Chen, R. Jha, V. Misra, Work function tuning via interface dipole by ultrathin reaction layers using AlTa and AlTaN alloys, *IEEE Electron. Device Lett.* 27 (2006) 731–733.
- C. Morant, L. Galan, J.M. Sanz, An XPS study of the initial stages of oxidation of hafnium, *Surf. Interface Anal.* 16 (1990) 304–308.
- M. Copel, R.P. Pezzi, D. Neumayer, P. Jamison, Reduction of hafnium oxide and hafnium silicate by rhenium and platinum, *Appl. Phys. Lett.* 88 (2006) 2004–2007.
- P.S. Bagus, F. Illas, G. Pacchioni, F. Parmigiani, Mechanisms responsible for chemical shifts of core-level binding energies and their relationship to chemical bonding, *J. Electron. Spectrosc. Relat. Phenom.* 100 (1999) 215–236.
- Peng Jin, Gang He, Dongqi Xiao, Juan Gao, Mao Liu, Jianguo Lv, Yanmei Liu, Miao Zhang, Peihong Wang, Zhaoqi Sun, Microstructure, optical, electrical properties, and leakage current transport mechanism of sol-gel-processed high-k  $\text{HfO}_2$  gate dielectrics, *Ceram. Int.* 42 (2016) 6761–6769.
- S.-W. Jeong, H.J. Lee, K.S. Kim, M.T. You, Y. Roh, T. Noguchi, W. Xianyu, J. Jung, Effects of annealing temperature on the characteristics of ALD-deposited  $\text{HfO}_2$  in

- MIM capacitors, *Thin Solid Films* 515 (2006) 526–530.
- [45] Rui Ma, Mao Liu, Gang He, Ming Fang, Guoliang Shang, Jiweng Zhang, Xuefei Chen, Juan Gao, Guangtao Fei, Lide Zhang, Effects of rapid thermal annealing on interfacial and electrical properties of Gd-doped HfO<sub>2</sub> high-k gate dielectrics, *J. Alloy. Comp.* 646 (2015) 310–314.
- [46] Zhen Xu, Michel Houssa, Stefan De Gendt, Marc Heyns, Polarity effect on the temperature dependence of leakage current through HfO<sub>2</sub>/SiO<sub>2</sub> gate dielectric stacks, *Appl. Phys. Lett.* 80 (2002) 1975–1977.
- [47] T. Yu, C.G. Jin, Y.J. Dong, D. Cao, L.J. Zhuge, X.M. Wu, Temperature dependence of electrical properties for MOS capacitor with HfO<sub>2</sub>/SiO<sub>2</sub> gate dielectric stack, *Mater. Sci. Semicond. Process.* 16 (2013) 1321–1327.
- [48] Hiroya Ikeda, Tomokazu Goto, Mitsuo Sakashita, Akira Sakai, Shigeaki Zaima, Yukio Yasuda, Local leakage current of HfO<sub>2</sub> thin films characterized by conducting atomic force microscopy, *Jpn. J. Appl. Phys.* 42 (2003) 1949–1953.
- [49] C.-H. Lin, Y. Kuo, Ruthenium modified Zr-Doped HfO<sub>2</sub> high-k thin films with low equivalent oxide thickness, *J. Electrochem. Soc.* 158 (2011) G162.
- [50] Hiroya Ikeda, Satoru Goto, Kazutaka Honda, Mitsuo Sakashita, Akira Sakai, Shigeaki Zaima, Yukio Yasuda, Structural and electrical characteristics of HfO<sub>2</sub> films fabricated by pulsed laser deposition, *Jpn. J. Appl. Phys.* 41 (2002) 2476–2479.

## CURRICULAM VITAE



**Mr. Arun Vinod,**  
**Azhakath, R.S.P.O.,**  
**Thiruvalla, Kerala-689111**  
**Mob: +91-8696732567**  
**Email ID: [aruvinod@gmail.com](mailto:aruvinod@gmail.com),**

---

### Educational Qualification :

- Ph.D. (Physics), Department of Physics, Malaviya National Institute of Technology, Jaipur, (2019)
- Master of Science (Physics), Mahatma Gandhi University, Kottayam, Kerala (2009)
- Bachelor of Science (Physics), Mahatma Gandhi University, Kottayam, Kerala (2007)

### Journal Publications :

1. **Arun Vinod**, Mahendra Singh Rathore, Srinivasa Rao Nelamarri, “Investigation of electrical and compositional properties of SiO<sub>2</sub>/Au/SiO<sub>2</sub> for nonvolatile memory application”, **Applied Physics A**, 124 (2018) 548.
2. **Arun Vinod**, Mahendra Singh Rathore, Srinivasa Rao Nelamarri, “Role of annealing temperature on charge storage characteristics of Au nanocrystals with HfO<sub>2</sub> tunneling and blocking layers”, **Superlattices and Microstructures**, 120 (2018) 616.
3. **Arun Vinod**, Mahendra Singh Rathore, N Srinivasa Rao, “Effects of annealing on quality and stoichiometry of HfO<sub>2</sub> thin films grown by RF magnetron sputtering”, **Vacuum**, 155 (2018) 339.
4. **Arun Vinod**, Mahendra Singh Rathore, T. Santhosh Kumar, D. Pamu, A. P. Pathak, N Srinivasa Rao, “Ion beam induced modification of structural and optical properties of MgTiO<sub>3</sub> nanocrystalline thin films”, **Radiation Effects & Defects in Solids**, 172 (2017) 81.
5. Santhosh Kumar, **Arun Vinod**, Mahendra Singh Rathore, A.P. Pathak, Fouran Singh, D. Pamu, N. Srinivasa Rao, “Effects of high-energy ion-beam irradiation on structural and optical properties of (Mg<sub>0.95</sub>Co<sub>0.05</sub>)TiO<sub>3</sub> thin films” , **Radiation Effects and Defects in Solids**, 173 (2018) 128.
6. Mahendra Singh Rathore, **Arun Vinod**, A. Rambabu, A. P. Pathak, Fouran Singh, T. Santhosh Kumar, N. Srinivasa Rao, “Ion beam modification of structural and optical properties of GeO<sub>2</sub> thin films deposited at various substrate temperatures using pulsed laser deposition”, **Applied Physics A**, 123 (2017) 708.
7. Mahendra Singh Rathore, **Arun Vinod**, N. Srinivasa Rao, “Effects of annealing temperature on structural, optical and electrical properties of Ge nanocrystals embedded in GeO<sub>x</sub> matrix” **Macromolecular Symposia**, 376 (2017) 1700024.
8. Mahendra Singh Rathore, **Arun Vinod**, N. Srinivasa Rao, “Structural and Optical Properties of GeO<sub>2</sub> Thin Films Prepared by E-Beam Evaporation”, **Advanced Science Letters**, 22 (2016) 3798.

## **Conferences/Workshops attended**

1. Presented poster at International Conference on Thin Films (ICTF-17) at CSIR-NPL, New Delhi, India, November 2017.
2. Presented a poster at an International Conference on Soft Materials (ICSM 2016), Jaipur, Dec 2016.
3. Participated in INUP Familiarization Workshop on Nanofabrication Technologies, Aug 2016, MNIT Jaipur.
4. Presented a poster at an International conference on Radiation Effects in Insulators, REI-18, Oct 2015
5. Presented a poster at National Conference on Recent Advancements in Chemical Sciences, Aug 2015 at MNIT Jaipur.
6. Participated in an International Conference on Soft Materials (ICSM 2014), Jaipur, October 2014.

## **ACADEMIC ACHIEVEMENTS**

- Received Best Out-going Student (High School) Award, Syrian Christian Seminary Higher Secondary School, Kerala, India, 2002.
- Best Oral Presentation Award, National Seminar on Nanoscience and Nanotechnology (NANO 2019), Bishop Moore College, Mavelikara, Kerala, Feb 2019.

## **PERSONAL PROFILE**

**Name** : Arun Vinod

**Father's Name:** Vinod George

**Date of Birth** : 01-October-1985

**Languages Known:** English and Malayalam

I hereby declare that above mentioned information is correct to the best of my knowledge and belief.

Arun Vinod